Ionospheric Convection and Auroral Responses to Solar Wind Driving

Maria-Theresia Walach

Radio and Space Plasma Physics Group

Department of Physics and Astronomy

University of Leicester

A thesis submitted for the degree of

Doctor of Philosophy

January 2017

Ionospheric Convection and Auroral Responses to Solar Wind Driving

Maria-Theresia Walach

Abstract

This thesis studies the large-scale dynamics in the Earth's magnetosphere due to solar wind driving. When the interplanetary magnetic field (IMF) is orientated southward, reconnection on the dayside magnetopause opens magnetic flux, which eventually reconnects in the magnetotail. When dayside reconnection is dominant, the polar cap, the area where open magnetic flux meets the Earth's surface, increases. Similarly, when nightside reconnection is dominant, the polar cap decreases in size. This framework is known as the expanding and contracting polar cap paradigm (ECPC). Part of this thesis considers the ionospheric flows, a part of the ECPC, which relates global auroral imagery of the size of the polar cap through a physics-based model of the ECPC, and compares the calculated ionospheric flow velocities to satellite, and ground-based measurements of plasma drift. The comparison also discusses the known limitations of the model and the observations. In the following chapters, specific events within the ECPC, or magnetospheric modes, are put into the context of solar wind driving and the auroral response. Substorms are a sporadic magnetospheric response mode, where the polar cap expands at first, followed by a distinct nightside brightening of the aurora and a decrease in polar cap flux. Steady magnetospheric convection events (SMCs) are times when the day-and nightside reconnection rates are balanced, such that the polar cap flux stays constant. By considering dayside reconnection rates and the magnetospheric response during these events, it is established that the majority of SMCs are part of the substorm cycle. Sawtooth events (SEs) appear as a quasi-periodic version of substorms, but occur under more extreme solar wind driving. It is shown that the aurora behaves according to the ECPC in terms of latitudinal expansions and contractions, but the temporal behaviour is significantly different from substorms.

Declaration

The research presented in this thesis is the work of the author. Information which has been taken from external sources has been appropriately referenced. The following scientific works have been published based on the studies presented in this thesis:

Walach, M. -T. ., and S. E. Milan (2015), Are steady magnetospheric convection events prolonged substorms?. J. Geophys. Res. Space Physics, 120, 17511758. doi: 10.1002/2014JA020631.

M.-T. Walach, The irregular pulse of the magnetosphere. A & G 2016; 57 (1): 1.34-1.36. doi: 10.1093/astrogeo/atw041.

Acknowledgements

Completing this thesis and the work within it has been a long and at times a circular walk, but thanks to all the support I have had, it has also been a joyful journey.

I thank my supervisor, Steve, who thought it was a good idea to take me on as a student in the first place and without whom this project would not have existed - I hope the disappointment is rather minor! I could not have asked for a better supervisor, so thank you for always being there, providing extensive guidance and wisdom, taking so much time to discuss and explain things, and reading all the words I have written over the years so swiftly - and thank you for teaching me all those transferable skills, like 'how to spot a circle', and perhaps most importantly, sarcasm.

Thank you, Tim, for being an excellent secondary supervisor, providing a witty commentary, and making the time for all those meetings. My gratitude goes out to 'Clan Milan' and all the RSPPers, for having provided crosswords, chocolates, cakes, support, words of wisdom and predominantly, FUN! Particularly, I thank Suzie, Jenny, Henrik and Jasmine for being excellent role-models, all the encouragement you have provided, and always taking the time to help me.

Completing a PhD is certainly not always easy or simple, so I thank the people from the University of Leicester Fencing Club for having provided a healthy environment for stress-relief. It has been a lot of fun being part of the women's team for so many years and having something to work on alongside research has helped me to stay focused.

I thank my family, for always having been supportive and encouraging, especially leading up to this great adventure.

Lastly, I thank Ben for having been on this incredible journey with me and always believing in me. It has kept me going, and made it all possible and worthwhile.

Contents

List of Figures

List of Tables

1

Introduction

'One loadstone[1] appears to attract another in the natural position; but in the opposite position it repels it and brings it to rights.'

from *De Magnete* by William Gilbert, translated by *Mottelay* [1893].

The subject of this thesis is the solar wind-magnetospheric and ionospheric coupling at Earth during Southward IMF. As this is a very broad field of research, the topic here focuses on the large scale phenomena, such as solar wind-driven dayside reconnection, subsequent nightside reconnection and the resulting plasma flows in the ionosphere.

There are some underlying physics concerning magnetohydrodynamics and space plasma physics, which are assumed to be true for the Earth's magnetospheric system (see section 1.6) throughout this work. These assumptions and physical principles are discussed in the following sections.

Plasmas occur naturally in many different places and forms. The term was first introduced by Langmuir for ionised gases, where only weak electric fields exist [*Langmuir*, 1929; *Alfvén and Faelthammar*, 1963]. In space plasma physics, it can usually be assumed that the number of positively charged particles is equal to the number of negatively charged particles, which is known as quasi-neutrality [*Alfvén*, 1950]. The flow of ionised plasmas, such as can be found in the solar wind, magnetosphere and ionosphere [*Alfvén*, 1950] can be expressed in terms of charged particles moving in

[1]Gilbert referred to, what is now commonly known as magnets as loadstones in his thesis.

electric and magnetic fields, but also as a fluid. Thus the term *magnetohydrodynamics*, which refers to a combination of the two is often used to group the equations which govern such space plasmas. This will be discussed in this chapter, along with single particle motion in space plasmas.

1.1 Lorentz Force

The Lorentz force [*Grant and Phillips*, 1990], **F**, which describes the force exerted on a charged particle of charge q travelling through magnetic and electric fields of strengths **B** and **E**, with velocity, **v** is given by

$$\mathbf{F} = q(\mathbf{E} + \mathbf{v} \times \mathbf{B}). \tag{1.1}$$

This equation can be likened to the equation of motion for plasma particles and can be applied to plasma particles travelling in fields, which will be discussed in a further subsection.

1.2 Maxwell's Equations

Maxwell's equations [see e.g. *Grant and Phillips*, 1990], valid for stationary electric and magnetic fields in a vacuum, can be written in their differential forms as

$$\nabla \cdot \mathbf{E} = \frac{\rho_q}{\varepsilon_0}, \tag{1.2}$$

where ρ_q is the charge density and ε_0 is the permittivity of free space in a vacuum, which is constant (8.854×10^{-12} F m^{-1} [e.g *Panofsky and Phillips*, 1956; *Grant and Phillips*, 1990]). Equation 1.2 is known as **Gauss' law**, named after the German mathematician Carl Friedrich Gauss, and describes mathematically how the divergence in the electric field is dependent on the charge density.

The divergence of a magnetic field is always zero, expressed mathematically as

$$\nabla \cdot \mathbf{B} = 0. \tag{1.3}$$

This is also known as the **No Monopoles Law**, as each magnetic field must have two poles.

Faraday's law, which describes that the curl of $\mathbf{E}$ induces a temporal magnetic field change, is defined as

$$\nabla \times \mathbf{E} = -\frac{\partial \mathbf{B}}{\partial t}. \tag{1.4}$$

The **Ampère-Maxwell** equation describes the contribution of a current and electric fields to the magnetic field strength:

$$\nabla \times \mathbf{B} = \mu_0 \left(\mathbf{j} + \varepsilon_0 \frac{\partial \mathbf{E}}{\partial t} \right). \tag{1.5}$$

1.3 Motion of Charged Particles in Magnetic and Electric Fields

In this subsection, the implications of the Lorentz force (see equation 1.1) in different fields, which are relevant to the Earth's magnetospheric system, are described.

1.3.1 Uniform Magnetic Field

A particle moving with a velocity, $\mathbf{v}$, perpendicular to a spatially and temporally uniform magnetic field of arbitrary magnetic field strength, $\mathbf{B}$, in a system where $\mathbf{E} = 0$, will experience the Lorentz force of the strength $q\mathbf{v} \times \mathbf{B}$ (eq. 1.1). This is visualised in the schematic in Figure 1.1, where the resulting motions of positively and negatively charged particles are shown in black. This force (orange arrows in Fig. 1.1) will act perpendicular to the particles' direction of travel and perpendicular to the magnetic field direction. As the force continually changes the trajectory of the particle, the result will be a gyrating motion of the particle around the magnetic field lines. As the force is only perpendicular to $\mathbf{v}$, the particle's overall velocity does not change. The direction in which the particle will gyrate will depend on whether it is positively or negatively charged, as shown in Fig. 1.1. The radius of the gyration, r_g, is given by

$$r_g = \frac{mv}{qB}, \tag{1.6}$$

where m is the mass of the particle. This implies that particles of the same mass will always take the same time for one qyration, even if they travel at different speeds [*Baumjohann and Treumann*, 1997].

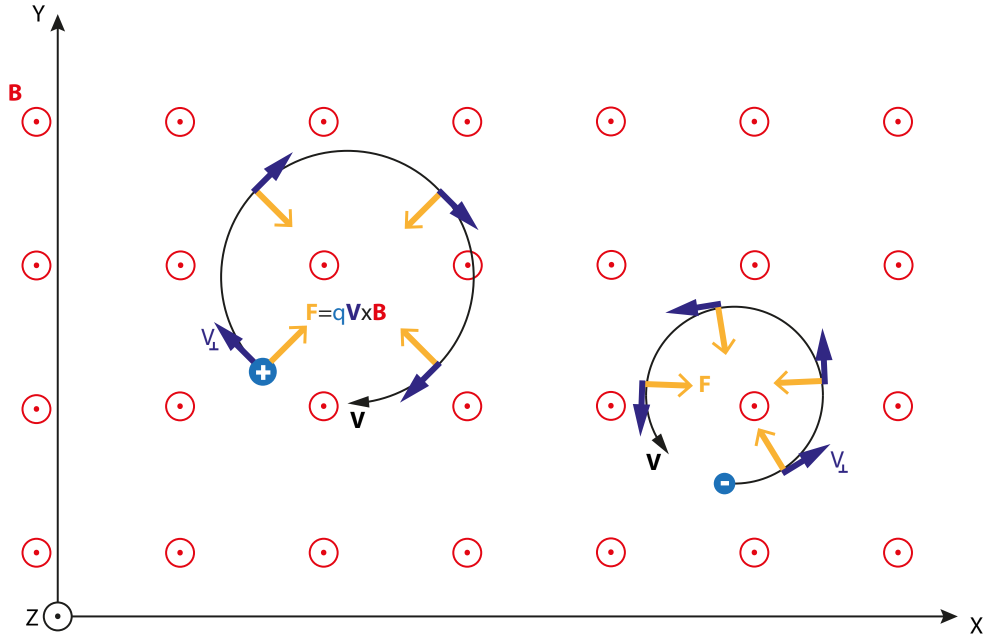

Figure 1.1: Visualisation of the motion of positively and negatively charged particles in a uniform magnetic field (red) with no electric field. The direction of the force each particle experiences will change as the particle moves and is shown with the orange arrows.

Assuming the particle also has a velocity component parallel to $\mathbf{B}$, the Lorentz force does not change the gyration radius or the overall speed of the particle, but instead the particle will travel in a helix. This type of motion is also known as guiding-centre motion, as the particle gyrates around a fixed axis in space, known as the guiding centre or centre of curvature [*Alfvén*, 1950]. The work in this thesis relies on the assumptions that all the plasmas we consider are collissionless (except for the ionosphere), which is to say that a charged particle moving through a magnetic field can be assumed not to collide with another particle during one gyration.

1.3.2 Non-Uniform Magnetic Field

If a particle travels through a non-uniform magnetic field with a velocity which has components perpendicular and parallel to the magnetic field, the particle's velocity will change. Assuming the lines of magnetic flux converge in one direction, as shown

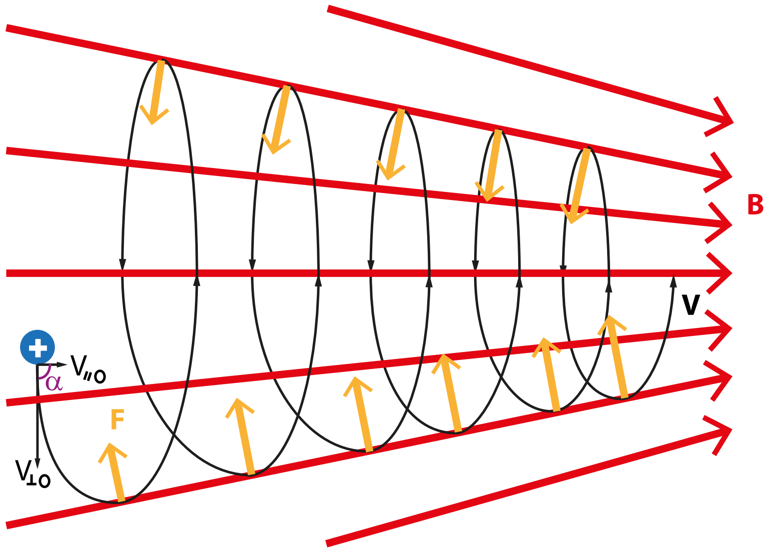

Figure 1.2: Visualisation of the motion of a positively charged particle in a non-uniform magnetic field (red) where the electric field is zero. The motion of the particle is shown by the black arrows and examples of the varying force vectors are shown in orange.

in the schematic in Figure 1.2, such that the magnetic field becomes stronger, the particle will still gyrate around the magnetic field, but in a spiralling motion. As **B** increases, the particle will also experience a Lorentz force component pointing in the other direction to the focus of the converging field, which will slow the particle's motion parallel to the magnetic field. The overall velocity of the particle is conserved, but the velocity component parallel to the magnetic field will decrease until it is zero at which stage the particle will accelerate back out the way it came.

This type of motion is also known as magnetic mirroring. If the magnetic field increases, the force which the particle experiences during one gyration is larger than in the initial magnetic field, so the magnetic moment, μ, is conserved [*Baumjohann and Treumann*, 1997]. This quantity can be expressed mathematically as

$$\mu = \frac{\frac{1}{2}mv_{\perp}^2}{B}, \tag{1.7}$$

which is also referred to as the first adiabatic invariant. In eq. 1.7, m is the particle's mass, $v_{\perp}$ is the particle's velocity perpendicular to the magnetic field, which possesses a magnetic field strength, B. To find the point along the converging magnetic field where a particle will mirror, the conservation of the particle's velocity has to be considered. Hereby the particle's total velocity, v, is given by

$$v^2 = v_\perp^2 + v_\parallel^2, \tag{1.8}$$

where $v_\parallel$ is the particle's velocity parallel to the magnetic field.

As eq. 1.7 and the total velocity stay conserved, it can be established that the particle will mirror when $v_\parallel$ is zero, at a point where B is B_m (the subscript denotes the mirror point):

$$B_m = B_0 \left(\frac{v}{v_{\perp 0}} \right)^2. \tag{1.9}$$

The mirror point is thus specified by the particle's velocity components and the magnetic field strength. This can also be expressed in terms of the particle's pitch angle, the angle of it's velocity vector with respect to the magnetic field lines, α as shown in Fig. 1.2, where

$$\tan\alpha = \frac{v_\perp}{v_\parallel}. \tag{1.10}$$

The Earth's dipolar field, converging at both ends of the field lines, is an example of a natural field configuration which allows magnetic mirroring to occur [*Baumjohann and Treumann*, 1997].

Other variations in $\mathbf{B}$ also induce particle motions, such as when $\nabla\mathbf{B} \neq 0$ and changes over a distance scale smaller than the particle gyroradius [*Baumjohann and Treumann*, 1997]. For example, if there was a gradient in $\mathbf{B}$ in the y-direction of the scenario shown in Fig. 1.1, the gyroradius of the particle would decrease as it entered a stronger field and thus, a particle-drift in the x-direction (or more generally, perpendicular to both $\nabla\mathbf{B}$ and $\mathbf{B}$) would be induced.

Similarly, if the magnetic field lines were to be curved, and the particle had an initial $\mathbf{v}_\parallel$ component, it would also drift perpendicular to the magnetic field and its curvature, which is known as curvature drift.

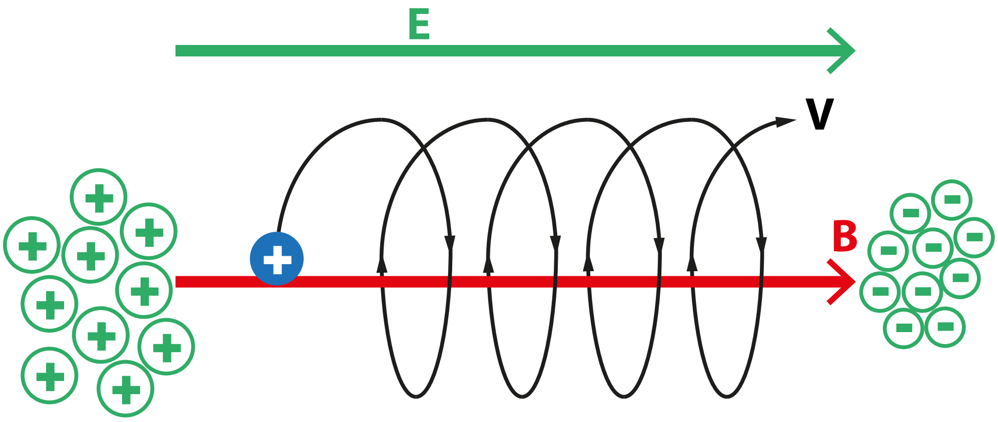

Figure 1.3: Visualisation of the motion of a positively charged particle in a uniform magnetic field (red) with a parallel electric field (green) applied to it.

1.3.3 Electric Field

As can be seen from equation 1.1, the Lorentz force exerted on a particle due to an electric field, is in the same direction as the field itself, independent of the direction of travel, unlike the case for a magnetic field. If an electric field exists parallel to a magnetic field, the particles will not only gyrate around the fields, but positively charged particles will also be moved along it (and negatively charged particles will be moved in the opposite direction to the field), as is shown in the schematic in Figure 1.3. As an electric field implies an initial charge unbalance (i.e. positively and negatively charged particles at a distance to each other), the particles will thus rearrange themselves very quickly to counteract the parallel electric field. It can therefore be said that in a plasma, which coexists with a magnetic field, all electric fields parallel to the magnetic field do not exist over noticeable timescales, such as the ones which will be considered in this thesis.

If the electric field is again constant, but perpendicular to the direction of the magnetic field, as shown in the schematic in Figure 1.4, any positive charges at rest will initially be accelerated along the direction of the electric field. As the magnetic field is perpendicular to the particles trajectory, the Lorentz force (orange arrows) will pull the particle around in a semi-circle. When the particle completes the semi-circle, the electric field will decelerate the particle, such that it comes to rest. At this

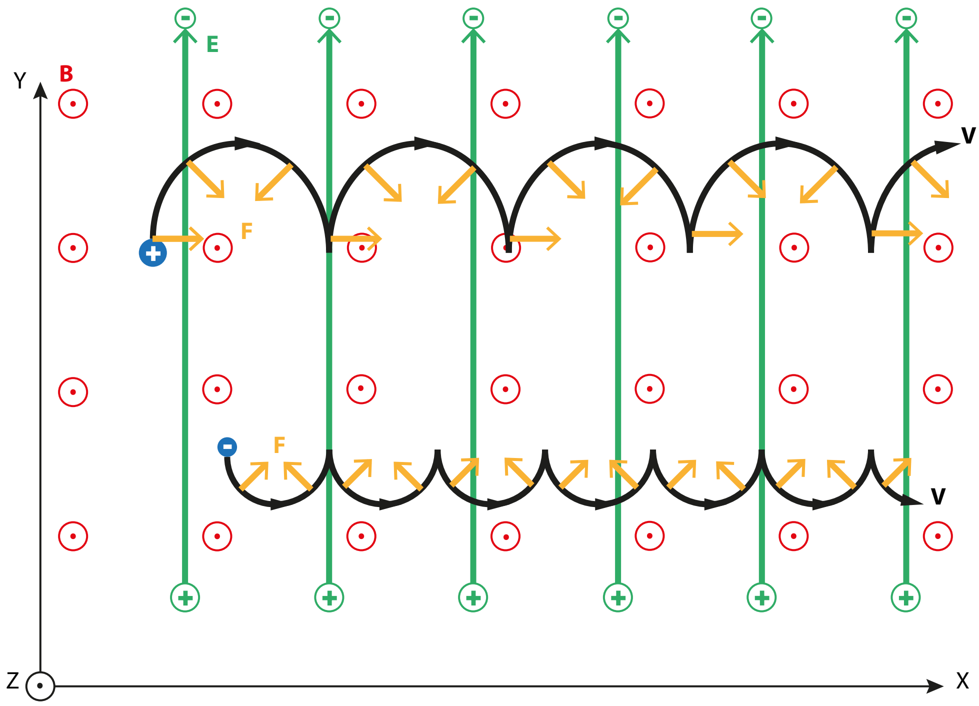

Figure 1.4: Visualisation of the guiding centre motion of a positively and a negatively charged particle in a uniform magnetic field (red) with a uniform perpendicular electric field (green) applied to it.

point the process will start again. For negatively charged particles, the mechanism is the same, but the acceleration and deceleration will be in opposite directions and the guiding centre arcs (as shown in Fig. 1.4) along which the particles travel will be smaller, due to the gyration radius being dependent on the mass of the particles. On top of the shown guiding centre motion of the particle, the particle will also gyrate, which is not shown in Fig. 1.4.

Overall, the electric field in this scenario will exert a drift, known as $\mathbf{E} \times \mathbf{B}$-drift, on the plasma for which the drift speed, $\mathbf{V}_{drift}$ [*Baumjohann and Treumann*, 1997] is given by

$$\mathbf{V}_{drift} = \frac{\mathbf{E} \times \mathbf{B}}{B^2}. \tag{1.11}$$

When $\frac{d\mathbf{E}}{dt} \neq 0$, polarisation or inertia drift will occur, meaning that the ions and electrons will also drift away from each other and thus a polarisation current will flow.

1.4 Magnetohydrodynamics

As mentioned earlier, rather than considering the individual particle motions, the bulk motion of the plasma can also be used to describe plasma motions. This is done by considering the plasma as a fluid.

Mass density in a plasma can be described as

$$\rho = n_e m_e + n_i m_i, \tag{1.12}$$

where n_e and m_e are the electron density and mass, respectively. The i-subscript refers to the ions in the plasma [*Schunk and Nagy*, 2000].

The **continuity equation**, or conservation of mass equation, is given by

$$\frac{\partial \rho}{\partial t} + \nabla \cdot (\rho \mathbf{V}) = \frac{d\rho}{dt}, \tag{1.13}$$

where ρ is the mass density, and $\mathbf{V}$ is the plasma velocity and $\frac{d\rho}{dt}$ combines sources and losses [*Schunk and Nagy*, 2000].

Similarly to equation 1.12, the **charge density**, ρ_q, in a plasma can be formulated as

$$\rho_q = e(n_i - n_e), \tag{1.14}$$

where $-e$ is the charge of an electron [*Schunk and Nagy*, 2000].

The **Poynting vector**, S, is a measure of the magnetic energy flow and is given by

$$\mathbf{S} = \frac{1}{\mu_0}\mathbf{E} \times \mathbf{B}, \tag{1.15}$$

where μ_0 is the permeability of free space in a vacuum, a constant of $4\pi \times 10^{-7}$ H m^{-1} [e.g. *Panofsky and Phillips*, 1956; *Grant and Phillips*, 1990].

1.4.1 Bulk Flow

The bulk ion motion, $\mathbf{V}_i$, is given by the average velocity of all ions,

$$\mathbf{V}_i = \frac{1}{n_i}\sum_j \mathbf{v}_{ij}, \tag{1.16}$$

where the subscript i stands for ions and j represents the number of individual ions. A similar equation can be established for electrons.

Current density is given by,

$$\mathbf{j} = n_i e \mathbf{V}_i - n_e e \mathbf{V}_e, \tag{1.17}$$

where V_e and V_i refer to the bulk velocities of the electrons and ions [*Schunk and Nagy*, 2000] and the **current strength** is

$$\mathbf{I} = \sum_s n_s e_s \mathbf{v}_s, \tag{1.18}$$

where the subscript s denotes the species of charge carriers, which in space plasma physics can be considered to be electrons only, as they move with respect to ions and are more mobile [*Baumjohann and Treumann*, 1997].

The equation of motion [*Schunk and Nagy*, 2000] of the bulk ion movement is given by

$$n_i m_i \frac{d\mathbf{V}_i}{dt} = n_i m_i \mathbf{g} - \nabla \mathbf{P}_i + n_i e \mathbf{E} + n_i e \mathbf{V}_i \times \mathbf{B} + \mathbf{F}_{ie}, \tag{1.19}$$

where g is the acceleration due to gravity, $\mathbf{P}_i$ is the ion pressure and $\mathbf{F}_{ie}$ is the force due to ion-electron collisions, given by

$$\mathbf{F}_{ie} = n\nu_{ie} m_i (\mathbf{V}_e - \mathbf{V}_i). \tag{1.20}$$

The equation of motion for electrons can be established in the same way, such that

$$n_e m_e \frac{d\mathbf{V}_e}{dt} = n_e m_e \mathbf{g} - \nabla \mathbf{P}_e - n_e e \mathbf{E} - n_e e \mathbf{V}_e \times \mathbf{B} + \mathbf{F}_{ei}, \tag{1.21}$$

where $\mathbf{F}_{ei}$ is equal and opposite to $\mathbf{F}_{ie}$. In order to find the overall movement of a plasma, the two equations of motions (eqs. 1.19 and 1.21) are added. By making the assumption that the plasma is charge neutral, such that $n_e \simeq n_i \simeq n$, and by applying equations 1.14 and 1.17, the general expression for the equation of motion then becomes the **momentum equation** for a quasi-neutral plasma

$$\rho \frac{d\mathbf{V}}{dt} = \rho \mathbf{g} - \nabla \mathbf{P} + \mathbf{j} \times \mathbf{B}, \tag{1.22}$$

where $\mathbf{V}$ is the mass-weighted average velocity of ions and electrons [*Schunk and Nagy*, 2000].

1.4.2 Ohm's Law

Ohm's law is often quoted as

$$\mathbf{E} = \frac{\mathbf{j}}{\sigma}, \tag{1.23}$$

where $\mathbf{E}$ is the electric field strength, associated with a current of strength, $\mathbf{j}$, flowing, for example in a wire with a certain conductivity, σ [*Grant and Phillips*, 1990]. However, Ohm's law can also be derived specifically using the MHD equations for a plasma.

If the two equations of motions (eqs. 1.19 and 1.21) are multiplied by m_e and m_i, respectively and then subtracted from each other, we get the generalised Ohm's law for MHD plasma [*Baumjohann and Treumann*, 1997]:

$$\mathbf{E} + \mathbf{V} \times \mathbf{B} = \eta \mathbf{j} + \frac{1}{ne}\left(\mathbf{j} \times \mathbf{B}\right) - \frac{1}{ne} \nabla \cdot \mathbf{P}_e + \frac{m_e}{ne^2} \frac{\partial \mathbf{j}}{\partial t}, \tag{1.24}$$

assuming $\frac{m_e}{m_i} < 1$, $n_i \approx n_e$, and $\mathbf{V}_i = \mathbf{V}$ Here, η is the resistivity and $\mathbf{P}_e$ is the electron pressure. Physically, the first term on the right-hand side is a resistive term, the second one is often referred to as the Hall term, introduced via the Lorentz force (see section 1.1), the third term is due to anisotropic electron pressure and the last term is formed due to the contribution of electron inertia to the current.

The last three terms in eq. 1.24 are important when for example hot plasmas are considered, but they tend to be small in space plasma physics, such that Ohm's law becomes

$$\mathbf{E} = -\mathbf{V} \times \mathbf{B} + \frac{\mathbf{j}}{\sigma}. \tag{1.25}$$

1.4.3 Magnetic Pressure and Tension

Using Ampère's law (1.5), it can be established that

$$\mathbf{j} \times \mathbf{B} = \frac{1}{\mu_0}(\nabla \times \mathbf{B}) \times \mathbf{B} = \frac{1}{\mu_0}(\mathbf{B} \cdot \nabla)\mathbf{B} - \nabla \frac{B^2}{2\mu_0}. \tag{1.26}$$

By comparing this equation to eq. 1.22, it can be established that the first of the two terms on the right hand-side can be interpreted as the **magnetic pressure**, P_{mag}, equivalent to

$$P_{mag} = \frac{B^2}{2\mu_0}. \tag{1.27}$$

The other term is given by a force which acts to reduce curvature in field lines, known as the **magnetic tension force**, $\mathbf{T}_{mag}$ [*Kivelson et al.*, 1995]. This acts towards the centre of curvature of the field lines, with radius $\mathbf{R}_c$, and is given by

$$\mathbf{T}_{mag} = -\frac{B^2}{\mu_0}\frac{\hat{\mathbf{R}}_c}{R_c}. \tag{1.28}$$

The ratio of the thermal plasma pressure to the magnetic pressure is known as the plasma beta, β, given by

$$\beta = \frac{n_i k T_i + n_e k T_e}{B^2/2\mu_0}, \tag{1.29}$$

where k is the Boltzmann constant [*Kivelson et al.*, 1995]. A plasma is described as *cold* if $\beta \ll 1$, and *warm* if $\beta \geq 1$, which is when currents become dominant in the plasma [*Kivelson et al.*, 1995].

1.4.4 Frozen-in Flow

By combining Ohm's law for an ideal MHD plasma (1.25) with Faraday's law (1.4) and Ampère's law (1.5), the induction equation can be established:

$$\frac{\partial \mathbf{B}}{\partial t} = \nabla \times (\mathbf{V} \times \mathbf{B}) + \frac{1}{\sigma\mu_0}\nabla^2\mathbf{B}, \tag{1.30}$$

where the first term on the right hand-side is a convective term and the second term is a diffusive term. When the magnetic field varies slowly with respect to the particles' gyroradii and gyration speeds, the diffusive term is negligible, but if sharp variations over small length scales develop, it can become significant. If the diffusion term in eq. 1.30 is negligible, the plasma is therefore dominated by convective flows.

If particles in a collisionless plasma are subjected to magnetic or electric fields which are slowly varying with respect to the particles' gyroradii and gyration speeds and if the first adiabatic invariant (eq. 1.7) is conserved, assuming Faraday's law (eq. 1.4) holds, the particles undergo *Frozen-in Flow*, meaning the plasma will travel with the magnetic fields and vice versa [*Alfvén and Faelthammar*, 1963]. This is also known as *Alfvén's Theorem*, named after Hannes Alfvén.

When the frozen-in condition applies, Ohm's law, eq. 1.24, becomes

$$\mathbf{E} + \mathbf{V} \times \mathbf{B} = 0, \tag{1.31}$$

as the plasma is collisionless, the terms on the right-handside of eq. 1.24 are approximately zero.

If the conductivity, σ, is very large, then the plasma is in a state which is known as ideal MHD. This means that there are no collisions, the plasma is charge neutral and Ohm's law becomes

$$\mathbf{E} = -\mathbf{V} \times \mathbf{B}. \tag{1.32}$$

When convection is dominant, a moving magnetised plasma therefore has an electric field associated with it.

When the frozen-in flux approximation applies, the plasma which is on the magnetic-field lines moves, but vice versa, the flux can be thought of as moving with the plasma. Which one of the two dominates the movement, will be determined by which of the two energies is larger: the magnetic energy (in this case the plasma follows the flux) or the thermal plasma energy (in which case the flux follows the plasma). Therefore, when the frozen-in condition applies, plasmas from different sources can not mix and different magnetic fields stay separated.

1.4.5 Magnetic Reconnection

When two magnetic fields are oppositely directed and border each other, despite the frozen-in approximation applying initially, they can mix when the diffusive term in equation 1.30 becomes significant.

This is known as magnetic reconnection, where a topological field change takes place. During this, the magnetic field lines 'break off' and 'reconnect'. The reconnection is driven by an inflow of plasma (see Figure 1.5), which has electric and magnetic fields associated with it. The electric field associated with the inflowing plasma is also known as the reconnection rate. Plasma is then accelerated away from the reconnection region by the tension force as magnetic energy is released (shown schematically in Fig. 1.5). In the centre of Fig. 1.5, where the reconnection takes place, an area exists (blue), where the ions and electrons are decoupled from each other, also known as the diffusion region. This is where the frozen-in approximation breaks down, due to the sharp gradients in $\mathbf{B}$.

Reconnection can for example, be observed in solar flares [e.g. *Yokoyama et al.*, 2001], at the subsolar magnetopause [e.g. *Phan et al.*, 2003; *Gosling et al.*, 2005] and also in the magnetotail [e.g. *Øieroset et al.*, 2001]. There are many direct, but mainly indirect, observations of reconnection occurring at the subsolar magnetopause and in the magnetotail. Magnetic reconnection occurring at the magnetopause and in the magnetotail are central to this thesis, as they drive large-scale convective flows in the magnetosphere and ionosphere.

1.5 Solar Wind

The thermal pressure in the Sun is too high for gravity to contain it, so it continually escapes through space. This escaping atmosphere, known as the solar wind, is too hot for electrons to remain bound to nuclei and it is thus a fully ionised plasma. Along with the plasma, travels the Sun's magnetic field, known as the interplanetary magnetic field (IMF). Magnetised bodies in space and their magnetic fields, such as the the Terrestrial system pose obstacles to the solar wind.

When the solar wind encounters such an obstacle, a shock boundary known as the bow shock is formed. This is where the supersonic solar wind flow is slowed to subsonic

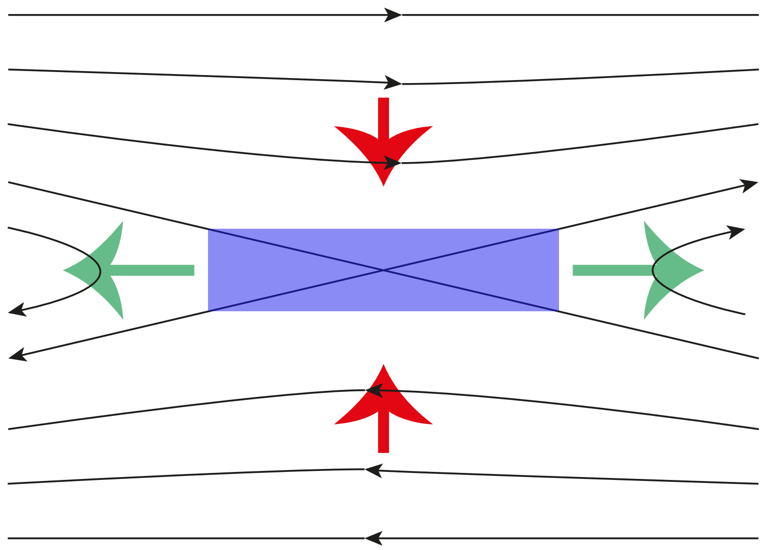

Figure 1.5: Schematic of the reconnection geometry showing the magnetic flux in black, the inflow and in red and green, respectively, and the diffusion region in blue. [adapted from *Øieroset et al.*, 2001]

velocities. Earthward of the bow shock, where the shocked plasma accumulates, lies a region called the magnetosheath, and within it, the magnetosphere [*Baumjohann and Treumann*, 1997].

1.6 The Terrestrial Magnetosphere

The Earth has a planetary magnetic field, which is approximately dipolar, with strength ∼31000 nT at the equator [*Alfvén*, 1950]. The magnetosphere was first defined by *Gold* [1959] as

> 'the region above the ionosphere in which the magnetic field of the earth has a dominant control over the motions of gas and fast charged particles.'

The Earth's magnetosphere is enclosed by the magnetopause, the boundary layer between the shocked solar wind plasma and the magnetosphere, as shown in Figure 1.6. Due to the frozen-in flow approximation being valid in both magnetospheric and solar wind plasma, the two populations do not mix, except for when reconnection occurs.

Close to the Earth, the ionosphere, located at altitudes of ~80-2000 km, forms the base to the magnetosphere, as well as the top layer of the atmosphere.

The stand-off distance of the magnetospheric boundary towards the Sun can be defined mathematically, in terms of a pressure balance between the the solar wind and the terrestrial field, whereby the solar wind ram pressure (also referred to as dynamic pressure), P_{SW} applied onto the magnetopause is given by

$$P_{sw} = nm_p V_{sw}^2. \tag{1.33}$$

In eq. 1.33, m_p is the mass of a proton, n is the number density and V_{sw} is the speed at which the solar wind travels. Eq. 1.33 is composed of the change of momentum, $m_p V_{sw}$, and the number of particles hitting the unit area of the magnetopause in unit time, nV_{sw}.

The magnetic pressure exerted by the Earth's magnetic field on the solar wind, P_{mag} is given by

$$P_{mag} = \frac{B_{MP}^2}{2\mu_0}, \tag{1.34}$$

where B_{MP} is the Earth's magnetic field strength at the magnetopause [*Baumjohann and Treumann*, 1997]. Of course the solar wind also has a magnetic pressure term, such as 1.34, but this is comparatively small to the dynamic pressure term (1.33) and vice versa for the magnetosphere. The magnetic field strength at the Earth's magnetopause is approximately twice the dipolar magnetic field strength, $\mathbf{B}_{dip}$, so by balancing equations 1.33 and 1.34 and knowing that the equatorial magnetic field strength of a dipolar field can be defined as

$$B_{dip} = B_{eq}\left(\frac{R_P}{R_{MP}}\right)^3, \tag{1.35}$$

where B_{eq} is the equatorial field strength, R_P is the planetary radius and R_{MP} is the stand-off distance of the magnetopause. Rearranging these equations for R_{MP} and using typical numbers for the solar wind at 1 AU ($n \sim 7$ cm^{-2}, $B_{eq} \sim 31000$ nT, V ~400 km s^{-1}), R_{MP} is thus approximately 9 Earth radii on the dayside.

At the nightside of the Earth, the terrestrial magnetic field stretches out, as there is no solar wind pressure stopping it from expanding away from the Earth, such that

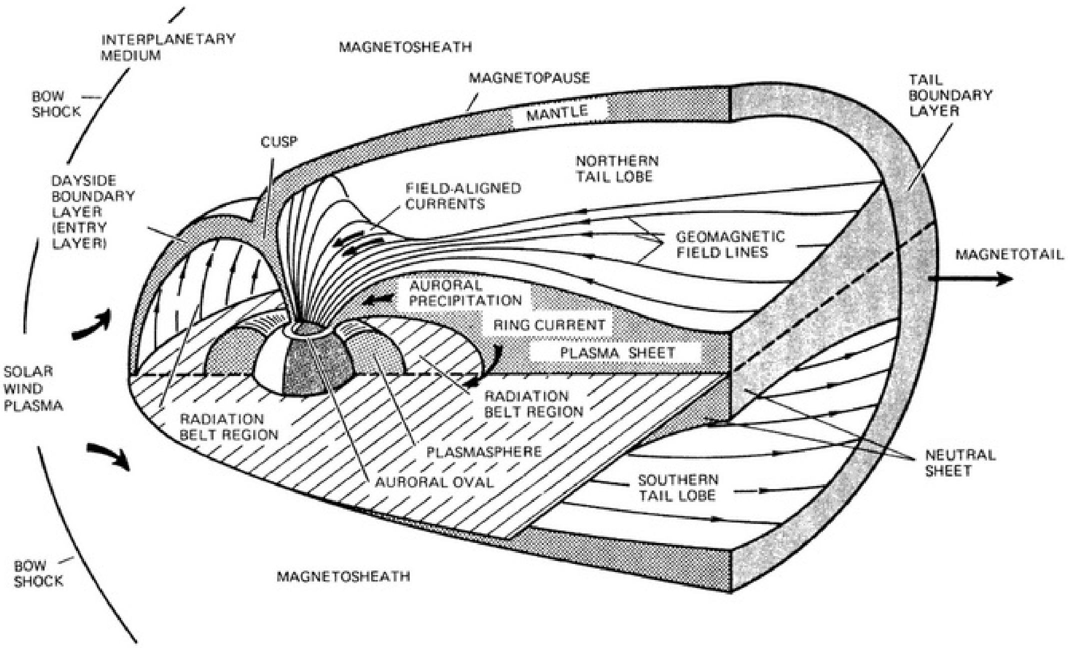

Figure 1.6: Schematic of the Earth's magnetosphere (not to scale) showing the different parts due to the interaction with the solar wind. The thin black lines with arrows show the sense of the magnetic field within the magnetosphere, whereas the thick arrows show plasma movements and currents [Original figure by J. G. Roederer, taken from *Evans et al.*, 1981].

the magnetosphere is asymmetrically shaped, like a bullet [*Sonett et al.*, 1960; *Heppner et al.*, 1963; *Ness*, 1965]. Away from the nose, at the flanks, the solar wind strikes the magnetosphere obliquely, such that it flares out (see schematic in Fig. 1.6).

Figure 1.7(a) shows a schematic view of the Earth's magnetospheric flux. Field lines in blue show the inner magnetosphere, which is made up of closed field lines. The open field lines (red) connect to the Earth's surface near the poles. The terminology of open and closed field lines originates from reconnection at the dayside magnetopause, whereby the Earth's magnetic field connects with solar wind flux [*Dungey*, 1961]. This open flux then continues to be pushed by the solar wind and drapes over the polar cap away from the Sun. At the nightside, the open flux tubes from the two hemispheres can then reconnect with each other once more, creating a cycle of opening and closing of flux. This is known as the Dungey cycle and will be revisited in chapter 2.

The majority of plasma in the Earth's magnetosphere can be defined as cold, meaning that the gyration radius (as described in section 1.3) is small in comparison to the curvature of the Earth's dipolar field [*Alfvén*, 1950]. This means that the cold plasma particles will gyrate around the Earth's magnetic flux. Superimposed on this motion are other particle motions as well: in the closed magnetosphere, most particles will also mirror when they reach their mirror points. Furthermore, mirroring particles will also drift, with the electrons moving eastward and the protons moving westward [*Singer*, 1957]. Most particles on open field lines, will mirror and eventually be lost to interplanetary space. Some do however collide with the ionosphere, lower atmosphere or even the surface in extreme cases.

1.6.1 Currents in the Magnetosphere

The terrestrial magnetosphere is laced with currents due to spatial gradients in **B**.

At the magnetopause, a current forms due to the gradient in the magnetic field (see eq. 1.5), brought about by the pressure balance between the two different regions. As the solar wind ions enter the region of denser magnetic field in the magnetopause, the Lorentz force exerted on them will make them turn around on themselves. The same happens for electrons, but they will circle in the opposite direction. This snaking movement of the particles along the boundary in opposite directions, will produce an overall current flowing along the magnetopause. This is shown schematically in Figure 1.7(b) in green. This magnetopause current, also known as the Chapman-Ferraro current, increases when the solar wind pressure increases, as it leads to a more compressed magnetosphere, meaning the magnetic field strength and the number of charge carriers inside the magnetopause increase [*Chapman and Ferraro*, 1931].

In the central plane of the magnetospheric tail, there is also a gradient in the magnetic field, as it points in the negative x-direction in the Southern hemisphere and the opposite way in the Northern hemisphere (see Fig. 1.7). Similar to the Chapman-Ferraro current, this leads to a current flowing (pink in Fig 1.7(b)), as the plasma will gyrate one way in one hemisphere and the opposite way in the other hemisphere. This is known as the cross-tail current. Overall, electrons will travel dawnward and ions will travel duskward, snaking along the y=0 plane, and thus giving the magnetopause currents a way to close on themselves.

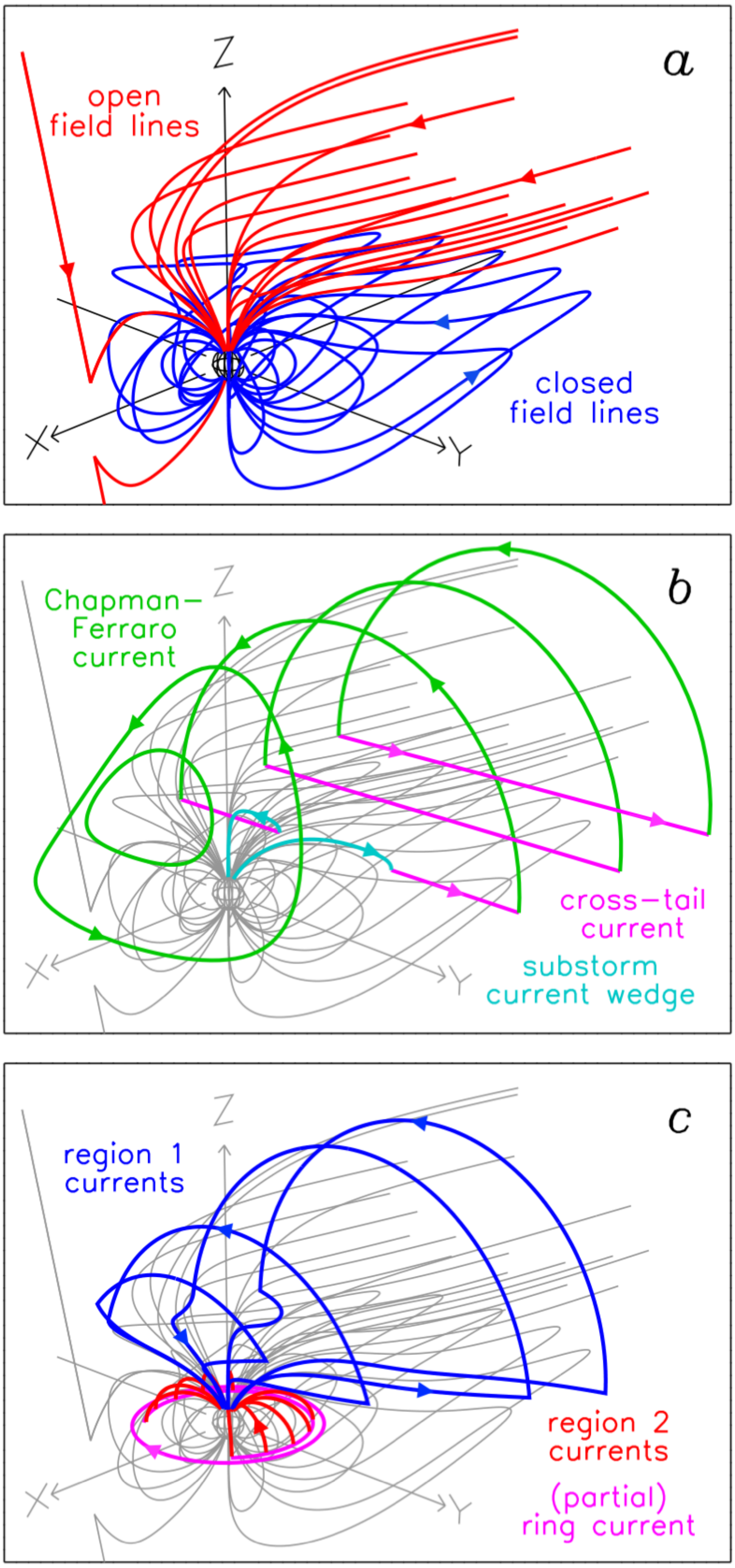

Figure 1.7: A schematic view from *Milan et al.* [2017] of the magnetospheric flux (panel a) and a view of where the global current systems close (b and c).

The substorm current wedge, which is a special case when the cross-tail current collapses into the inner magnetosphere, is shown in turquoise in Fig. 1.7(b) and only occurs during substorms, which will be explained in further detail in chapter 2.

The inner (closed) magnetosphere is inflated away from a perfectly dipolar configuration by the pressure of hot plasma. This gradient in the magnetic field and the field line curvature drive the westward-flowing ring current, shown in pink in Figure 1.7(c) [*Chapman and Ferraro*, 1931, 1941]. When the gas pressure in this region increases, the magnetic field is pushed outward and the ring current increases.

Field-aligned currents arise due the magnetosphere's interaction with the solar wind. Reconnection at the dayside magnetopause and in the nightside magnetosphere drives a convection of plasma and associated electric fields. This gives rise to further current systems, which is described in the next subsection.

1.6.2 Flows in the Magnetosphere

In the polar ionosphere, particles undergo $\mathbf{E} \times \mathbf{B}$-drift and as a result, there is an electric field across the polar cap, which is perpendicular to the magnetic field. This is driven by day- and nightside reconnection. In this section the flows resulting due to solar wind driving under southward IMF are explained.

Due to friction with the neutral atmosphere, the ionospheric plasma drags behind the convection in the magnetosphere. This causes a bend-back of the magnetic field lines, which kink in the ionosphere and at the magnetopause. The kinks in the magnetic flux are associated with perpendicular currents. In the ionosphere, these are known as Pedersen currents, $\mathbf{j}_P$, which merge at the magnetopause with the Chapman-Ferraro currents [*Milan et al.*, 2017].

The Pedersen currents going across the polar cap are shown schematically with the green arrows in Figure 1.8(a), which shows a top-down view of the polar ionosphere, enclosed by the purple oval showing the open/closed field line boundary.

The Pedersen and Hall currents can be thought of as positively and negatively charged particles drifting in opposite directions with respect to each other. These ionospheric currents are highly dependent upon the electron density and collisional cross-section of the plasma with the neutrals [*Milan et al.*, 2017].

The schematic in Fig. 1.8(a) also shows where the aforementioned substorm current wedge closes on the nightside (cyan). When this occurs, an additional current, the substorm electrojet can be measured (via magnetometer deviations) on the nightside (see thick green arrow in Fig. 1.8(a) denoted as DP1). This particular feature will be discussed further in the next chapter.

As the Dungey cycle requires flux being closed on the nightside, a current system driven by the return flows is set up surrounding the polar cap, as also shown in Fig. 1.8(a), which also gives rise to the eastward and westward auroral electrojets, named after the directions they flow in. These can be measured on the ground, as magnetic perturbations, known as DP2 systems. The deviations of the measured North-South component of the magnetic field on the ground are thus an indicator of these currents increasing or decreasing in strength. The opening and closing cycle therefore stirs magnetospheric flux around the system and with it, the plasma also moves (black arrows in Fig. 1.8(a)).

Fig. 1.8(a) and (b) also show schematically the expected locations of the FACs, also known as Birkeland currents, named after the Norwegian explorer, Kristian Birkeland [*Birkeland*, 1908; *Iijima and Potemra*, 1976]. The region 1 (R1) FACs are expected at the flow boundaries between the open field line region and the return flow region, as this is where a flow shear occurs [*Milan et al.*, 2017].

Also shown in Fig. 1.8(a) and (b) are the region 0 (R0) currents, which are located poleward of the region 1 and 2, or R1 and R2, systems near midday. If the IMF has a B_Y component, an east-west flow shear occurs at the dayside polar cap, which then brings about the DPY and R0 current system, with a positive IMF B_Y component bringing upward R0 FACs in the northern hemisphere and the opposite in the southern hemisphere [*Milan*, 2015].

Region 1 currents then close above the polar cap along the magnetopause currents, whereas region 2 currents close via the nightside ring current, as shown in Fig. 1.7(c). The aurora are expected to mainly occur between the footprints of the R1 and R2 FACs, as this is where downward streaming particles are accelerated on closed field lines. These can then interact with the ionosphere to energise atoms, which then emit photons as they decay back to the ground state.

Figs. 1.8(c) and 1.8(d) show the expanding and contracting polar cap. When dayside reconnection rate, Φ_D, is dominant over the nightside reconnection rate, Φ_N,

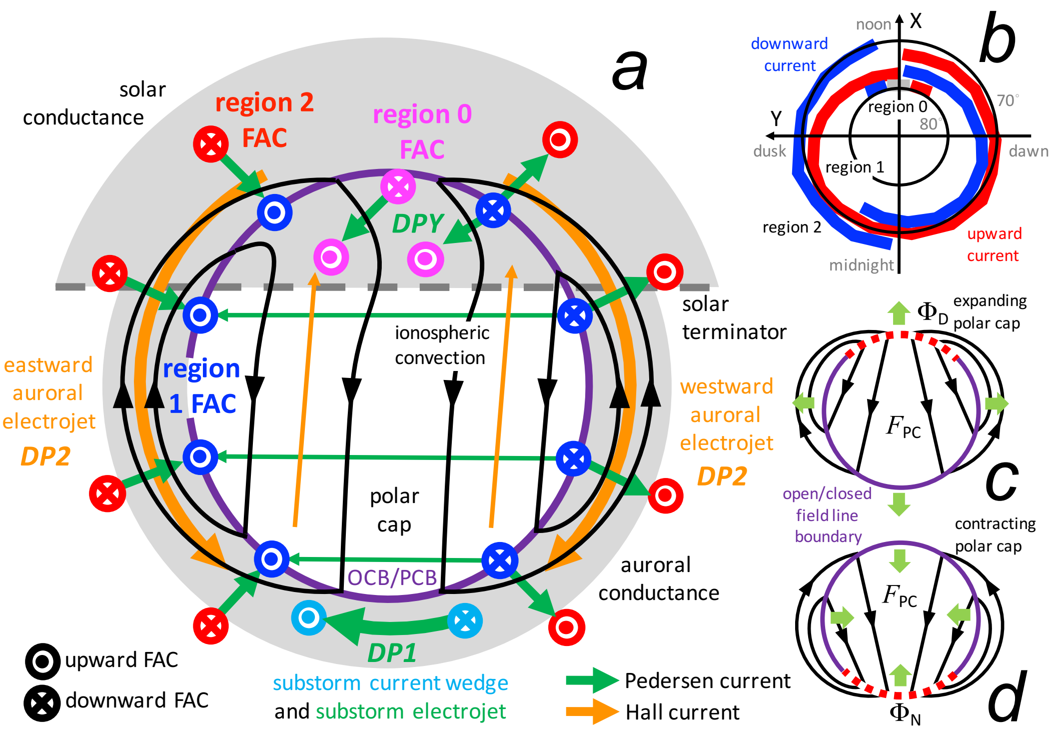

Figure 1.8: Schematics from *Milan et al.* [2017] of the where the currents close in the Northern polar ionosphere (panels a and b) and the ionospheric convection due to day- and nightside reconnection (panels a, c and d), with respect to the open closed field line boundary.

the polar cap will increase in size as more open flux is added to the system, shown in green arrows in Fig. 1.8(c). Vice versa, when $\Phi_N > \Phi_D$, the polar cap decreases in size, as shown in Fig: 1.8(d). This paradigm and the resulting dynamics will be discussed in further detail in the following chapters.

2

Literature Review

'Iron ore has and acquires poles, and arranges itself with reference to the Earth's poles.'

from *De Magnete* by William Gilbert, translated by *Mottelay* [1893].

In this chapter, literature relevant to the studies in chapters 4, 5 and 6 is presented and discussed.

The solar wind and magnetosphere-ionospheric system are coupled. This coupling is thought to be mainly driven by magnetic reconnection, which is defined as the process of plasma flowing across a surface which separates regions containing topologically different magnetic field lines [*Vasyliunas*, 1975]. *Paschmann et al.* [1979] showed for the first time that the reconnection occurs at the Earth's dayside magnetopause by providing evidence for the fast reconnection jets, matching the theoretical predictions of *Petschek* [1964].

In the literature, solar wind conditions which have a measurable effect on the Earth's magnetosphere are often characterised as 'geoeffective'. The solar wind can however vary in different ways, but under southward IMF the classical Dungey-cycle reconnection is favoured (see section 2.1). This is however not to say that the magnetosphere is not solar wind driven under different conditions. During northward IMF, for example, lobe reconnection can occur, which can manifest itself as bright aurora underneath the cusp (see Fig. 1.6), also known as the cusp spot [e.g. *Imber et al.*, 2007]. In the context of this work however, solar wind driving of the magnetosphere is considered in terms of dayside reconnection during southward IMF.

Fairfield and Cahill [1966] studied magnetic field data from the Explorer 12 satellite in conjunction with ground based magnetometer data. They found that out of a total of 82 hours of observations, 14 out of 18 bays[1] in the ground magnetometer data occurred during intervals of southward IMF (three medium and small sized bays occurred during undetermined IMF direction and only one very small bay occurred during northward IMF). This was one of the many studies which led the way to our current understanding of solar wind-magnetospheric coupling.

2.1 Large Scale Convection

In the field of magnetospheric physics, the term magnetospheric or ionospheric convection refers to both the plasma and magnetic flux moving 'frozen' together through the system as a result of reconnection at the magnetopause and in the magnetotail, and the two are used interchangeably.

During solar wind driving (i.e. reconnection under southward IMF), the polar ionospheric convection resembles two flow vortices, also known as twin-vortex flow or twin or dual cell convection [*Heppner and Maynard*, 1987]. The two cell convection pattern has been observed and studied by many scientists in the past, but for a long time, the physical cause was debated [e.g. *Axford and Hines*, 1961; *Dungey*, 1961; *Hines*, 1986].

Similarly, after *Ness* [1965] discovered that the Earth's magnetosphere is asymmetric and has a long tail of magnetospheric flux on the nightside, several scientists set out to explain these attributes of the magnetosphere.

2.1.1 The Dungey Cycle

Dungey [1961, 1963] in his attempt to explain the dual convection vortices, as well as the asymmetry of the magnetosphere, proposed the open magnetosphere model,

[1] In general, 'bays' refer to positive or negative deviations in the magnetometer measurements, which are usually attributed to the enhancements of the ionospheric auroral electrojets.

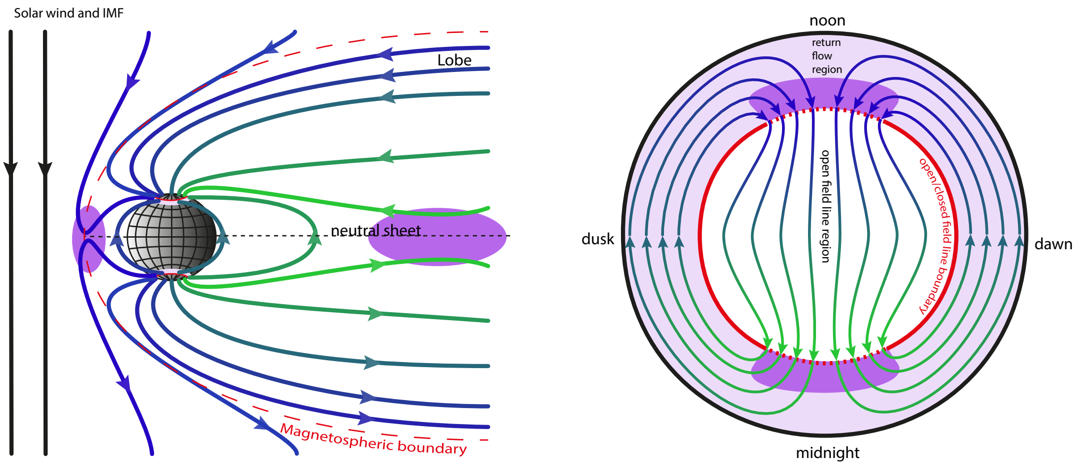

Figure 2.1: Schematic showing the Dungey cycle and the resulting ionospheric convection [adapted from *Walach and Milan*, 2016]. The diagram on the left depicts the magnetic fields (IMF in black and magnetospheric field in colour) from the side, whereas the view on the right depicts a top down view onto the magnetospheric pole. The lines in the schematic on the right depict the flow lines of plasma, with the colours corresponding to the colours of the magnetic flux as it proceeds through the Dungey cycle shown on the left. The purple areas in the schematic on the left show areas where we expect the separatrix to be and the purple areas in the diagram to the right, show where the reconnecting magnetic flux maps to in the ionosphere.

which is now known as the Dungey cycle. In *Dungey*'s model, magnetospheric flux is opened on the dayside by reconnecting with the IMF. The solar wind then pushes the open field lines anti-sunward [*Cowley and Lockwood*, 1992, 1996], where field lines from opposite hemispheres will reconnect again. How the magnetic flux progresses through the magnetosphere is indicated by the side view of the magnetosphere in the left schematic in Figure 2.1). The schematic on the right shows a top-down view of the polar regions where the lines indicate the flow of plasma. The colouring of the flow lines in the schematic on the right shows where the flux maps to.

As Alfvén's theorem applies to most processes in the magnetosphere (i.e. the ideal-MHD approximation applies), the plasma is bound to the magnetic field and vice-versa. Thus, the Dungey cycle does not only drive the magnetic fields around the system, but also stirs the plasma, which is bound to the field lines.

Lin and Anderson [1966] showed that part of the magnetospheric flux must be open and reconnected to the IMF, as solar flare electrons (> 40 keV) can propagate into the high latitude geomagnetic field regions containing open flux, i.e. the polar cap.

Although the Dungey cycle has since become a very powerful framework, which has helped to explain many idiosyncrasies of the terrestrial magnetospheric system, it has not always been accepted by the scientific community.

Axford and Hines in particular, decided that the open magnetosphere model as suggested by *Dungey*, could not explain the asymmetry in the magnetotail as well, as a closed system, which is solely driven by a viscous interaction. Albeit using different means of explaining the convection pattern, both *Axford and Hines* [1961] and *Hines* [1986] acknowledged the importance of the convection patterns:

> 'Regardless of its manner of generation ... the convective system that we discuss has consequences of far-reaching import, and it is these that we wish to emphasize in the present paper.'

Fairfield and Cahill's study however gave credibility to *Dungey*'s idea that the dayside reconnection is driven by southward IMF and it also paved the way for trying to understand what drives the dayside reconnection.

Since *Dungey* first proposed his model, it has become evident that the day- and nightside reconnection rates are not always balanced and constant [*Coroniti and Kennel*, 1973; *Meng and Makita*, 1986; *Cowley and Lockwood*, 1992; *Milan et al.*, 2009a; *Milan*, 2015], which led to the formulation of the expanding and contracting polar cap paradigm,. This forms an underlying theme of this thesis.

2.1.2 The Expanding and Contracting Polar Cap Paradigm

If the day- and nightside reconnection rates, Φ_D and Φ_N, vary, the amount of open magnetic flux in the magnetosphere must also be a time-dependent variable. The polar cap flux, or the amount of open magnetospheric flux, F_{PC}, is thus given by

$$\frac{dF_{PC}}{dt} = \Phi_D - \Phi_N, \tag{2.1}$$

where the day- and nightside rates of reconnection, Φ_D and Φ_N, are time-dependent variables [*Siscoe and Huang*, 1985; *Cowley and Lockwood*, 1992; *Lockwood and Cowley*, 1992; *Milan et al.*, 2003, 2007].

This means that when Φ_D is dominant over Φ_N, the polar cap will increase in size and with it, F_{PC}, as

$$F_{PC} = \int_{PC} \mathbf{B} \mathrm{d}A_{PC}, \tag{2.2}$$

where A_{PC} is the area, enclosed by the polar cap and $\mathbf{B}$ is the magnetic flux enclosed within it [*Siscoe and Huang*, 1985; *Cowley and Lockwood*, 1992; *Milan et al.*, 2003]. Similarly, when Φ_N is dominant, the polar cap reduces in size and F_{PC} decreases.

As plasma flows across the polar cap, an electrostatic potential has to exist perpendicular to the flow lines, with the minimum at dusk and the maximum at dawn [*Cowley and Lockwood*, 1992; *Lockwood and Cowley*, 1992]. If the reconnection on the day- and nightsides of the magnetosphere occur symmetrically along the separatrix and there is no asymmetry in the dusk-dawn direction of the pressure applied onto the magnetosphere, the minimum and maximum potentials will be equal. That is to say, the convection cells are equal in size, as depicted in the right-hand panel in Fig. 2.1. The electrostatic potential across the polar cap, or the cross polar cap potential, Φ_{PC}, is thus given by

$$\Phi_{PC} = \frac{1}{2}(\Phi_D + \Phi_N). \tag{2.3}$$

The rate at which magnetospheric flux is opened at the dayside, Φ_D, is dependent on the solar wind conditions [*Caan et al.*, 1977; *Perreault and Akasofu*, 1978; *Meng and Makita*, 1986; *Milan et al.*, 2007, 2012] (as will be discussed in the following section), whereas the rate at which open flux is closed in the magnetotail, Φ_N, is thought to vary independently of the solar wind conditions and as a result, F_{PC} is variable and difficult to predict.

The magnetospheric response to dayside driving can be measured in different ways. A popular, and perhaps the oldest measure, is to study the auroral response. Along with changes in the aurorae, the magnetospheric and ionospheric current systems also respond [*Birkeland*, 1908]. The enhancements of the eastward and westward electrojets is inferred from the intensification in the Auroral Upper (AU) and Auroral Lower (AL) indices, where AU and AL are computed by tracing out the upper and lower envelopes of overlaid measurements of the North-South magnetic deviations in the auroral zones [*Davis and Sugiura*, 1966].

2.2 Estimating Reconnection Rates and the Open Closed Field Line Boundary

Being able to predict the reconnection rates at Earth has been of great interest to many scientists. In-situ measurements of reconnection are difficult, as the spacecraft has to be in the frame of reference of the separatrix, which is often in motion. Thus a number of remote sensing methods to estimate reconnection rates have been developed.

The component of the ionospheric convection electric field which lies tangential to the ionospheric projection of the reconnection separatrix (i.e. the X-line), in the frame of reference of the separatrix, gives the reconnection rate [*Chisham et al.*, 2008]. Therefore, when ground based measurements are used to estimate reconnection rates, care has to be taken because plasma convecting across the separatrix can contribute, as well as the separatrix moving itself.

Blanchard et al. [1996] for example utilised a ground based incoherent scatter radar to measure ionospheric flows across the nightside separatrix, the region along the polar cap boundary which maps to the reconnection X-line, and calculate the nightside reconnection electric field. Another study by the same author looks at the dayside magnetic separatrix in the prenoon and noon sectors using similar methods [*Blanchard et al.*, 2001]. By tracking the location of the separatrix and measuring ionospheric plasma velocities using the incoherent scatter radar, the local dayside reconnection rate is inferred. Whilst their method ensures a high accuracy, it also has limitations: the estimation of dayside or nightside reconnection electric field and locating of the separatrix is limited to the radar's location. Thus it is impossible to have measurements of the day- and nightside reconnection rates, unless an extensive incoherent scatter radar network is put in place. Another limitation is that measurements of the reconnection rates can only be inferred when the polar cap boundary is within the field of view of the radar. The method used by *Blanchard et al.* [2001] for determining the dayside reconnection electric field requires the knowledge of the ionization rate as a function of altitude. From this, the photoionization rate is deduced and the result is then used to determine the average energies of precipitating electrons. The altitude of peak ionization and the maximum ionization rate are then used to determine whether or not the field lines are open or closed, assuming that the electron precipitation on trapped magnetospheric field lines is much harder than the electron precipitation on open field lines. *Blanchard et al.* [2001] found that with a moderate peak ionization rate (900 to 2200 $cm^{-3}s^{-1}$), the field line is considered closed if the peak ionization occurs below 140 km and open if it occurs above it. Their method allows an identification of open/closed field line region with an accuracy of 0.36° and a precision of ±0.39°. Unfortunately, they also found that in the postnoon sector, it is difficult to employ this method as the electron precipitation is generally weaker and the differences between peak ionization and peak ionization rate on open and closed field lines are not as systematic as in the prenoon and noon sectors. Therefore the method is unreliable postnoon or cannot be used there at all, constraining the location of the measurements considerably.

Chisham et al. [2008] used the SuperDARN radars (see chapter 3) to estimate the global ionospheric convection velocity field and thereby estimate reconnection rates. The advantage of this is that the SuperDARN network covers a large portion of the ionospheric convection regions. The main weakness of this technique, is that, although the network is extensive and purposely built to measure the ionospheric convection potential, good quality measurements are not always available in the desired locations, and the technique is not suitable for small-scale structures of less than ∼100 km [*Chisham et al.*, 2008].

Hubert et al. [2006] proposed a method for measuring reconnection rates from auroral IMAGE FUV SI12 and SuperDARN data. With their method, they determined the open- and closed-field line boundary and its motion using the auroral data. Then *Hubert et al.* [2006] used the radar data and Faraday's law to determine the convection electric field along the boundary. With this method, the resolution of day- and nightside reconnection rates, as well as the polar cap flux can be resolved to 15 minutes time-resolution, but similarly to the aforementioned methods, it relies on having a timeseries of good IMAGE and SuperDARN data available.

After the work of *Fairfield and Cahill* [1966], tying solar wind activity or IMF orientation to magnetospheric activity, became of interest to many scientists. *Arnoldy* [1971] for example showed that an enhanced AE index, and therefore substorms, occur mostly after the IMF has been southward for approximately an hour to fuel the magnetosphere with open flux. After this, it soon became apparent that not only auroral activity levels, but also the amount of open flux via the dayside reconnection

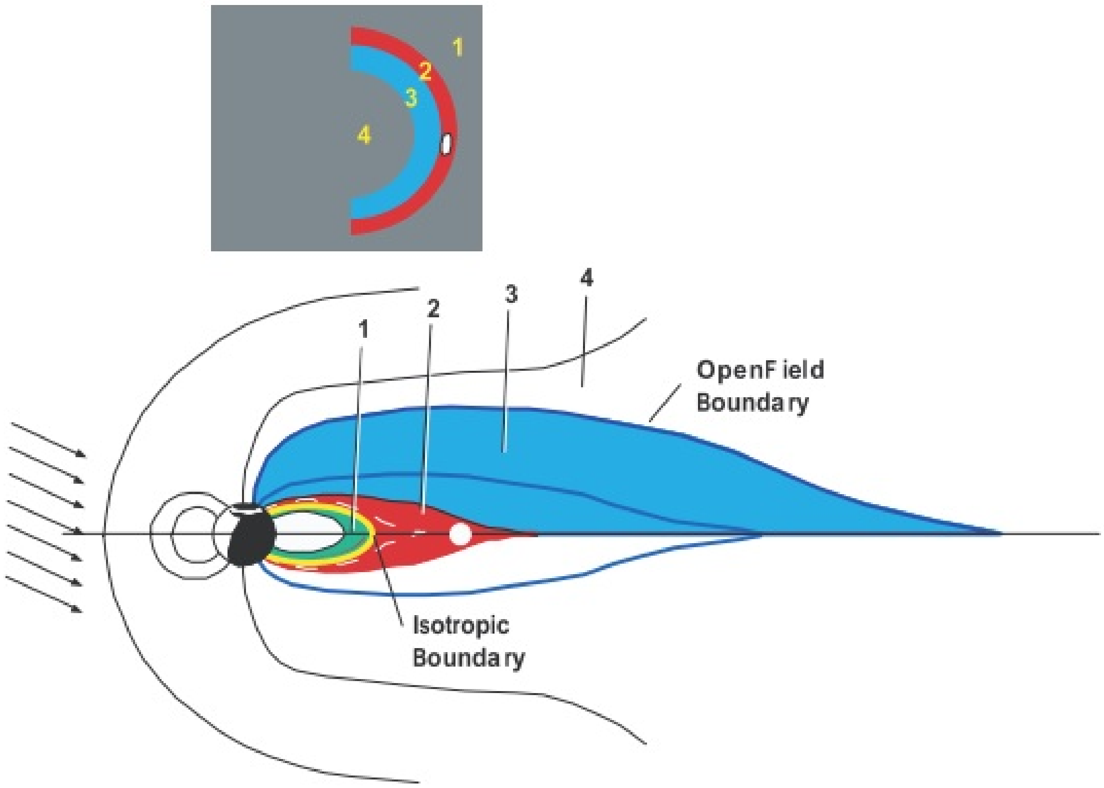

Figure 2.2: Diagram showing the nightside particle distributions and where they map to in the auroral zones at substorm onset, adapted from [*Mende et al.*, 2003]. Region 1) (green) shows trapped ring current particles; the region in yellow shows the isotropic boundary; regions 2) and 3) (red and blue) show the the diffuse electron and intense proton auroral regions, respectively. The white spot marks where substorm onset occurs and region 4 shows the open field line region.

rate, and therefore much of the magnetospheric activity, is controlled by the solar wind. These topics will be explored further in the following sections.

2.2.1 Mapping the Aurorae

The aurora is made up of different particle distributions which map to distinct parts of the magnetosphere. Using this information, the open closed field line boundary can be inferred. An example of this is shown in the diagrams in Figure 2.2 [*Mende et al.*, 2003].

The diagram (Fig. 2.2) shows where the particle distributions in the tail (large diagram showing magnetosphere from the side) map to with respect to the aurora (small diagram showing the nightside aurora). Region 1 (green) shows the ring current particles, which do not create aurorae, as they are trapped on very dipolar field lines. The thin yellow region shows the isotropic boundary. This maps to the low latitude boundary of the proton aurora [*Sergeev et al.*, 1983]. Here, low altitude satellites measure a double loss cone ion distribution, which indicates particles are trapped by bounce motion on closed field lines [*Sergeev et al.*, 1983]. Outside of the isotropic boundary (region 2 in red) is where the magnetic field lines in the tail are stretched enough for a considerable amount of pitch angle scattering of protons to occur, such that protons from the central plasma sheet enter the loss cone, collide with the atmosphere and produce proton aurora. Region 3 in blue shows where the diffuse electron aurora occurs, which is also driven by pitch angle scattering. This is primarily where the visible aurora occurs. *Sergeev et al.* [1983] found that the magnetic field radius of curvature at the equator divided by the particle gyroradius has to be less than 8 for enough ions to fill the loss cone and be able to scatter into the atmosphere. The red region in Fig. 2.2 shows the more energetic proton emission and the blue region the more diffuse and structured aurora. *Blanchard and McPherron* [1995] in particular showed that the polar cap boundary, the boundary between open and closed field lines, is identifiable by 6300 Å (red line) auroral emission caused by low energy electrons ($\lesssim$ 1 keV). Region 4 in Fig. 2.2 links to the polar cap where we do not expect to see much aurora [*Mende et al.*, 2003]. *Makita et al.* [1988] however showed that the open field line region can host burst-type soft electron precipitation, in particular during northward IMF. The white spot in Fig. 2.2 shows where substorm onset is thought to occur most of the time, which is discussed further in section 2.3.1.

Each particle distribution always possesses a variety of energies and the particle boundaries are not always as clear cut as is made out in the diagram in Fig. 2.2. *Lockwood* [1997] explained this: 'Thus not only does a spectrum of particle energies from one point in the magnetosphere map to a spread of locations in the ionosphere, but also, a spread of energies seen at any point (at a fixed pitch angle) in the ionosphere maps to a spread of source locations in the magnetosphere.'

Similarly, *Blockx et al.* [2005] used IMAGE SI12 data to show that there is good correspondence between the latitude of the maximum proton auroral intensity, and the isotropic boundary measured by the DMSP satellites, and that it varies with magnetic local time. They used magnetic field measurements from the GOES 8 satellite to find the relation between the position and brightness of the maximum proton aurora intensity and the magnetic field distortion. The main finding of *Blockx et al.* [2005] is that SI12 images can be used as a tool to globally determine the isotropy boundary, as the data acts as a proxy for the level of stretching in the magnetotail.

Lockwood et al. [1998] discussed the results of *Shirai et al.* [1997] who found in a case study that the open-closed field line boundary is $\sim 2^{\circ}$ poleward of any plasma sheet particle distribution, which includes a significant amount of magnetic flux. *Lockwood et al.* [1998] make the observation that taking the aurora as a proxy for the open-closed boundary is therefore likely to overestimate the amount of open magnetospheric flux. *Sandholt et al.* [1998] for example showed that the equatorward boundary of the aurora also recesses equatorward in a stepwise manner every time the IMF turns southward. They found that in some cases the motion covers ~100-200 km in ~ 5-10 minutes.

The majority of electron aurora is a diffuse emission, which is thought to be caused by pitch-angle scattering of central plasma sheet electrons into the loss cone [*Newell et al.*, 1991]. The intense electron aurora, the discrete emission, on the other hand is thought to originate from electrons which are accelerated along the magnetic field lines in the boundary layer of the plasma sheet [*Craven and Frank*, 1985].

As already alluded to, the electron aurora can also be mapped to specific regions in the magnetosphere. For example, the open field line region surrounding the pole can contain sporadic electron precipitation known as polar rain [*Winningham and Heikkila*, 1974; *Newell and Meng*, 1990]. The electron aurora data which is presented in this thesis however is not sensitive enough to show this. This does mean that the electron aurora is not as good an indicator of the open-closed field line boundary as the proton aurora, as the boundary can be blurred by the polar rain [*Mende et al.*, 2003].

The equatorward boundary of the diffuse aurora (blue region in Fig. 2.2 was found to be collocated with the inner edge of the plasma sheet [*Eather and Mende*, 1972].

Care has to be taken when using measurements of the electron aurora from different instruments to identify magnetospheric regions as the features and locations of electron aurora observations can differ significantly from ground and space [*Mozer and Bruston*, 1966].

Work by *Hubert et al.* [2006] and *Boakes et al.* [2008] showed (using data from the IMAGE satellite) that the inner edge of the proton aurora can be used as an adequate locator for the open-closed field line boundary with the spatial uncertainty being smaller than that of *Shirai et al.* [1997] ($\sim 1°$).

2.2.2 Driving Functions

Inspired by the early work linking magnetospheric and solar wind activities, numerous solar wind-magnetosphere coupling functions or driving functions have been devised and studied [see for example table 1 in *Newell et al.*, 2007] to serve as proxies for the dayside reconnection rate or energy input into the magnetosphere. Some formulations such as the ones proposed and discussed by *Borovsky et al.* [2008], and *Borovsky and Birn* [2014] are based solely on numerical simulations, and as the proposed coupling functions exist aplenty, only some of the most common used and empirically-derived ones are discussed here.

One of the most popular driving functions from *Perreault and Akasofu* [1978], also known as the ε-parameter, envisaged to encompass the energy input from the solar wind to the magnetosphere and is given by

$$\epsilon = \frac{4\pi}{\mu_0} L_0^2 V_X B^2 \sin^4 \frac{1}{2}\theta, \tag{2.4}$$

which was derived using the equation for the Poynting flux (equation 1.15).

This driving function in eq. 2.4 was obtained by studying 17 interplanetary and geomagnetic parameters during storm time intervals. The resulting coupling function (equation 2.4) is given in units of Watts, where L_0 is the length of the cross-section of the magnetosphere where Poynting flux is transferred from the solar wind to the magnetosphere (L_0 is approximately 7 R_E according to *Perreault and Akasofu* [1978]).

The sine-function in eq. 2.4 is a geometric factor, included in most coupling functions. Sometimes a different (positive) exponential is used, but always with a similar result. This has been the case ever since *Sonnerup* [1974] suggested it should be taken into account that reconnection can still occur, even if the two magnetic fields (the Earth's and the IMF) are not perfectly anti-parallel. This is modulated by the IMF clock angle, θ, which is the angle between the IMF components in the GSM Y-Z plane and the Z axis, such that the sine-function maximises the reconnection rates when the two magnetic fields are perfectly anti-parallel.

Using the Perreault-function (equation 2.4) to estimate the energy input into the magnetospheric system and then study where in the magnetosphere the energy is deposited can be problematic: The coupling function was specifically determined for geomagnetic storms and as such, the coupling may take on a slightly different form during quieter times. Furthermore, *Perreault and Akasofu* [1978] did not discuss energisation of their measured quantities from other sources, for example the nightside reconnection rate.

Another way of finding the coupling function is by correlating the solar wind parameters, or combinations thereof, with magnetospheric parameters, such as AL, AU and AE until the best fit is found [e.g. *Bargatze et al.*, 1986]. This technique was also employed by *Newell et al.* [2007], who used 10 different magnetospheric parameters to find the best correlation for a coupling function. The coupling function determines the rate at which open magnetospheric flux is opened at the magnetopause:

$$\frac{d\Phi_{MP}}{dt} = V_X^{4/3} B_T^{2/3} \sin^{8/3} \frac{1}{2}\theta, \tag{2.5}$$

where V_X is the speed at which the IMF approaches the magnetopause, B_T is the total magnetic field strength of the IMF, and the sinusoidal component can be thought of as an efficiency parameter, similar to the one in eq. 2.4.

Newell et al. [2008] improved upon their previous coupling function, equation 2.5, by combining it with a viscous term[1],

$$\left.\frac{d\Phi_{MP}}{dt}\right._{NEW} = \left.\frac{d\Phi_{MP}}{dt}\right._{OLD} + N^{1/2} V_X^2, \tag{2.6}$$

where $\left.\frac{d\Phi_{MP}}{dt}\right._{OLD}$ is the coupling function in eq. 2.5 and N is the solar wind density. They arrived at this solution, by again finding the best correlation (eq. 2.6 accounts for 61% of the variance, as opposed to 55% for eq. 2.5) between a number of solar wind and magnetospheric parameters, and a coupling function, a combination of one of twenty possible viscous interaction terms with one of twelve possible reconnection rate terms. Whilst the correlation between their coupling function and the magnetospheric

[1]The viscous interaction is thought to be generated due to the antisunward dragging of plasma inside the magnetopause by the solar wind and magnetospheric plasma interacting through friction.

parameters improves significantly from eq. 2.5 to 2.6 (e.g. the percentage of predicted variance in Kp rises from 57.8% to 75.0%), *Newell et al.* [2008] note that their viscous term only applies over the hourly timescale and longer, and cannot predict variability well on a smaller timescale.

Other scientists undertook similar correlation studies, *Boynton et al.* [2011] for example used a mathematical method to find correlations between non-linear systems, and found a very similar coupling function to that of *Newell et al.* [2007]. Although the method of *Boynton et al.* [2011] was more complicated, it may be argued that the *Newell et al.* [2007] coupling function is superior, as *Boynton et al.* only used Dst as a dataset to compare with the solar wind parameters.

Milan et al. [2012] set out to find a refined form of the coupling function by combining a physical understanding, similar to the *Perreault and Akasofu* [1978] approach, with some of the mathematical methods employed by *Newell et al.* [2007, 2008]. Rather than trying to fit a coupling function to a number of magnetospheric parameters and thus assuming they are all driven in the same way, they fitted functional forms of the solar wind coupling function to measures of the open flux content of the magnetosphere. To do this, *Milan et al.* [2012] identified 25 intervals where the nightside reconnection rate was thought to be very low or non-existent, such that all variability in F_{PC} is controlled by the solar wind coupling function. F_{PC} was determined using the inner auroral boundary from IMAGE as a measure of the OCB. For their analysed intervals, they use the parameterisation of the dayside reconnection rate, Φ_D,

$$\Phi_D = \Lambda N^{\alpha} V_X^{\beta} B_{YZ}^{\gamma} \sin^{\delta} \frac{1}{2}\theta, \tag{2.7}$$

where Λ, α, β, γ and δ are found by fitting solar wind data to the observations of F_{PC}. B_{YZ} is the IMF component in the GSM Y-Z plane, such that $B_{YZ} = \sqrt{(B_Y^2 + B_Z^2)}$. Λ is a constant of proportionality, dependent on α, β, and γ, in order for the units of Φ_D to be in Volts. Using an iterative process for finding the best correlation between 2.7 and F_{PC}, eq. 2.7 becomes

$$\Phi_D = 3.3 \times 10^5 V_X^{4/3} B_{YZ} \sin^{9/2} \frac{1}{2}\theta, \tag{2.8}$$

where α is 0, making the solar wind density contribution to the coupling function also 0, and the units of Λ are $m^{2/3}s^{1/2}$. In order to test their driving function, *Milan* *et al.* [2012] calculate Pearson's correlation coefficient between the F_{PC} data and the eight different coupling functions, including eq. 2.8 (a scaling factor is added where necessary). The highest ρ is found for eq. 2.8 with 0.972, followed by three simplified versions of the same function (the coefficients are integers as opposed to fractions) with ρ being 0.967, 0.960, and 0.952. The *Newell et al.* [2007] relation (eq. 2.5) ranks fifth with a ρ of 0.949 whilst the ε parameter (2.4) ranks seventh (ρ=0.899). In order to validate their coupling function, Φ_D was compared with the cross polar cap potential from SuperDARN for a previously studied interval. They found that, aside from a ~25 kV offset, which was added to Φ_D, the data fitted the coupling function well. *Milan et al.* [2012] postulate that this offset is likely due to the SuperDARN fitting analysis, but note that it could also be due to a viscous interaction.

Aside from the *Milan et al.* [2012] coupling function representing the variability in the polar cap area data best, it has the included benefit of representing data at a higher cadence best: *Newell et al.* [2008] and *Newell et al.* [2007] only use data averages with cadences of hours as opposed to minutes.

In chapters 4 and 5, eq. 2.8 is used to compute the reconnection rate at the dayside of the magnetosphere.

2.3 Magnetospheric Modes

The magnetosphere also responds in different ways to the opening of magnetic flux. These are referred to as magnetospheric modes [*Henderson*, 2004; *McPherron et al.*, 2008; *Partamies and Pulkkinen*, 2009; *Huang et al.*, 2009; *Pulkkinen et al.*, 2010; *Cai and Clauer*, 2013; *Walach and Milan*, 2015].

McPherron et al. [2008] lists substorms, sawtooth events or injections, steady magnetospheric convection events, poleward boundary intensifications (PBIs), storm-time activations, high-intensity long-duration continuous AE activities (HILDCAAs) and magnetic storms in his list of magnetospheric modes.

The way in which each of these event types can be observed and distinguished varies significantly. HILDCAAs, for example are traditionally identified by using the AE index, which is derived from magnetometer data in the auroral zones, whereas magnetic storms are identified using magnetic indices such as Dst or Sym-H, which are obtained by using magnetometer data from equatorial latitudes to reflect ring-current activities. The methods used to obtain these indices and the interpretation of them are discussed in chapter 3.

Extreme care has to be taken when characterising or identifying any magnetospheric mode, as there can be considerable overlap between different modes, but also because the identification methods are not universal.

In this work, the focus is on substorms, steady magnetospheric convection events and sawtooth events, as the overlap between these modes is easiest to distinguish, but the physics is thought to be similar, so a meaningful comparison can be made.

2.3.1 Substorms

One of the most well-known modes is the substorm, which has been studied for a long time: One of the first scholars who studied and recorded the occurrence of substorms was *Birkeland* [1908], who called them 'polar elementary storms'. He went on a polar expedition between the years of 1902-1903, visiting the auroral regions in the Northern hemisphere and observed magnetic disturbances with the most sophisticated network of magnetometers of his time (25 observatories). *Birkeland* observed characteristic north- and southward directed deviations of the magnetic field strength, depending on the location of his magnetometers. In his book, he relates the aurora and magnetic disturbances he measures to 'corpuscular rays' emitted by the Sun. The phenomenon of 'corpuscular rays' refers to what is now known as currents aligned with the magnetic field (also known as Birkeland currents), i.e. particles precipitating along magnetic field lines. *Birkeland* draws the conclusion that these magnetic deviations he measures during 'polar elementary storms' (i.e. substorms), must be caused by an increase or enhancement of the field aligned currents (FACs). Many years later, *Akasofu and Chapman* [1961] referred to the same 'polar elementary storms', as 'DP substorm' (where the D stands for disturbance and the P for polar) and only later coined the term substorm [*Akasofu*, 1964]. The name substorm has since stuck, although in the older literature a difference is often drawn between a 'magnetic substorm' [e.g. *Akasofu*, 1968] or an 'auroral substorm' [e.g. *Akasofu*, 1964], depending on the available observations. Even though these names are sometimes used in the literature to refer to different aspects of the substorm, it is important to point out that as both the auroral and magnetic phenomena accompany a substorm, together they form the same event [*Akasofu*, 1968].

Since *Akasofu and Chapman*'s first substorm studies, a myriad of studies, some of which have been discordant, have uncovered what is now known about this intriguing phenomena. In this thesis, only a small fraction of studies, which are the most relevant to the work presented in subsequent chapters are discussed.

Akasofu [1964] defined the substorm in terms of auroral morphologies. He defined the auroral onset as the time when an equatorward arc in the auroral oval brightens explosively. This is followed by an expansion phase (∼0-5 minutes), whereby auroral arcs show a dynamic display of brightening and the auroral oval moves poleward, resulting in a bulge near the midnight meridian. A bulk of bright arcs then breaks off and moves westward, known as the westward surge. After this, a recovery phase follows, which *Akasofu* [1964] found to be the longest of the substorm phases (∼10-30 minutes). *Akasofu* [1964] determined that during this phase the bulge will reduce in size. During the most active substorms, the poleward boundary of the aurora may stay at it's most poleward expanded location for approximately 10-30 minutes before dimming and retreating equatorward.

Other than the systematic study of substorms, *Akasofu* [1964] also made the discovery of pseudo-breakups, which is an auroral phenomenon, similar to substorms. He defined them as events which start out as substorms, but do not include the full expansion phase and no recovery phase. A small auroral bulge may form, but there is no break-off of arcs or westward surge observed [*Akasofu*, 1964].

Whilst *Akasofu* [1964] formally defined a substorm, it was not until 6 years later when another integral part to substorms was discovered: the growth phase, which precedes the substorm onset[*McPherron*, 1970]. *Meng and Makita* [1986] showed that during this phase, the auroral oval expands equatorward.

As this means that during the classical substorm cycle the polar cap flux increases prior to onset and then decreases thereafter, an isolated substorm can be described as a quantum of the expanding and contracting polar cap paradigm. *Hubert et al.* [2006] showed that nightside flux closure is generally maximum at the time of the substorm onset (nightside reconnection rates exceed 100 kV), but also that it can start to increase prior to auroral onset. After the onset, the nightside reconnection rate or voltage slowly returns to values typical of quiet periods (~30-40 kV) [*Hubert et al.*, 2006].

The first studies of auroral substorms were observed using ground based cameras [e.g *Akasofu*, 1964], even though it is difficult to observe large scale auroral morphological changes from the ground due to the limited field of view. *Akasofu et al.* [1966] observed a poleward movement of the auroral boundary of speeds ranging from ~100 to ~1300 m s^{-1} with an average value of ~500 m s^{-1} during the expansion phase of 84 substorms. As pointed out by *Craven and Frank* [1987] and *Frank and Craven* [1988], using ground based measurements is problematic for this purpose as it is difficult to study the longitudinal variation of the poleward expansion. *Craven and Frank* [1987] therefore used satellite imagery to study the poleward expansion of the auroral oval during the expansion phase in the midnight MLT sector and found that the average speed was of the order of hundreds of m s^{-1}, but in one case it exceeded 1000 m s^{-1}. *Frank and Craven* [1988] concluded that the speeds at which the auroral oval moves towards the pole during the expansion phase of a substorm varies in speed, and is variable even throughout one event. Along with the varying expansion speeds, individual brightenings in the auroral oval can vary in intensity, but tend to move with the westward travelling surge [*Pytte et al.*, 1976], with the overall expansion lasting up to or even longer than an hour[*Frank and Craven*, 1988].

Hones et al. [1984a,b]; *Hones* [1985a] showed that only ~30-45 minutes after the auroral substorm onset a plasma sheet expansion in the tail is observed. *Hones* [1985b] further reported, inspired by auroral observations, that the auroral oval must undertake a poleward leap after onset, due to the plasmasheet thickness rapidly increasing in thickness and a near-Earth neutral line, a reconnection site close to Earth, retreating into the distant magnetotail. This topic has been extensively discussed in the literature, but numerous studies [e.g. *Craven and Frank*, 1985; *Rostoker*, 1986; *Craven and Frank*, 1987; *Hones et al.*, 1987] show evidence against this theory. *Frank and Craven* [1988] argue that the 'poleward leap' theory is a result of the time-resolution of the auroral data and that the aurora expands, rather than jumps to higher latitudes.

The recovery phase of a substorm, as seen in the aurora from a spacecraft, can be described as a decrease in the latitudinal width of the oval, accompanied by a dimming of the aurora [*Frank and Craven*, 1988].

This implies that the polar cap and with it, the amount of open flux in the system, increases and then decreases during a substorm cycle. Even though the extent to which this happens is highly variable, the substorm cycle would be expected to pose as a good example of the ECPC. Using flux conservation arguments, *Coroniti and Kennel* [1973] showed that the amount of energy the magnetotail holds, is proportional to the polar cap flux, although the uncertainty in the measurements increases during the most active substorm phases, such as close to auroral break-off, where the magnetotail reconfigures itself very quickly.

In 1954 *Heppner* made the observation that the appearance of the bright equatorward auroral arcs in the pre-midnight sector, which break-off from the auroral oval during substorms, is accompanied by a sharp decrease in the North-South component of the Earth's magnetic field measured on the ground (i.e. a magnetic bay). After *Birkeland*, this was the first peer-reviewed study linking auroral substorms to abrupt changes in magnetometer measurements.

The changes in the magnetic field strength measurements imply that the magnetospheric current systems also change morphologically during a substorm. Figure 2.3 (adapted from *Iijima and Nagata* [1972]) shows the AU and AL signatures during the growth and expansion phases of a substorm. During the growth phase, both AU and AL are only slightly active, with the characteristic AL intensification occurring just after onset due to 'the rapid expansion of an intense auroral electrojet field' [*Iijima and Nagata*, 1972]. This is then followed by a slow decrease in the magnitude of AL. Although AU is also elevated during the expansion phase, it does not vary in the same way as AL [*Iijima and Nagata*, 1972]. The sudden decrease (or enhancement) in AL during the expansion phase, is due to a westward current flowing in the nightside ionosphere. This is brought about by a collapse in the cross-tail current to form a feature known as the substorm current wedge [*McPherron et al.*, 1973]. How this results in the ring current being coupled with the ionosphere via field aligned currents, which close as the auroral electrojet is shown in Figure 2.4.

When reconnection in the tail occurs during substorms, the previously stretched magnetotail undergoes dipolarisation, meaning the field lines become more dipolar. This feature is thought to be associated with the formation of the substorm current wedge. During dipolarisation, energetic particles are injected near the inner edge of the plasma sheet and they are a fundamental signature of substorms [*McIlwain*, 1974;

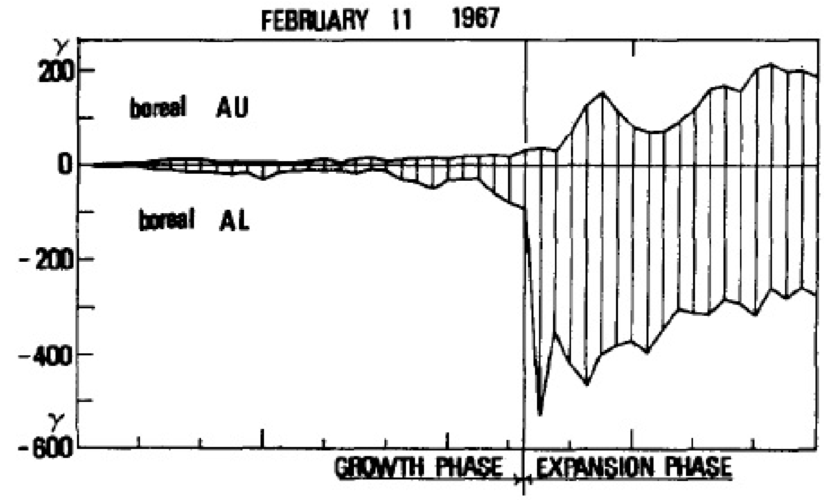

Figure 2.3: Example AU and AL signatures for a substorm adapted from *Iijima and Nagata* [1972]. The growth and expansion phase are marked below the plots and the onset is shown by a vertical line.

Kamide et al., 1998]. During a substorm injection a sharp increase in electron and proton fluxes of a wide range of energies is seen at geosynchronous orbit, usually from tens to hundreds of keV, over their presubstorm levels [*Meng and Liou*, 2004]. Injections where the increase in particle fluxes at different energies are seen simultaneously are known as dispersionless and indicate that the measurement was taken where the injection occurs. Injections become more significant during substorms which occur simultaneous to or as a part of geomagnetic storms as there may be many injections occuring compared to just the one injection during an isolated substorm [*Kamide et al.*, 1998]. However, the topological changes during geomagnetic storms in the tail magnetic field and particle injections can happen very quickly, such that it is difficult to identify individual substorms [*Kamide et al.*, 1998].

Prior to a geomagnetic storm, the tail field lines are so stretched that the particle fluxes appear to decrease. During the geomagnetic storms, when dipolarisation occurs, the particle fluxes return to undisturbed levels but are enhanced due to an energisation of the distribution, which can cause more energetic substorms [*Kamide et al.*, 1998].

Whilst *Hones* may have been wrong about the aurora taking a ‘poleward leap’, his theory about the near-Earth neutral line (NENL) migrating downtail to become a distant-neutral line (DNL) has been evidenced by *Baumjohann et al.* [1999].

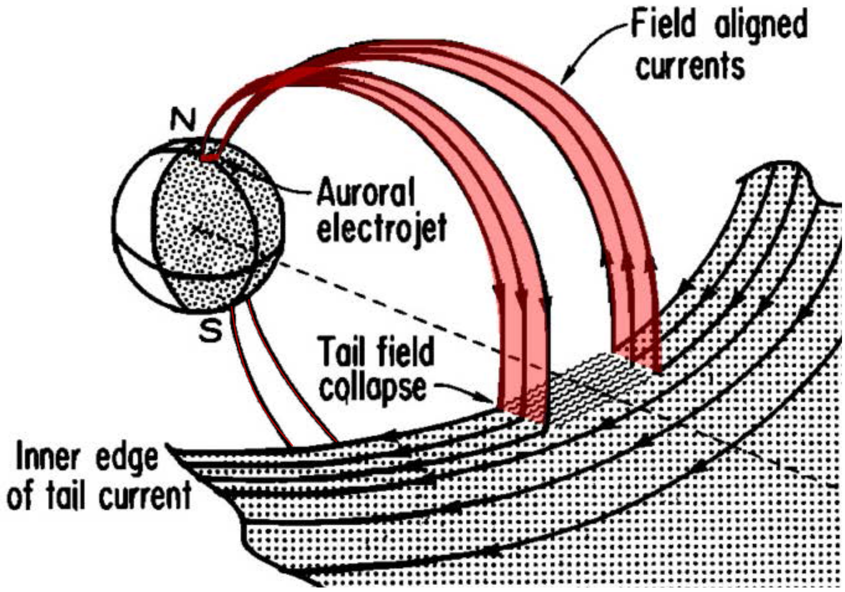

Figure 2.4: Schematic of the substorm current wedge as depicted by *McPherron et al.* [1973]. The substorm current wedge, which is made up of the field aligned currents and the auroral electrojet, is shown in red.

Baumjohann et al. [1999] produced a superposed epoch analysis of 66 substorms, using Geotail data. In their analysis, they look at Geotail observations of the magnetic field elevation angle and high speed plasma flows at various stages of a substorm, as well as at different distances down tail in the premidnight sector. Their findings show that magnetic field dipolarisation is first seen at a tail distance of 16 R_E and then moves tailward at a speed of ∼35 km/s. From fast ion bulk flow speeds they infer that during the expansion phase, the near-Earth neutral line is located at ∼21-26 R_E. They further find that 45 minutes after substorm onset all fast flows inside 31 R_E are directed sunward. These findings imply that reconnection starts at 16 R_E, the reconnection region then moves tailward and 45 minutes post onset, it must be located beyond 31 R_E.

Following the discovery of the NENL migrating downtail to make the DNL, a substorm model was invented [*McPherron et al.*, 1973; *Russell and McPherron*, 1973; *Baker et al.*, 1996]. The key phases of the NENL model are shown in Figure 2.5.

Schematic (a) in Fig. 2.5 shows the substorm growth phase, where the tail flux

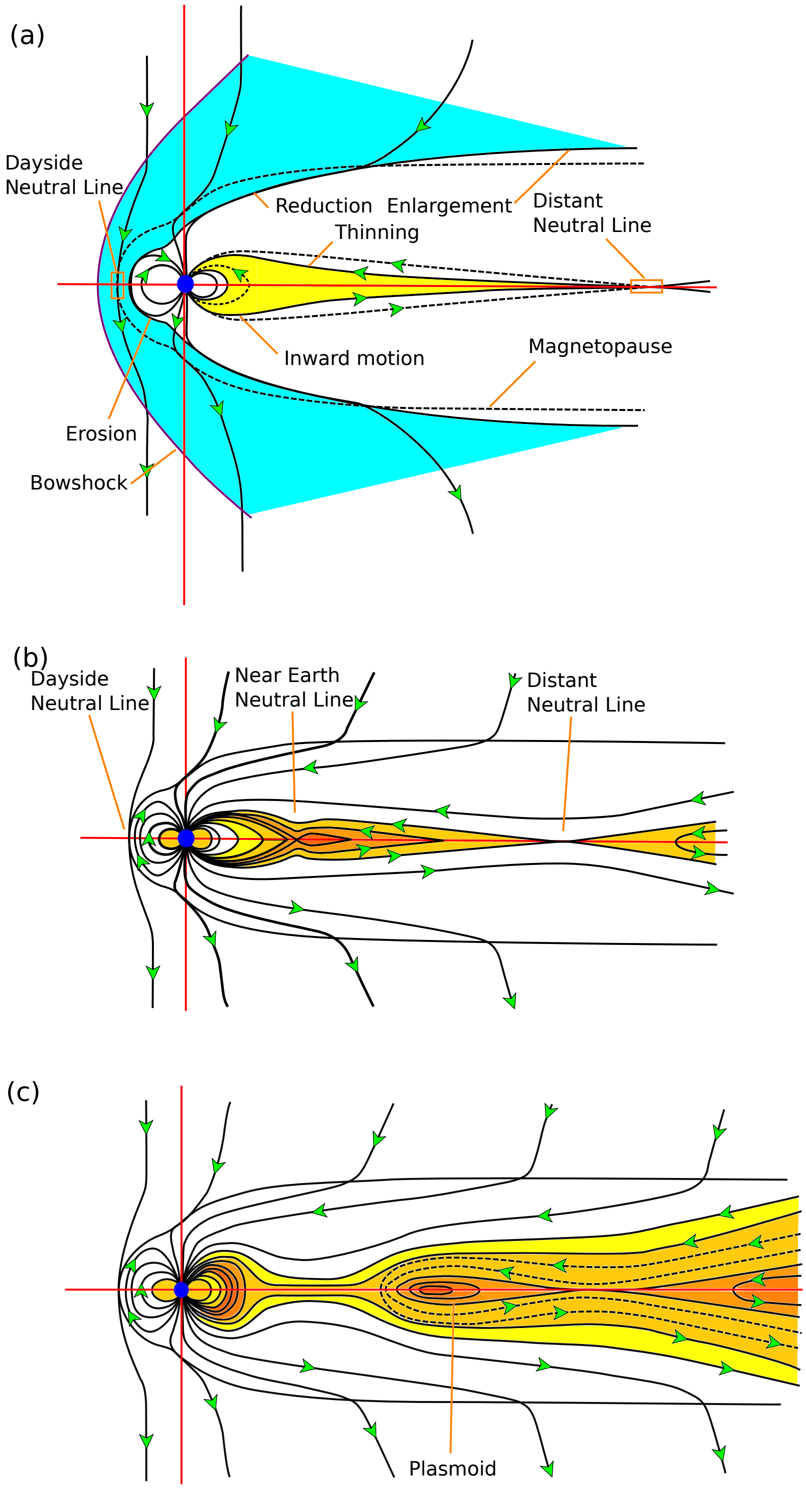

Figure 2.5: Schematic of the NENL model for substorms, taken from *James* [2014]. Diagram (a) shows growth phase of substorm, where thinning of the plasma sheet occurs due to an increase of flux being stored in the magnetotail; (b) shows the formation of a NENL, following the thinning of the plasma sheet; and (c) shows the expansion phase of the substorm, where a plasmoid formed between the two X-lines starts to accelerate tailwards.

increases and as a result, the plasma sheet in the centre of the tail thins [*Baker et al.*, 1996]. Once the pressure on the inner magnetosphere becomes too high to sustain, a NENL forms and plasmoids form between the NENL and DNL (schematic (b)). During the expansion phase of the substorm, the plasmoid is released tailward due to magnetic tension forces and reconnection continues at the NENL (schematic (c))[*Baker et al.*, 1996]. Eventually, the NENL will migrate tailward to become the DNL and the plasma sheet will thin once more until the magnetosphere reaches the initial state again.

Recently, *Kamide and Balan* [2016] suggested to subdivide substorms into five phases (quiet, growth, expansion, peak, recovery), instead of the traditional growth, expansion and recovery phases. In this work, however, the classic set of phases are used for reference, as they are more popular and thus lend for a better comparison to other works.

Even though visual identifications of events are very subjective, the onset of substorms is most reliably timed using auroral observations as opposed to magnetic field data according to *Mende et al.* [2003] and *Meng and Liou* [2004]. As such the substorm event list used in this work is determined from auroral data from the IMAGE satellite. The substorm onsets were identified by eye, with the criteria being: a clear local brightening of the aurora had to be observed, the initial auroral brightening had to expand to the poleward boundary of the auroral oval and spread in local time for at least 20 minutes after onset, and a substorm onset was only accepted as a separate event if it was separated from the previous onset by at least 30 minutes [*Frey et al.*, 2004]. In his initial study, *Frey et al.* [2004] only used data from the years of 2000 until 2002, as this is when the best IMAGE data was available in the Northern hemisphere. For the work presented in the following chapters, the entire substorm onset list compiled by *Frey et al.* [2004] was used instead, which comprises of data spanning until the end of the IMAGE mission, the year 2005.

2.3.2 Steady Magnetospheric Convection

Contrary to the dynamic substorm, periods of steady magnetospheric convection (SMCs) are times when the magnetosphere is driven, but does not undergo any of the substorm phases [*Pytte et al.*, 1978; *Sergeev et al.*, 1996; *O'Brien et al.*, 2002;

McPherron et al., 2005; *DeJong et al.*, 2009]. Instead, nightside and dayside reconnection rates are steady and roughly equal, such that they are also known as 'balanced reconnection intervals' [*DeJong et al.*, 2009].

As the day- and nightside reconnection rates are balanced during SMCs, the flows in the ionosphere and the polar cap flux are expected to stay constant [*McWilliams et al.*, 2008; *DeJong et al.*, 2009; *Walach and Milan*, 2015]. In the past AL and AU have often been used as a proxy for magnetospheric flux circulation, and thus, ionospheric flows. Using enhanced values of AU and AL to identify SMCs can be very problematic as AU and AL exhibit strong seasonal dependences [*McWilliams et al.*, 2008]. Both AU and AL tend to be higher in the summer compared to the winter, making the usage of a fixed threshold to identify events dangerous.

The SMC event list that is used in chapters 4, 5, and 6 is derived from the events identified by *Kissinger et al.* [2011], whose criteria were as follows:

1. AL $<$ -75 nT
2. AU $>$ 50 nT
3. 10 nT/min $> \frac{dAL}{dt} >$ -7.4 nT/min, where $\frac{dAL}{dt}$ is a 15 min sliding derivative operator, representing the rate of change in the AL index.
4. AL steadiness $\leq$20%, where the steadiness is given by the standard deviation divided by the mean. A running average and standard deviation is found for a 30 min period, advanced by 1 min increments. A value of 0.0 indicates a completely steady interval (flat line), while higher values are less steady.
5. The event has to last longer than 90 minutes to be longer than a typical substorm recovery period [*McPherron et al.*, 2005; *O'Brien et al.*, 2002].
6. At least 90% of data samples in any given interval have to satisfy criteria 1-5 for the event to be classified as an SMC.

In order to bring their work into line with *McWilliams et al.* [2008], *Kissinger et al.* decided to ignore condition 2 during the winter months.

An example plot of two SMC events as chosen by *Kissinger et al.* [2011] using these selection criteria is shown in Figure 2.6. The pale blue areas indicate two SMC

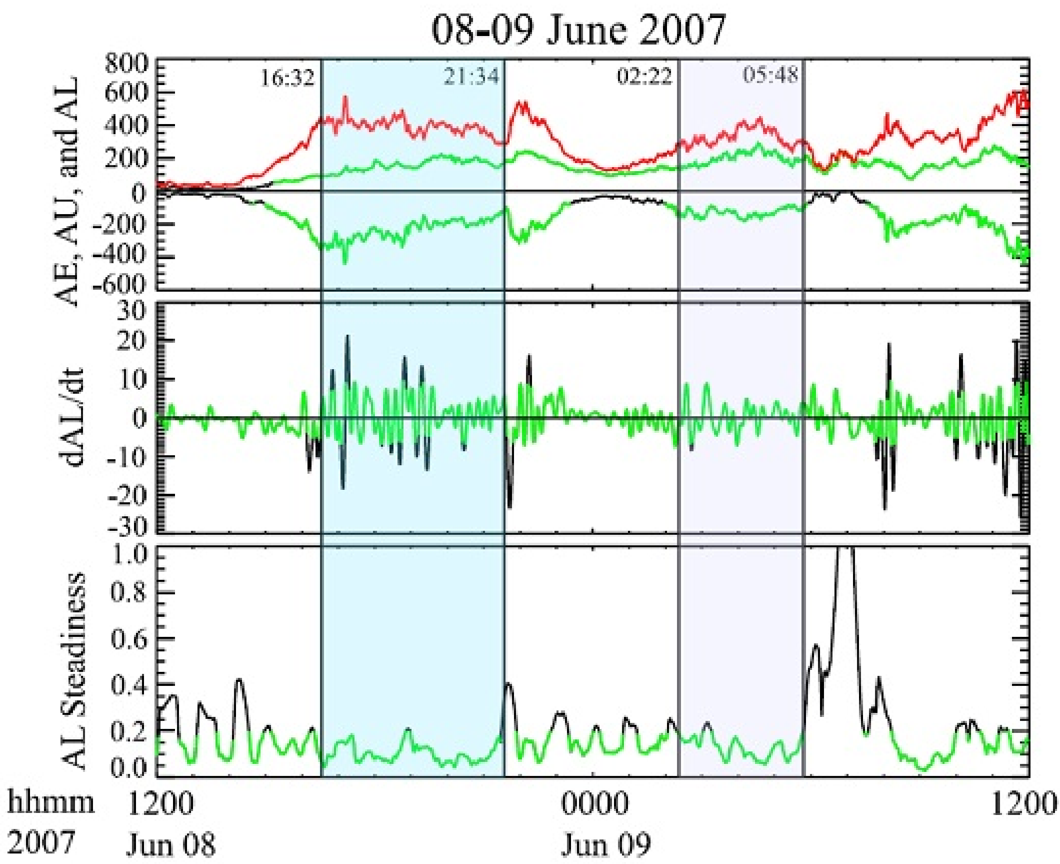

Figure 2.6: Example SMC plots from *Kissinger et al.* [2011]. The light blue areas indicate two SMCs occurring. The plots show AE in red and AL and AU (top); $\frac{dAL}{dt}$ (centre); and the AL steadiness operator. Where each of those quantities meets their criteria, the lines are traced in green.

events, of approximately 5 and 3.5 hours of length. The third criterion is not always satisfied during the first event, as AL has more spikes during this event but as the sixth criterion is still satisfied, *Kissinger et al.* still classifies the event as an SMC. The main characteristic of the SMCs to note here is the clear depression in AL, whilst not being too variable, which is distincly different from substorms, where the fluctuations are more sudden.

The event list by *Kissinger et al.* spans a solar cycle, but is easy to adapt over other time periods and as such it is ideal for large-scale studies. As alluded to earlier, AL and AU are only proxies for magnetospheric activity and there are times when they are not exact measures. This resulted in the *Kissinger et al.*'s event list being reduced further for the work presented in chapters 4, 5, and 6. A detailed description of this is given in chapter 3.

Sergeev et al. [2001] found that during SMCs, the auroral oval was wide at the nightside, the plasma sheet was thick and the lobe field was decreased with enhanced magnetic flux closure and multiple bursty earthward flows or bursty bulk flows (BBFs) in the midtail occurring. They further concluded that during SMCs, auroral streamers associated with both bursty bulk flows and narrow injections occurred [*Sergeev et al.*, 2001]. Their results imply that SMCs only occur when the pressure in the magnetotail is somewhat stable, such that efficient reconnection without explosive events like subsorms occur.

Though they have 'steady' in their name, SMCs are only quasi-steady in nature: previous studies reported that pseudo-breakups, occur frequently during SMCs [e.g. *Sergeev et al.*, 2001; *DeJong and Clauer*, 2005, and references therein]. These pseudo-breakups could be responsible for keeping the magnetosphere in a quasi steady convection state via reconnecting small amounts of open flux at a time [*DeJong and Clauer*, 2005; *Milan et al.*, 2006].

Yang et al. [2010] used the Rice Convection Model, a simulation of the Earth's magnetosphere, to study the dynamics in the magnetotail during an SMC. They found distinct features in the nightside near-Earth plasma sheet: in comparison to substorm growth phases close to the Earth the magnetic field is more stretched, and more dipolar in the plasma sheet, the plasma pressure is lower in the tailward plasma sheet, and the plasma sheet is thicker and its inner edge is closer to the Earth. All this implies that the auroral zone is thicker, matching the results from *Sergeev et al.* [2001]. *Yang et al.* [2010] also deduced that in order for the pressure in the tail to stay balanced for prolonged amounts of time, i.e. during SMCs, a low entropy boundary forms in the magnetotail rather than balancing the pressure via small reconnection channels as *DeJong and Clauer* [2005] inferred.

Sergeev et al. [1996] observed small-scale auroral activations during SMCs, including North-South aligned arcs and streamers, which they wrote

> 'might be the optical signature of the earthward plasma intrusions from the more distant tail.'

Relating to what was discussed earlier, the similar auroral features shared by SMCs and substorms does underline the need for a clearer definition for a magnetospheric mode. However, as we can distinguish between SMCs and substorms in terms of the magnetospheric response to solar wind driving (i.e. prolonged periods of convection and reconnection versus explosive, ephemeral events), in this work they will be considered as separate modes.

2.3.3 Sawtooth Events

Sawtooth events (SEs) are quasi-periodic events of unloading of open magnetic flux [*Borovsky et al.*, 1993; *Belian et al.*, 1995; *Cai et al.*, 2006a,b; *Walach and Milan*, 2015], separated by periods of approximately 2-4 hours [*Cai and Clauer*, 2009]. They were first observed as sawtooth-like oscillations in the particle fluxes at geostationary orbit, with sharp increases of particle fluxes (i.e. dispersionless injections) followed by gradual decreases. SEs appear to be large, quasi-periodic substorms, but it is still unclear if the tail dynamics are governed by different physical processes. For example, *Henderson* [2004] showed that a previously well-studied substorm interval was in fact an SE, which raises the question of whether any physical distinction exists between the two magnetospheric modes.

Using the Assimilative Mapping Technique (AMIE [*Richmond and Kamide*, 1988]), *Cai et al.* [2006a] found that the ionospheric electrostatic pattern during substorms and SEs is very similar, but sawtooth events are more intense and much more variable than substorms in terms of the ionospheric flow patterns.

Cai et al. [2006b] used measurements of the magnetic tilt angle from the GOES satellite at geostationary orbit to show that the dipolarization seen during sawtooth events is very similar to that of substorms. They found that SEs are primarily initiated at the nightside between 22 and 0 MLT, and compared to substorms, the magnetosphere is more stretched, prior to their dipolarization signatures. Subsequently, the SE's dipolarization expands both eastward and westward, similar to substorms; however expansion occurs over a wider local time extent than substorms, but it is nevertheless constrained to the nightside.

Henderson et al. [2006] independently reached similar conclusions: The dipolarization which initiates the teeth starts at the nightside of the magnetosphere and then spreads dusk- and dawnward. They conclude that SEs can be considered as a separate magnetospheric mode to substorms, but as the dayside reconnection rates are much larger than during substorms, a single dipolarization or substorm-like energy unloading process is not enough to unload all the energy stored in the magnetotail and as a result, the pulsing unloading events are seen.

A study by *Kavanagh et al.* [2007] looked at a series of sawteeth using riometer data, showing that three out of four teeth were consistent with the conjecture that sawteeth are recurring substorms. The timing for the fourth tooth was inconclusive as it was observed as two consecutive and barely spaced particle injections, where the first was not accompanied by a dipolarization and the second is a sustained injection with higher measurements of electron fluxes. The second injection thus looks more like a substorm but conclusive cosmic radio absorption measurements could not be made using the riometers due to the injection region being very asymmetric and shifted towards dusk.

Huang and Cai [2009] investigated the pressure in the magnetotail before and during SEs using measurements by the Geotail satellite. They found that the pressure is three times higher at SE onset than during quiet times and is dependent on solar wind parameters. Contrary to *Henderson et al.* [2006], this would suggest that rather than being different magnetospheric modes, SEs are simply large scale successive substorms resulting from enhanced and prolonged dayside reconnection.

Considering there is a disagreement in the field regarding the distinction between energetic substorms and sawtooth events, it poses the question if the two should be treated as separate magnetospheric modes. In this work, sawtooth events are considered to be a different mode, as they represent the periodic loading/unloading mode, which a substorm does not necessarily display.

The work in chapters 4, 5 and 6 utilises the SE lists from *Cai et al.* [2006a] and Henderson and McPherron [see *Pulkkinen et al.*, 2007]. To identify the SEs, they examined energetic particle fluxes at geosynchronous orbit and identified sharp enhancements followed by gradual decreases. Their criteria were that there had to be a series of quasiperiodic sawteeth in the data and that they had to be observed by at least two spacecraft, one near local noon and the other near midnight (± 3 h magnetic local time). Figure 2.7 shows 6 SE, their onsets marked with green vertical lines, identified using the same criteria as above [*Huang and Cai*, 2009]. The proton flux

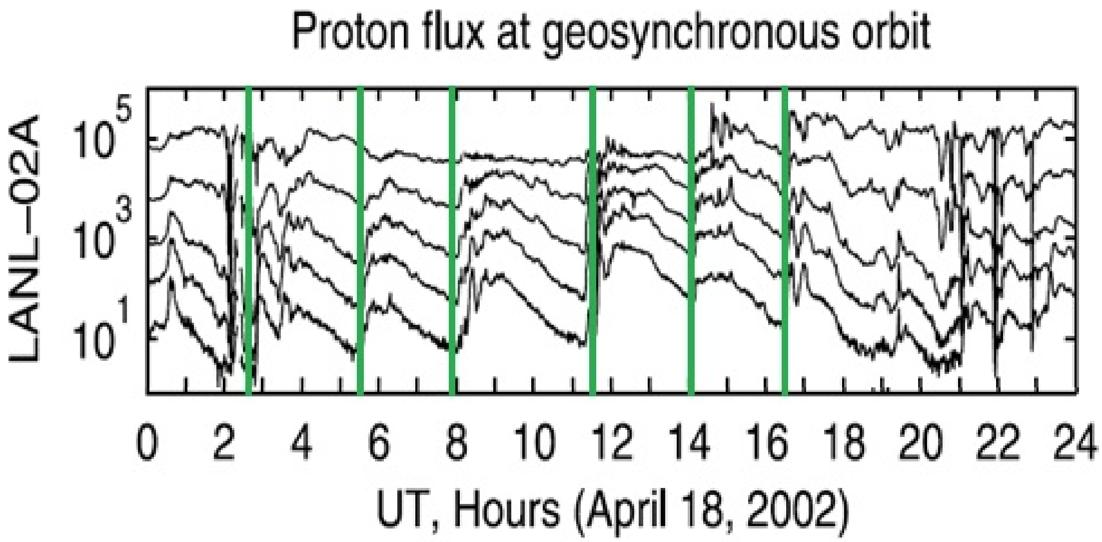

Figure 2.7: Particle fluxes as measured by the Synchronous orbit particle analyser (SOPA) instrument on board the LANL-02A satellite showing a series of SEs. Onsets are marked with the green vertical lines. The plot has been adapted from *Huang and Cai* [2009].

energy channels shown are 50-75, 75-113, 113-170, 170-250 and 250-400 keV (from top to bottom) and the measurements are given in particles/cm^2/sec/sr/keV. The SE onsets shown in Fig. 2.7 are seen in all channels, at the same time, whereas a substorm onset may only be seen in one channel or the signatures may be dispersed (i.e. not occurring at the same time).

The two event lists were combined for the studies presented here, as they cover different time periods, and further reduced as is described in chapter 5.

2.4 Aims

The ECPC paradigm has been used as a framework to explain numerous phenomena and observations over the years, including substorms [*Milan et al.*, 2007], but there has never been a quantitative study of the ionospheric flow velocities. In chapter 4 a simple physics based model of the ECPC is used to determine ionospheric flow velocities, which are then compared to in-situ (spacecraft) and remotely sensed (radar) measurements. This study is not a full quantification of the current understanding of solar wind-magnetospheric and ionospheric coupling, but rather a step towards a better understanding.

In chapters 5 and 6, the different magnetospheric modes are investigated and compared in large scale statistical studies. The solar wind driving during substorms, SMCs and SEs are discussed, along with the magnetospheric response, and in particular the auroral response. The aim is to build a better understanding of the differences and similarities of these modes to move towards a future where the physics of solar wind-magnetospheric and ionospheric coupling can be better understood.

In their recent review article, *Kamide and Balan* [2016] write:

> 'Once we understand properly the origins of ground magnetic perturbations in terms of various source currents, ground-based observations have an advantage over "more direct" measurements by radars and satellites, since temporal changes in the geomagnetic field are being monitored continuously at a relatively large number of fixed points on the Earths surface.'

Whilst this is a good argument for using ground based observations to study the magnetospheric system, the same argument can be turned on its head. With radars, such as the SuperDARN initiative, continuous measurements can be made [e.g. *Chisham et al.*, 2007] and by using in situ spacecraft data, no assumptions need to be made. Whilst it is essential to use both ground based and space based measurements of our system, there are still aspects, which are poorly understood. For example, the geomagnetic indices which are frequently used in studies of the magnetospheric-ionospheric system sometimes only express part of what is occurring, as will be further discussed in chapter 5.

3

Instrumentation, Datasets and Models

'To speak of an electric field without defining exactly the coordinate system to which it refers is meaningless.'

from *Alfvén and Faelthammar* [1963].

3.1 Introduction

Over the years, many datasets have become available to study the Earth's magnetosphere. In this chapter, the choice of data (sections 3.3 and 3.4) and models (section 3.5), and relevant coordinate systems (section 3.2) used for the work in this thesis are explained and described.

The main dataset used stems from the IMAGE (Imager for Magnetopause to Aurora Global Exploration) satellite and as a result, all of the other instrumentation and models used here were chosen specifically because they cover the same data period as the IMAGE dataset, June 2000 until October 2005.

3.2 Coordinate Systems

In the field of geophysics, it is often convention that the Earth is at the centre of the coordinate system. Most of the data that will be discussed here, will either be geocentric or magnetocentric, that is centred around the Earth or the magnetic pole, respectively. In geomagnetic coordinate systems, the z-axis is parallel to the Earth's magnetic dipole axis, defined by the International Geomagnetic Reference Field (IGRF) (see section 3.5.1). The y-axis is perpendicular to the geographic poles, and the x-axis completes the right-handed set [*Kivelson et al.*, 1995].

The DMSP and auroral data (in chapters 4 and 6), and the models discussed in chapter 4 are given by magnetic colatitude and magnetic local time, where the colatitude is given by the latitude (in degrees) measured from the closest pole towards the equator. The magnetic local time is the time at the relevant point on the Earth's surface with respect to the magnetic pole with the Sun being aligned with both noon and midnight.

In Geocentric Solar Magnetospheric (GSM) co-ordinates the x-axis is given by the line between the Sun and the Earth, the x-z plane contains the Earth's dipole and the y-axis completes the right-handed set. The z-axis is aligned with the magnetic dipole, such that the positive z-direction points the same way as the Northern hemisphere pole [*Kivelson et al.*, 1995].

Similarly, the Geocentric Solar Ecliptic (GSE) co-ordinate system has the Earth in its centre, the y-axis is chosen to be in the ecliptic plane pointing towards dusk (thus opposing planetary motion), the z-axis is parallel to the ecliptic pole, and the x-axis points towards the Sun in the ecliptic plane, forming a right-handed set [*Kivelson et al.*, 1995].

The GSM and GSE coordinate systems share an x-axis, but the y- and z-axes differ by a rotation about the x-axis. Due to this time-dependent dipole tilt of the Earth, care has to be taken when analysing solar wind data in conjunction with magnetospheric data, especially long-term seasonal variations as the choice of coordinate system may create bias results [*Russell and McPherron*, 1973]. The Earth's dipole is aligned with the GSM coordinate system, so using the IMF in GSE co-ordinates for solar wind data, would mean that a portion of the IMF GSE y-component, for example, contributes to the z-component in GSM coordinates, which is what the magnetosphere sees. As such, all the solar wind data presented in this thesis is in GSM coordinates, centred on the Earth. Albeit only being a small effect, even for the largest geomagnetic storms [*Lockwood et al.*, 2016], all IMF B_Z and B_Y data used in the work presented in this thesis is in the GSM co-ordinate system.

3.3 Space Based Instrumentation

To study the Earth's magnetosphere, and its interaction with the solar wind and the ionosphere, many options for placing instrumentation are available. Space based instrumentation provide the unique opportunity for taking in-situ plasma measurements, such as the solar wind parameters, or remote sensing, such as the IMAGE dataset.

3.3.1 OMNI Dataset

The Wind and ACE (Advanced Composition Explorer) spacecraft orbit around the first Lagrangian (L1) point, where they observe the incoming solar wind before it forms the Earth's bow shock. All the solar wind data used here, is from the High Resolution OMNI (HRO with 1-minute resolution) dataset. This data set is preprocessed, such that it is of easy use for studying solar wind-magnetospheric coupling [*King and Papitashvili*, 2005]. For the processing, each solar wind measurement is assumed to lie along a phase front which propagates past both spacecraft and later on meets the bow shock. Magnetic field measurements, resolved at 15-16 seconds, are used to calculate the phase front normal direction. This information, along with measurements of the solar wind propagation speed are then used to time shift the data to match the approximate bow shock nose location, calculated from the models by *Farris and Russell* [1994] and *Shue et al.* [1997]. An aberration of ~ 30 km s^{-1} due to the Earth's orbit is also included. This aberration is used as the Earth revolves around the Sun with an orbital velocity of approximately 30 km s^{-1} and thus with respect to the solar wind measurements. The data (15 second resolution for Wind and 16 second resolution for ACE) is then averaged to give a combined 1 minute dataset, which completes the pre-processing [1]. This dataset provides all the solar wind measurements of the magnetic field and flow velocity at one minute resolution, used for the work in this thesis. The dataset is publicly available from NASA's Coordinated Data Analysis Web [2].

3.3.2 IMAGE

All auroral data presented here were recorded with the IMAGE (Imager for Magnetopause to Aurora Global Exploration) mission, which was operational from June 2000 until October 2005 [*Burch*, 2000; *Mende et al.*, 2000a]. The timespan of this mission duration provides the opportunity for large scale data analysis. The IMAGE spacecraft was in a polar orbit with an initial inclination of 90°. The apogee of 44 000 km and perigee of 1 000 km allowed for observations of the whole auroral oval to be made of up to ∼10 continuous hours, which is a significant amount of the orbital period (∼ 13 hours) [*Burch*, 2000; *Mende et al.*, 2000a]. As the orbit precessed, the spacecraft went from observing the Northern aurora to observing the Southern aurora and as such there is a data gap of several months during the years of 2002 and 2003.

Amongst a number of instruments which were on board IMAGE, all data shown in this thesis are from the FUV (Far Ultraviolet) instrument suite [*Burch*, 2000; *Mende et al.*, 2000a]. This included two spectrographic imagers, of which only SI12 is used here [*Mende et al.*, 2000b]. SI12 is capable of minimizing the geocoronal Lyman alpha background (121.6 nm) and thus only observing the Doppler-shifted atomic hydrogen Lyman alpha emission at a very narrow wavelength of 121.8 nm [*Mende et al.*, 2000a,b]. At Earth, this is a measure for proton precipitation [*Mende et al.*, 2000a]. The other IMAGE data used here stems from the Wideband Imaging Camera (WIC), which observed 140-190 nm emission mainly composed of LBH N2 lines [*Mende et al.*, 2000a,c]. WIC thus mainly measures aurorae produced by electron precipitation and in the following chapters, the terms proton and electron aurora will be used to refer to SI12 and WIC emission, respectively. Both SI12 and WIC have a data cadence of ∼2 minutes, due to the spacecraft spinning [*Burch*, 2000].

[1] A full description can be found at http://omniweb.gsfc.nasa.gov/html/HROdocum.html
[2] CDAWeb at http://cdaweb.gsfc.nasa.gov/

The spatial resolution of SI12 and WIC were 90 and 70 km [*Mende et al.*, 2000a], which is processed into a 2° and 1° picture resolution, respectively [*Shukhtina and Milan*, 2014]. The unit of measurement of the auroral brightness from the IMAGE FUV data is given in Rayleighs (abbreviated as R), where 1 R $\sim$ 80 000 photons s^{-1} cm^{-2} strd^{-1}.

Other than the orbital constraints of this dataset, dayglow is a common issue, which is primarily observed in the FUV spectrum: it is weak from 100 to 170 nm [*Meier*, 1991] (100 R per nm), but this intensity doubles above wavelengths of 170 nm [*Mende et al.*, 2000a]. As a result, dayglow is primarily an issue in the WIC data. Efforts were made to filter the data, but unfortunately, dayglow obscures the sunlit part of all WIC images. To this day, no effective and accurate way of filtering the dayglow in WIC images has been found.

The auroral data which is shown in the later chapters is plotted with respect to the geomagnetic pole, with the noon-midnight meridian always being aligned with the y-axis of the picture, such that the Earth's rotation does not warp the results [*Shukhtina and Milan*, 2014]. Each auroral snapshot is centered on a grid with the magnetic pole in the centre and as a result, spacecraft and radar data, as well as models, which it is compared to are mapped onto the same grid (see chapter 4).

IMAGE-derived data

As part of the European Cluster Assimilation Technology (ECLAT) project, the IMAGE data were processed for easy usage, which is documented by *Shukhtina and Milan* [2014]. This section provides a quick overview of the resulting data products, which are used in later chapters.

This processed dataset includes measures of the inner and outer auroral boundaries, polar cap flux, total auroral emission (SI12 only) and maximum auroral brightness (WIC and SI12). In order to obtain these measures of auroral variability, the images were first gridded and spatially temporally averaged. The raw SI12 images are of a resolution of 128×128 pixel, which were projected onto a 40×40 pixel rectilinear grid of points centred on the geomagnetic pole, where each pixel is equivalent to 2°×2°. For WIC, the spatial resolution is 1°×1°, so each picture contains 80×80 pixels. All the individual auroral images used in the following chapters have been projected onto this same grid.

For further processing *Shukhtina and Milan* [2014] average images together: 5 successive images are taken (covering 10 minutes) and averaged spatially to increase the signal to noise ratio, similar to a low pass filter. They then median filtered each image, such that each pixel is replaced by the median of itself and its 8 nearest neighbouring pixels. This dataset was then used by S. E. Milan to find the inner and outer boundaries of the auroral oval by detecting gradients and fitting unconstrained ovals to the auroral edges. The inner boundary is taken to be equivalent to the open closed field line boundary, the OCB. By integrating over the area inside the auroral oval and assuming a dipolar magnetic field, the polar cap flux, F_{PC} is found. As part of the ECLAT dataset, the maximum auroral brightness (i.e. the brightest pixel), as measured by WIC and SI12, are also published along with the total SI12 brightness (i.e. all emission integrated over the area enclosed between the inner and outer ovals)[1].

3.3.3 DMSP

The Defense Meteorological Satellite Program (DMSP) has sent many satellites into sun-synchronous polar orbits since the 1960s, making it possible to take in-situ measurements of the polar ionosphere. In chapter 4, the ion drift-meter data from the DMSP F12, F13 and F15 spacecraft are used [*Greenspan et al.*, 1986; *Rich and Hairston*, 1994; *Hairston and Heelis*, 1996; *Heelis and Hanson*, 1998]. The ion drift meter on board these satellites measured the angle of arrival of ions onto a set of collector plates behind a square, planar aperture mounted facing forward, which was then converted into horizontal and vertical ion drift [*Greenspan et al.*, 1986; *Rich and Hairston*, 1994]. In order to ensure that no electrons enter the detector, a grid in front of the aperture is charged slightly negatively to repel them. For the work in this thesis, only the cross-track ion drifts were used, as the along track component can be inaccurate due to the spacecraft moving faster ($\sim$7.45 km s^{-1}) than the surrounding plasma ($\sim$hundreds of m s^{-1}) [*Rich and Hairston*, 1994].

[1]The ECLAT dataset is publicly available on the Cluster Science Archive: http://www.cosmos.esa.int/web/csa

The accuracy of the instrument becomes problematic when the H+ or He+ ions represent more than 20% of the ambient plasma, but any such data were filtered by the data providers and not used in the work presented here. The time resolution of the measurements by the ion drift meter on DMSP is 6 per second, which were averaged over 4 seconds by the data providers.

3.4 Ground Based Instrumentation

Ground based instrumentation is often much more economical than sending satellites into space and can also enable us to study the magnetosphere. The two types of ground-based datasets used for the work presented in this thesis stem from magnetometer measurements, which are used to infer the strength of magnetospheric current systems and radar measurements, which are used to remote-sense ionospheric convection. The origins of those datasets will be described in the following sections (3.4.1, and 3.4.2, respectively).

3.4.1 Magnetometer Derived Indices

Over the years, magnetometers have been one of the most popular types of instruments to measure magnetospheric activity. Currents flowing in the Earth's magnetosphere can be sensed on the ground, as changes in these currents produce magnetic deviations around them, much like an electric current flowing in a wire.

Measurements from individual magnetometers can also be combined to give a sense of the large scale activity in the magnetosphere. Examples of such activity measures are given by AU, AL, AE and Sym-H, which are discussed below and used in the following chapters. The indices are calculated by the Data Analysis Center for Geomagnetism and Space Magnetism in Kyoto and can be downloaded from their website [1] or through the CDAWeb page.

[1]See http://swdcwww.kugi.kyoto-u.ac.jp/aeasy/

3.4.1.1 AU, AL and AE

Magnetometers in the high-latitude regions (12 observatories at geomagnetic latitudes ranging from 60.44° to 71.21° are used [1]) can be used to sense the electrojet currents in the polar regions (see illustration a in Fig. 1.8; chapter 2), which manifests itself as a deviation in the southward (westward current) or northward (eastward current) component of the magnetic field in the Northern hemisphere [*Davis and Sugiura*, 1966].

The Auroral Upper (AU) and Auroral Lower (AL) indices are expected to be a measure of the electrojet systems. They are compiled from magnetometer measurements of individual stations: Measurements of southward and northward magnetic variations from the different stations are overlaid and the lines of the top and bottom envelopes are traced out to give the AU and AL indices. These indices therefore measure the maximum and minimum magnetic deviations at an any one time [*Davis and Sugiura*, 1966].

The Auroral Electroject (AE) index is defined as

$$AE = AU - AL, \tag{3.1}$$

providing a measure of the total amplitude of the east- and westward electrojets, as defined by *Davis and Sugiura* [1966]. The time resolution of all the AE indices used here, is of 1 minute.

AU, AL and AE are all endorsed by the International Association of Geomagnetism and Aeronomy (IAGA)[2], and as a result, these indices have often been used as a measure of magnetospheric activity, but as will be discussed further in chapter 5, they are not always a definite measure of magnetospheric activity.

3.4.1.2 Sym-H

The Symmetric Horizontal (Sym-H) index is often used as a measure of the enhancements in the magnetospheric ring current (see schematic c in Fig. 1.7; chapter 2). To compute the index, southward magnetic deviations are measured at mid-latitudes (all stations lie between geomagnetic latitudes of 49.75° and -46.22°) and averaged

[1] See http://wdc.kugi.kyoto-u.ac.jp/aedir/ae2/AEObs.html for location details and map

[2] See IAGA Bulletin 27, 1969, p.123, resolution 2

[*Wanliss and Showalter*, 2006]. This is done by first removing the background field (calculated on a monthly basis) from the measurements and then the solar quiet daily variation. The coordinates are then transformed into a magnetic dipole system, where it is assumed that the ring current flows parallel to the dipole equatorial plane. The average of the longitudinal symmetric magnetic field component of the 6 stations is then calculated, and after latitudinal corrections are made, the Sym-H index is complete [*Wanliss and Showalter*, 2006]. Similarly, the Dst index is a more established version of the Sym-H index, but it is only published in 1 hour resolution and only uses 4 magnetometer stations, whereas for the Sym-H index, 1 minute resolution exists and 6 magnetometer stations are used [*Wanliss and Showalter*, 2006].

3.4.2 SuperDARN

The Super Dual Auroral Radar Network (SuperDARN) consists of high frequency (8-20 MHz) radars, which can observe scatter from field aligned irregularities in the E- and F-regions of the ionosphere [*Greenwald et al.*, 1995; *Walker*, 1998; *Chisham et al.*, 2007]. Each radar field of view typically covers 2000×2000 km with ~50 km spatial resolution and 120 s temporal resolution [*Walker*, 1998]. Using the autocorrelation function of the backscattered signal, the power, Doppler-shifted line-of-sight velocity and spectral width of the irregularities from each beam can be found [*Chisham et al.*, 2007]. In this work, the velocities are of particular interest, as SuperDARN covers a large part of the polar regions, such that the large-scale flow patterns in the ionosphere can be studied with it. Figure 3.1 shows a map of the SuperDARN coverage in the Northern hemisphere on the 04^{th} of November 2001, which is the data interval studied in chapter 4. A backscattered radar beam measures the line of sight velocity of the ionospheric irregularities. Obtaining several velocity measurements from different locations makes it thus possible to measure the overall $\mathbf{E}\times\mathbf{B}$ drift of the plasma. Using a spherical harmonic fitting technique, weighted by average flow patterns categorised by solar wind parameters, global flow patterns are established [*Ruohoniemi et al.*, 1989]. For the years of interest, 2000-2005, the SuperDARN data was also made available through the ECLAT project and is also available for download from the Cluster Science Archive [1].

[1] see http://www.cosmos.esa.int/web/csa

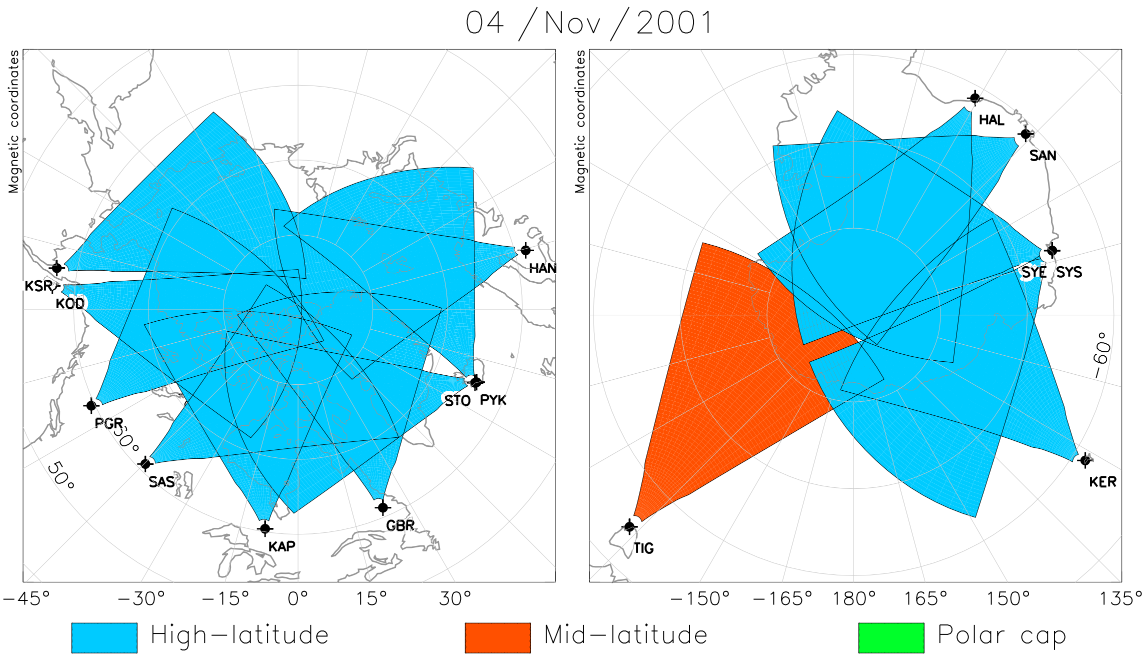

Figure 3.1: SuperDARN coverage map of 04/11/2001 (obtained from http://vt.superdarn.org) for the Northern hemisphere (left panel) and the Southern hemisphere (right panel).

3.5 Models

In chapter 4 the impact on the calculation of the polar cap flux using different magnetic field models is explored. For this, a dipolar magnetic field is compared to the International Geomagnetic Reference Field (IGRF-11), which is the most precise empirically determined model for the Earth's magnetic field [*Finlay et al.*, 2010]. The main work in chapter 4, is a comparison of the ionospheric flow velocities computed by a simple physics-based model of the expanding and contracting polar cap model, and data. In the sections 3.5.1 and 3.5.2, these models are described.

3.5.1 IGRF-11

The IGRF-11 is a reference field, which is updated every 5 years and takes all components of the geomagnetic field into account by taking data from magnetometers on the ground and on satellites [*Finlay et al.*, 2010]. The magnetic field strength, **B** is given by

$$\mathbf{B}(r, \theta, \phi, t) = -\nabla V(r, \theta, \phi, t), \tag{3.2}$$

where r is the radial distance from the centre of the Earth, θ and ϕ are the geocentric co-latitude and the east longitude, respectively, V is a scalar potential and t is the time (temporal changes, such as the movements of the poles, to the IGRF are given at 5 year intervals). Spherical harmonics are used to calculate V, such that

$$V(r, \theta, \phi, t) = a \sum_{n=1}^{N} \sum_{m=0}^{n} \left(\frac{a}{r}\right)^{n+1} \left[g_n^m(t) \cos(m\phi) + h_n^m(t) \sin(m\phi) \right] P_n^m(\cos\theta), \tag{3.3}$$

where g_n^m and h_n^m are numerical Gauss coefficients, a is the Earth's radius (6371.2 km), $P_n^m(\cos\theta)$ are Schmidt semi-normalised associated Legendre functions of degree n and order m. [1] Further details about the model, such as the coefficients themselves are discussed by *Finlay et al.* [2010]. Since the work for chapter 4 was done, the next iteration of the IGRF model, IGRF-12, has been released, but this will not be discussed here as IGRF-11's definition of the years 1945-2005, covering the time period discussed in the following chapters (years 2000-2005), is final [*Finlay et al.*, 2010].

3.5.2 The ECPC Model

The model for the expanding and contracting polar cap model which is used in chapter 4 is a simple physics based model from *Milan* [2013]. It is the only published model, based on the expanding and contracting polar cap paradigm, which can predict ionospheric flows due to day- and nightside reconnection rates.

The physical basis of the model was already discussed in chapter 1, but the underlying assumptions are discussed in this section and the restrictions in chapter 4.

The ionospheric plasma can be approximated to be incompressible, meaning that the flow is divergence free, such that if $\Phi_D > \Phi_N$ the polar cap has to expand and if $\Phi_N > \Phi_D$, the polar cap has to decrease in size. Thus the velocity of the plasma, $\mathbf{v}$, is defined by

$$\nabla \cdot \mathbf{v} = 0, \tag{3.4}$$

[1] The IAGA website (http://www.ngdc.noaa.gov/IAGA/vmod/igrf.html) provides Fortran and C programs for the IGRF-11 models which were used for the comparison in chapter 4.

such that the flows are divergence free [*Ruohoniemi et al.*, 1989; *Chisham et al.*, 2007; *Milan*, 2013].

The model assumes that the polar cap, containing the open flux, F_{PC}, is circular, as is the equatorward boundary of the convection pattern. The OCB has a magnetic colatitude of λ_{OCB}, dictated by the amount of open flux. The colatitude of the equatorward boundary of the convection, the return flow boundary (RFB), also known as the Heppner-Maynard boundary [*Heppner and Maynard*, 1987], is given by λ_{RFB}. As the polar cap expands and contracts under the action of Φ_D and Φ_N, the flows are determined based on the following assumptions: a) the convective flows are incompressible, b) non-reconnecting portions of the polar cap boundary are 'adiaroic', that is the north-south component of the flow at the boundary is equal to the motion of the boundary itself [*Siscoe and Huang*, 1985], so that the electric field in the frame of reference moving with the boundary is zero, i.e. no flows across the boundary occur.

A dipolar magnetic field is assumed, which means that if circular symmetry is assumed, F_{PC} is given by

$$F_{PC} = 2\pi R_E^2 B_{eq} \sin^2 \lambda_{OCB}, \tag{3.5}$$

where R_E is the Earth's radius (6371.2 km), and B_{eq} is the magnetic field strength at the equator (31000 nT).

Following the mathematical trail from *Milan* [2013], the electrostatic potential at any point within the polar cap, Φ_{PC}, and the return flow region, Φ_{RFB}, is given by

$$\Phi_{PC}(\Lambda, \theta) = \sum_{m=1}^{N} s_m \sin(m\theta) \exp(m(\Lambda - \Lambda_{OCB})), \tag{3.6}$$

$$\Phi_{RFB}(\Lambda, \theta) = \sum_{m=1}^{N} s_m \sin(m\theta) \frac{\sinh(m(\Lambda - \Lambda_{RFB}))}{\sinh(m(\Lambda_{OCB} - \Lambda_{RFB}))}. \tag{3.7}$$

Φ_{PC} and Φ_{RFB} can be calculated at any geomagnetic co-latitude, λ, and azimuth from the midnight meridian, θ, within these regions. Λ is computed using the conversion $\Lambda = \log_e \tan \frac{1}{2}\lambda$. Λ_{RFB} and Λ_{OCB} are thus conversions of the geomagnetic latitudes of the return flow boundary, RFB, and the open-closed field line boundary, OCB. As in *Milan* [2013], N is truncated at the order of 20 and the coefficients, s_m are given by

	$\lambda \leq \lambda_{OCB}$:	$\lambda_{OCB} < \lambda < \lambda_{RFB}$:
$\dfrac{\partial \Phi}{\partial \theta}$:	$\sum_{m=1}^{N} m s_m \cos(m\theta) \exp(m(\Lambda - \Lambda_{OCB}))$	$\sum_{m=1}^{N} m s_m \cos(m\theta) \dfrac{\sinh(m(\Lambda - \Lambda_{RFB}))}{\sinh(m(\Lambda_{OCB} - \Lambda_{RFB}))}$
$\dfrac{\partial \Phi}{\partial \Lambda}$:	$\sum_{m=1}^{N} m s_m \sin(m\theta) \exp(m(\Lambda - \Lambda_{OCB}))$	$\sum_{m=1}^{N} m s_m \sin(m\theta) \dfrac{\cosh(m(\Lambda - \Lambda_{RFB}))}{\sinh(m(\Lambda_{OCB} - \Lambda_{RFB}))}$
V_λ:	$\dfrac{1}{R_E B_r \sin\lambda} \dfrac{\partial \Phi}{\partial \theta}$	
V_θ:	$-\dfrac{1}{R_E B_r \sin\lambda} \dfrac{\partial \Phi}{\partial \Lambda}$	

Table 3.1: Latitudinal and longitudinal ionospheric flow velocities are summarised via the open and closed magnetic field regions.

$$s_m = -\frac{1}{m^2\pi}\left\{(-1)^m \frac{\Phi_D \sin(m\theta_D)}{\theta_D} - \frac{\Phi_N \sin(m\theta_N)}{\theta_N}\right\}, \tag{3.8}$$

where θ_D and θ_N are the angular half-widths of the merging gaps of the day- and nightside, respectively.

The electric field, $\mathbf{E}$, at any point within λ_{RFB} is thus given by

$$\mathbf{E} = -\nabla\Phi = -\left(\frac{\partial \Phi}{\partial \Lambda} + \frac{\partial \Phi}{\partial \theta}\right), \tag{3.9}$$

where the two components on the right hand side give the latitudinal and longitudinal components, respectively. Using the equation for drift velocities, $\mathbf{V} = \dfrac{\mathbf{E} \times \mathbf{B}}{B^2}$, the horizontal flows in the latitudinal, $\mathbf{V}_\lambda$, and longitudinal, $\mathbf{V}_\theta$, directions are found to be as summarised in table 3.1. The components of the velocities that change depending on which part of the convection cells are considered, are $\dfrac{\partial \Phi}{\partial \theta}$ and $\dfrac{\partial \Phi}{\partial \Lambda}$, which are also shown in table 3.1.

By definition of the twin cell convection pattern, all flows enclosed by λ_{OCB} therefore have to be anti-sunward and all flows enclosed by λ_{OCB} and λ_{RFB} are largely directed towards the Sun.

To calculate plasma flow velocities or electric fields in the polar ionosphere using this model then, a measure of Φ_D, Φ_N and either F_{PC} or λ_{OCB}, as well as λ_{RFB}, θ_D and θ_N are required, which will be discussed in more detail in chapter 4.

4

Dual Cell Polar Cap Convection as part of the Expanding and Contracting Polar Cap Paradigm

'The real problems remain at the boundaries, both above and below;
i.e. the interactions with the lower atmosphere and the magnetosphere.'

from *Rishbeth* [1988].

4.1 Introduction

As was alluded to in chapter 2 and 3, the expanding and contracting polar cap paradigm (ECPC) is discussed in this chapter in terms of large-scale magnetospheric and ionospheric convection. The study discussed here contains a direct comparison between modelled convection and in-situ ionospheric flow measurements observed from the DMSP satellites, as well as remotely-sensed SuperDARN convection data.

Providing a framework for the current understanding, *Siscoe and Huang* [1985], *Freeman and Southwood* [1988], *Cowley and Lockwood* [1992] and *Lockwood and Cowley* [1992] established the expanding and contracting polar cap paradigm. The ideas behind this framework were discussed in chapter 2, section 2.1.2.

The results of studies by *Grocott et al.* [2002, 2003]; *Milan et al.* [2003]; *Milan* [2004]; *Hubert et al.* [2006]; *Coumans et al.* [2007]; *Milan et al.* [2007]; *Hubert et al.* [2008]; *Boakes et al.* [2009]; *Lockwood et al.* [2009]; *Milan et al.* [2009b]; *Clausen et al.* [2013]; *Coxon et al.* [2014], and many others, used the ECPC as a context within which to explain aspects of the solar wind-magnetosphere-ionosphere coupling and dynamics. Although the ECPC is well understood and the framework has been shown to fit many observations, the relationship between Φ_D, Φ_N, F_{PC} (see eq. 2.1) and ionospheric convection has not been tested. The aim of this chapter is thus to test this understanding on a case study basis, which is done using quantitative measurements, and to discuss knowledge gaps.

Figure 4.1 presents a schematic of the ionospheric flows when dayside (left) or nightside (right) reconnection dominates. In the former case the polar cap expands, and flow crosses the dayside merging gap. In the latter case flows cross the nightside merging gap and the polar cap contracts. The flow in the ionosphere is incompressible leading to interchange motions or return flows at lower latitudes. In Fig. 4.1, the plasma flows in the ionosphere are shown by black arrows, whereas the large dashed arrows indicate the expansion/contraction of the open-closed field line boundary (OCB). The red arrows indicate the measurements a cross-track ion drift-meter on a DMSP spacecraft would take.

To predict Φ_D, upstream solar wind conditions (OMNI 1-minute) are used with the solar wind driving equation from *Milan et al.* [2012]. A time series of magnetospheric open flux content from auroral observations is obtained from IMAGE data. These are combined in the *Milan*-model relating Φ_D and F_{PC} to ionospheric flows, as shown in Fig. 4.1. The model output is then compared with observations from DMSP ion drift-meters, as indicated in red in Fig. 4.1, and SuperDARN.

In section 4.2 the data used for the model comparison, specifics about the model that are employed (section 4.2.1) and the results found (section 4.2.3) will be discussed.

4.2 Data and Model Comparison

As already explained in more detail in chapter 3, the DMSP data that is used originates from the SSIES instrument, on board DMSP F12, F13 and F15, which measures

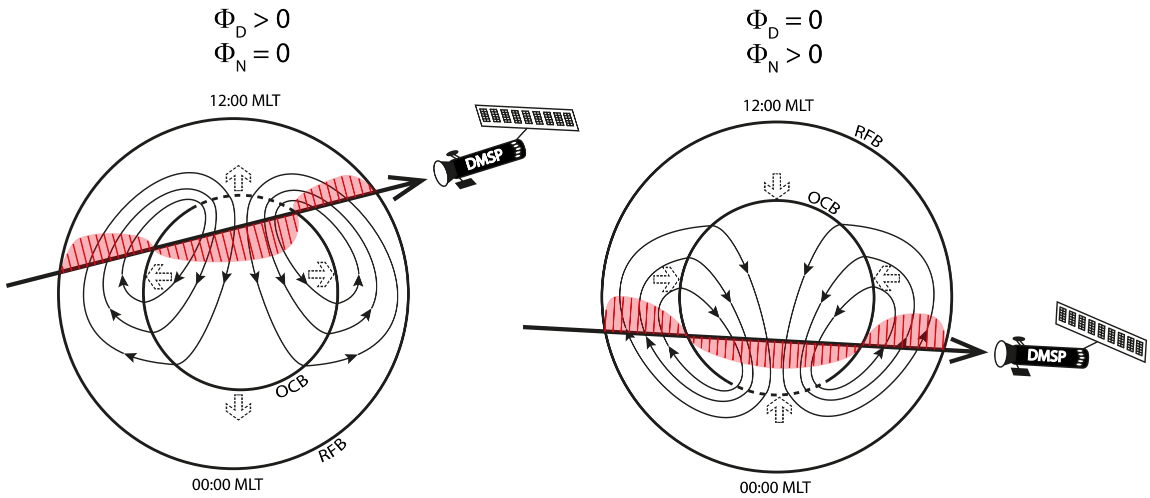

Figure 4.1: Schematics showing the polar cap convection, adapted from *Cowley and Lockwood* [1992] and *Lockwood and Cowley* [1992]. The schematics on the left and right show the effects of day- and nightside reconnection, respectively. The black arrows indicate the resulting ionospheric flows and the flow lines are equivalent to the locations of the equipotentials. The dashed arrows indicate the expansion and contraction of the polar cap, resulting from reconnection. The dashed part of the open-closed field line boundary (OCB) indicates the location of the merging gaps. The lines in red indicate the expected velocities measured by the cross-track ion drift-meter on board the DMSP satellites for a hypothetical satellite path, indicated by the thick black line. The outer circle indicates where the return flow boundary (RFB) is.

bulk ion flow in 3 orthogonal directions. For the purpose of this study only the cross-track ion drift velocities are used, V_Y, which are measured at ionospheric altitudes (∼850 km for the time period covered here) and thus give the convective flows due to day- and nightside reconnection. In this study only data that were flagged as good by the data-providers (see http://cindispace.utdallas.edu/DMSP/) is used.

For this model-data comparison, periods stretching several hours over three different days of the IMAGE mission were selected. The first one is 2^{nd} October 2000, which is a day that includes a substorm growth phase and expansion that then continues into an SMC. The second period during 4^{th} November 2001, includes several expansions and contractions of the auroral oval, as well as an expansion that develops into a short SMC. Finally, the last period during 20^{th} March 2005 includes an SMC at the beginning of the studied interval and a substorm a few hours later.

The minimum and maximum altitudes for all the polar cap crossings for each of the days analysed, respectively are: 844.2 km and 870.7 km for 2^{nd} October 2000, 838.6 km and 874.5 km for 4^{th} November 2001, and 838.7 km and 870.7 km for 20^{th} March 2005.

All DMSP data used here were flagged as good by the data-providers[1], such that all DMSP orbits which have less than 100 good quality data points at geomagnetic latitudes above 50 degrees were discarded along with any polar passes which do not cross the areas encompassed by the return flow boundaries (selected by visual inspection). For 2^{nd} October 2000 we have a total of 17 good DMSP polar crossings with overlapping IMAGE data, for 4^{th} November 2001 we have 32 polar crossings and for 20^{th} March 2005 we have 31, leaving a total of 80 polar crossings for this study period.

During each interval IMAGE was observing either the Northern or Southern hemisphere, though DMSP sampled both. It is well known that flows and aurora in the Northern and Southern hemisphere are not always symmetrical [e.g *Grocott et al.*, 2010; *Reistad et al.*, 2013]. All DMSP data obtained from the other hemisphere to the IMAGE data were thus discarded. For 2^{nd} October 2000 a total of 9 good DMSP polar crossings with overlapping IMAGE data occurred, for 4^{th} November 2001 17 polar crossings occurred, and for 20^{th} March 2005 there were 13 satellite passes with good data, totalling 39 polar crossings for this study period.

The SuperDARN data used here (fitted potential pattern and flow vectors) have been processed as part of the ECLAT project (see also chapter 3). Unlike the DMSP and IMAGE data, whose availabilities are both primarily orbit constrained, SuperDARN data availability has other instrumental constraints. For the data intervals that were chosen, the most SuperDARN data was available for the 4^{th} November 2001. As such it is only used for this day in the data-model comparison.

Before the results are presented (see section 4.2.3), the model inputs are discussed in the next subsection, as the model was already explained in chapter 3.

[1] See http://cindispace.utdallas.edu/DMSP/

4.2.1 The Expanding and Contracting Polar Cap Model

The employed model is equivalent to the one defined by *Milan* [2013], where a mathematical model of the expanding and contracting polar cap is used to quantify the strength of the convection and the field aligned currents in the Earth's magnetosphere for given levels of dayside and nightside reconnection, as described in chapter 3.

Geometry is used to resolve what would be the cross-track velocities based on the DMSP passes from the equations summarised in table 3.1 and to compare it with the real ionospheric plasma flows measured by DMSP, as well as cross-track velocities derived from the SuperDARN potential maps. Before this is discussed further (see section 4.2.3), the origins of the data which are fed into the model are explained.

4.2.2 Model Inputs and Considerations

Some of the data sources that were used as input values into the model have already been discussed in chapter 3. Here, a summary of the model inputs used are explained first, followed by specific considerations which were applied when running the model.

4.2.2.1 Model Inputs

Other than the location of the centre of the convection cells with respect to the magnetic pole, the required inputs to calculate electrostatic potentials within the convection regions are λ_{OCB} or F_{PC} (can be converted using equation 3.5), Φ_D, Φ_N, θ_D, θ_N and λ_{RFB} or $\Delta\lambda$, where $\Delta\lambda = \lambda_{RFB}$ - λ_{OCB}.

In order to obtain λ_{OCB} and λ_{RFB}, two concentric circles were fitted to auroral data from the IMAGE SI12 instrument, where the radius of the inner auroral boundary provides a measurement for λ_{OCB} and the radius of the outer boundary corresponds to λ_{RFB}. Unlike the dataset obtained by *Shukhtina and Milan* [2014], this was done manually to obtain circular boundaries in order to comply with the model. Using this as input, F_{PC} is determined from equation 3.5, for a circular polar cap. Furthermore, the Earth's magnetic field was also assumed to be a perfect dipole, as will be discussed in the next subsection.

To estimate Φ_D, the functional form from *Milan et al.* [2012] was used in conjunction with data from the OMNI (1-minute resolution) dataset [*King and Papitashvili*, 2005]. Φ_N is found by using equation 2.1 and fitting values for F_{PC}, assuming $\Phi_N = 0$ to the timeseries of F_{PC} at first. The first instance where the fitted F_{PC} is larger than the estimated F_{PC}, Φ_N is increased manually until a good fit is found. This process is then repeated at manually selected intervals, such that an estimated timeseries for Φ_N is found.

Milan et al. [2012] noted that, to bring the solar wind-estimated Φ_D to the same magnitudes as SuperDARN-derived Φ_{PC} values, 25 kV have to be added to Φ_D. *Milan* [2004, and references therein] calculated that residual flows may be of ~25 kV of the cross polar cap potential, setting the viscous interaction to orders of 10 kV. DMSP data analysed by *Lockwood et al.* [2009] also suggested it may only be of the order of 10 kV. In this study, we thus add a constant 25 kV to Φ_D and Φ_N, to accommodate for any viscous-driven flows and possible underestimation of the reconnection rates. This offset of the reconnection voltages is further discussed in section 4.3.

As the method chosen to calculate Φ_N may appear not very rigorous at first, the results will now be contrasted with the values obtained independently, using a different method, to ensure validity of the estimates.

Hubert et al. [2006] developed a different technique to calculate F_{PC} and Φ_N, for which he used SuperDARN data to obtain the ionospheric electric field: the electric field in the frame of reference moving with the OCB (derived from IMAGE data) is computed accounting for the ionospheric field and the motion of the boundary. The total reconnection rate is then the line integral of the total electric field along the OCB, which can then be used to resolve Φ_D and Φ_N.

Figure 4.2 shows a comparison between the Φ_D (top panel), Φ_N (middle panel), and F_{PC} (bottom panel) values obtained by two slightly different methods. The time period shown in the panels covers 4^{th} November 2001, the same as is discussed later on. The data shown in black and red are data obtained by *Hubert* [2016], whereas the data shown in turquoise and green are the data used in this study, as described earlier.

Overall, the Φ_D values computed by the two different methods arrive at similar values (25 kV offset included). Despite the method used to obtain Φ_N values in this study being a crude estimate, again, the magnitudes are predicted well. As a result, the estimated values for the F_{PC} are also very similar. In fact, the variations in the values show a very good match, but the magnitudes are consistently offset (by

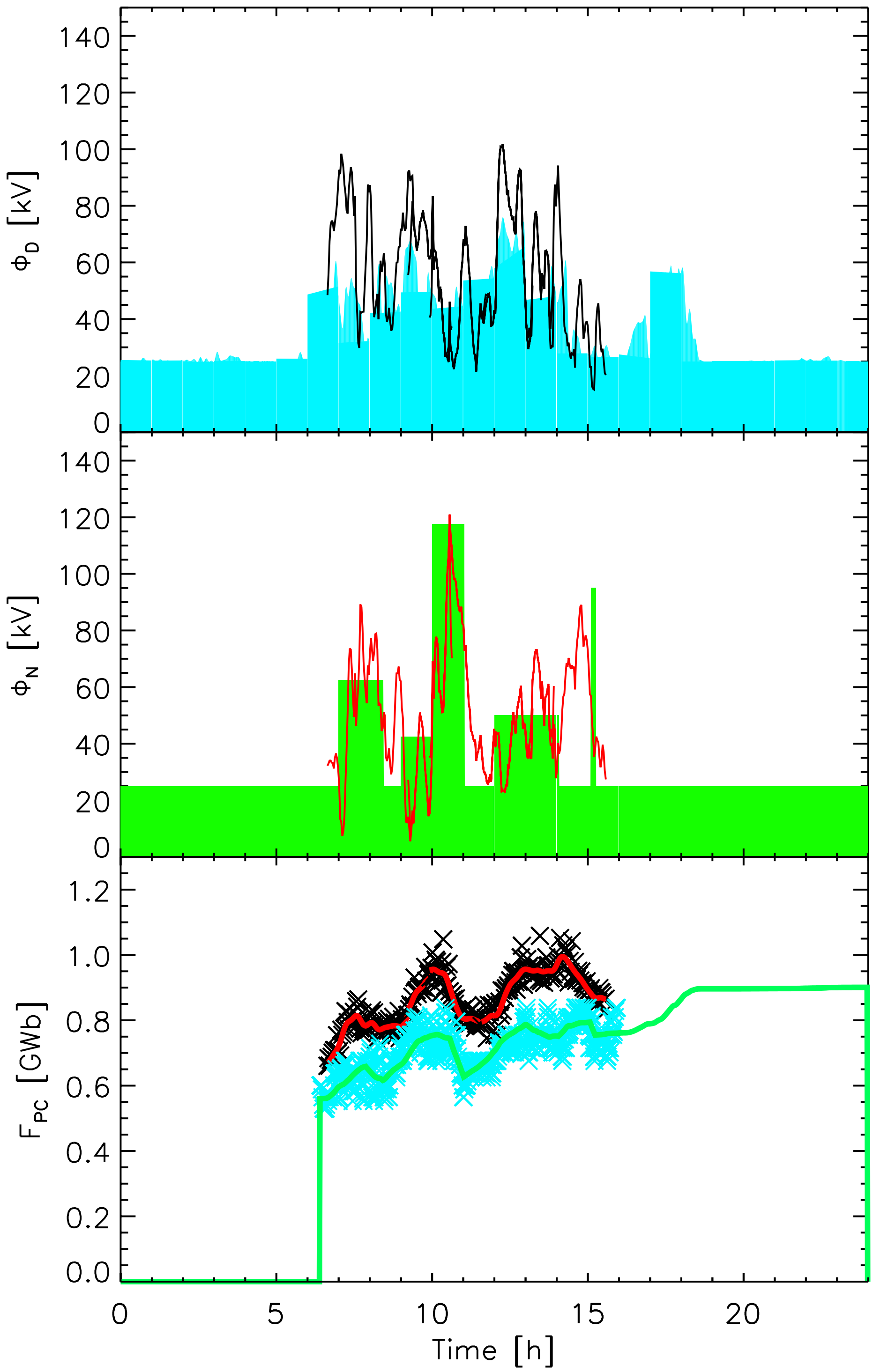

Figure 4.2: The top panel shows a comparison of Φ_D from *Hubert* [2016] (black) and the data used in this study (blue), followed by a panels showing a comparison between Φ_N from *Hubert* [2016] (red) and the values used here (green). The bottom panel shows a comparison of the F_{PC} values obtained using the two different methods described in the text with the estimates from *Hubert* [2016] in black and red, and the values used for this study in blue and green. The time range shown covers 4^{th} November 2001.

approximately 0.15 GWb). This offset is reasonable, as a comparison between values of F_{PC} obtained from IMAGE data by different fitting methods showed a consistent offset in the polar cap area [see Figures 10 and 11 in *Shukhtina and Milan*, 2014]. For example, the oval fitting by *Shukhtina and Milan* [2014] was on average offset by 0.1 GWb from the values estimated by *Boakes et al.* [2008], who used an automated algorithm to determine the location of the polar cap boundary along meridians of magnetic local time, assuming a Gaussian distribution for the emission intensity with latitude. According to *Shukhtina and Milan* [2014], this algorithm may have missed faint auroral emission near the polar cap boundary. The offset in Fig. 4.2 could be due to a similar reason, but *Hubert et al.* [2006] also fitted ovals to the auroral data instead of circles, so an offset is expected.

When running the model, lower values of F_{PC} will decrease the predicted flow velocities of the model, but this is not expected to have a very large impact on the relative changes in flow velocities: For this Φ_D and Φ_N are more crucial and Fig. 4.2 shows that these are well represented in comparison to data obtained by the method of *Hubert et al.* [2006]. This provides confidence in the Φ_D, Φ_N, and F_{PC} for the model inputs.

The other necessary model inputs, θ_D and θ_N, the half-sizes of the day- and night-side merging gaps, are held at a constant 30° each, with respect to the centre of the pattern (as was done by *Milan et al.* [2013]). Figure 7 of *Milan et al.* [2013] explores the possibility of a variable convection throat size. It shows that changing the merging gaps from being very narrow to very wide (θ_D and $\theta_N = 10°$ to $60°$) has much less of an effect on the model output than changing the other variables, for example the reconnection rates.

4.2.2.2 Geometric Considerations

The potentials calculated from equations 3.6 and 3.7 are centred about the geomagnetic pole. It is known from observations of the auroral oval, which is used as a proxy of the polar cap, that its centre is usually offset from the pole. Most notably, the centre of the polar cap is usually shifted towards midnight by a few degrees (see for example Figures 12 and 13 in *Shukhtina and Milan* [2014] or statistical study by *De La Beaujardière et al.* [1991]). As the polar cap is approximated to be a circle here, the centre of it will not be offset by the same amount and thus sometimes move even more than in *Shukhtina and Milan* [2014]), both in the noon-midnight and dusk-dawn directions.

The equations describing the model geometry from *Milan et al.* [2013] are thus transformed, such that the centre of the model output corresponds to the centre of the fitted circles, rather than the pole.

In order to shift the coordinate system in the noon-midnight and then dusk-dawn directions, the coordinate system is first converted into a Cartesian (x, y, z) system, then the rotations are applied and then the system is converted back to a (λ, θ) system. For the coordinate system conversion, the following equations are used:

$$\begin{aligned} x &= \sin\lambda\cos\theta \\ y &= \sin\lambda\sin\theta \\ z &= \cos\lambda, \end{aligned} \tag{4.1}$$

where z is aligned with the geomagnetic pole and the x-y plane is analogous to the equatorial plane. Now, a rotation of δ, is applied, where δ is the rotation angle from the geomagnetic pole in the noon-direction or z-axis. The rotated Cartesian coordinate system of (x', y', z') thus becomes

$$\begin{aligned} x' &= x\cos\delta - z\sin\delta \\ y' &= y \\ z' &= x\sin\delta + z\cos\delta. \end{aligned} \tag{4.2}$$

The same is done for the dusk-dawn direction, by rotating the system about x' by γ, such that the system becomes (x'', y'', z'') and δ and γ give the offset in degrees of the fitted auroral circles.

Now, the (x'', y'', z'')-system is converted back into a spherical coordinate system to obtain the shifted coordinates, (λ'', θ''),

$$\begin{aligned} \lambda'' &= \cos^{-1} z'' \\ \theta'' &= \sin^{-1}\frac{y''}{\sin(\cos^{-1} z'')}, \end{aligned} \tag{4.3}$$

which are then used to shift the model according to where the centre of the fitted auroral circle is.

To complete this discussion of geometry, why a dipolar magnetic field model is used in this analysis, as opposed to a more accurate magnetic field model, such as the IGRF-11 model (see introduction in chapter 3), is discussed next.

4.2.2.3 Magnetic Field Model Considerations

Figure 4.3 shows two theoretical curves of what F_{PC} would be for a circular polar cap with a varying radius, measured in geomagnetic colatitude, λ. Two curves were calculated: The black curve uses a simple dipolar field model with the magnetic field strength at the equator, B_{EQ}, set to 31000 nT and the blue curve uses the IGRF-11 field model, which were discussed in subsection 3.5.1, in chapter 3.

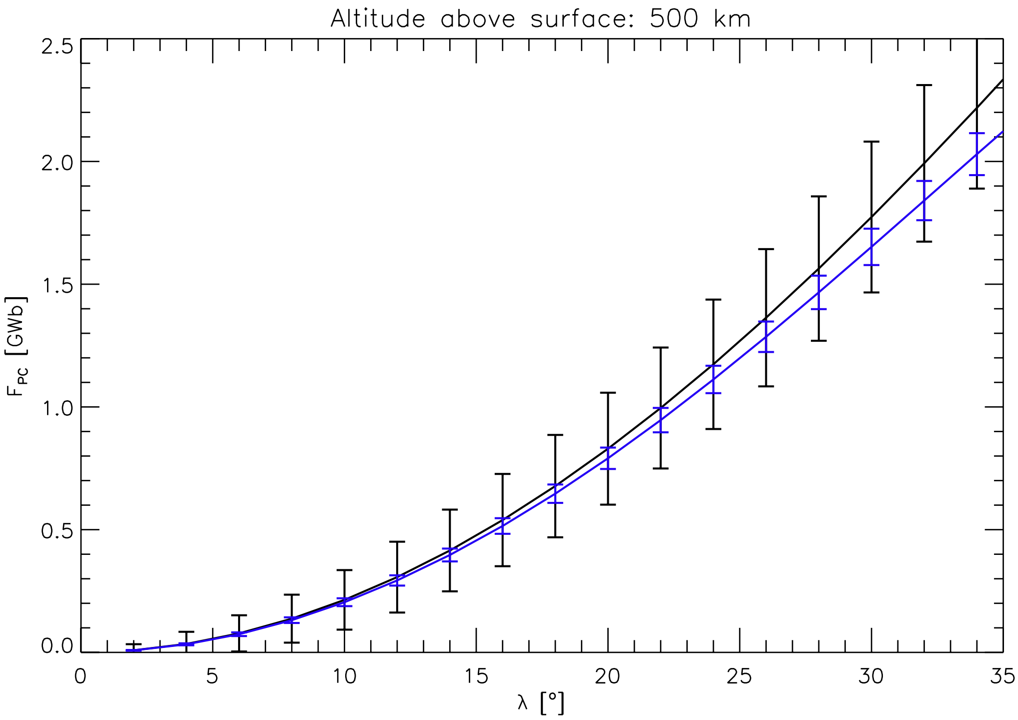

Figure 4.3: A plot of F_{PC} against the radius, assuming a circular polar cap. The blue line is calculated using the IGRF-11 model and the black line is calculated using a dipolar magnetic field model with $B_{EQ} = 31000$ nT. The calculation of error bars is further explained in the text and assumes an uncertainty in λ and B of 0.05° and 100 nT, respectively.

To calculate the values for F_{PC} in Fig. 4.3, the definition of F_{PC} (eq. 2.2) is utilised.

Similarly to the methods employed by *Shukhtina and Milan* [2014], the polar cap is divided into a grid of 1° by 1° tiles, in geomagnetic co-latitude and geomagnetic longitude. For the blue curve in Fig. 4.3, eq. 2.2 is converted into a spherical polar coordinate system, such that

$$F_{PC} = \int_{\lambda}\int_{\theta} B_r r^2 \sin\lambda \mathrm{d}\theta \mathrm{d}\lambda, \tag{4.4}$$

where λ and θ have the same meaning as previously and r is the distance from the Earth's centre. The assumption is made that around the poles, B_r is equivalent to B_z, where z is the direction aligned with the poles in a Cartesian coordinate system. As B_r is a function of λ and θ, which is calculated for each tile within the polar cap, by using the IGRF-11 model at an altitude of 500 km and then use eq. 4.4 to calculate F_{PC}. Equation 4.4 for each tile thus becomes

$$F_{PC}(\lambda, \theta) = B_r r^2 (\cos\lambda_1 - cos\lambda_2)(\theta_2 - \theta_1), \tag{4.5}$$

where the subscripts of 1 and 2 signify the limits for each tile, centred on λ and θ.

For the dipolar field model, the calculation is a little simpler, instead of eq. 4.4,

$$F_{PC} = 2\pi r^2 B_{EQ} \sin^2\lambda_{OCB} \tag{4.6}$$

is used, where λ_{OCB} is again the geomagnetic colatitude or radius of the circular polar cap. Note that eq. 4.6 is effectively the same as eq. 3.5, except for the altitude, r, which has been changed. Numerically, this makes a small difference. The error bars in Fig. 4.3 represent a lower limit of uncertainties and are calculated using simple formulae for propagation of error, as discussed next. The error propagation formulae that are used are given by *Vaughan* [2013], and are described in appendix 1.

Even though the values for the two curves of F_{PC} in Fig. 4.3 are very similar, the error bars differ slightly due to the disparate mathematical approaches. Up to a radius of ∼25° both curves are within all error bars. This means that the choice of magnetic field model makes little difference to the accuracy of the outcome, as the polar cap radius is on average smaller than this. Even though the error bars for the IGRF-11 model are much smaller than for the dipolar magnetic field model, it is concluded that the measurement error in deriving the size of the polar cap from IMAGE data plays a much greater role than the accuracy of the magnetic field model, as taking ($\Delta\lambda$) as 0.05° was a very conservative lower estimate, and thus a dipolar magnetic field model is used for the rest of this study.

4.2.3 Results

In this section, the comparison of the data and the model are shown. The focus is on the data from the interval of 4^{th} November 2001, but the data for the other days studied are presented in the same way in the appendix (2). First, an overview of the data period is introduced and then some example orbits are presented. A quantitative overview for how well the model compares to the data is also given. The implications and pitfalls of these results are further discussed in section 4.3.

Figure 4.4 gives an overview of 4^{th} November 2001. Panels c and d show the IMF components and solar wind speed for this day. The solar wind speed was almost constant, at 320 km s^{-1}, throughout the day. Before 06 UT and after 18 UT the IMF B_Z was directed northwards. In the intervening period, the IMF B_Z was southwards with B_Z ~-5 nT.

Panel a shows the AU and AL indices as a proxy for the magnetospheric response. AU and AL were very quiet for the periods of northwards IMF. AL bays suggest substorm onsets near 07 UT, 10 UT and 12:45 UT. The red line in this panel shows a steady magnetospheric convection event (SMC), as discussed in chapters 2, 5, and 6. This SMC followed a substorm, which is an event type further discussed in *Walach and Milan* [2015] or chapters 2, 5, and 6).

Panel g shows a dusk-dawn slice, or auroral keogram, of the SI12 data, evolving with time. Each slice's centre shows the geomagnetic pole, stretching towards 40° of geomagnetic colatitude toward dusk (bottom) and dawn (top). The keogram shows the auroral brightness with light and dark red indicating the least bright and brightest pixels and white showing data gaps. From this panel it can be seen that the auroral oval expands equatorward (the top and bottom of the panel) before substorm onsets and with a subsequent contraction as the substorms progress.

Panel f shows the total auroral brightness calculated from SI12 [see *Shukhtina and Milan*, 2014, for measuring technique] (in arbitrary units). Peaks in brightness are seen at the time of substorm onset.

The red circles in panel e show F_{PC} measurements based on the circles fitted to the inner auroral boundary. These were smoothed over three data points to reduce quantization noise.

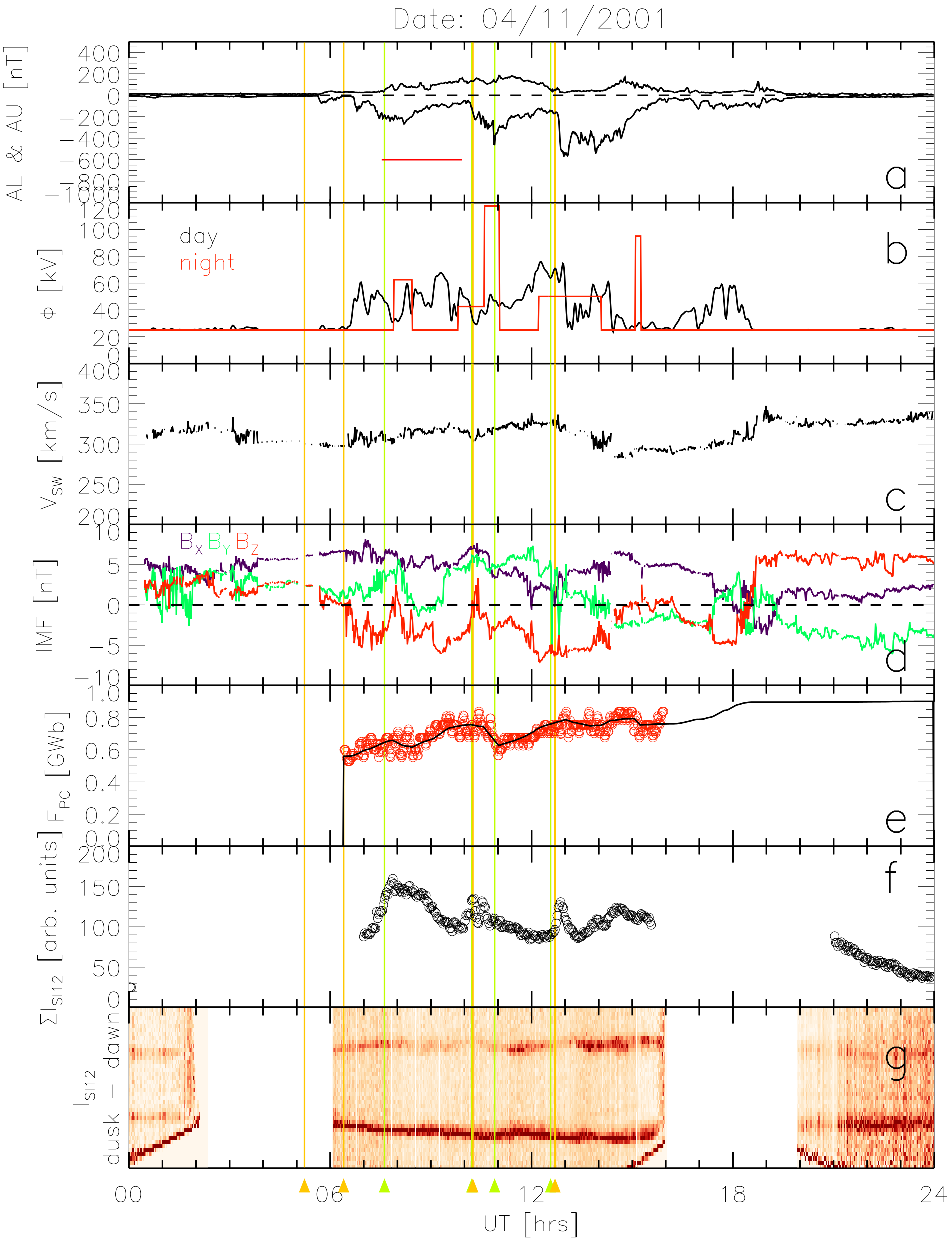

Figure 4.4: Data for the interval of interest (4^{th} November 2001). The panels show: a) AL & AU; b) Φ_D+25 kV (black) and Φ_N+25 kV (red); c) V_{SW}; d) IMF B_X (purple), B_Y (green) and B_Z (red); e) F_{PC} (data in red and estimator used to calculate Φ_N in black); f) Total auroral brightness (from SI12 instrument) in arbitrary units; g) dusk-dawn keogram of the proton aurora (from SI12 instrument), reaching down to 40° of colatitude. The green/orange arrows (top and bottom) and green/orange lines indicate substorm onsets, from Frey's and the SuperMAG event lists, respectively.

Φ_N was obtained by fitting calculated values of F_{PC} to the slope of F_{PC}, using $\frac{dF_{PC}}{dt} = \Phi_N + \Phi_D$. Initially Φ_N was kept at 0 kV and then incrementally changed, such that the curve of calculated F_{PC} matched the measured F_{PC} as closely as possible (a similar technique was used by [*Milan et al.*, 2007]). The black line shows the final curve of F_{PC}, which was used to calculate Φ_N and the red shows the F_{PC} measurements.

Panel b shows Φ_D and Φ_N, with the addition of 25 kV, as discussed previously to account for a viscous interaction.

Substorm onsets, as identified by *Frey et al.* [2004] from the IMAGE dataset, are indicated by the green triangles below the bottom panel and the vertical green lines, whereas the orange triangles and vertical lines show substorms identified by the SuperMAG dataset [*Newell and Gjerloev*, 2011]. All the Frey-substorm onsets, except for the second one, appear to be well identified, as they match auroral brightenings and expansions. Leading up to a substorm, the aurora is expected to expand equatorward and thus F_{PC} increases, which is shown in panel e. At onset the nightside aurora brightens explosively (panel f) and contracts again (as shown in panels e and g). These features are further discussed in chapter 5. There are some discrepancies between the substorm timings and the onset timings of SuperMAG-substorms. For the first two SuperMAG substorms there are not enough auroral data to discuss them in detail, but the third and last one occur within minutes of a Frey-substorm, providing confidence in the timing of the onset.

The IMF conditions for this day do not make for very high reconnection rates (i.e. Φ_D >100 kV), but there is dayside driving of the magnetosphere, as Φ_D is elevated. The B_Y component of the IMF is ~4-7 nT from 9:30 UT until 12:30 UT, but is otherwise between -2 to 2 nT.

Figures 4.5 and 4.6 show individual polar passes of DMSP F12, F13 and F15. Each orbit shows the IMAGE SI12 FUV data in a white to red map in the top left panel (the same colour scheme as the keogram in Fig. 4.4). The dark red circles indicate the concentric boundaries used for the model. Each DMSP pass shows the cross-track velocity measurements in black lines (grey for quality flags other than 'good') (bottom left panel). The black potential patterns in the top right panels are derived from the model with the cross-track velocity component shown in blue along the DMSP trajectory. Green contours (bottom left panel where applicable) show the SuperDARN convection equipotentials. The dotted grey circles indicate concentric circles spaced at 10° around the geomagnetic pole. Each panel has the hemisphere of the DMSP pass indicated to the left, followed by which satellite the measurements were obtained from and the time at which the satellite was closest to the pole (i.e. time at the centre of the polar pass). The number to the right side of the polar pass panels with SuperDARN data indicates the number of SuperDARN measurements the green potential pattern was based on, with 100 being the minimum requirement.

The potential patterns obtained by the model for 4^{th} November 2001 (see Fig. 4.5 are rotated by 1 hour MLT in a westerly direction. This was done to accommodate for the persistent rotation in the convection throat seen in the SuperDARN patterns throughout this day. Similarly, *Ruohoniemi and Greenwald* [2005] find also that statistically the convection pattern appears rotated in a westerly direction during southward IMF B_Z. In some locations, especially near the merging gaps in the first pass shown in Fig. 4.5, additional rotations in the pattern are seen, associated with IMF B_Y, which are not reproduced by the model. As a result of the rotation of the convection pattern, the modelled equipotentials are generally more accurately aligned with the ones computed by SuperDARN than they were before. As the SuperDARN coverage for the 2^{nd} October 2000 and the 20^{th} March 2005 are not very good, these data have not been included here and dawn-dusk asymmetries were not corrected for in the convection pattern.

Overall, a visual inspection of the maps in Figures 4.5 and 4.6 suggests that the locations, directions and magnitudes of the flow velocities are predicted well, but problems arise near the boundaries: DMSP measures flows which gradually change from one extreme to the other across a boundary, whereas the model's flow regimes change more abruptly. This is most probably due to the distributed nature of the field aligned currents, as the model presumes that these boundary regions are infinitely thin. The result is that the largest flow velocities are underestimated, the medium scale flows are estimated well and the very slow speeds near the boundaries are overestimated by the model. This effect can clearly be seen in the first orbit in Fig. 4.5 in the return flow regions.

The fourth panel for Fig. 4.5 and 4.6 shows the data of the polar passes in a different format. Here scatter plots of the cross-track model velocities versus the cross-track DMSP velocities (black points) and the model derived cross-track velocities against the SuperDARN derived cross-track velocities (green points) are shown. To reduce

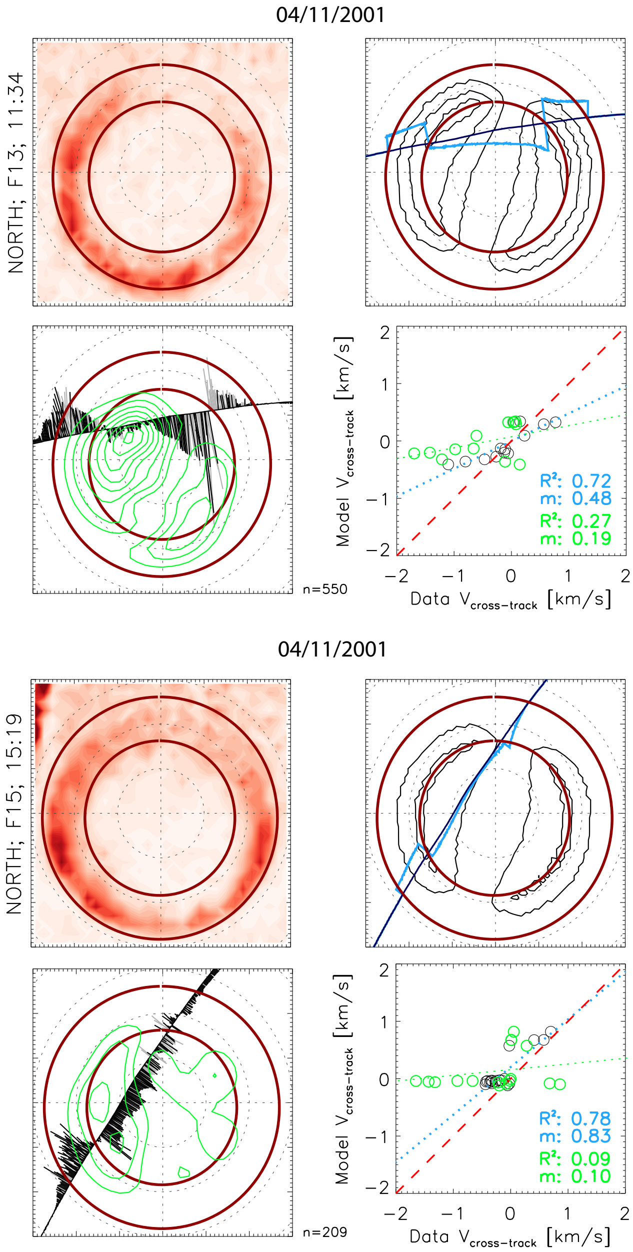

Figure 4.5: Two individual DMSP orbits for 4^{th} November 2001, showing the IMAGE data with fitted circles (top left panel); the model equipotentials (black) and cross-track velocities (blue) (top right panel); DMSP cross-track velocities and SuperDARN equipotentials (bottom left) and a scatter plot of the cross-track velocities (bottom right panel). The potentials are spaced at regular intervals of 6 kV. Each orbit is centred on the geomagnetic poles and the concentric circles in dashed grey are spaced at 10° of geomagnetic latitudes each. The green data in the scatter plots show the cross-track velocities derived from SuperDARN. The red dashed line shows the line of unity and the dotted lines show the lines of best fit (green=SuperDARN and blue/black=DMSP).

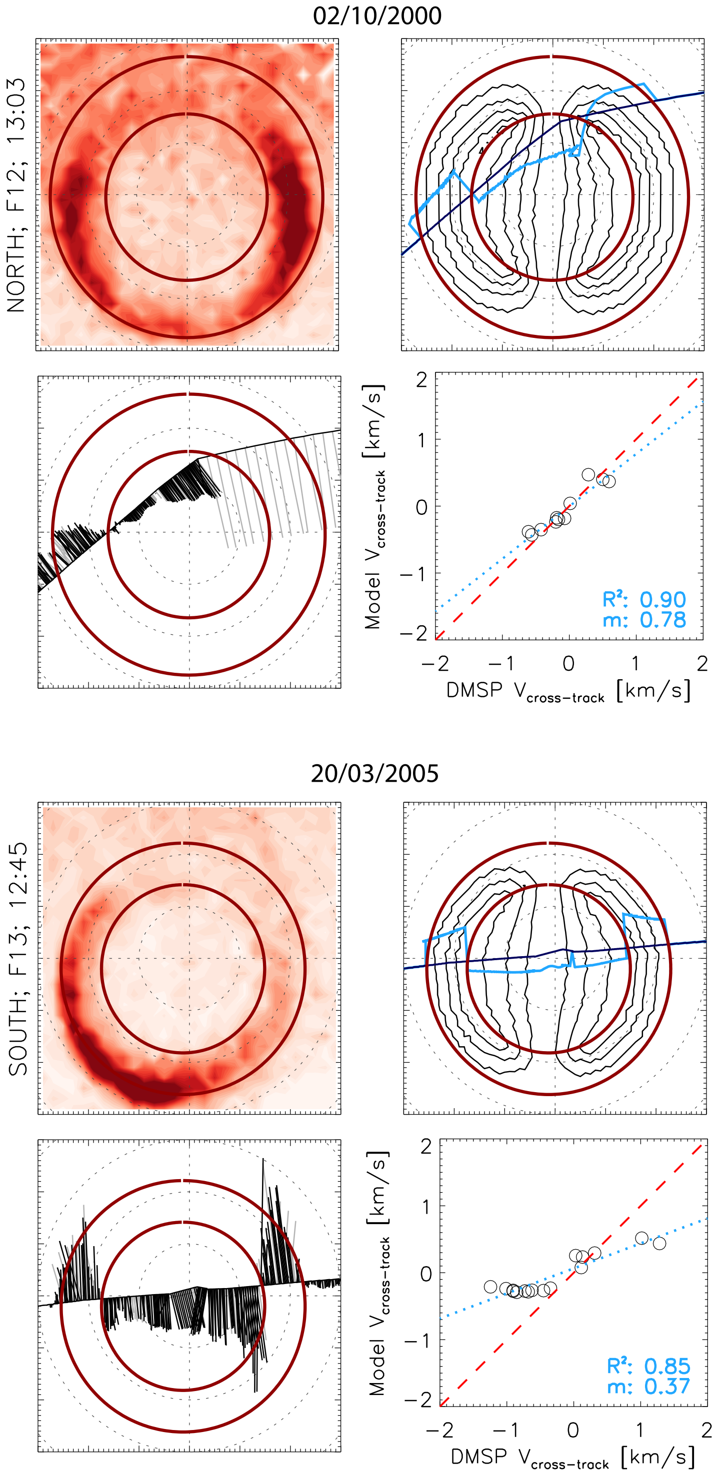

Figure 4.6: Two individual DMSP orbits for 2nd October 2000 and 20th March 2005, presented in the same way as the data in figure 4.5.

some of the most obvious problems with the data, namely changes in the convection pattern that occur on smaller timescales than the time taken by DMSP to pass the flow regions (∼10-15 minutes) and the regions near the boundaries being misrepresented by the model, the data were processed slightly from the polar pass panels to the scatter panels. For this the DMSP data were first split into intervals where IMAGE data were available (usually ∼ 2 minute length). For each of these data bins the model input was adjusted. Any data within ±1° of any boundary was then discarded and the remaining data was averaged over 10 datapoints. Binning the data and varying the model input achieves that the results are less likely to be skewed by quickly varying reconnection rates. Only considering data which is not too close to the boundaries and taking averages over 10 datapoints removes the abruptly changing variations, which are not always physical. These processed data are used for the scatter plots.

The dotted lines in the scatter plots indicate the line of best fit, calculated using linear regression, whereas the red dashed line shows the line of unity. The general trend that was already seen in the pass plots, with the model underestimating both the DMSP data and the SuperDARN derived velocities is mirrored here. If the model predicted all flows well, the correlation coefficient, R^2, and the gradient, m, would both always be equal to 1.

The first pass projection in Fig. 4.5 does not show a very good match between the model and the SuperDARN velocities, but the DMSP velocities agree well with the model (R^2 of 0.72 and 0.78).

The second orbit in Fig. 4.5 is an example where the SuperDARN data do not match the model very well. This is perhaps partially due to fewer SuperDARN datapoints being available, so the reconstructed flow patterns are less reliable. The SuperDARN flows are underestimated, resulting in the distinct horizontal scatter of the points in the plot.

Both satellite passes in Fig. 4.5 show examples where the model velocities match the DMSP measurements better than the SuperDARN velocities. This is because both the model and DMSP predict fairly large flows in the morning sector of the flow regions, whereas SuperDARN sees no flows there and instead larger flows in the dusk cell.

The first pass in Fig. 4.6 shows the highest correlation (R^2=0.90) for the model versus the DMSP measurements, even though only two thirds of the DMSP data were usable. The gradient of the linear regression is also close to 1 at 0.78.

An example where the boundary predictions are poor is given by the second orbit in Fig. 4.6. The correlation in the scatter plot shows a good agreement between model and data (R^2=0.85), but the velocities are underestimated. This becomes apparent when looking at the pass plot or the gradient in the scatter plot (m=0.37).

Figure 4.7 shows a summary of all the polar passes of DMSP from 4^{th} November 2001. The data shown here were obtained in the same way as the data shown in the individual scatter plots, but all orbits for this day were combined in one panel.

Overall, the modelled flows are broadly consistent with the data, but they are often underestimated, as already shown. Indeed m indicates that the model flows are approximately a third of the magnitude of the DMSP measurements, but R^2 and the overall data distribution indicate a correlation of the model and the data, showing that the model predicts the trends in the flows well. The results from the other 2 days considered were broadly consistent with these results (for 2^{nd} October 2000, m=0.45 and R^2=0.56, and for 20^{th} March 2005, m=0.41 and R^2=0.51).

As can be seen by comparing the data presented in the appendix (Figures 2.2, and 2.3; with 2.5, 2.6, 2.7 and 2.8; with 2.10, 2.11, and 2.12), the model does not fit the DMSP velocities as well for 20/03/2005 as for the other days. Nevertheless, example and summary scatter plots are included in the appendix for comparison.

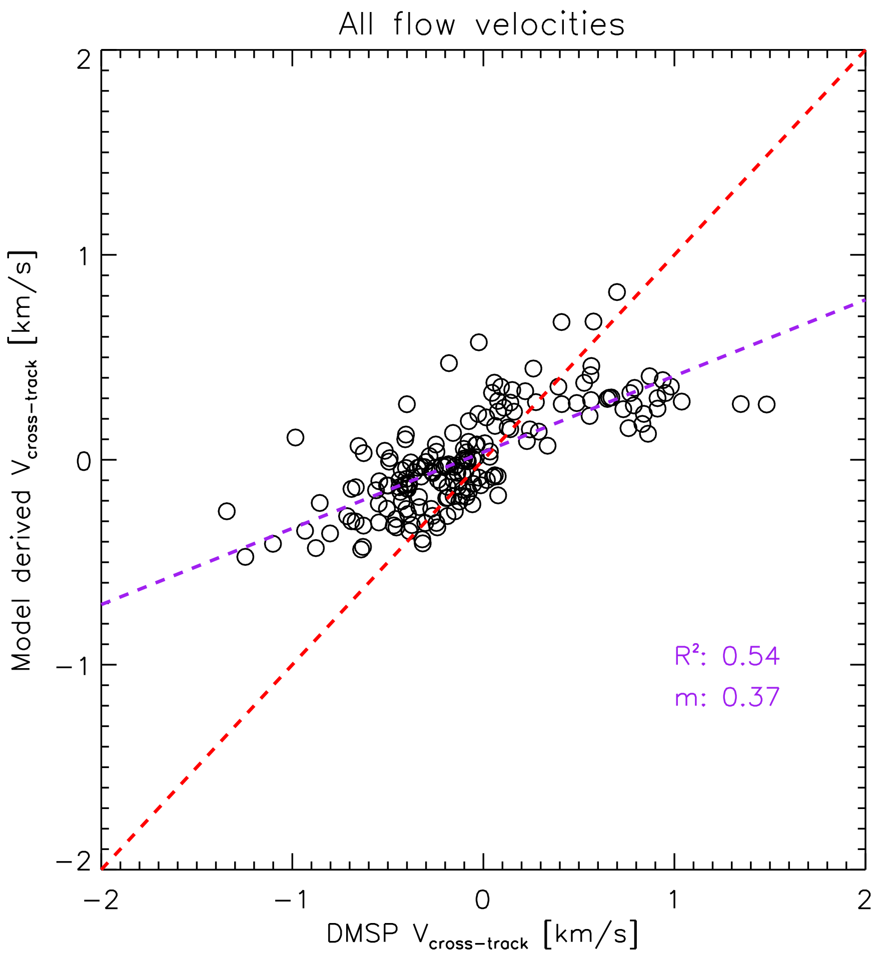

Figure 4.7: Scatter plot of cross-track velocities derived from the model against all the cross-track velocities measured by DMSP for each polar pass of 4^{th} November 2001. The purple dotted line shows the line of best fit, calculated using a linear regression and the red dashed line shows the line of unity.

4.3 Discussion

The expanding and contracting polar cap model has been used for over two decades to discuss and explain ionospheric and magnetospheric convection flows, but it has never been tested qualitatively in terms of ionospheric flows. It was already shown in the previous section that the model can predict flow velocities and flow magnitudes of the right order, so the limitations of the method and data employed here are discussed in further detail.

4.3.1 The ECPC Model

Other models for the ECPC are discussed quantitatively for example by *Lockwood* [1991], who explored the necessity of allowing the expanding and contracting polar cap model to hold a history of previous polar cap flows. Although the model employed here has no memory per se, the history of the system is kept in the time series of F_{PC}. A very similar model based on the ECPC has also been developed by *Lockwood and Morley* [2004], involving however a time-delayed magnetospheric reaction, which does not exist here. Their model is more sophisticated and as such, requires further information for the model input, for example the speed of the flows across the merging gap. Another model based on the ECPC was formulated by *Freeman* [2003], but their model does not include the nightside reconnection rate. In this study a simple model of the expanding and contracting polar cap [*Milan*, 2013] is used to calculate ionospheric velocities using changes in Φ_D, Φ_N and the flow regions, assuming an incompressible ionosphere and circular symmetry. Model flow velocities are compared to in-situ measurements from the ion drift-meter on board the DMSP satellites and ground based measurements from SuperDARN. This study outlines some distinct weaknesses of the model which we will now discuss in more detail. Whilst the simplicity allows the model to be driven by our understanding of the physical processes, it also imposes some constraints on this study.

4.3.2 Model Inputs

Two input values (θ_D and θ_N, the widths of the merging gaps), were picked to be fixed constants that the authors thought to be appropriate from visual inspection of the data. *Milan et al.* [2013] showed that varying these values does not have a significant impact on the polar cap dynamics (see Fig. 7 in *Milan et al.* [2013]). It is however possible that these values may vary with time. For example, they may be dependent on solar wind-driving of the magnetosphere or activity within the magnetopshere-ionosphere system. If this is the case, it would lead to the largest discrepancies, during more active periods. For example *Milan et al.* [2016] showed that during flux transfer events when the solar wind was travelling at larger speeds, θ_D must have spanned more hours of MLT than otherwise (results show that $V_{SW} = 380$ km s^{-1} lead to $\theta_D = 30°$ and $V_{SW} = 650$ km s^{-1} lead to a merging line width of up to 105°). As V_{SW} is very constant and not excessively high during the period of interest here, it is assumed that the 30° is a fair estimate.

Increasing Φ_D and Φ_N, has the clear result that the magnitudes of the modelled velocities and electrostatic potential increase. Changing the sizes and locations of the open closed field line boundary and the return flow boundary would change the patterns of the flows.

4.3.3 Irregular and Time Dependent Flows

The first orbit in Fig. 4.6(top) shows an example of an orbit where considerable convection occurs outside the polar cap and auroral zones in the evening sector. An example of irregular sunward flows which can occur at latitudes much lower than the auroral oval are sub-auroral polarization streams (SAPs) [*Foster and Vo*, 2002]. SAPs occur mainly on the duskside in the Northern hemisphere and appear separated latitudinally from the dual cell convection pattern with possible peak velocities above 1 km s^{-1}, which the model does not allow for. The flows seen outside the auroral oval, however appear as part of the dual cell convection pattern, so they may not be SAPs.

A further problem presents itself in that the magnetosphere dynamics change on short time scales, for example during substorm onset and the early stages of substorm expansion [see *Akasofu*, 1964, for example], but the DMSP spacecraft take much longer to traverse one polar cap (up to ∼27 minutes). As the polar cap dynamics and flows can change on a time scale of minutes, any orbital plots close to substorm onset will show some flows from just before and during the substorm, but perhaps even from the recovery phase [*Lockwood and Freeman*, 1989]. This hindrance was overcome by varying and binning the model input for the scatter plots, which appears to improve the model-data fits.

As previously discussed by *Morley and Lockwood* [2006], the timescales on which magnetospheric flows respond to reconnection, and especially how the polar cap expands in shape may be variable. As such, the assumption of the polar cap expanding and contracting at the first instance radially, as opposed to just at the merging gaps with a time delay on the whole convection pattern, have been discussed and modelled in different ways. A comparison of such models was also discussed in depth by *Freeman* [2003], leading to the conclusion that the overall modelled velocities are very similar. Modelling the convection pattern with an instantaneous response will most likely introduce the largest errors when there is a sudden change in the solar wind-driving (for example if the IMF is pointing northward for a prolonged period of time and then observes a sudden southward turning). As such it may be a source of error, especially when the reconnection rates change.

Furthermore, the assumption of the electric potential pattern being static, but instantly responsive has also been challenged in the past, as discussed by *Morley and Lockwood* [2006] and references therein. However, the assumption of a static pattern here is fair, due to the time resolution of the data (i.e. minutes).

4.3.4 SuperDARN Data Comparison

Fig. 4.4 shows an enhanced and steady IMF B_Y component for many hours before the shown orbits (Fig. 4.5), which results in an imbalance in the size of the dawn and dusk ionospheric convection cells and a dawnward rotation of the dayside merging line [*Cowley et al.*, 1991; *Ruohoniemi and Greenwald*, 1996]. This trend persists throughout most of the interval shown for this day. When comparing the convection patterns to the SuperDARN patterns, small scale features can be seen in the SuperDARN flows, such as crinkled flows across the polar cap or a further rotation at the Harang reversal boundary [*Harang*, 1946; *Heppner*, 1972]. The model can not predict these. To make future models more physically accurate, asymmetries arising in the Northern and Southern hemispheres and IMF B_Y-induced asymmetries will have to be addressed.

Despite the Northern polar region being well covered by SuperDARN observations, there are still many instances where even when many datapoints are available ($n \geq 200$), they seldom fall in the same place as DMSP observations. As such, the SuperDARN data used for the direct one-to-one comparison in Fig. 4.5 are deduced from the overall SuperDARN convection pattern, imposing a trade-off of quality versus quantity of observations [*Ruohoniemi and Baker*, 1998]. Furthermore, as there are sometimes spatial data gaps in the SuperDARN coverage across the dayside, there tends to be a shift of the convection pattern on the dayside towards the pole due to a lack of data being filled in by the empirical models [*Ruohoniemi and Greenwald*, 1996].

4.3.5 Underestimation of Flows

To try to overcome the possible underestimation of reconnection rates or viscous interaction (the implications on the CPCP would be the same) 25 kV are added to both Φ_D and Φ_N. The size of the viscous interaction, and how it may change with differing solar wind conditions, is however still poorly understood [*Milan*, 2004].

Even though 25 kV were added to Φ_D and Φ_N, the model underestimates the flows measured by DMSP (see Fig. 4.5, 4.6 and 4.7). The scatter plots shown, suggest that the DMSP data are underestimated by a factor of 2-3. A similar offset in flow magnitudes was found statistically between SuperDARN and DMSP data by *Xu et al.* [2008] and *Drayton et al.* [2005], with SuperDARN velocities being ∼30% smaller than DMSP velocities. Furthermore, *Xu et al.* [2001], *Gillies et al.* [2011], and *Davies et al.* [1999] all used different methods to show that SuperDARN tends to underestimate flows, indicating that the model must also be underestimating the flows, despite the additional 25 kV added to the day and nightside reconnection rates. Studies by *Gillies et al.* [2009, 2010, 2011, 2012] showed that the methods employed to obtain ionospheric convection velocities from SuperDARN data typically underestimate the refractive index of the ionosphere, or in most cases, overlook it. This is due to the refractive index being estimated for large volume of the ionosphere and non-localised electron densities, rather than more refined measurements. The studies by *Drayton et al.* [2005] and *Gillies et al.* [2009, 2012] only used line-of-sight SuperDARN data, which may add a geometrical error to comparing the SuperDARN and DMSP datasets. As was shown by *Imber* [2008], when SuperDARN data from the same location in the cross-track direction are compared to DMSP data statistically, the two datasets do match very well (full results to be published soon [*Imber*, 2016]). The SuperDARN data which are shown in the model-data comparison were obtained from SuperDARN potential maps, as even though good coverage was available for one of the days studied, the SuperDARN measurements did not coincide spatially with the location of the DMSP pass. This may add an extra uncertainty, as the SuperDARN statistical models are not necessarily accurate.

Above all, the analysis fulfils the main aim of this study, which was to show that flow velocities from DMSP can be predicted qualitatively when the convection is driven by day- and nightside reconnection (i.e. when a dual cell convection pattern is dominant).

4.4 Summary

The solar wind drives the magnetosphere-ionosphere system through dayside reconnection. This moves plasma across the polar cap towards the nightside, creating ionospheric convection. The flows are sometimes driven by Φ_D or Φ_N and at times, by both.

This study has investigated the convection velocities, predicted with the simple expanding-contracting polar cap model. The quantitative analysis show that the magnitudes of the flows are, on average underestimated, but can be predicted qualitatively by the physics. The conclusion is reached that the offsets may well be a combination of both measurement errors and underestimation of reconnection rates. Overall, the locations of the flows match the auroral boundaries well and the relative flow magnitudes agree well.

The main weakness of the considered model itself is that the convection cells, and indeed the polar cap itself, are not always symmetric. Deviations from symmetry can be introduced due to an enhanced IMF B_Y component: reconfigurations of the convection cells, for example one growing larger than the other or a shift of the convection boundaries can both lead to asymmetric flows. There are also many small scale deviations from symmetry, as seen in the SuperDARN convection maps, which are not captured by the model. Although the auroral boundaries represents the flow boundaries very well, the model predicts sharp edges as the boundaries are assumed to be infinitely thin sheets, which is not representative of the data.

Although the flow strengths can be predicted, in the near future, IMF B_Y-related asymmetries must be built into the model in order to improve accuracy, as a simple rotation of the convection pattern is not enough to compensate for asymmetries.

5

Magnetospheric Response Modes to Solar Wind Driving

'The German or Gothic letters employed by Maxwell I could never tolerate, from inability to distinguish one from the other in certain cases without looking very hard.'

from *Heaviside*'s monograph, republished in 2011.

5.1 Introduction

In the previous chapter, the ECPC was described, tested and discussed. What was largely described in chapter 5 as one cycle of the polar cap expanding and subsequently contracting, can often be described as a substorm, a sporadic magnetospheric mode, invoked by dominant dayside reconnection, which is followed by nightside reconnection. This is however only one mode the magnetosphere can undergo. Different magnetospheric response modes to solar wind driving, as already described in chapter 2, also include steady magnetospheric convection events (SMCs) and sawtooth events (SEs), which will be compared to substorms in this chapter and the next. In this chapter, the general magnetospheric dynamics of these event types will be compared to substorms.

A relation between substorms and SMC occurrences has been shown in the past. *Sergeev et al.* [1996], for example, noted that all SMCs either start or end with a substorm. They concluded that SMCs are either just an active period between substorms or that they can only occur following a substorm. *McPherron et al.* [2005] showed a similar relationship between substorms and SMCs and suggested that substorms are necessary for the termination of SMC events. *Kissinger et al.* [2012] supported the findings of *Sergeev et al.* [1996], as they showed that most SMCs follow substorm-like signatures and only 1% of SMCs are initiated without much preceding magnetospheric activity.

Event lists compiled by previous workers are used in this chapter to identify periods undergoing different magnetospheric modes. First, the event lists and datasets are described briefly, followed by an outline of how the lists are combined and how ambiguous events are removed. Then, a large scale statistical analysis in the form of superposed epoch analysis of substorms, SMCs and SEs is shown, to identify how they behave in terms of open magnetospheric flux and other measures of magnetospheric activity.

5.2 Data and Data Reduction

For the SE two event lists, described in chapter 2 were used: one produced by *Cai et al.* [2006b] and the other by Henderson and McPherron [see *Pulkkinen et al.*, 2007]. Both examined energetic particle fluxes at geosynchronous orbit to identify the characteristic sawtooth signature of sharp enhancements followed by gradual decreases.

The substorm list utilised here was compiled by *Frey et al.* [2004], who used observations from the Far Ultraviolet Imager (FUV) instrument suite [*Mende et al.*, 2000a,c] onboard the Imager for Magnetopause-to-Aurora Global Exploration (IMAGE) satellite [*Burch*, 2000] to identify the onset of auroral brightenings associated with substorms.

The SMCs used were identified by *Kissinger et al.* [2011], who studied the electrojet indices AL and AU as a proxy for magnetospheric convection. The SMC list included start and end times of each event, whereas the substorm and SE lists included onset only.

These event lists are supplemented with observations of the auroras from the IMAGE satellite taken with the Wideband Imaging Camera (WIC) and Spectrographic Imager (SI12) instruments, part of the FUV suite, which primarily measure electron and proton aurorae, respectively, at a cadence of approximately 2 minutes. Data coverage from IMAGE was not continuous with there being a data gap of approximately 4 h every 13 h orbit. As reported by *Shukhtina and Milan* [2014] and explained in chapter 2, these images have been processed to extract integrated brightnesses, as well as an estimate of the open magnetic flux content of the magnetosphere, F_{PC}, using the size of the polar cap as a proxy.

In conjunction with these datasets 1 min OMNI data are used for solar wind parameters (solar wind speed, V_{SW} and the interplanetary magnetic field components, B_X, B_Y, B_Z), as well the SYM-H, AU and AL indices. The solar wind parameters are used to estimate the dayside reconnection rate, Φ_D, based on the formulation of *Milan et al.* [2012].

Simply using the aforementioned event lists by themselves is problematic. For example, SEs are known to be characteristically similar to substorms and as a result, SEs have been described as substorms before [e.g. *Henderson*, 2004]. There is some overlap in our lists with *Frey et al.* [2004] having identified all brightenings as substorms; all substorms which are also classified as an SE ($\pm$15 min of onset) are removed from the substorm list. Similarly, only using auroral electrojet index thresholds are not necessarily a reliable indicator of steady magnetospheric convection as shown by *McWilliams et al.* [2008].

In order to avoid ambiguities between event types, the event lists were examined for inconsistencies. Each SMC event was studied individually to ensure that they fitted the physical criteria for 'balanced reconnection interval' as described by *DeJong et al.* [2009, 2008]. For all SMC, where more than 50% of an event interval had corresponding IMAGE data available (391 events), F_{PC}, WIC brightness, AU, AL, IMF B_z (in GSM coordinates) and Φ_D were examined to manually deselect SMC events that are either not steady (F_{PC} and WIC brightness show substorm signatures) or not convective (Φ_D is below 20 kV for most of the event). SMCs where less than 50% of the data from IMAGE were unavailable were also deselected.

Figures 5.1, 5.2 and 5.3 show three example events as identified by *Kissinger et al.*. Each of Fig. 5.1, 5.2 and 5.3 show several panels: the top panel shows F_{PC} with the time stamp of the beginning and end of the event, followed by AL and AU (red dashed lines show *Kissinger et al.*'s criteria 1 and 2 (see chapter 2, section 2.3.2)), followed by the maximum intensity of aurora as measured by WIC, the IMF B_Z component, and Φ_D.

Figures 5.1 and 5.3 show why some events were rejected, whereas Fig. 5.2 shows an example SMC event which was chosen for the further event selection. Although F_{PC} stays fairly constant over the event shown in Fig. 5.1, which could indicate the occurrence of an SMC, Φ_D is below $\sim$ 20 kV for the duration of the interval, indicating that there is insignificant convection within the magnetosphere, which is why this event was deselected. WIC brightness is also plotted, which was used in some cases to help identify substorms, but the brightness peak in this case was not used as such an identifier, as there are no changes in F_{PC} occurring at that time.

The event shown in Fig. 5.2 shows an example of an SMC: F_{PC} and I_{WIC} stay steady throughout the event; Φ_D is elevated and fairly constant and AL and AU fulfill the *Kissinger et al.*-criteria.

The event shown in Fig. 5.3 shows that even though this event obeys the *Kissinger et al.*-criteria, it is not steady: the vertical orange lines show two *Frey et al.*-substorms, which occur during this SMC. Leading up to each substorm, F_{PC} and I_{WIC} increase and then decrease after substorm onset, indicating clear substorms. Furthermore, Φ_D is far from constant throughout this event, primarily due to the wildly varying IMF B_Z component. It shows that the criteria set out by *Kissinger et al.* [2011] are not definite indicators of SMCs and for these reasons this event was deselected from the final SMC list.

Figure 5.4 shows the occurrence of substorm onsets in relation to the onset and end of SMCs used in this study. As all SMCs have differing event lengths, each SMC's event duration was normalised, such that we can consider the event timings in terms of percentage of event, with 0% at the start and 100% at the end. The occurrences of substorms were then binned with a bin length of 10% of SMC event length. The occurrences of substorms prior to and subsequent to SMCs were also plotted. The average duration of the SMC events was just less than 200 minutes. The grey histogram has been calculated using the original SMC list, whereas the blue histogram only uses the manually selected SMCs. Both occurrence distributions show peaks just before and just after the SMC events start and end. Fig. 5.4 also shows that some

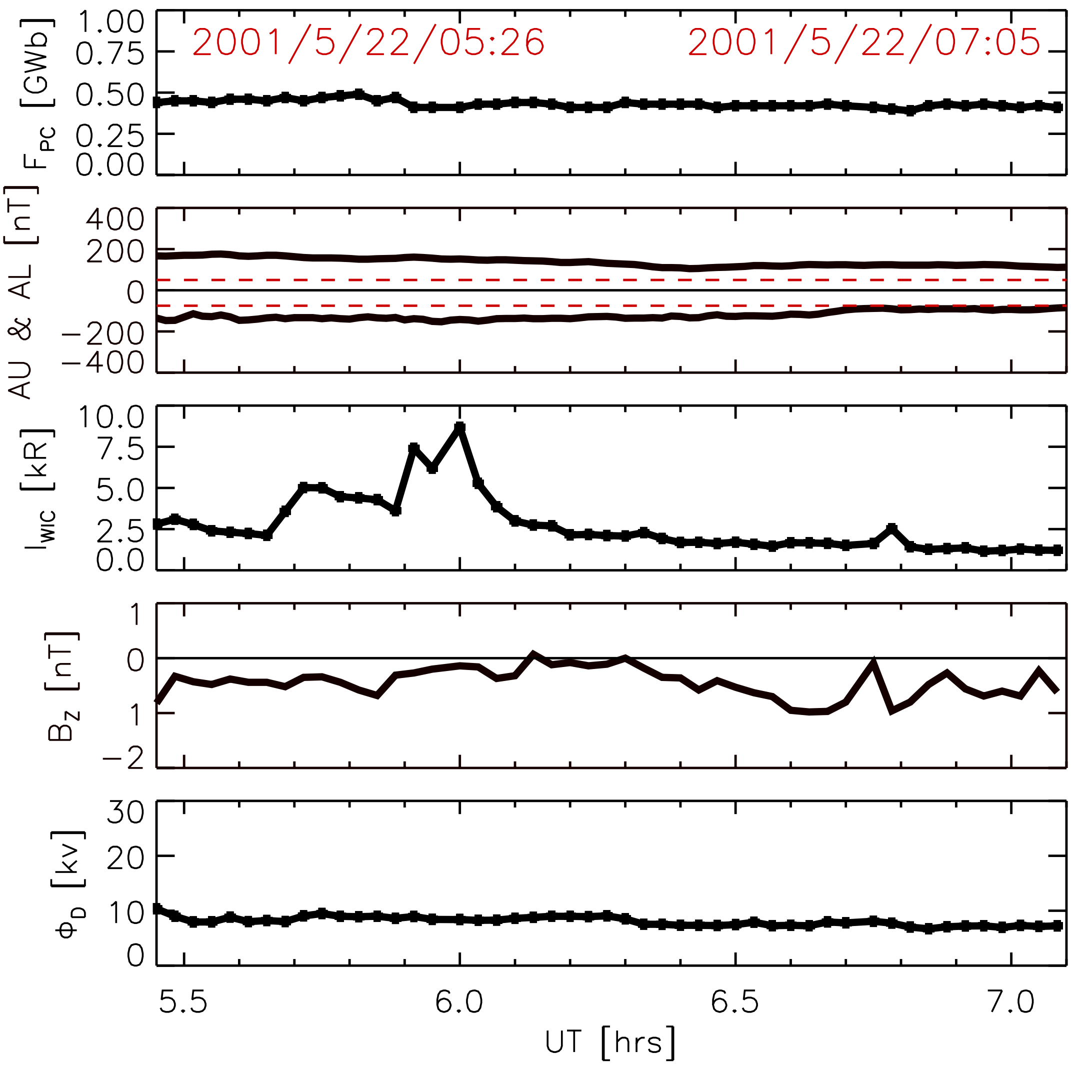

Figure 5.1: Example of rejected SMC event, showing F_{PC}; AU & AL; auroral brightness as measured by WIC; IMF B_Z and Φ_D. The dashed lines in the AU & AL plots indicate the thresholds as set out by *Kissinger et al.* [2011] criteria. The data derived from IMAGE measurements are plotted as crosses, joined up by lines to indicate the data density.

of the *Frey et al.* substorms occur during the SMCs, but the number of these events is relatively small. These substorms are pseudo-breakups and similar brightenings, as each SMC was checked for substorm occurrence (plotted as in Fig. 2.6) and deselected all SMCs with obvious substorms occurring. As a result of the large number of substorm events occurring during the time leading up to the SMCs, the SMC list was further sub-divided: for all the SMCs, which have a substorm occurring during the 2

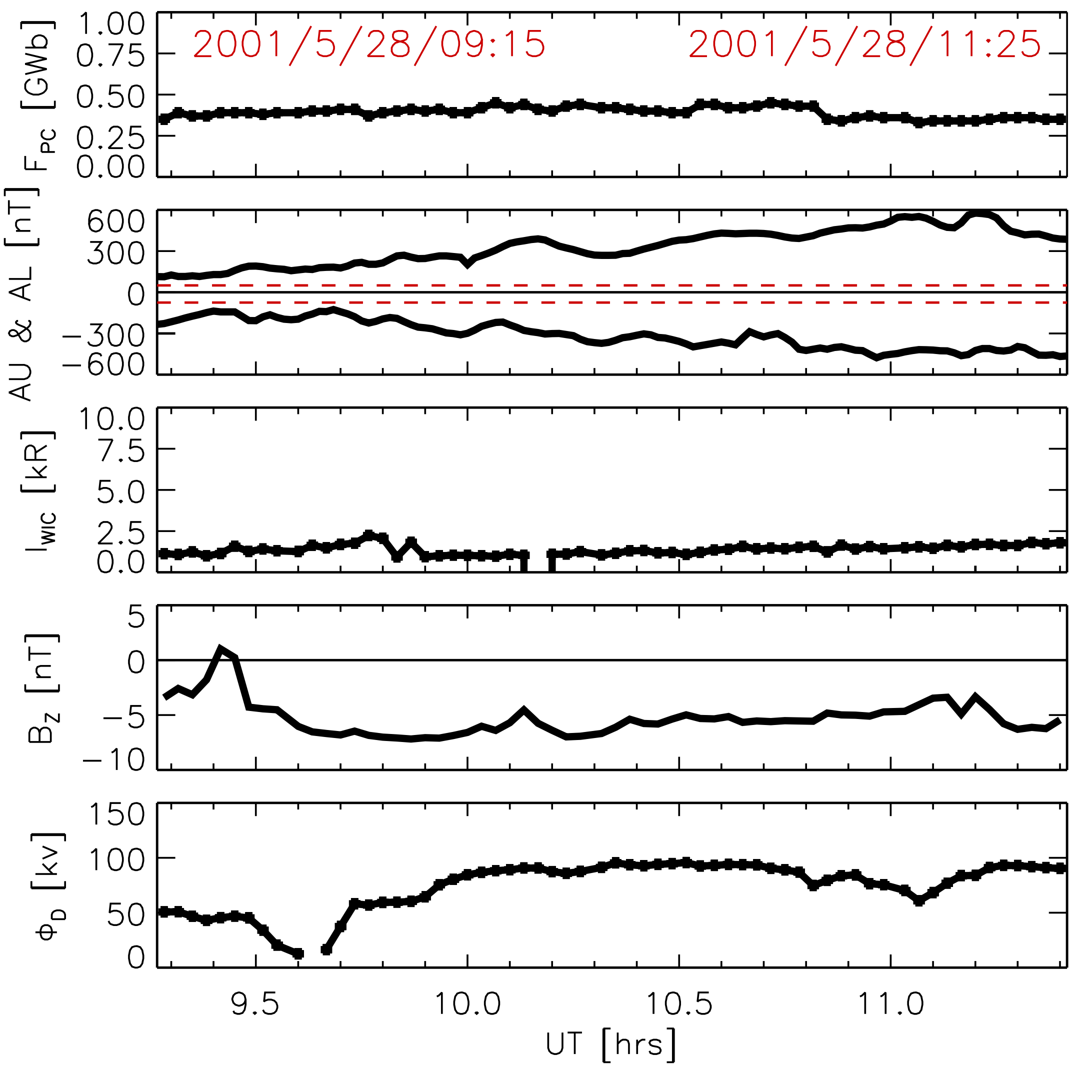

Figure 5.2: Example SMC event, showing F_{PC}; AU & AL; auroral brightness as measured by WIC; IMF B_Z and Φ_D. The dashed lines in the AU & AL plots indicate the thresholds as set out by *Kissinger et al.* [2011] criteria. The data derived from IMAGE measurements are plotted as crosses, joined up by lines to indicate the data density.

hours preceding the SMC interval the SMC event is re-timed, such that the beginning of the event is shifted to match the closest substorm onset. Two hours were chosen to find preceding substorms, as this is characteristically the duration of substorms. For all other SMCs the onset and end times are kept the same. Refining the start of SMCs preceded by substorms allows for a study of the evolution of magnetospheric

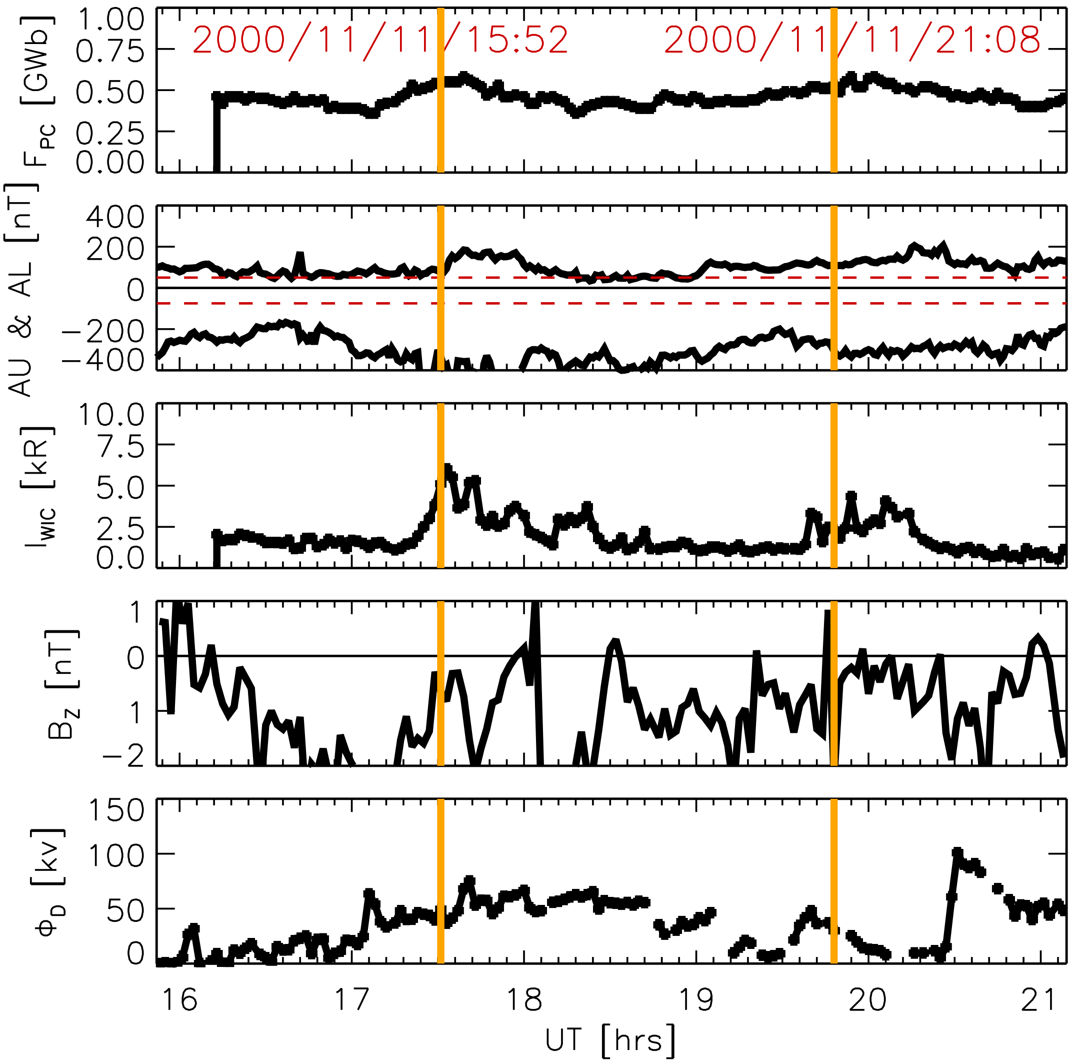

Figure 5.3: Example of rejected SMC event, showing F_{PC}; AU & AL; auroral brightness as measured by WIC; IMF B_Z and Φ_D. The dashed lines in the AU & AL plots indicate the thresholds as set out by *Kissinger et al.* [2011] criteria. The data derived from IMAGE measurements are plotted as crosses, joined up by lines to indicate the data density. Vertical orange lines show onsets of *Frey et al.*-substorms.

behaviour from the initiating substorm into the following SMC.

DeJong et al. [2007] and *Huang et al.* [2009] composed superposed epoch analysis of the F_{PC} for SEs, SMCs and substorms, but this analysis adds to their studies because a much larger dataset is used here. *DeJong et al.* [2007] used only 45 SMCs,

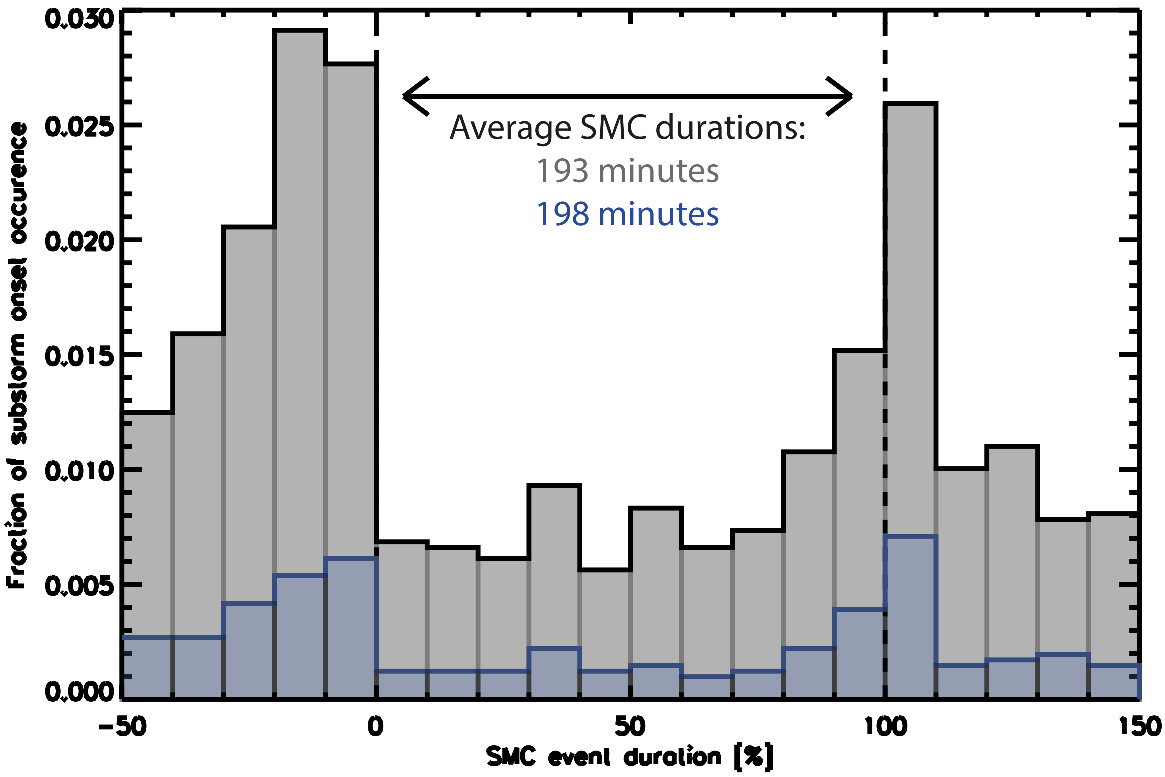

Figure 5.4: Occurrence distribution of substorms with respect to the onset and the end of SMCs. The number of substorms per bin are normalised by the total number of substorms considered (4083 substorms). The black histogram shows the substorms in relation to the original SMC list and the blue histogram shows the substorm occurrence in relation to the manually selected SMC list.

29 SEs and 31 isolated substorms, whereas here, 4083 substorms, 273 SEs, 154 SMCs with preceding substorms, and 113 SMCs without preceding substorms are used. The number of SMCs which conclude with a substorm (i.e. where a substorm occurs in the two hours after the SMC ends), is considerably less with only 85 SMCs concluding with a substorm. Furthermore, the superposed epoch analysis is also utilised to look at the end time of the SMCs as zero epoch to establish how the SMCs conclude.

5.3 Results

Figure 5.5 shows a series of superposed epoch analysis for the substorms, SMCs and SEs. The substorms are shown in red, the SEs in orange and the SMCs in green and blue. The blue SMCs have preceding substorms during the 2 hours beforehand and their zero epoch has been shifted to match the substorm onset, whereas the green SMCs do not have preceding substorms. The paler areas indicate the sizes of the standard errors on the means and the zero epochs are shown by the dashed lines. The horizontal black lines show the averages for each parameter for the whole period from May 2000 to October 2005. For the first column, onset was taken as the zero epoch, and the superposed epoch analysis were calculated with a cadence of 2 minutes. The second column shows superposed epoch analysis where the timescales have been stretched, relative to the start and end times of the SMCs, the data were binned and averaged at a cadence of 2% of the event duration.

The signatures of the substorms in Fig. 5.5 show a decrease in the IMF B_Z component, becoming clearly southward prior to their onset, peaking about 25 minutes before onset, which is followed by a gradual recovery towards 0 nT. B_Z is plotted along with V_{SW} as the only solar wind parameters, as they directly modulate Φ_D and with it the magnetospheric dynamics. V_{SW} shows no particular characteristics for substorms. Φ_D thus mirrors the behaviour of B_Z, so the substorm average increases before onset, reaching a maximum at T = - 25 minutes and then decreases again, all beginning and ending near the global mean. The integrated emission intensity of the auroral oval has values near the global mean at the beginning and increases sharply at onset, as expected due to Frey's selection criteria. The integrated intensity for the substorms then stays elevated for an hour or so before decreasing again. The maximum intensity given by the SI12 and WIC instruments onboard IMAGE show similar patterns to the integrated brightness for the substorms: a sharp increase is seen at onset, followed by a gradual decrease during the substorm toward normal values. The polar cap flux for the substorms is near the average value, 0.4 GWb, at the beginning of the interval shown, and increases to 0.5 GWb at onset. F_{PC} then decreases again to its starting point. The AU index for substorms is slightly below the average for the dataset and increases to values slightly above it at onset, whereas the AL index starts off above the average and shows a clear decrease, commencing at onset, which is followed by a gradual increase. The SYM-H index for the substorms is near the average and shows a very gradual decreasing trend over the period shown.

In almost all respects, the blue SMC traces, which are initiated by substorms, follow those of the substorms up to and including onset. Thereafter, the substorm traces

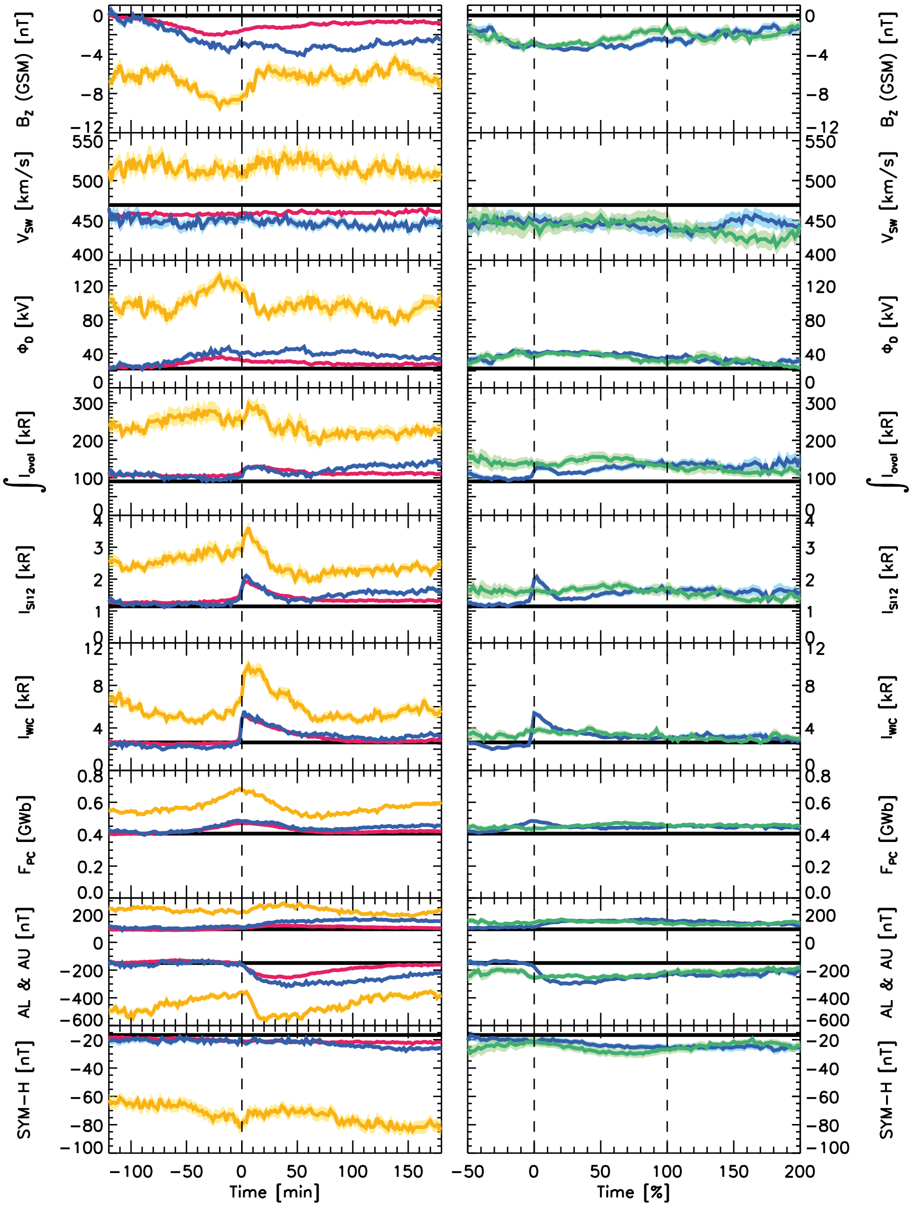

Figure 5.5: Plots showing a superposed epoch analysis of substorms (red), SEs (orange), and SMCs (blue and green). The paler areas indicate the size of the standard errors on the mean. The averages for the whole dataset are shown by the black horizontal lines and zero epochs are indicated by the dashed lines. The blue lines show the mean of the SMCs that have a preceding substorm and the onset of those events has been shifted to the onset of the substorms, whereas the green SMCs are the remaining SMCs with no preceding substorm. The column on the left uses onset as a zero epoch and the second column has a timescale normalised to event duration. The green SMCs have been omitted from the left panels for clarity. The rows show the superposed epoch analysis of the IMF B_Z component; the solar wind speed; Φ_D; integrated oval intensity; maximum oval intensity as measured by the SI12 and WIC instruments; F_{PC}; AL & AU and SYM-H.

subside towards average values, whereas the SMC traces remain elevated, that is, B_Z remains uniformly southwards, F_{PC} and Φ_D remain enhanced above the average, the aurorae remain bright and the AU & AL indices remain elevated.

Green SMCs, which are not initiated by a substorm, show similarities and differences to blue SMCs. B_Z remains negative for the duration of the events and AL and AU are elevated. However, green SMCs do not show an abrupt onset in AL or auroral intensity as they do not begin with substorms. The main difference is in SYM-H, which is more negative than the blue trace at T=-50%; then the green trace increases slowly until onset, when it becomes more negative again.

Figure 5.6 shows a superposed epoch analysis of the two SMC types and substorms on a longer timescale than the previous superposed epoch analysis. The top panel shows F_{PC} and the bottom panel shows the IMF B_Z component. The aim of this figure is to draw attention to what distinguishes SMCs with preceding substorms from those without: the prolonged driving of the magnetosphere due to a southward IMF prior to onset. Whilst SMCs with preceding substorms (blue) show a clear increase in southward IMF from $\sim$2 hours prior to onset to onset (which is similar to substorms), SMCs without preceding substorms (green) have, on average, a considerable southward component in the IMF for over 10 hours before onset. It appears that there is an increase and decrease in F_{PC} for SMCs with preceding substorms a few hours before onset: although this is not a sharply defined feature, such as the substorm at onset, it may be another preceding substorm, which is blurred out in the averaging process.

The SE signatures in Fig. 5.5 are very similar to substorms, as they show the same variations, though significantly more enhanced. The only one that does not show the same signature is the integrated auroral oval intensity, which shows that the aurorae are on average approximately twice as bright prior to SE compared to just before substorm onset. The SE do show an overall increase in oval intensity but the onset is not as clearly defined as for substorm onsets.

To look at SEs in more detail, Figure 5.7 has been included: this series of superposed epoch analyses compares the data shown previously for SEs (i.e. where each tooth is counted as an onset (in red)) to a superposed epoch analysis where just the first tooth of each series is counted as an onset (orange in Fig. 5.7). The time period shown from onset here is $\pm$12 hours, which is longer than the timescale chosen for

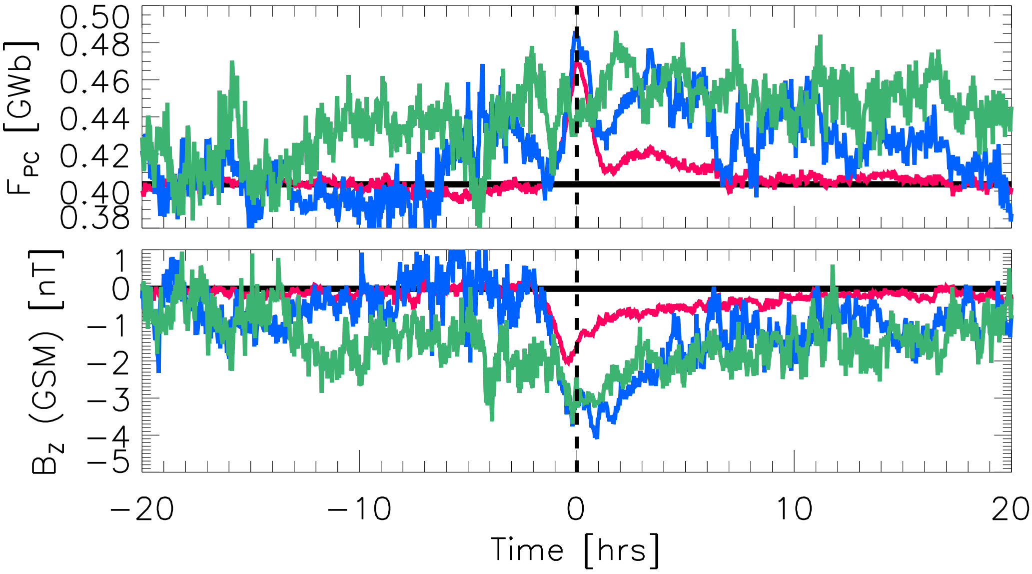

Figure 5.6: Superposed epoch analysis of F_{PC} (top) and B_Z (bottom), showing substorms (red), SMCs with preceding substorms (blue) and SMCs without preceding substorms (green) on a longer timescale of ±10 hours from onset. The dashed vertical line shows onset and the black horizontal lines show the averages across the entire datasets.

Fig. 5.5, which was done to see if there is a pre-conditioning for the first tooth in comparison to the general SE behaviour. The red lines, showing the average of the onset of each tooth series, display similar features to the general SEs in most panels around onset. Prior to onset all parameters shown are elevated in comparison to the blue horizontal lines (data averages over the entire dataset). Especially, the auroral intensities, F_{PC}, SYM-H, Φ_D, AU & AL all show elevated levels in comparison to the average parameter values, with the IMF B_Z component also also showing a strong southward character for several hours before onset. In comparison to the average SE values (red), these parameters are lower for the first tooth (orange), but nevertheless elevated from average values. SYM-H indicates that the first tooth in a series on average occurs during less geomagnetically disturbed times than SEs in general, which is expected as the sawtooth injections will add to the ring current.

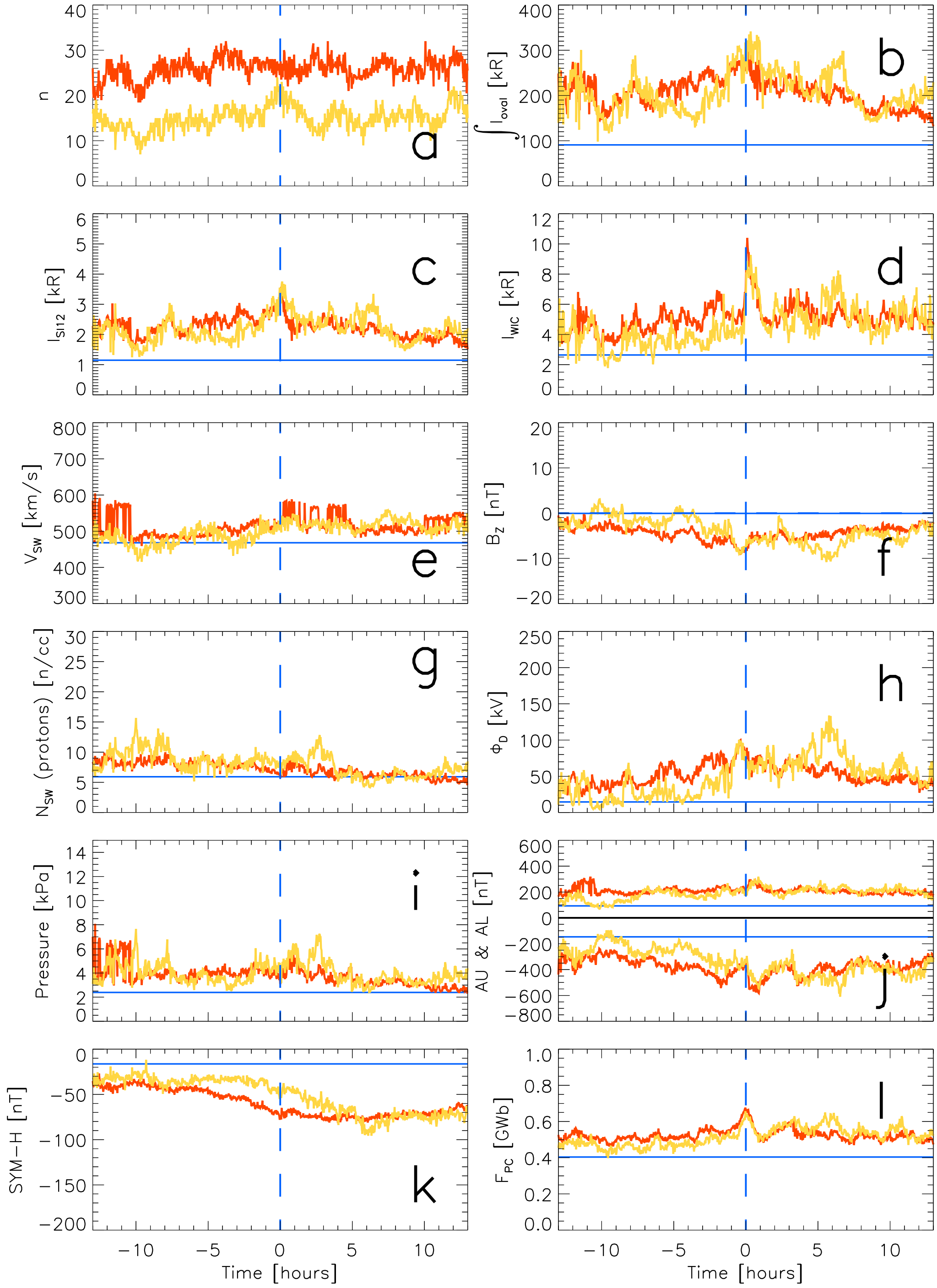

Figure 5.7: Plots showing a superposed epoch analysis of SEs (red), and the first tooth in each SE series (orange) from 12 hours before onset to 12 hours after onset. The averages for the whole dataset are shown by the blue horizontal lines and zero epochs are indicated by the dashed lines. The individual panels show the number of datapoints, n, in each series (a), a superposed epoch analysis of the integrated oval intensity (b); maximum oval intensity as measured by the SI12 and WIC instruments (c and d, respectively); the solar wind speed (e); IMF B_Z component (f); solar wind proton density (g); Φ_D (h); solar wind pressure (i); AL & AU (j); SYM-H (k) and F_{PC} (l).

5.4 Discussion

Out of the 391 SMC events where IMAGE data are of good quality [see *Shukhtina and Milan*, 2014, for definition], 32% of events were rejected as either Φ_D was close to zero for most of the event or F_{PC} was too variable. This illustrates how problematic it is to just use AU and AL as proxies for magnetospheric convection. 229 SMCs were considered and sub-divided into two categories: events where substorms occurred during the 2 hours preceding the SMC and events where no substorm occurred before SMC onset. The SMCs with preceding substorms were re-timed, such that the SMC onset matches substorm onset.

The superposed epoch analysis for the substorms show very distinct features just before or at onset, followed by gradual recoveries: prior to onset the dayside reconnection rate reaches a maximum, as B_Z is most southward approximately half an hour before onset; the intensity of the aurorae peak at onset, as well as the open magnetospheric flux; AL decreases sharply at onset to reach a minimum after onset. These signatures are well known for substorms, where a period of southward IMF leads to magnetopause reconnection, such that the accumulation of newly open magnetic flux in the lobes is associated with an expansion of the polar cap, and AL & AU enhance as convection is excited. At some point reconnection in the magnetotail is initiated, leading to auroral brightenings and the formation of the substorm current wedge and thus the characteristic substorm bay in AL. The trend of a decrease in the magnitude of B_Z prior to substorm onset has been widely reported, as well as the suggestion that substorms are triggered by a northward turning of the IMF [e.g. *Caan et al.*, 1977; *Lyons*, 1995]. This was disputed by *Morley and Freeman* [2007] and *Freeman and Morley* [2004, 2009] and *Wild et al.* [2009] (among others) to be as a consequence of the natural variability of the IMF and the fact that after substorm onset it is no longer required that the dayside reconnection continue for the substorm to be initiated.

Approximately 58% of all SMCs we examined have a substorm occuring during the 2 hours preceding the SMC onset. If this is to be considered the onset of an event, almost identical signatures are seen for substorms following the pre-SMC substorm onset. The introduced time-shift makes it possible to see the substorm at the onset, as well as the following SMC. The difference between these SMCs and substorms is that the IMF remains southward beyond the time of onset and magnetopause reconnection continues into the expansion phase, when magnetotail reconnection has also commenced.

This means that the polar cap contracts slower than it usually does for substorms after onset; it continues to be enlarged for longer and the open flux content of the magnetosphere stays approximately constant throughout the event. The IMF B_Z component will gradually turn more northward toward the event conclusion and the SMC will end at some point during this transition. At this point, the dayside reconnection decreases but the magnetotail continues into a 'recovery phase' as F_{PC} continues to decrease very gradually for several hours (not shown on this time scale). The intensity of the aurorae, as well as AL will decrease at this time. A decrease in the southward component of the IMF can be seen in the blue trace in Fig. 5.5 toward the conclusion of these SMCs, at approximately T=60%.

DeJong et al. [2008] showed an example of an SMC event in their study that appears similar to our substorm-following SMCs: a substorm initiates nightside reconnection but F_{PC} remains enhanced and steady, along with the auroral brightness during their event. The end of the auroral activity is marked in their event by B_Z becoming more northward. Their data suggests that the extended southward component of the IMF and its gradual northward turning allows the reconnection rates to continue to be enhanced and balanced whilst the magnetotail is relaxing back to a quiet state. The substorm-following SMCs presented here progress in a similar manner and it can be seen clearly that it is the substorm onset that initiates the necessary flux closure. These events are not strictly driven recovery phases, but rather driven expansion phases, as flux continues to be closed after the SMC has concluded. It is hard to distinguish where the event phases start and end in our superposed epoch analysis, so the SMC may be part of the expansion or early recovery phase. The analysis shows that the recovery phase continues after the SMC as the auroral brightness continues to decrease, as well as the dayside reconnection rate and the open flux, and thus the magnetosphere is still relaxing after the SMC event has ended.

In the past, researchers [e.g *McPherron et al.*, 2005; *DeJong et al.*, 2009; *Kissinger et al.*, 2011, 2012] thought that the event-preceding substorms are necessary for SMCs to occur and precondition the magnetosphere in some way, whereas in the work presented here, approximately half of SMCs are part of the substorm cycle. We would reclassify 'classic' substorms as those which coincidentally have a decrease in Φ_D, following the clear enhancement prior to onset, whereas 'substorms + SMCs' events are those for which Φ_D remains elevated after onset. This naturally explains the debate regarding the occurrence of northward turnings for triggering substorms: some substorms which do not have a northward turning or rather a reduction in the southward component do on average not look like classic substorms and develop into SMCs instead.

Sergeev et al. [1996] suggest that it is necessary for SMCs to have a preceding substorm as the magnetosphere needs this release of flux in order to be able to reach a quasi-steady state, as their data suggests that SMCs are an active period between substorms. The percentage of events with preceding substorms in this study is considerably lower than theirs, suggesting that the substorms may not be necessary for the establishment of steady convection. The superposed epoch analysis presented here shows that the SMCs with preceding substorms are part of the evolution of the substorm event.

The rest of the SMCs (42% of all considered events) do not share exactly the same characteristics as the substorm preceded SMCs, instead the aurorae are intensified before onset, as well as the AL index and continue to be throughout the events. The SYM-H index indicates more disturbed geomagnetic conditions, but most significantly, the dayside driving is much more prolonged than for the SMCs with preceding substorms. These SMCs show a long stretch of southward IMF, which starts approximately 13 hours before onset (see Fig. 5.6), whereas substorm preceding SMCs only show a southward IMF leading up to the event as the substorm growth phase occurs (shown in Fig. 5.5). This may be due to the magnetosphere needing either this prolonged dayside driving for steady convection to occur, or a substorm to help initiate the flux closure.

Similar to this study, *Kissinger et al.* [2012] found that 92% of all SMCs occur within 75 minutes of a substorm onset. Although they use the same SMC criteria, their fraction of events with or without preceding substorms differs to the one presented here because they do not exclude events where no dayside driving occurs. Although they find that 1% of SMCs occur after a quiet magnetosphere and the remaining events after substorm-like behaviour, it is speculated that their 1% belongs to the events have been excluded due to insufficient dayside driving.

O'Brien et al. [2002] show that for SMCs to occur, V_{SW} values below 450 km/s are preferential; the data shown here agrees with this. For all of the events, except SEs, V_{SW} stays just below the average for the whole dataset, which is around 470 km/s. For SEs, the V_{SW} average stays at or above 500 km/s. This indicates that fast solar wind speeds are not necessarily needed for active periods in the magnetosphere.

In their studies of SEs, SMCs and substorms, *DeJong et al.* [2007] and *Huang et al.* [2009] showed that on average, F_{PC} for SE reaches at least 1 GWb before onset. The dataset shown here however barely ever reaches such high values, so the average F_{PC} for SE at onset is just below 0.7 GWb. The superposed epoch analysis agree with those of *DeJong et al.* [2007] and *Huang et al.* [2009] in terms of the overall shape of F_{PC}, the values however, differ. This is most likely due to a systematic offset brought about by different F_{PC}-estimation methods. The interpretation of the data shown here, in line with that of *DeJong et al.* [2007] and *Huang et al.* [2009], is that SEs show all the characteristics of substorms occurring during disturbed geomagnetic conditions, storm conditions even, and strong solar wind driving. Due to the larger selection of events, we can now be more certain of these characteristic condition within SEs occur.

Fig. 5.7 showed that solar wind driving is enhanced prior to the first tooth in a series of SE. This preconditions the magnetosphere, similar to substorms and SMCs, but perhaps in a more energetic way, which can be seen in AL, AU, SYM-H and auroral brightnesses being enhanced for many hours, even prior to the first tooth. The series showing the average behaviour for the first tooth in a series (orange) also shows the quasi-periodic nature of a series of SE better: F_{PC} and AL show clear re-intensifications every $\sim$2.5 hours after onset. Whilst Φ_D and B_Z do not share this character, they do show a ramping up of dayside driving of the system (i.e. IMF B_Z becomes more negative and Φ_D increases), leading up to each following tooth after onset. SYM-H indicates that the ring current is enhanced in general for all SEs, but when comparing the first tooth to all tooth onsets, it is more enhanced for the series showing an average across all teeth. This indicates that as a series of SEs progresses, the ring current becomes stronger as more particles are injected into the ring current with each dipolarisation.

5.5 Summary

Approximately 58% of all SMCs considered have a substorm occurring in the 2 hours before onset. These events show signatures just like substorms with the expansion phase stretched over a longer timespan. It is concluded that the majority of SMCs flagged by the *Kissinger et al.* [2011] selection criteria are driven expansion or recovery phases of substorms, which show an increase of the polar cap flux before onset. During the event itself, the prolonged enhanced dayside reconnection rate is continually driving the convection, unlike for substorms, during which the dayside driving is lower and does not dominate throughout the event. This means that the polar cap cannot contract and elevated auroral intensities are seen throughout the event. AL and AU remain elevated throughout this period, as given by the definition of an SMC by the *Kissinger et al.* [2011] criteria. The recovery phase commences when the dayside driving decreases and polar cap flux decreases and thus the substorm recovery continues after the SMC has concluded. Around 42% of the SMCs do not have substorms occurring during the 2 hours prior to the events and occur after prolonged dayside driving (approximately 13 hours thereof). Thus, the majority of SMCs, as they have been selected in the past, are part of the substorm process and could also be considered driven expansion or driven recovery phase due to continued dayside driving.

Similarly, SEs occur during enhanced geomagnetic activity and convection. They show the same signatures as substorms, but the characteristics are more enhanced and extreme. Most significantly, the magnetospheric response is qualitatively the same for substorms and SEs in terms of flux closure, although on a differing scale. Before the first tooth of a series of SEs can occur, the magnetosphere is driven by southward IMF for approximately 4 hours, with the SEs occuring as a response to a ramping up in dayside reconnection rates. As the series of SEs progresses, the ring current enhances due to the injection of particles via dipolarisations.

6

Auroral Responses During Substorms, Sawtooth Events and Periods of Steady Magnetospheric Convection

> 'It was ten minutes to six on the evening of the 5th February, when we were some miles from Hammerfest, the weather clear and the moon shining, when there appeared a sharply-defined arc of light from east to west through the zenith. From the very first, the arc was very intense, but very narrow, right above our heads. Notwithstanding the bright moonlight, the aurora, which soon began to pass through various phases of development with draperies and sheaves of rays, was visible up to half past seven, when it disappeared.'
>
> Observations from *Birkeland* [1908].

6.1 Introduction

Chapter 5 compares SMCs, substorms and SEs in terms of the opening and closing of polar cap flux and general magnetospheric dynamics. In this chapter however, the focus is on the nightside morphological auroral changes during different magnetospheric modes, highlighting the differences which may be the result of varying physical processes occurring during each mode.

The average behaviour during substorms, SMCs and SEs, is studied using data from the Imager for Magnetopause-to-Aurora Global Exploration (IMAGE) FUV instrument suite [*Mende et al.*, 2000a]. In the past, studies of the aurorae during SMCs and SEs have been focused on small datasets and case studies. For example, *Sergeev et al.* [1996] observed small-scale auroral activations during SMCs, including North-South aligned arcs and streamers. To this date though, no large statistical comparison of aurorae during different modes has been undertaken. This study provides the first comprehensive statistical study of auroral oval configurations and dynamics during different magnetospheric modes to determine what the differences are.

6.2 Method

The IMAGE satellite was operational from June 2000 until October 2005, such that the dataset is suitable for large-scale studies, as discussed in previous chapters.

For this comparative study, the event lists used are identical to those employed for the work in chapter 5. The main difference here is, that the SMCs without preceding substorms will not be discussed, as their auroral signatures show no unique or surprising features on the large scale, other than a bright aurora. Here the focus is on substorms, SMCs commencing with substorms and sawtooth events.

To compare the auroral imagery of the different event types, a superposed epoch analysis is performed. For each event type average images at 2 minute cadence from 2 hours before onset to 4 hours after onset are created. WIC data are averaged onto a 80×80 grid by calculating the median for each pixel, where each grid cell is the equivalent of 1° of latitude to a side. For SI12 data, a 40×40 grid of 2° cells is used due to the lower resolution of the camera.

To analyse the auroral dynamics in more detail, the pixels for each average image are binned into MLT sectors of the nightside and latitudinal. The individual bin sizes are shown by the white lines in the schematic of Figure 6.1. To mask the main parts of the aurora, two concentric circles are used as boundaries for the binning. The circles were chosen manually, with the centre defined as [-1°,-3°], with respect to the geomagnetic pole. The smallest circle was chosen to have a radius of 12° and the outer boundary was chosen to have a radius of 31°. The dayside is also omitted in this analysis due to the presence of dayglow. To eliminate dayglow as much as possible, only WIC data from the winter months (spring equinox to autumn equinox) are used. For the time evolution in the MLT bins shown later, the mean is taken across latitudinal bins and to find the longitudinal evolution, the mean is calculated across MLT bins.

Figures 6.2, 6.3, and 6.4 show the binned superposed epoch analyses of the IMAGE FUV SI12 and WIC data.

Panels c and d show the averaged pixels by MLT bins (SI12 and WIC, respectively) with respect to time from onset. Panels e (SI12) and f (WIC) show the averaged latitudinal bins with respect to onset. Onset is marked by the dashed vertical line at t=0. The bottom two rows of panels in Figs. 6.2, 6.3, and 6.4 show selected averaged images from the superposed epoch analysis from SI12 (top row) and WIC (bottom row). The selected individual images (bottom two rows) are taken from -60, 0, 20, 40, 60 and 120 minutes with respect to onset.

The top panel (a) in each figure shows the brightness evolution of the MLT bins measured by SI12, with each MLT bin normalised to the pre-onset brightness (average across t=-5 minutes from onset to onset) and the same is shown for WIC in panel (b). The grey contours in panels (a) and (b) indicate the boundary between brighter and dimmer aurora, in comparison to pre-onset brightness (i.e. the values of the contours are set to 1.1). This is instructive for studying the post-onset brightenings, as the grey contours indicate when the auroral intensity returns to pre-onset levels in each MLT sector.

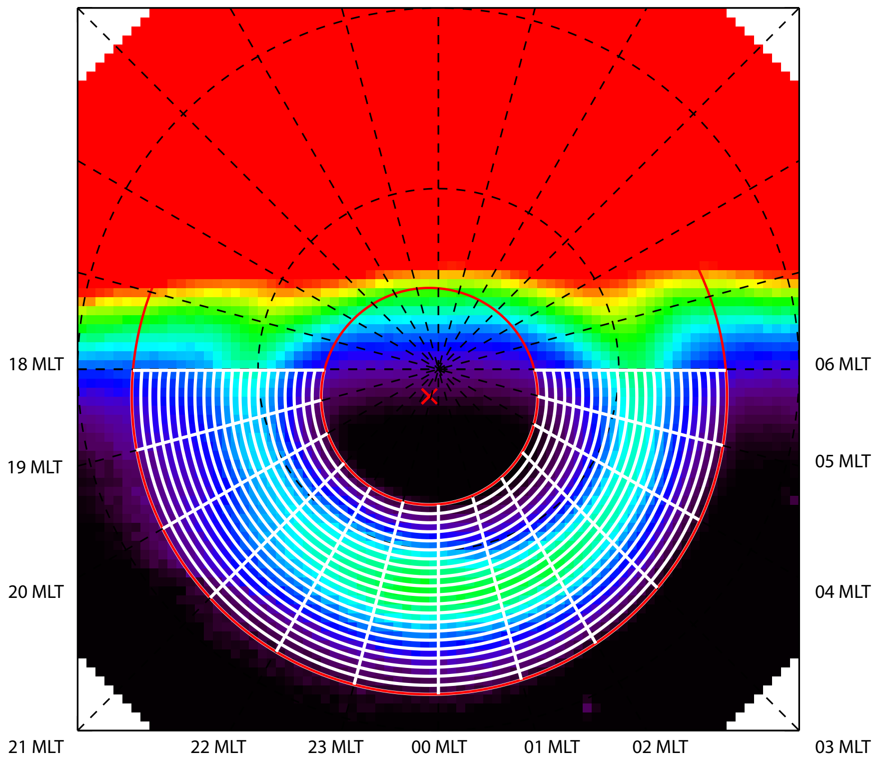

Figure 6.1: Schematic illustrating the data binning. The underlying image is an example of a WIC-averaged picture from the superposed epoch analysis for substorms. The dashed black dashed lines divide the MLT sectors and circles separated by 10° of geomagnetic latitude, centred on the geomagnetic North pole located at the centre of the image. The red lines show the inner and outer boundary circles defined for the analysis in figures 6.2, 6.4, and 6.3, which hold the majority of auroral power for all images. The inner and outer circles have radii of 12° and 31°, respectively. The centre of these circles is shown by the red cross (centred on [-1°,-3°] with respect to the geomagnetic pole). The white lines indicate the bins selected for the radial superposed epoch analysis (semi circles), separated by 1° of latitude and MLT bins (lines).

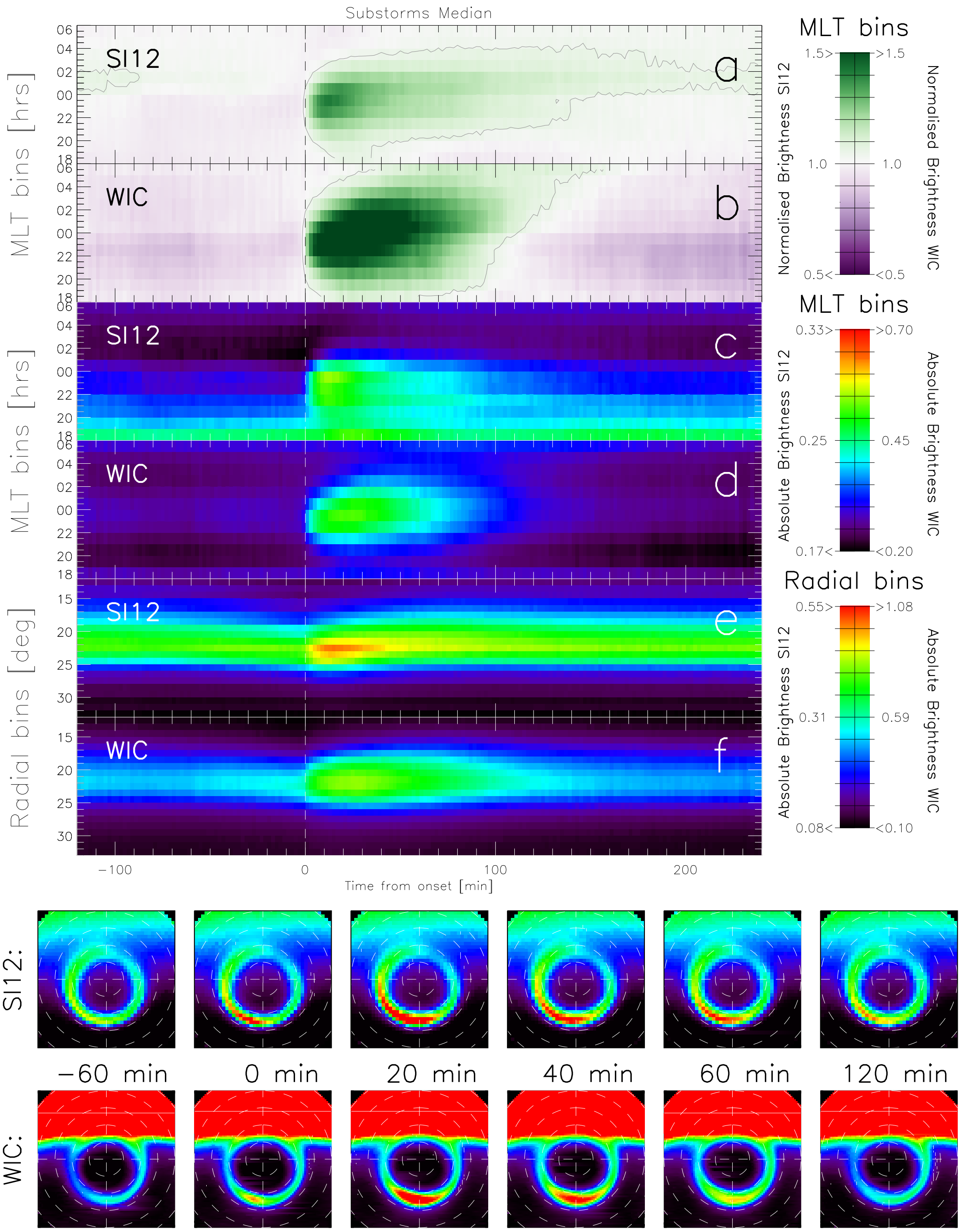

Figure 6.2: Superposed epoch analysis of substorms from IMAGE FUV SI12 and WIC data. Panels show the brightness across the nightside MLT bins, normalised by pre-onset brightness (a) for SI12 and WIC (b), the absolute auroral brightness per MLT bin for SI12 (c) and WIC (d) and the auroral brightness per radial bin for SI12 (e) and WIC (f). The dashed line indicates substorm onset. The bottom two rows of panels show excerpts from the superposed epoch analysis of SI12 and WIC data at t=-60, 0, 20, 40, 60, and 120 minutes with respect to onset.

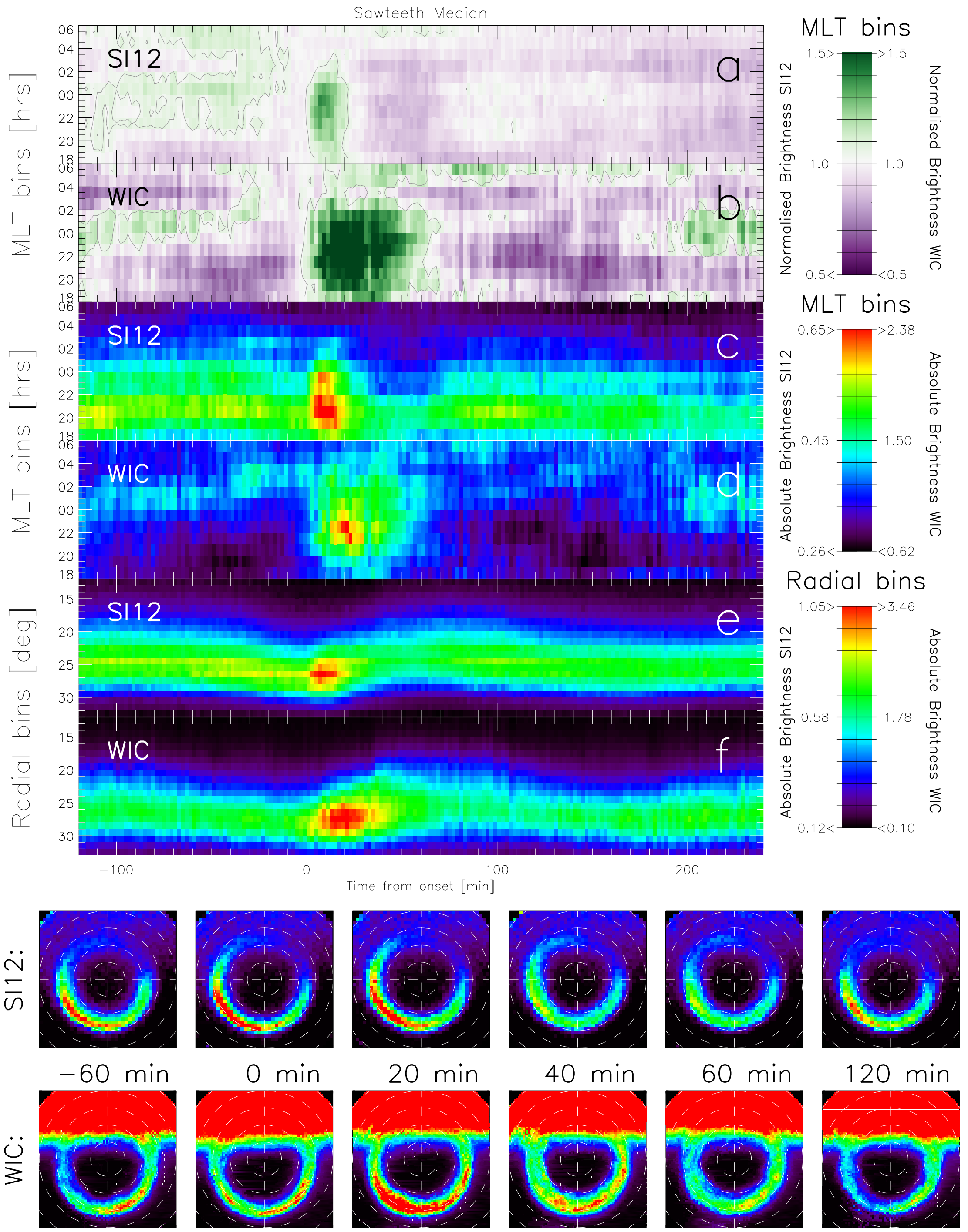

Figure 6.3: Superposed epoch analysis of sawteeth from IMAGE FUV SI12 and WIC data. Panels show the brightness across the nightside MLT bins, normalised by pre-onset brightness (a) for SI12 and WIC (b), the absolute auroral brightness per MLT bin for SI12 (c) and WIC (d) and the auroral brightness per radial bin for SI12 (e) and WIC (f). The dashed line indicates sawtooth onset. The bottom two rows of panels show excerpts from the superposed epoch analysis of SI12 and WIC data at t=-60, 0, 20, 40, 60, and 120 minutes with respect to onset.

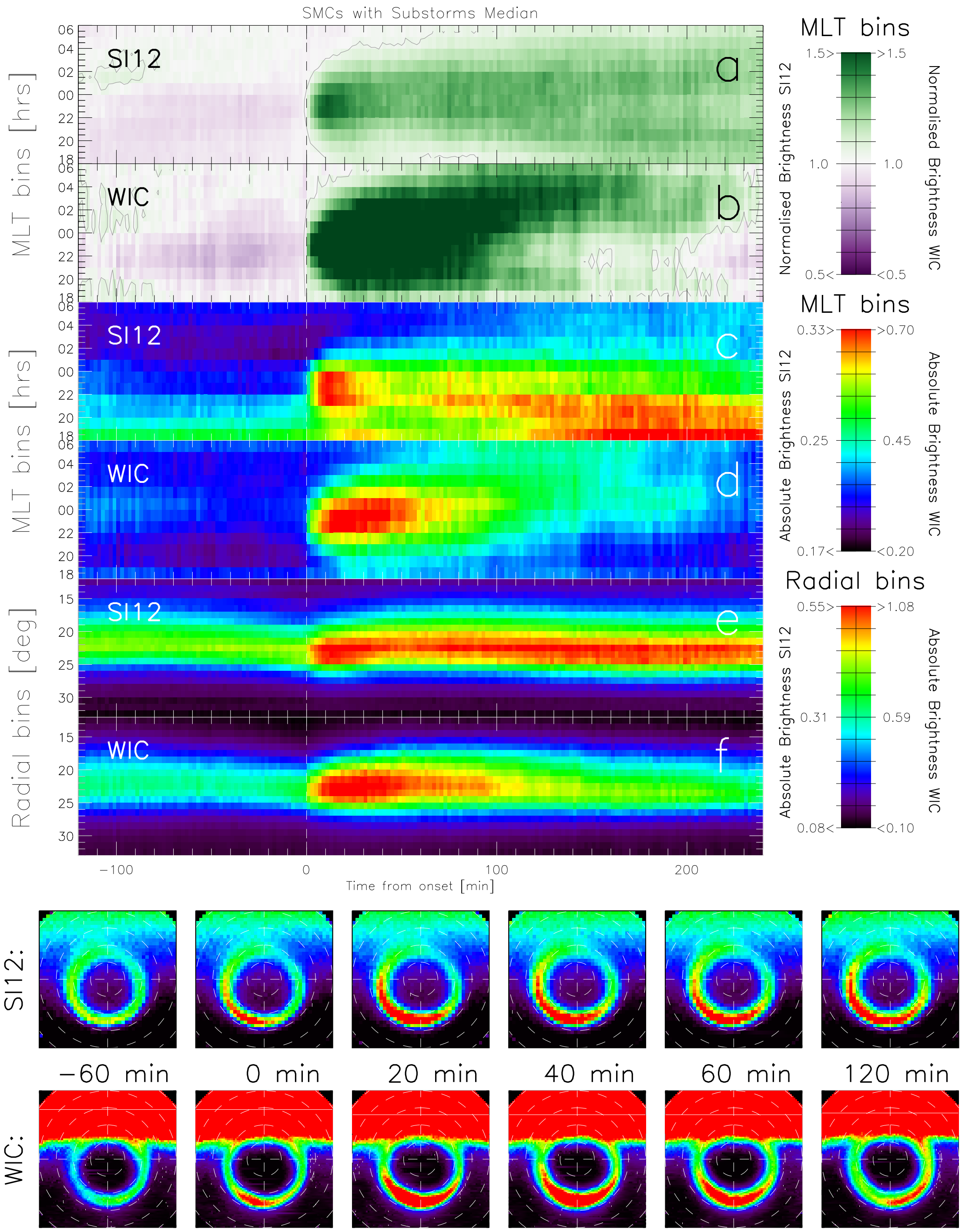

Figure 6.4: Superposed epoch analysis of SMCs with preceding substorms from IMAGE FUV SI12 and WIC data. Panels show the brightness across the nightside MLT bins, normalised by pre-onset brightness (a) for SI12 and WIC (b), the absolute auroral brightness per MLT bin for SI12 (c) and WIC (d) and the auroral brightness per radial bin for SI12 (e) and WIC (f). The dashed line indicates substorm onset, which precede the SMCs. The bottom two rows of panels show excerpts from the superposed epoch analysis of SI12 and WIC data at t=-60, 0, 20, 40, 60, and 120 minutes with respect to onset.

6.3 Results

First the results of the substorm analysis presented in Fig. 6.2 are discussed, followed by the other modes. Prior to onset, the auroral oval gradually expands equatorwards to lower latitudes (see Fig. 6.2, panels e and f). Panels c and d (Fig. 6.2), displaying the MLT dependent behaviour, show that in all nightside MLT sectors, both the electron and proton aurorae are dim prior to onset, with the proton emission being generally higher at dusk than at dawn. Nevertheless, the auroral oval never fully disappears (Fig. 6.2, panels e and f). In panels e and f, in both the WIC and SI12 data, the oval is confined to radial bins ∼18-25°, just before onset. At onset, the aurora brightens between 22 and 0 MLT in the WIC data and between 22 and 1 MLT in the SI12 data (panels a to d). In the superposed epoch analysis this brightening seems to occur over a few hours of MLT, but this is because auroral onset occurs in very confined locations, which vary and are therefore blurred in the averaging process. Latitudinally (see Fig. 6.2, panels e and f), the auroral oval also expands poleward and equatorward after onset, with the radial expansion toward the pole being more obvious. The brightening expands to cover a wider MLT extent, which primarily develops in the 10-40 minutes after onset (panels a and b). The brightening in the electron aurora moves across the midnight meridian towards dawn after expansion, covering 18-06 MLT at t=40 minutes, whereas the brightest proton aurora stays closer to midnight (20-04 MLT), relative to pre-onset brightness (panels a and b). The electron aurora starts to recover from the brightening and expansion after approximately 60 minutes (panel b), whereas the proton aurora takes almost twice as long (panel a). After ∼130 minutes after onset, all proton brightness lies in the post midnight sectors. For all MLT sectors to return to pre-onset brightness also takes less time for the electron aurora (less than ∼2 hours) than the proton aurora (more than 4 hours; c.f. grey contours in panels a and b).

For SEs, the superposed epoch analysis are plotted on a different colour scale, as the aurora is overall much brighter, as also shown in the previous chapter (chapter 5 and *Walach and Milan* [2015]). The superposed epoch analysis of the radial bins reveals that the auroral oval for SEs also expands to lower latitudes prior to onset, but much more significantly. Unlike substorms, the auroras are already very bright before onset (Fig. 6.3, panels e and f). At onset, the brightness seen in the proton aurora increases and it begins to move poleward, similar to the electron aurora, however the electron aurora brightening occurs on a longer timescale of approximately one hour. After the poleward contraction (∼one hour after onset), the auroral oval then moves again to lower latitudes (Fig. 6.3, panels e and f), which is indicative of the conditions preceding the next tooth. Due to the slightly different timings of each tooth, any periodicity will be somewhat smoothed.

Before onset, the electron aurora is brightest in the early morning sectors (1-4 MLT) (Fig. 6.3, panel d). At onset a brightening occurs, which is centred at 21 MLT in the electron aurora (panels b and d). This brightening then expands dusk- and dawnward very rapidly and reaches its full MLT extent within approximately 10 minutes (panels a and b). Within the timespan of 10 minutes, all nightside sectors from 18 to 4 MLT see a brightening in the electron aurora. Coincidentally, the bright electron aurora also expands latitudinally, to cover a latitudinal band of over $\sim 10°$. This feature then continues to exist for approximately one hour, after which the onset brightening in the electron aurora starts to fade and the MLT sectors from 18 to midnight become much less active in the WIC data. The proton aurorae behave differently to the electron aurora during SEs (Fig. 6.3 panel a). Longitudinally, the bright aurora prior to onset is spread out more, especially towards dusk, and does not change significantly at onset. This only shows in panel c, but not panel a and is thus more of a general feature, as opposed to onset-related. At onset, the proton aurorae brighten near midnight (panel a). The brightening is confined to MLTs from 18 to 4 and is very short lived. After 20 minutes post onset, the brightening in the proton aurora has dimmed to pre-onset brightness levels in all MLT sectors (see grey contour in panel a), which is inherently shorter than the recovery time for substorms.

Similar to substorms, SMCs with preceding substorms are dim in all MLT sectors, except for the proton aurora on the duskside, which is bright throughout the considered period (Fig. 6.4, panels c and d) and show a more latitudinally-confined auroral oval, prior to substorm onset (Fig. 6.4, panels e and f). The brightening at onset is also extremely similar to substorms, but generally, the auroral oval is much brighter during these types of events and stays much brighter after the substorm expansion has occurred, especially in the SI12 data (c.f. panels a, b, c, and d). To facilitate comparison, the substorms and SMCs were plotted with the same colour scale as substorms.

Instead of the brightening in the MLT sectors returning to pre-onset brightness after $\sim$100 minutes, as occurs after substorms, the electron brightening stays primarily dawnward (see panel b) at $\sim$120 minutes post onset and stays bright for many hours, with the brightening strongest at 2 MLT. The proton aurora behaves very differently to substorms, as it covers a much wider MLT extent: Approximately 100 minutes after onset, it covers the whole nightside from 18-06 MLT. The proton aurora begins to dim slightly in the nightside MLT sectors around midnight at approximately the same time as the electron aurora and the bright proton aurora then mainly covers the dusk and dawn regions toward the end of the shown interval (during steady convection) rather than being centred around the midnight MLT sector, as it happens during the preceding substorm onset. During SMCs the bright aurora appears to cover not only a wider MLT extent, but also on average a wider latitudinal range than substorms.

6.4 Discussion

The auroral evolution during substorms, SEs, and SMCs preceded by a substorm onset has been examined in the last section, which will now be followed by a discussion of the commonalities and differences.

Prior to substorm onset, when dayside reconnection is dominant and nightside reconnection is thought to be minimal (see chapter 4), mild equatorward expansion of the aurora is seen, which is more visible in the WIC data than in the SI12 data (Fig. 6.2, panels e and f). This may be a result of the WIC data being more sensitive to variations than the SI12 data, in general.

At substorm onset the auroral oval brightens. The brightest segments of the SI12 and WIC emission are at first centred near 23 MLT, with the brightest SI12 emission being shifted slightly more towards dawn than the WIC emission (see individual thumbnails below panels in Fig. 6.2). This spatial divergence in brightenings may be a manifestation of the substorm current wedge forming [*Kepko et al.*, 2015; *Milan et al.*, 2006]. In the traditional picture of the substorm current wedge, field aligned currents will flow from the plasma sheet along the magnetic field lines into the ionosphere, as discussed in chapter 2. There, they will flow westward and form the auroral electrojet. Further towards the west, the current will again flow along magnetic field lines and close with the tail currents. Different models of this substorm current wedge have since emerged [see *Kepko et al.*, 2015, for a more complete discussion], including detailed observations, which indicate that the current wedge may actually consist of more than one 'wedge' or multiple sheets of upward and downward field aligned currents [*Forsyth et al.*, 2014; *Murphy et al.*, 2013]. As the brightest segments of the electron aurora at onset are shifted westward, compared to the proton aurora, upward field aligned currents flowing would be expected there, which is analogous to the radial outward part of the current wedge towards the cross-tail current (by convention, downward flowing electrons are equivalent to an upward current). Where protons precipitate downward on the other hand, electrons may move upward with respect to the protons, meaning a planetward field-aligned current will form. Thus, these initial brightenings at, and just before substorm onset, may be a statistical view of the substorm current wedge forming, as was also shown in a case study by *Milan et al.* [2006, see Figure 7 in their study].

After onset, the auroral oval retreats poleward, which is more rapid than the previous equatorward movement, the development of the substorm auroral bulge. This is unsurprising, as a previous superposed epoch analysis of the same events revealed that the polar cap flux, F_{PC}, shows a clear increase prior to onset and a decrease after onset for substorms (see chapter 5). *Mende et al.* [2003] also performed a superposed epoch analysis of SI12 and WIC data for substorms and although they binned the data with respect to local onset, they found that the polarward and equatorward auroral boundaries with respect to latitude trace out the same pattern that we see in Fig. 6.2 (panels e and f). The main difference is that their traces are displaced equatorward by $\sim 10^o$ of our bright aurora, which is due to their use of a smaller dataset (91 substorms) and are thus likely to have missed many weak substorms, where the auroral oval is generally closer to the geomagnetic pole [*Milan et al.*, 2009b].

At onset, both the proton and electron aurorae brighten explosively, which primarily occurs at 23 MLT, but can cover most nightside MLT sectors [*Frey et al.*, 2004; *Meng and Liou*, 2004; *Newell et al.*, 2001]. This brightening then spreads dusk- and dawnward, extending across midnight from ∼18-4 MLT (SI12) and ∼18-6 MLT (WIC) 20 minutes after onset, which is when AL is on average the most enhanced during the substorm cycle (see chapter 5). We can see from panels a and b in 6.2, that in both cases the expansion of the brightening towards dusk occurs faster than the expansion towards dawn. Concurrent with the longitudinal spreading of bright aurora, the intensification of the aurora (especially the electron aurora) also spreads latitudinally. After this (approximately one hour after onset), the proton aurora begins to dim with the electron aurora staying bright for another hour, before it begins to dim. As shown in the previous study (chapter 5), the majority of the brightening lasts for approximately one hour. Fig. 6.2, panels a and b reveal however, that the brightening lasts much longer in the proton aurora, compared to the electron aurora. The electron aurora has almost dimmed back to pre-onset levels approximately 3 hours after onset in all MLT sectors. The brightening in the electron aurora lasts longest in the dawn sectors, with the brightening relaxing to pre-onset intensities approximately 160 minutes after onset at 6 MLT. Compared to pre-onset levels, the proton aurora brightening at 2 MLT takes over 4 hours to recover. In a statistical study, *Blockx et al.* [2005] found that generally, the location of the brightest SI12 emission is a good locator for where the magnetotail is the most stretched. The prolonged brightening at 2 MLT thus implies that the magnetotail is stretched at this location, leading to a high curvature of the field lines in the equatorial plane and thus a pitch angle scattering of protons [*Sergeev et al.*, 1983].

These intensifications cannot be driven by particle acceleration due to reconnection, as no particular electron brightenings are seen in these MLT sectors. As such, it follows that the majority of protons, which create these aurora are drifting on closed field lines and as they enter a still stretched tail region, they will pitch-angle scatter and create the aurora.

Mende et al. [2003] further find that '*as the substorm expansion proceeds poleward, the electron precipitation remains relatively constant, while the protons fade because less energy is available from dipolarization. Thus in the early phases we see the proton precipitation expanding with the surge electrons and in later phases they do not seem to be present in the leading edge of the substorm surge*'. Whilst this makes physical sense, it is not a shared conclusion. Although the electron precipitation is stronger, compared to pre-onset levels, the proton precipitation is the one found to be more persistent after onset, even though it appears to start fading first. This is particularly obvious when comparing panels a and b in Fig. 6.2. This may be due to how the data were binned and could be alleviated by binning the data relative to substorm onset location, as was for example done by *Mende et al.* [2003]. The main purpose of this study is to compare the auroral distributions of the different magnetospheric response modes and whilst most substorms have a clearly defined onset location, SMCs do not and SEs can cover a large range of MLTs.

Sawtooth events appear to be quasi-periodic substorms, which occur during geomagnetic storms, when the solar wind driving of the magnetosphere is very high (see chapter 5). Unsurprisingly, the superposed epoch analysis of SEs (Fig. 6.3) looks very similar to substorms prior to onset, as the auroral oval moves equatorward. At onset the electron aurora (WIC) brightens explosively near local midnight and then expands very rapidly dusk- and dawnward, (which agrees with *Cai et al.* [2006b]; *Henderson et al.* [2006]), whilst retreating towards the pole. *Mende et al.* [2003] find that the auroral oval moves equatorward, prior to substorm onset, but only by a marginal $\sim$1-2^o. The superposed epoch analysis shown in this chapter reveals the same growth phase characteristic for substorms, but for sawteeth events, this auroral expansion prior to onset is larger ($\sim$5-10^o of latitude for WIC and $\sim$2-3^o of latitude for SI12 data). This is due to the elevated levels of dayside reconnection during these events [*Walach and Milan*, 2015].

On average, we find that SI12 precipitation is higher from 18-00 MLT than from 00-06 MLT, indicating that injected protons drift westward from midnight, but as panels a and b do not show this feature, it is unrelated to event onset. Prior to SE onset, the SI12 aurora clearly moves to much lower latitudes than it ever sits at during the other types of events and the magnetotail must be much more stretched during those periods than during ordinary substorms. This fits the previous results from chapter 5, where it was shown that the solar wind driving is $\sim$3 times as large during SEs than during substorms and as a result, F_{PC} is also much higher. The brightening we see at SE onset occurs between 20 and 00 MLT, similar to substorms. This confirms the results of *Cai et al.* [2006b] who showed that SEs are primarily initiated between 22 and 0 MLT. *Cai et al.* further find that prior to SEs the magnetotail is more stretched, in comparison to substorms, which can be confirmed with the results shown here, as the SI12 emission is higher leading up to the SEs. Their further result that the longitudinal expansion is similar to substorms is also confirmed. Although it happens faster for SEs, it is not seen to be occuring over a wider local time extent, as postulated by *Cai et al.* [2006b].

Also similar to substorms, a brightening is seen at onset in the radial bins, in the SI12 data, but it is only a marginal increase in brightness. Similarly, *Walach and Milan* [2015] found that the total brightness seen in the SI12 emission only increases slightly at SE onset. This implies that many protons are pitch angle scattered into the atmosphere and as such the pressure on the central plasma sheet in the magnetotail is very high prior to onset due to there being a significant amount of open flux prior to the onset of an SE. As each tooth of a series of sawteeth has been considered as it's own event, although faint, we see the beginning of the following tooth in Fig. 6.3 at approximately 120 min, where the auroral oval moves poleward again.

Henderson et al. [2006] observe a double auroral oval configuration just before SE onset or between teeth. This is a feature, which cannot be distinguished here due to the averaging process.

It is important to note that for SEs there is a duskward bias of auroral emission seen by SI12 and a weaker, but still noticeable dawnward bias of WIC emission, as also found by *Milan et al.* [2010]. After being injected into the inner magnetosphere via nightside reconnection, the electrons will drift eastward and the ions will drift westward, which is why the bright SI12 and WIC aurora move duskward and dawnward, respectively, after reconnection [*Gussenhoven et al.*, 1987; *Milan et al.*, 2009a]. Other than the general dawn-dusk asymmetry in WIC and SI12 emission, an expansion of the brightening in the MLT sectors, which resembles the brightening after substorms, is also seen. The MLT-expansion of the brightening after onset takes approximately 10 minutes to reach its full extent for SEs, whereas for substorms this takes approximately twice as long. As shown in chapter 5, the reconnection rate, as well as the overall auroral brightness and thus energy input into the inner magnetosphere are approximately twice as high near SE onset as for substorms, meaning that the azimuthal spreading of the brightening at onset is directly related to these quantities.

In general, as well as during the substorms and SEs, the electron aurora appears to be more prevalent in the dawn sector than elsewhere. This is due to electrons drifting generally eastward in the magnetosphere on closed field lines. However, it does not explain why the duskward expansion after onset is faster than the dawnward expansion and why a similarly prominent feature is not seen in the proton aurora. The faster westward expansion of the onset brightenings is due to the westward travelling surge observed during substorms [*Akasofu*, 1964], whereas the eastward drift of the bright WIC aurora after onset is related to injected electrons drifting eastward and eventually scattering in the ionosphere to produce aurora. Whilst a similar feature is seen in the panels showing the absolute proton brightness, it does not appear in the normalised brightness panels (panels a and b). This may be due to the protons being less likely to enter the loss cone once they are on closed, non-stretched field lines (i.e. once they are on field lines which have undergone nightside reconnection and the initial particle injection has occurred).

The reconnection X-line in the tail must thus expand east- and westward in the 20 minutes after onset to cover the nightside from ~18-04 MLT, as this is where the brightest aurora is seen. After approximately 100 minutes, the electron and proton aurorae start to dim, indicating the end of a Near-Earth Neutral Line (NENL) [e.g. *Baker et al.*, 1996], followed by a clear eastward drift of injected electrons, which is to be expected.

The main difference between SEs and substorms is that, although the energy input into the magnetosphere is much higher during SEs due to enhanced reconnection rates, as was shown in chapter 5, the onset related brightening takes less time to dim to preonset levels than for substorms (~20 minutes for the proton aurora, as opposed to over an hour post-substorm). This means that there is a non-linear relationship between the energy input and the recovery time of the system, which is a novel result.

In comparison to the substorms, the SMCs with preceding substorms show very similar signatures prior to and at onset. This is no surprise as the SMCs' onsets were shifted to match the preceding substorm onset. The main differences between substorms and these SMCs are seen after the substorm preceding the SMC has developed, especially in the proton aurora. Whereas usually, substorms start to decrease in auroral brightness approximately 20 minutes after onset, these substorms continue to produce bright aurora, and are much brighter in general, seen by both WIC and SI12. This is due to the event being a driven expansion phase: The work in the previous chapter revealed that substorms end as both day- and nightside reconnection reach very low levels, whereas for SMCs, both day- and nightside reconnection rates continue to be elevated. As the magnetospheric system continues to be driven by reconnection, plasma is circulated around the magnetosphere. Seemingly the magnetotail reaches a state where it is stretched and reconnection occurs, as the SMC itself implies reconnection to take place, whilst the proton aurora continues to be bright for hours after the SMC preceding substorms.

Whereas at substorm onset a localised (temporal and spatial) brightening is seen, the auroral brightenings seen during SMCs (after the substorms have subsided) are much less confined. Latitudinally, the bright aurora during SMCs cover a larger latitudinal extent than during substorms, as also observed by *Sergeev et al.* [2001] and *Yang et al.* [2010]. In MLT, the SI12 aurora spreads across the nightside, with a slight dimming around midnight later on. WIC shows more variability across the MLT sectors: after the expansion phase of the substorm, the brightest MLT sectors on the nightside move from being at 22-0 MLT to 2-6 MLT, but after this, the WIC intensity continues to be enhanced across the nightside (Fig. 6.4, panel b), which is interpreted to be the result of continued dayside driving and multiple injections. At approximately 120-150 minutes after substorm onset, a reconfiguration occurs where the aurora near midnight dims, but brightens in the dusk- and dawn sectors (Fig. 6.4, panels a and b). This has implications for the magnetotail structure, as it implies an asymmetry in the location of its stretching. The electrons are primarily associated with reconnection, meaning the magnetotail reconnection site during SMCs has shifted towards dawn, whereas during substorms, it is primarily located near 23 MLT. The magnetotail is generally stretched, as bright proton aurora are seen in both the dusk- and dawn sectors.

This timescale of $\sim$120-150 minutes itself is very interesting: It is approximately the duration of the substorm repetition rate (similar timescales were found by *Borovsky et al.* [1993]; *Newell and Gjerloev* [2011]), but even when the magnetosphere continues to be driven, there appears to be a marked change at $\sim$120-150 minutes. This is obviously a characteristic timescale in the evolution of the tail in response to the onset of nightside reconnection. This break in the timescale can also be seen in the superposed epoch analysis of the SMCs with preceding substorms in Figure 3 of *Walach and Milan* [2015]. The question of what sets this timescale remains open, but it may be that after the SMC-preceding substorm the NENL, the reconnection X-line moves tailward to form a Distant Neutral Line (DNL) and reconnection continues in the more distant tail. The 120 minutes could be the timescale taken by a distant neutral line to form. Furthermore, the poleward edge of the aurora does not brighten or move rapidly during SMCs, which also indicates that the tail is stretched, but not stretched enough for a near earth neutral line to form.

The electron aurora behaviour is thus overall very similar for substorms and SMCs, but much more prolonged for SMCs, whereas for the protons, the auroral behaviour is very different.

In the past a double auroral oval has been observed during steady convection intervals [*Sergeev et al.*, 2001; *McWilliams et al.*, 2006], but it cannot be said here how persistent this feature is, as a double oval would be smeared out in the averaging process.

6.5 Summary

In this study, data from the IMAGE SI12 and WIC instruments were used to produce superposed epoch analyses of the nightside aurora to compare substorms, sawtooth events and steady magnetospheric convection events with preceding substorms. The data was binned latitudinally and by nightside MLT sectors, to resolve general auroral patterns in the electron and proton emission.

The analysis confirms the well-known behaviour of the aurorae during substorms:

1. Prior to substorm onset, a general equatorward movement and thinning of the auroral oval are seen, both of which are more pronounced in the electron aurora than the proton aurora.

2. At substorm onset, the aurorae brighten explosively, which occurs primarily near 23 MLT.

3. The most intense parts of the initial brightening of the electron and proton aurorae are shifted slightly in MLT, which are interpreted to be an observation of the substorm current wedge.

4. The aurorae then expand poleward and the bright emission spreads dusk- and dawnward from onset location, with the duskward spreading being approximately twice as fast as the dawnward spreading, a feature thought to be related to the westward travelling surge.

5. Approximately 20 minutes after onset, the bright proton aurorae cover the nightside from 18-4 MLT and the bright electron aurorae cover primarily 18-6 MLT.

6. After ∼100 minutes after onset, the aurorae decrease in brightness, with the brightening in the proton aurorae being much more persistent (lasting for several more hours).

In addition to these well-studied features, the substorm current wedge is also observed, but this disappears after onset as the aurora becomes more dynamic and the detail is lost in the averaging process.

Prior to SE onset, the aurora moves equatorward, similar to substorms. At onset, the WIC emission brightens near local midnight and then expands dusk- and dawnward. The brightenings over the nightside MLT sectors are also distributed similarly to substorms, but the aurorae are much brighter. This may be due to a more stretched tail, driven by the higher dayside reconnection.

As a result of the enhanced reconnection-related driving during and before SEs, both the proton and electron aurorae are much brighter. Nevertheless, the onset related brightening is much short-lived than the substorm and SMC related brightenings. In fact, the time taken for the aurora to recover from an SE injection is approximately half that taken by substorms. This suggests that the relationship between the auroral recovery time after onset and energy input is non-linear, suggesting that the auroral recovery time is controlled by another parameter.

The SMCs with preceding substorms start out in the same way as the substorms, but instead of dimming after ∼20 minutes post onset, the auroral emission continues to be high in both SI12 and WIC, indicating that nightside reconnection continues and the tail is stretched. Approximately 100 minutes after onset, the proton brightening covers the whole nightside and subsequently there is a change from the substorm-like recovery: The proton brightenings continue to cover the nightside, with slightly increased brightenings in the dusk and dawn sectors. The brightest electron aurorae move from primarily covering 22-0 MLT to covering dawn sectors, followed by a dimming after approximately 150 minutes post onset and a latitudinal narrowing of the WIC aurora. This break in behaviour from 100 minutes post-onset onwards is perhaps a sign of a migration of the NENL towards a DNL.

In summary, the findings show that

- The electron and proton aurora around SE onset appear like an energetic substorm onset, but the brightening after onset spans over a larger MLT extent, as they involve a larger amount of magnetic flux throughput and thus the nightside reconnection site must be wider.

- Whereas the proton aurora during substorms takes over two hours to fade back to a dim aurora, during SEs this process takes less than one hour, despite the ongoing day- and nightside reconnection. This shows that the high levels of continued driving may play an important role in not only the brightening, but also the dimming of the aurora.

- Auroral signatures during SMCs with preceding substorms appear like substorms, but despite continued dayside driving of the system, a break in the nightside auroral activity is seen, which reactivates 150 minutes after onset. Perhaps this signals a characteristic timescale of the evolution of the tail.

- SMCs in general display brighter auroral emission than substorms as a result of continued dayside driving, but covering a larger latitudinal and longitudinal range.

- The latitudinal expansion and contraction of the auroral oval as a whole moves on similar timescales during substorms, SMC preceding substorms and SEs, despite different levels of dayside driving.

7

Review and Further Work

'It was originally intended to discuss an electromagnetic theory of the origin of the solar system in an eighth chapter. This has been excluded, however, because it would require rather too much space.'

from *Cosmical Electrodynamics* by *Alfvén* [1950].

In this chapter, the main conclusions of this thesis are briefly discussed (section 7.1), along with some remaining open questions and ideas for further work (section 7.2).

7.1 Summary of Main Conclusions

The work presented in chapter 4 explored the validity of the expanding and contracting polar cap paradigm. A physics-based model of the ECPC was used to compare ionospheric convection velocities to measurements. The utilised *Milan*-model allows for a calculation of the velocities using the day- and nightside reconnection rates, and the polar cap flux as primary inputs, which no other previous model has achieved.

A quantitative comparison with in-situ satellite measurements of flow velocities showed that the magnitudes of the flows are, on average underestimated by a factor of 2-3, but can be predicted qualitatively. The offsets may be due to a combination of reasons, such as measurement errors and underestimation of reconnection rates.

Furthermore, the circular symmetry of the model will add uncertainties to the flow values, which are difficult to estimate. Overall, the locations of the flows match the auroral boundaries well and the relative flow magnitudes agree well, showing that the ECPC is consistent with measurements.

Chapter 4 explores substorms and periods of steady magnetospheric convection as a natural part of the ECPC, whereas the work in chapters 5 and 6 studies the response modes of the magnetosphere to solar wind driving more explicitly.

Chapter 5 compared SMCs, substorms and SEs using superposed epoch analysis of solar wind and magnetospheric parameters, whereas chapter 6 looked specifically at the auroral response.

Substorms show an increase in polar cap flux prior to onset, followed by a sudden and distinct increase in auroral brightness. The auroral brightening occurs near 23 MLT and then spreads dusk- and dawnward, in both the electron and proton aurora. Approximately 20 minutes after onset, the bright proton aurorae cover the nightside from 18-4 MLT and the bright electron aurorae cover primarily 18-6 MLT, with the longitudinal expansion of the onset-brightening being faster in the duskward, than in the dawnward direction. This duskward bias of the latitudinal expansion is the same for substorms, substorms preceding SMCs and SEs, but it occurs much faster for SEs.

Approximately 58% of all considered SMCs have a substorm occurring in the 2 hours before SMC-onset. These events were compared to substorms and SEs in both chapters 5 and 6, whereas the remaining SMCs, which were found to occur without substorms, are only discussed in chapter 5.

The SMCs with preceding substorms show signatures similar to substorms with the expansion phase stretched over a longer timespan. These SMCs are driven expansion or recovery phases of substorms, which show an increase of the polar cap flux before onset and produce on average brighter aurora than substorms due to continually elevated dayside reconnection rates. The continued dayside driving but steady F_{PC} means that AU and AL are also elevated during SMCs. When dayside driving and F_{PC} decrease, the SMC is over and the recovery phase of the SMC-preceding substorm can set in. The majority of SMCs are thus part of the substorm process and can be considered a driven expansion or recovery phase due to continued dayside driving. The other 42% of SMCs were not found to have a preceding substorm in the 2 hours before SMC-onset, but they were found to occur after prolonged periods of dayside driving. On average, the aurorae are brighter during SMCs than during substorms, however there are some differences, for example extended longitudinal and latitudinal coverage. Auroral signatures during SMCs with preceding substorms appear like substorms near onset, but as the system continues to be driven by reconnection, the brightening in the nightside electron aurora continues at 18-21 MLT for approximately 2 hours and at 01-06 MLT for at least 4 hours after substorm onset. Similarly, the proton aurora continues to be spread across the nightside for hours after the initial substorm. Despite continued dayside driving of the system, a restructuring of the nightside auroral activity is seen from 120 to 150 minutes post onset: the electron aurora moves dawnward and the proton aurora becomes more pronounced in the dusk- and dawn sectors than near midnight, which may be due to the nightside reconnection site moving further downtail and the magnetotail being stretched on the flanks. This agrees with the findings by *Kissinger et al.* [2012] who found that the x-line retreats tailward (on average beyond 31 R_E) during SMCs. *Kissinger et al.* [2012] also find that the magnetotail pressure is higher on the flanks during SMCs, which is likely to be resulting in a stretched magnetotail.

SEs also occur during enhanced and prolonged (southward IMF for approximately 4 hours preceding first onset) geomagnetic activity and convection, however, the initial magnetospheric response here is sporadic, as during substorms, but each series of injections has a quasi-periodic character. Qualitatively, the flux closure is the same as for substorms, but occurring at much higher rates. The quasi-periodicity of these events may come about as they continue to be driven by enhanced Φ_D, continually opening flux, unlike for sustorms, where a decrease in the driving is seen ~20 minutes after onset. The ring current enhances as the series of sawtooth events progresses, which may be due to the repeated injection of particles into the ring current. As a result of the continuous opening of flux, the aurorae are on average much brighter during SEs than during substorms. Around onset, the SEs appear like an energetic substorm onset with the brightening being located near 23 MLT, but the brightening after onset spans over a much larger MLT extent than for substorms. This means that not only is the rate of flux closure higher for SEs than for substorms, but the nightside reconnection site must also be wider. A further difference between the aurorae during SEs and substorms, is that the onset-related brightenings take a considerably different amount of time to recover: for substorms, this process takes over two hours, whereas during SEs it takes less than one hour, despite the ongoing day- and nightside reconnection.

The latitudinal expansion and contraction of the auroral oval as a whole moves on similar timescales during substorms, SMC preceding substorms and SEs, despite different levels of dayside driving.

7.2 Unanswered Questions and Further Work

The work by *Coxon et al.* [2014] shows that the latitudinal change of the field aligned current locations derived from the Active Magnetosphere and Planetary Electrodynamics Response Experiment (AMPERE) during a substorm cycle matches, at least qualitatively, that of the inner auroral boundary (see chapter 5). Considering our current understanding of the ECPC, as portrayed by the *Milan*-model, this would be expected. *Carter et al.* [2016] however showed, using IMAGE and AMPERE data that the locations of the field aligned currents do not match the aurora locations as well as expected, on a statistical basis, even when they are parameterised by solar wind conditions. The field aligned current data and auroral data used by *Carter et al.* [2016] stems from different time periods in the solar cycle, which could be a problem and needs to be investigated.

The *Milan*-model is capable of predicting the strength of the field-aligned currents, and comparisons with real data show that these predictions work well [*Milan*, 2016], but an extensive comparison of this is yet to be published.

Care has to be taken when flows are mapped from the magnetosphere to the ionosphere and vice versa, as during very active times, field-aligned electric fields which decouple magnetospheric and ionospheric motions will become more significant according to *Hesse et al.* [1997], but it has not been established yet how significant they may be.

Data from different sources, such as models, DMSP and SuperDARN all give different measurements for the cross polar cap potential, and ultimately the convection strength. Until a consensus is reached on which convection measurements are correct, it remains difficult to model them.

The uncertainties were problematic in chapter 4, where 25 kV were added to Φ_D and Φ_N and yet the model estimates appear to underestimate the flows. Most prominently, the modelled flows are $\sim 30\%$ of the flows measured by DMSP. As the offset seen is very consistent, it could be experimental, but this has not been discerned yet.

Despite there being a large number of studies supporting the hypothesis that the opening and closing of magnetospheric flux drives the convection, the question of how important a viscous interaction remains. A number of studies have attempted to answer this in the past, but since *Coroniti and Kennel* [1973] suggested that the contribution of the viscous interaction should be tested during times of northward IMF, the focus has been on these conditions and we do not know if this is different for southward IMF.

Efforts have been made to estimate the viscous interaction between the solar wind and the Earth's magnetosphere, but no all-encompassing statistical survey on this exists yet [*Axford and Hines*, 1961; *Axford*, 1964; *Cowley*, 1982; *Heelis and Reiff*, 1985; *Akasofu*, 2015]. It is understood, that a viscous interaction transfers momentum from the magnetosheath to trapped plasma on the inside of the magnetopause, but how significant this interaction is, is still a topic of debate. Past studies suggest that the potential imposed on the magnetosphere-ionosphere system by viscous interaction lies somewhere between 5 and 40kV [*Reiff et al.*, 1981; *Doyle and Burke*, 1983; *Milan*, 2004; *Drake et al.*, 2009; *Bruntz et al.*, 2012a,b; *Bhattarai and Lopez*, 2013]. Whilst 5kV is a very small proportion of the total cross polar cap potential under normal circumstances (40-100kV [*Cowley*, 1982]), 40kV would be a significant amount. The majority of past attempts in quantifying the viscous interaction are not purely based on measurements and instead often rely on estimations, simulations [e.g. *Bhattarai and Lopez*, 2013] and modelling [e.g. *Bruntz et al.*, 2012a,b]. Furthermore, it is often assumed that the return flows during northward IMF are solely due to the viscous interaction [e.g. *Sundberg et al.*, 2009; *Bruntz et al.*, 2012b], but they can also be driven by nightside reconnection, making it difficult to isolate viscous-driven flows.

It is known that B_Y components of the IMF will change the convection patterns, but to quantify this temporally and spatially is difficult without a fuller understanding of the physics. As such, the addition of this asymmetry to the model is also difficult to achieve and justify with the current knowledge available.

In addition to this, during northward IMF, reconnection, known as lobe reconnection, between the solar wind and open field lines of the magnetosphere [e.g. see Figure 1 in *Imber et al.*, 2007] can occur, changing the convection pattern. This has not been discussed in this thesis, but it is important to mention, as it is also something not currently present in any models of the ECPC. This is mainly because lobe reconnection is thought to occur with open magnetic flux, which will result in convection, but it will not change the polar cap flux in the same way as during periods of southward IMF. Lobe reconnection can either occur in one hemisphere (single lobe reconnection), which does not change the open flux, or both hemispheres at once (dual lobe reconnection), which would decrease the open flux [*Imber et al.*, 2007]. Although lobe reconnection has been observed, it is yet to be included in models of the ECPC. Furthermore, there are many mesoscale convection features that are currently not modelled due to a limited understanding of the physics.

Ergo the model provides a very simplistic view of ionospheric convection and only models the most idealistic conditions. In order to include more realistic values for the model inputs, a better understanding of the locations and sizes of the merging gaps also has to be established.

In the broader context of this field of research, it is important to understand which part of the puzzle is missing here, in order to be able to constrain and improve models such as the one used in chapter 4.

Further unanswered questions from chapters 5 and 6 include the classification of the individual magnetospheric modes. Whether a substorm+SMC event can be called a substorm or an SMC or should be considered its own event-type is a question of semantics and not physics. Nevertheless, the classification will have an impact on the findings. If the onset of the SMCs had not been shifted to match the preceding substorms, for example, the findings would have been quite different. As such, it is important to keep these events apart until the physics occurring in the magnetotail are better understood.

A question that was unanswered in previous chapters, concerns the selection of events: a large proportion of SMCs do not appear to have preceding substorms, which is a different ratio to what has been found by other researchers in the past [e.g. *McPherron et al.*, 2005, found 80% of SMCs had preceding substorms]. This is likely to have been due to the limitation imposed by IMAGE's orbit: all SMCs which did not have IMAGE coverage were not included in the study, but if they were occurring during times of good coverage, it is likely, that there was no coverage in the two hours preceding the interval and thus, substorms may have been missed.

In chapter 6, it was shown that the recovery of the onset-related auroral intensifications during SEs occur on a distinctly shorter timescale than for substorms, despite higher levels of dayside driving. This was done on a statistical basis and it remains to be shown how persistent this result is. It does pose the question of how different the tail processes are during SEs in comparison to substorms and if the two are indeed different response modes.

Furthermore, the discussion regarding magnetotail dynamics during the events in chapter 6 was solely based on auroral dynamics, which only tells part of the story. In order to understand the response modes better, and answer questions about the location and extent of reconnection, data from the mid and distant magnetotail needs to be studied. Flow measurements in the tail obtained by *Kissinger et al.* show Earth-ward flowing plasma at all radial distances up to 31 R_E during SMCs. This suggests that, on average, the reconnection site is tailward of 31 R_E and a dataset covering larger radial distances should be recruited.

Other than improving the understanding of all the aspects of the aforementioned physics, the model utilised in chapter 4 could also be improved. In order to make the *Milan*-model more realistic, the asymmetries have to be accounted for by changing the symmetry of the model itself. This could include the shape of the boundaries (i.e. using ovals instead of circles), using asymmetric convection cells and merging gap that is variable in size and location. The magnetic field model could also be made more accurate (i.e. by using the IGRF-11 model), but as shown in section 4.2.2 this does not necessarily improve the overall accuracy when the model boundaries are derived from IMAGE data.

In order to conclude to what extent substorms, SMCs and SEs are different modes, further datasets will have to be studied. Studying the dayside reconnection rate and response of the polar cap flux, it appears as if these events are responses to different levels of driving, but when examining the auroral response, the dynamics appear to be quite different, even though commonalities exist. How this maps to dynamics in the tail is not a trivial matter, but will nevertheless have to be explored in the future.

Furthermore, the auroral dynamics in chapter 6 were discussed on a statistical basis, so the persistence of these results shall be explored in a future paper.

The ECPC is thus useful for understanding magnetospheric dynamics, but much further work is to be done.

1

Appendix: Error Propagation Formulae

This appendix describes the error propagation used for Fig. 4.3 in chapter 4. *Vaughan* [2013] defines the propagation of errors in terms of the variance of uncorrelated variables, X_i. Their definition of the variance or sought after uncertainty of quantity Z, ΔZ is

$$(\Delta Z)^2 \approx \sum_{i=1}^{n} \left(\frac{\partial f(X_i)}{\partial X_i} \Delta X_i \right)^2, \tag{1.1}$$

where $f(X_i)$ is a function of variables X_i, which are uncorrelated and i can have any number as long as $n \geq i \geq 1$. These variables all have uncertainties associated with them, which are given by the variances of X_i, ΔX_i. Further error propagation formulae that are used, also given in *Vaughan* [2013] are

$$\begin{aligned} \Delta Z = (\Delta X)^2 + (\Delta Y)^2 \qquad & \text{for} \quad Z = X + Y \qquad \text{or} \quad Z = X - Y \\ \frac{(\Delta Z)^2}{Z^2} = \frac{(\Delta X)^2}{X^2} + \frac{(\Delta Y)^2}{Y^2} \qquad & \text{for} \quad Z = XY \qquad \text{or} \quad Z = X/Y. \end{aligned} \tag{1.2}$$

To estimate the uncertainties for the IGRF-11 model, eq. 1.1 are first applied to $(\cos\lambda)$ to find the uncertainty in this function, such that $\cos\lambda = Z$ and $\lambda = X$. Therefore $\Delta(\cos\lambda) = -(\Delta\lambda)\sin\lambda$. Propagating this error to $(\cos\lambda_1 - \cos\lambda_2)$, using the first formula in eq. 1.2, the resulting functin is thus $\Delta(\cos\lambda_1 - \cos\lambda_2) = \sqrt{\Delta(\cos\lambda_1)^2 + \Delta(\cos\lambda_2)^2} = \sqrt{(\Delta\lambda)^2(\sin^2\lambda_1 + \sin^2\lambda_2)}$.

Using the second formula in eq. 1.2 and applying it to eq. 4.5, the error in F_{PC} for each tile, ΔF_{PC}, is then given by

$$\Delta F_{PC} = F_{PC}\sqrt{\left(\frac{(\Delta\lambda)^2(\sin^2\lambda_1 + \sin^2\lambda_2)}{(\cos\lambda_1 - \cos\lambda_2)^2}\right)^2 + \left(\frac{\Delta B}{B_r}\right)^2}, \tag{1.3}$$

where ΔB is the uncertainty in B_r and $\Delta\lambda$ is the uncertainty in the measurement of the polar cap radius. These values are taken to be 100nT and 0.05°, respectively, where ΔB is the accuracy of the IGRF-11 model and 0.05° is a very conservative estimate of the accuracy in the polar cap boundary estimation. Furthermore, the assumptions are made that there is no considerable error in the altitude and the longitude measurements.

Calculating the error bars for the dipolar magnetic field model (black line) in Fig. 4.3, is a little bit more straightforward. Using the same uncertainty values as before for ΔB and $\Delta\lambda$, and applying the error propagation formula, eq. 1.1 to $\sin\lambda$, resulting in $\Delta(\sin\lambda) = ((\Delta\lambda)\cos\lambda)$. Applying the second formula from eq. 1.2 to $\Delta(\sin^2\lambda)$, $\Delta(\sin^2\lambda)$ becomes $(2(\sin^2\lambda)\frac{\Delta(\sin\lambda)}{\sin\lambda})$, which equates $((\Delta\lambda)\sin 2\lambda)$. Applying eq. 1.1 to eq 4.6 and substituting these pieces in, the uncertainty in F_{PC}, ΔF_{PC} for the dipolar field model is then

$$\Delta F_{PC} = F_{PC}\sqrt{\left(\frac{(\Delta\lambda)\sin(2\lambda)}{\sin^2\lambda}\right)^2 + \left(\frac{\Delta B}{B_{EQ}}\right)^2}. \tag{1.4}$$

2

Appendix: Extra Figures from Expanding and Contracting Polar Cap Study

In this appendix, data complementary to the work shown in chapter 4 is presented.

Figures 2.1 and 2.9 show an overview of the data available for the considered study periods of 02^{nd} October 2000 and 20^{th} March 2005. The data shown in the panels is presented in the same way as the data shown in Fig. 4.4 in chapter 4.

Figures 2.2, 2.3, 2.5, 2.6, 2.7, 2.8, 2.10, 2.11, and 2.12 show the data available for each individual DMSP orbit available for the three study periods, some of which were discussed in more detail in chapter 4. Each row of panels in these Figs. represents one DMSP polar pass, with the panel in the left column showing the auroral data, the centre panels showing the model outputs, and the panels in the right column showing the DMSP data (and SuperDARN convection patterns for Figs. 2.5 to 2.8.)

Figures 2.4 and 2.13 show each 4 examples of scatter plots for DMSP orbits from 02^{nd} October 2000 and 20^{th} March 2005, respectively. The bottom panel in each Figure shows a summary of the data for each of the days with each DMSP orbit contributing two datapoints: The maximum and minimum flow velocities. This sums up the most extreme measurements and shows that the model underestimates the flows, even though the character of the flows are well predicted.

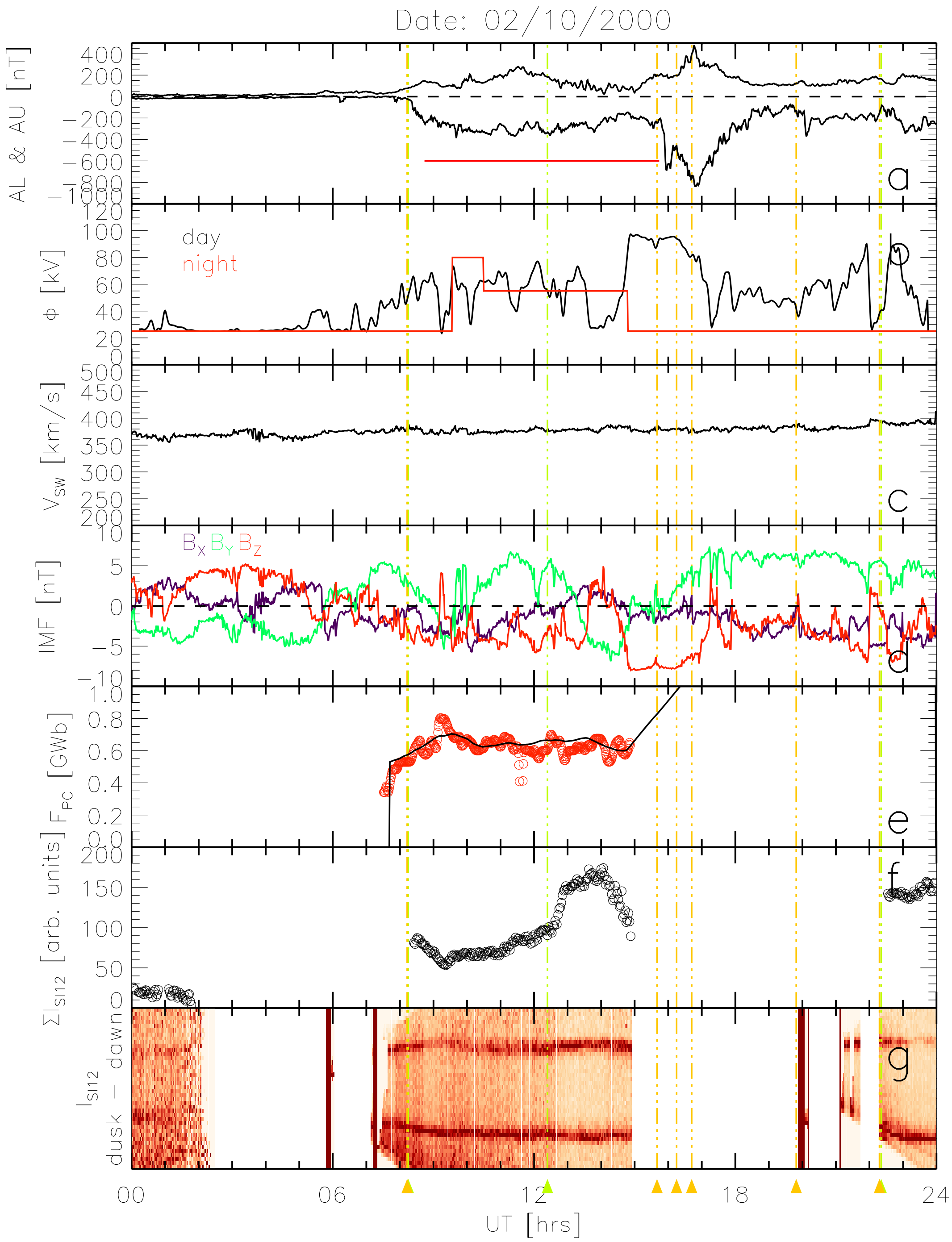

Figure 2.1: Data for the interval of interest 1 (02/10/2000). The panels show (top to bottom): AL & AU; Φ_D+25 kV (black) and Φ_N+25 kV (red); Φ_{PC} (DMSP in blue and $\frac{1}{2}(\Phi_D + \Phi_N)$ in black); V_{SW}; IMF B_X (purple), B_Y (green) and B_Z (red); F_{PC} (data in red and estimator used to calculate Φ_N in black); Total auroral brightness (from SI_{12} instrument); dusk-dawn keogram of the proton aurora (from SI_{12} instrument). The green/orange arrows (top and bottom) and green/orange lines indicate substorm onsets, from Frey's and the SuperMAG event lists, respectively.

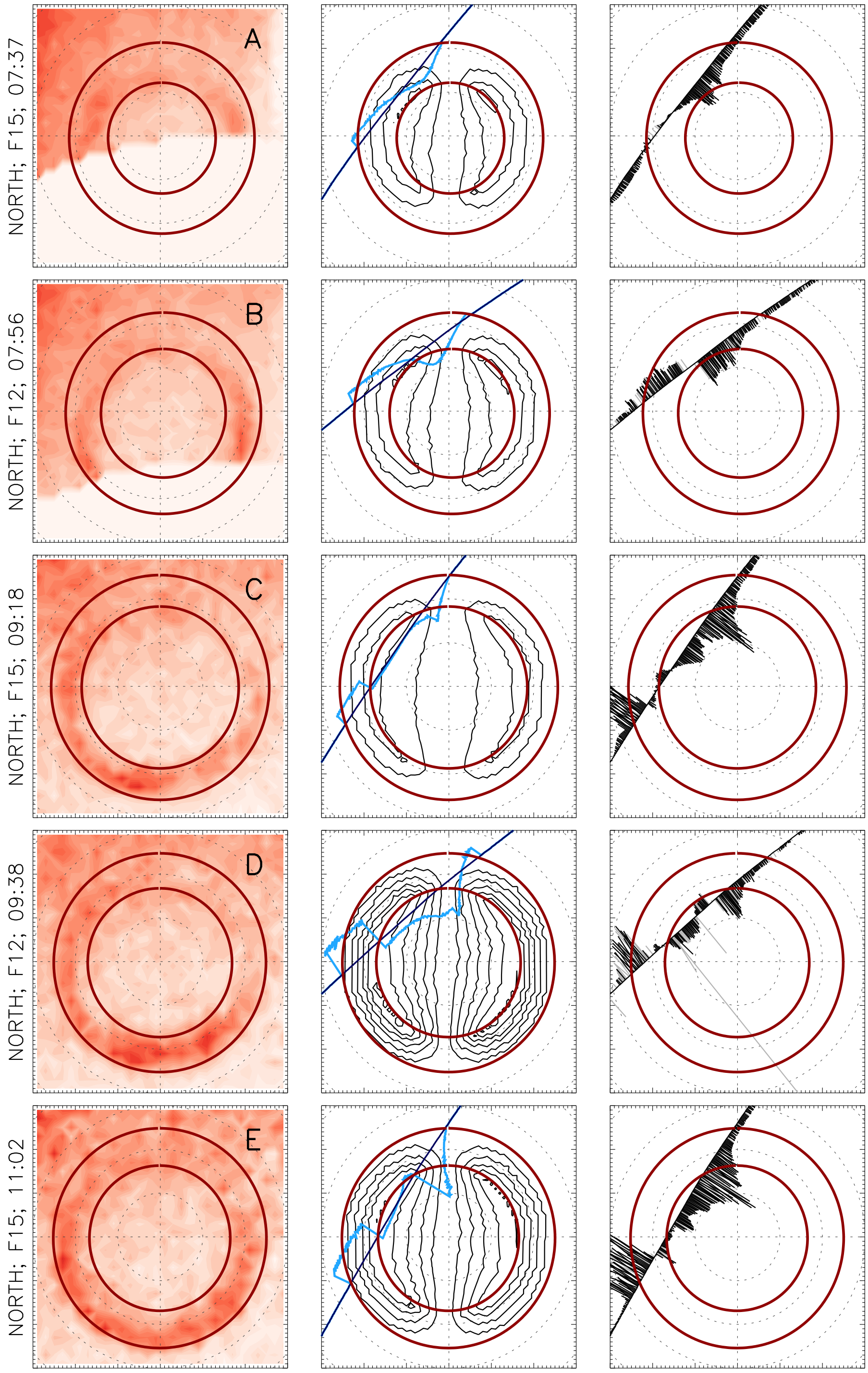

Figure 2.2: Individual DMSP orbits for 02/10/2000 (A to L), showing the cross-track velocities; IMAGE data (coloured map) and the model predicted cross-track velocities (blue); the model boundaries (dashed lines) and the model predicted flow pattern or electrostatic pattern (black lines). Each orbit is centred on the geomagnetic poles and the concentric circles in dashed grey are spaced at 10° of geomagnetic latitudes each. The vertical lines across the two panels below (dawn-dusk keogram; Φ_D and Φ_N plot) indicate the timings of the orbits.

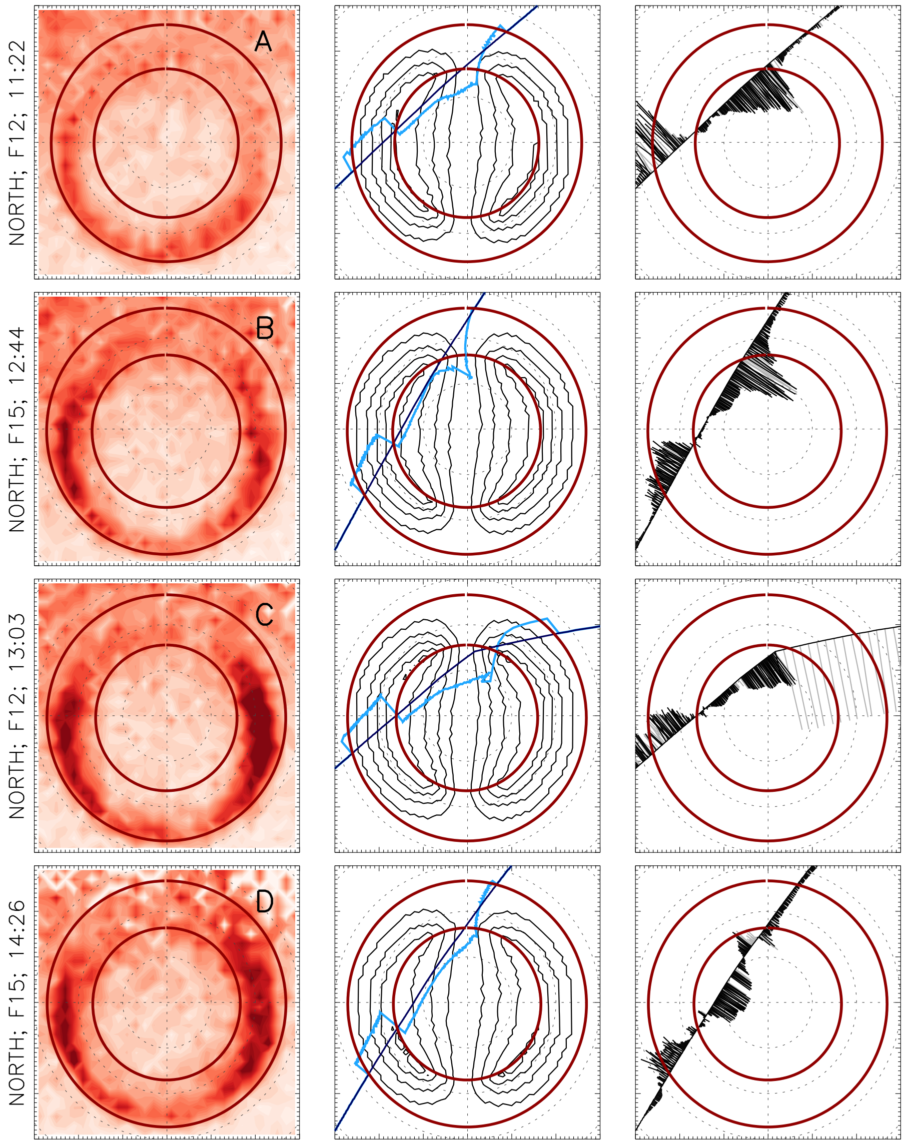

Figure 2.3: Individual DMSP orbits for 02/10/2000 (continued)

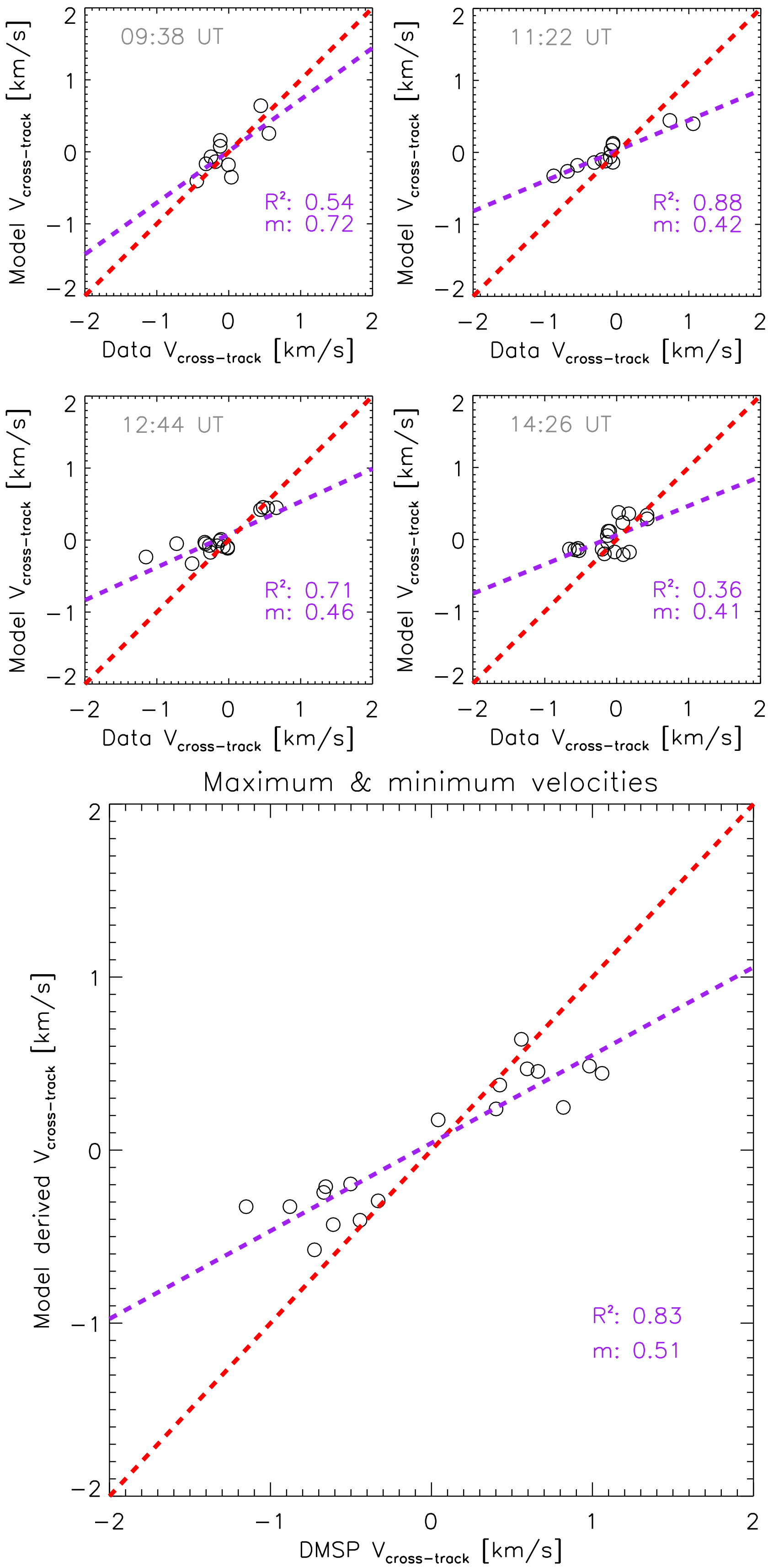

Figure 2.4: Scatter plot examples of the velocities for some orbits from 02/10/2000 (DMSP versus model). The purple line shows the line of best fit, determined from linear regression and the the red line shows the line of unity. The bottom plot shows the maximum and minimum flow velocities for all DMSP orbits of this day.

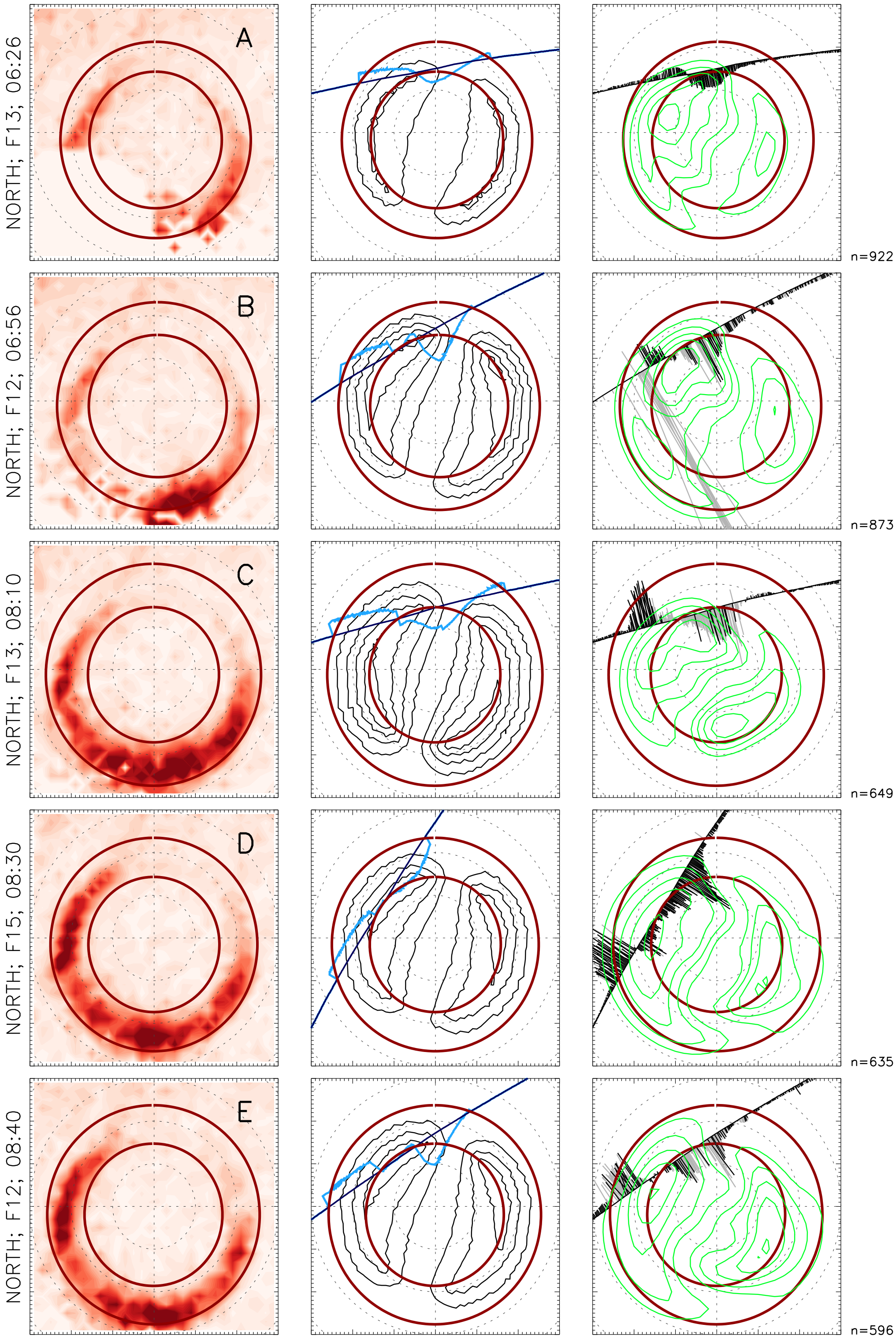

Figure 2.5: Individual DMSP orbits for 04/11/2001

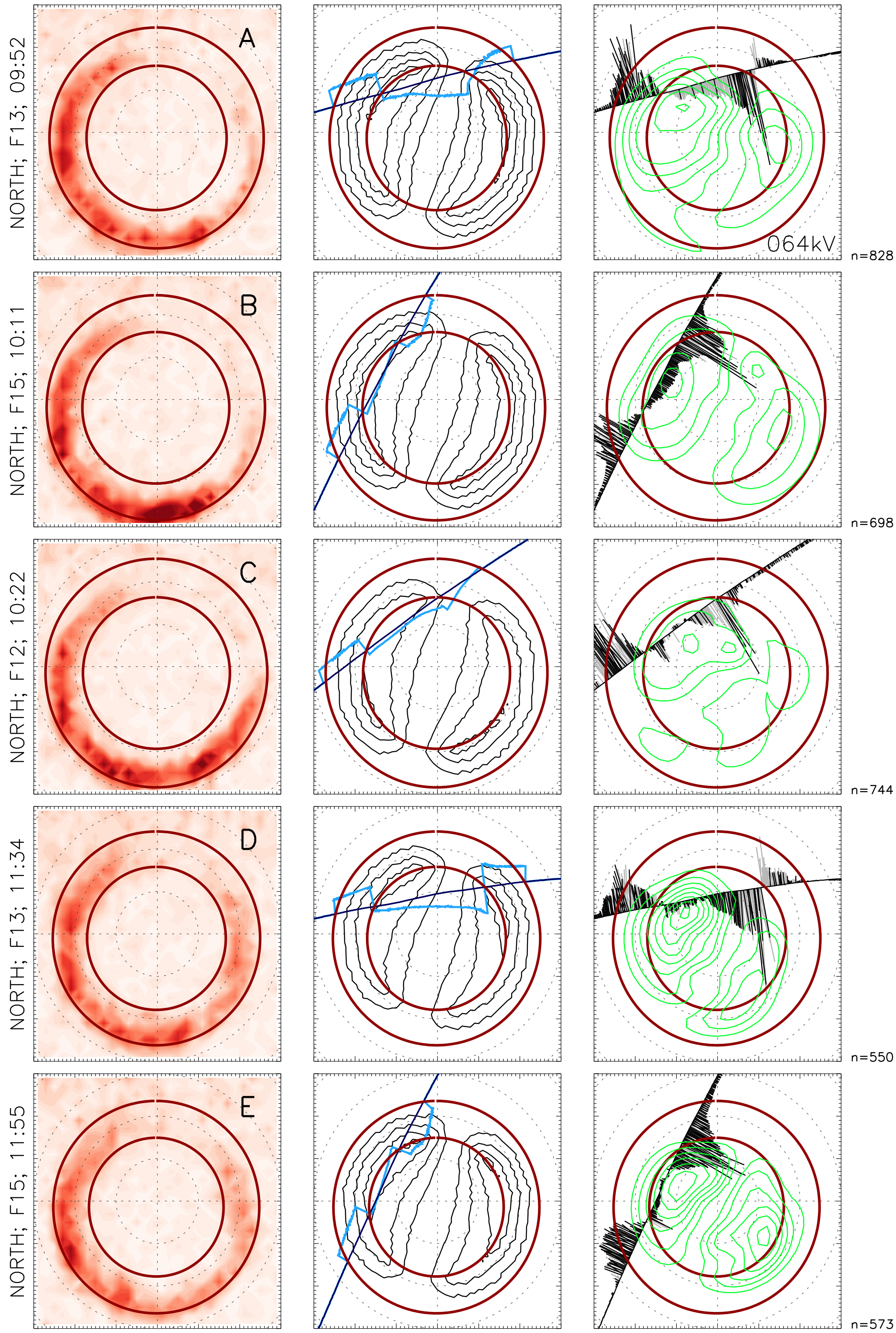

Figure 2.6: Individual DMSP orbits for 04/11/2001 (continued)

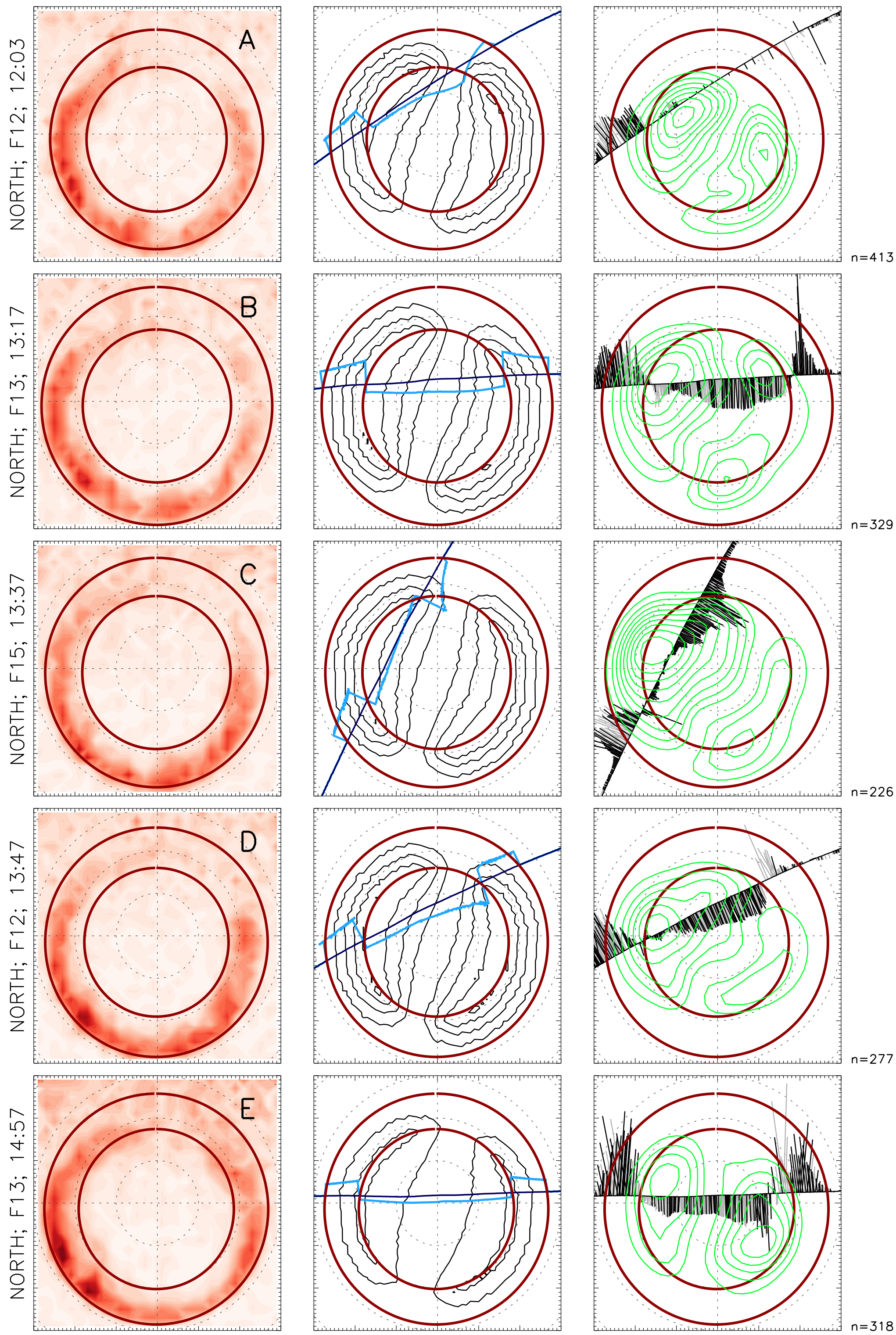

Figure 2.7: Individual DMSP orbits for 04/11/2001 (continued)

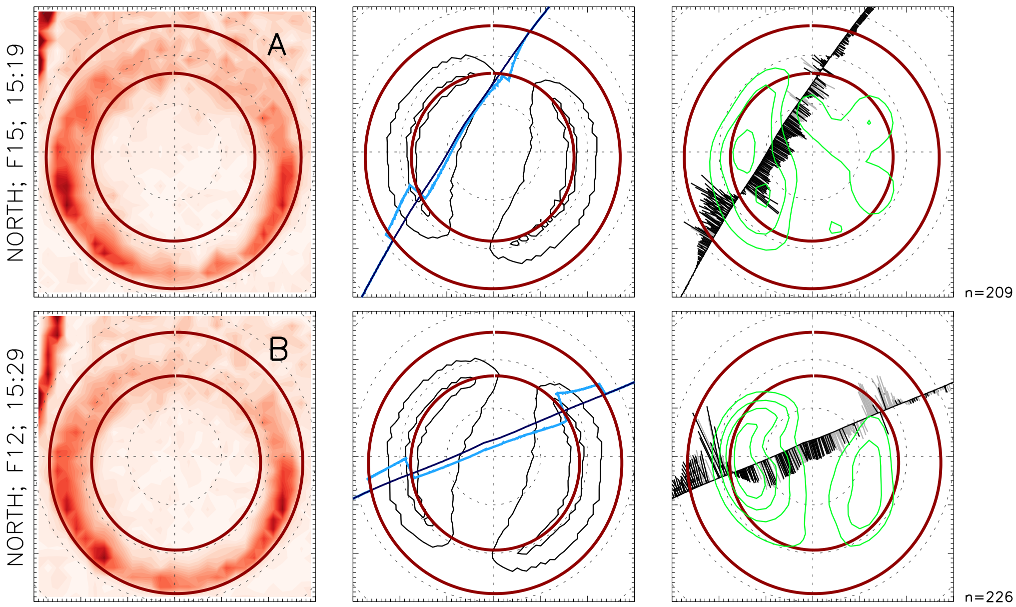

Figure 2.8: Individual DMSP orbits for 04/11/2001 (continued)

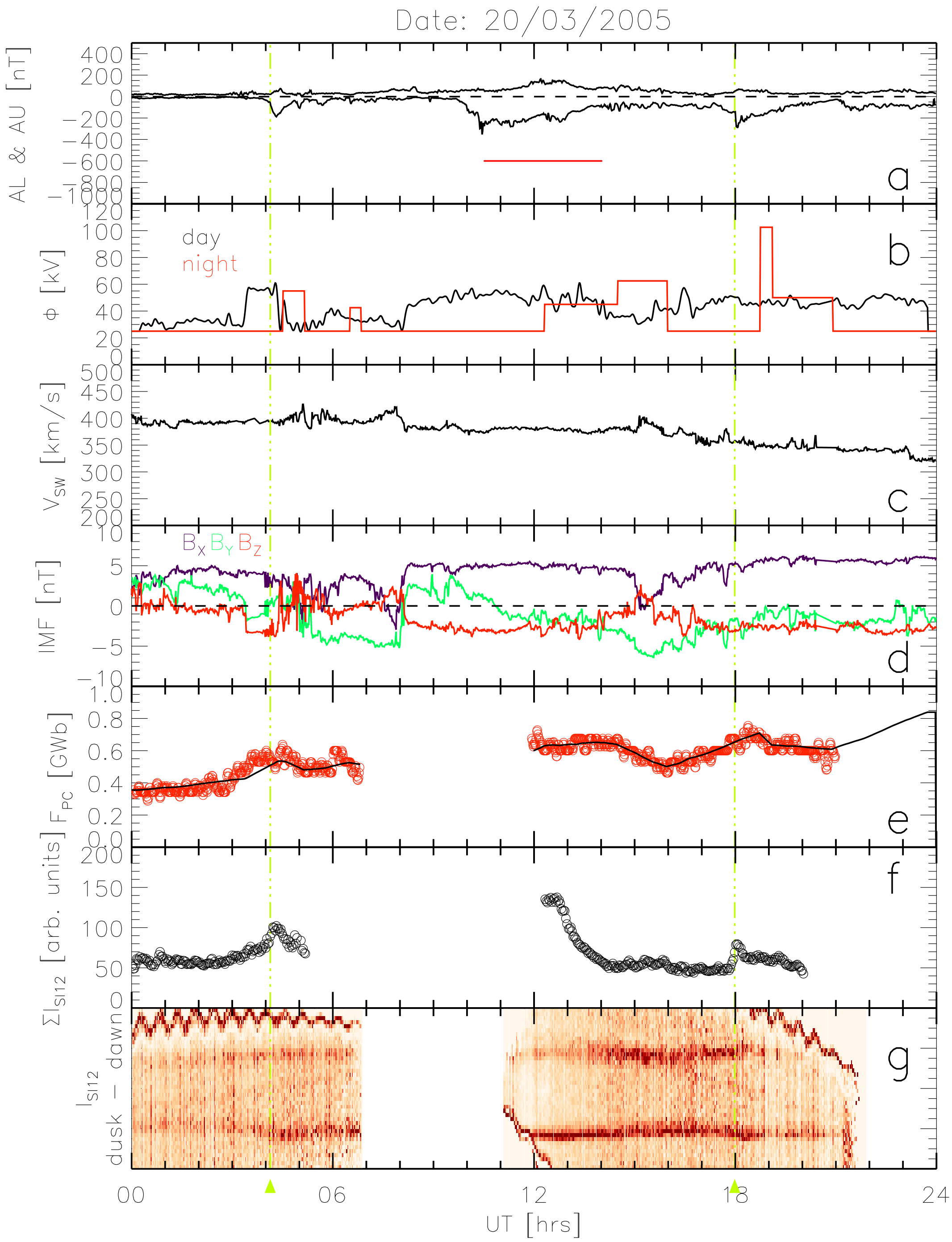

Figure 2.9: Data for the interval of interest 1 (20/03/2005). The panels show (top to bottom): AL & AU; Φ_D+25 kV (black) and Φ_N+25 kV (red); Φ_{PC} (DMSP in blue and $\frac{1}{2}(\Phi_D + \Phi_N)$ in black); V_{SW}; IMF B_X (purple), B_Y (green) and B_Z (red); F_{PC} (data in red and estimator used to calculate Φ_N in black); Total auroral brightness (from SI_{12} instrument); dusk-dawn keogram of the proton aurora (from SI_{12} instrument). The green/orange arrows (top and bottom) and green/orange lines indicate substorm onsets, from Frey's and the SuperMAG event lists, respectively.

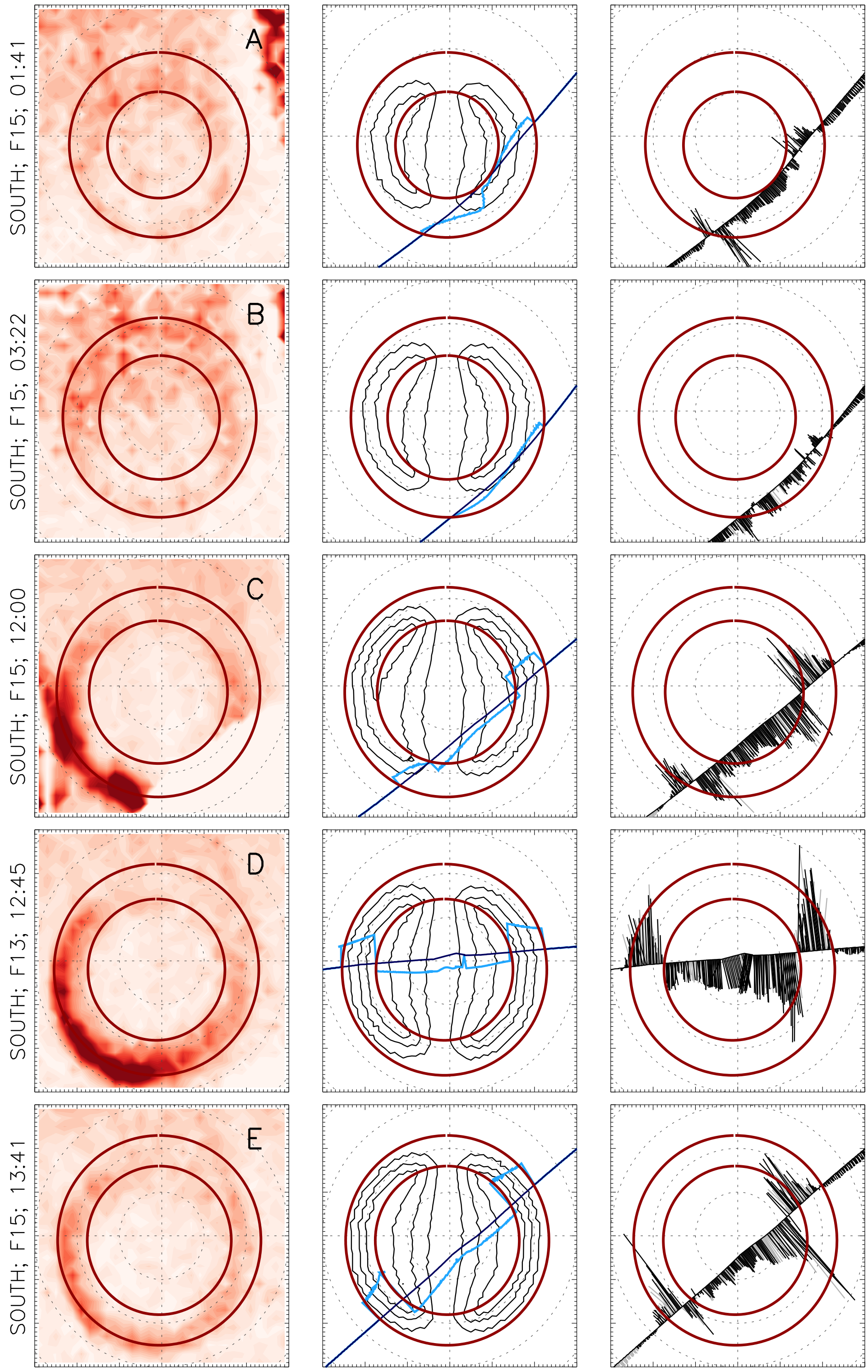

Figure 2.10: Individual DMSP orbits for 20/03/2005

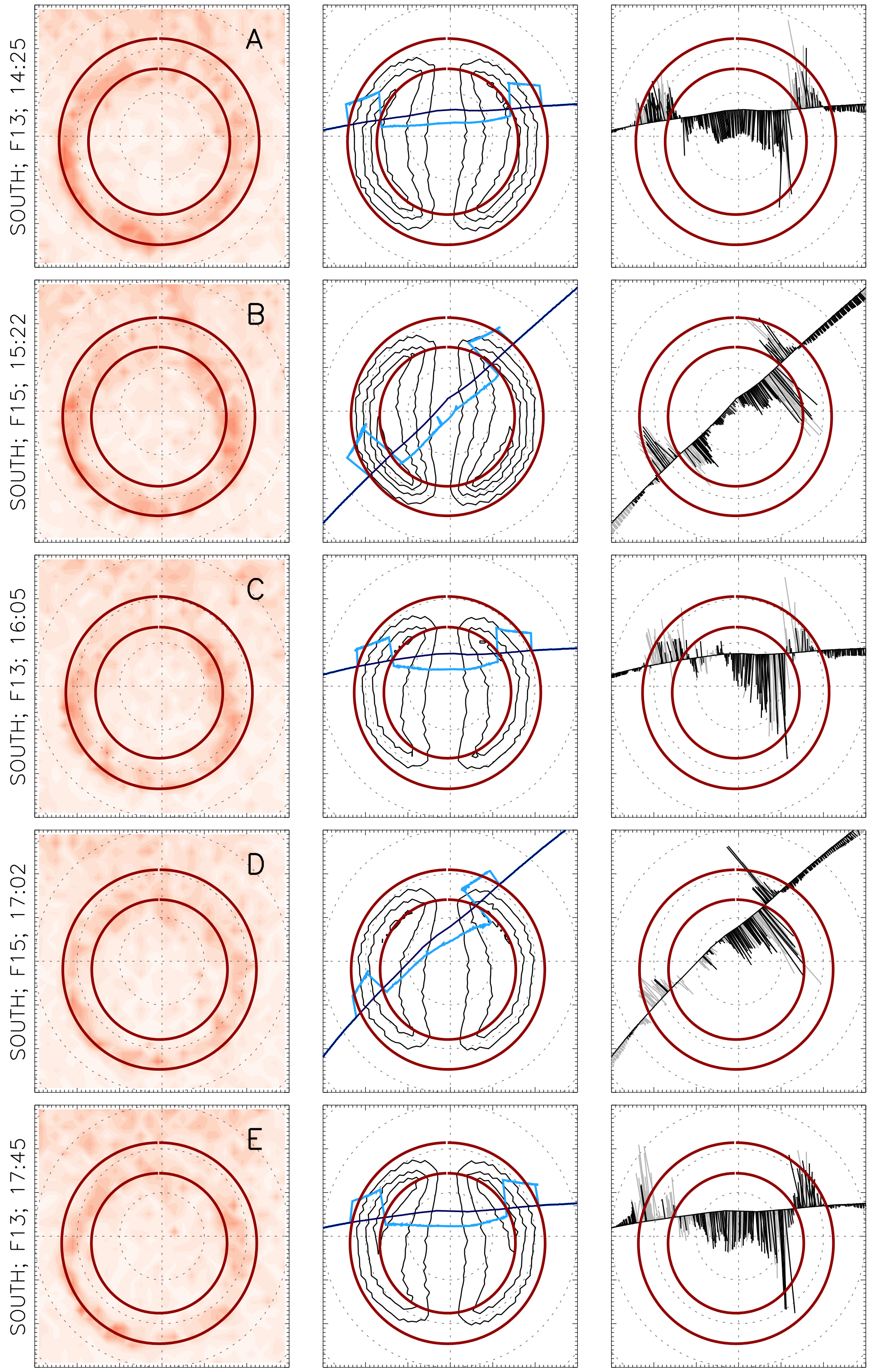

Figure 2.11: Individual DMSP orbits for 20/03/2005 (continued)

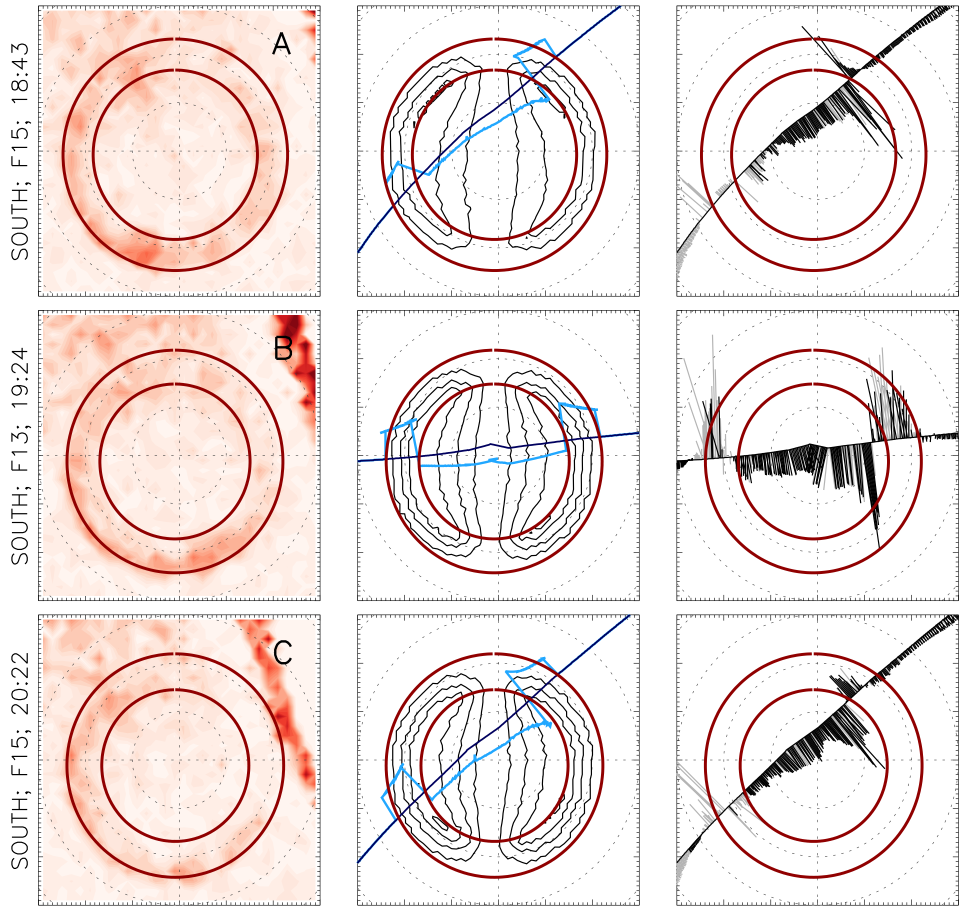

Figure 2.12: Individual DMSP orbits for 20/03/2005 (continued)

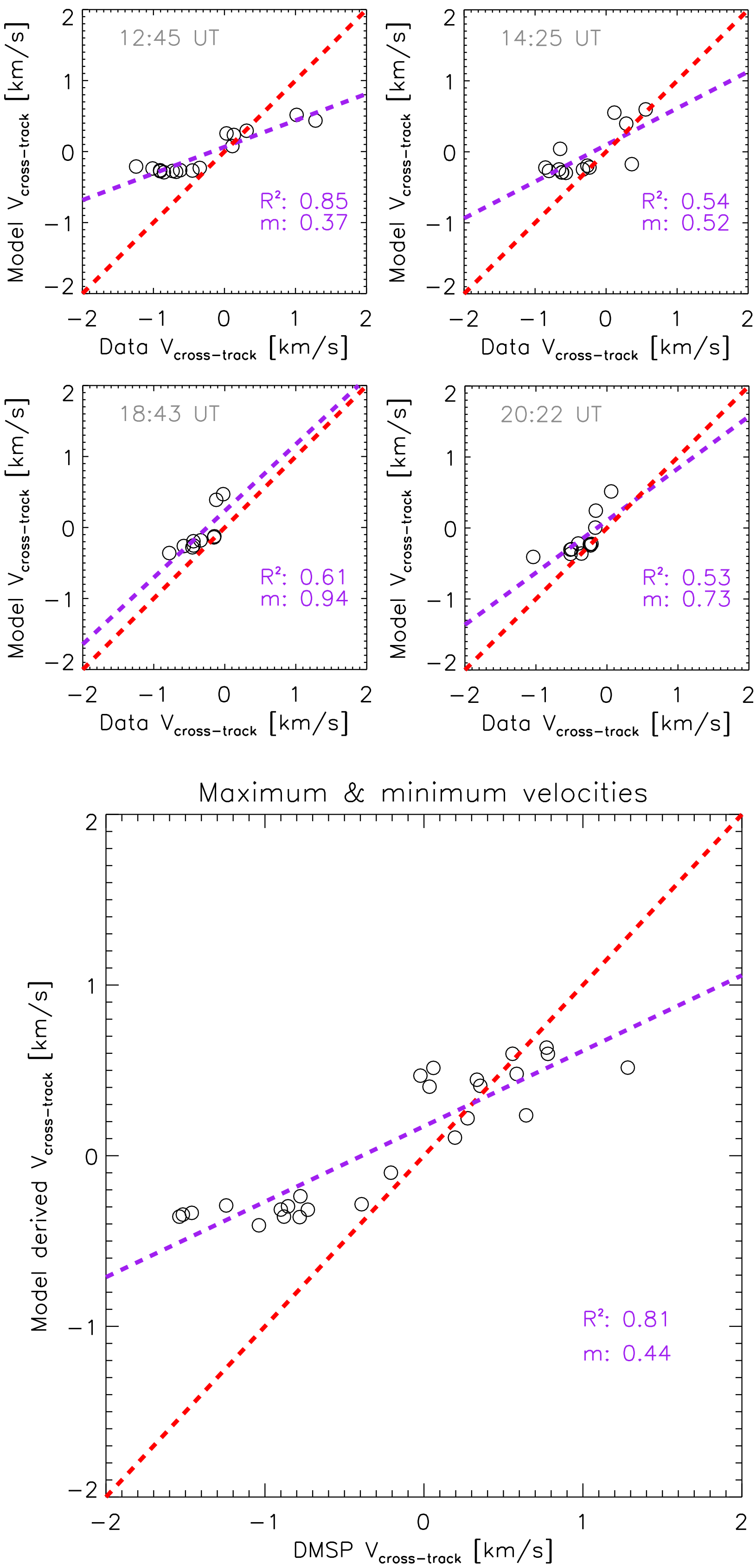

Figure 2.13: Scatter plot examples of the velocities for some orbits from 20/03/2005 (DMSP versus model). The bottom plot shows the maximum and minimum flow velocities for all DMSP orbits of this day.

References

Akasofu, S.-I. (1964), The development of the auroral substorm, *Planetary and Space Science*, *12*, 273–282, doi: 10.1016/0032-0633(64)90151-5. 37, 38, 39, 87, 123

Akasofu, S.-I. (1968), *Polar and Magnetospheric Substorms*, 1–280 pp., D. Reidel Publishing Company, Dordrecht. 37, 38

Akasofu, S.-I. (2015), Auroral substorms as an electrical discharge phenomenon, *Progress in Earth and Planetary Science*, *2*(20), doi:10.1186/s40645-015-0050-9. 133

Akasofu, S.-I., and S. Chapman (1961), The ring current, geomagnetic disturbance and the van allen radiation belts, *Journal of Geophysical Research*, *66*(5), 1321–1350, doi:10.1029/JZ066i005p01321. 37, 38

Akasofu, S.-I., D. S. Kimball, and C.-I. Meng (1966), Dynamics of the aurorav: Poleward motions, *Journal of Atmospheric and Terrestrial Physics*, *28*(5), 497 – 503, doi:0021-9169(66)90059-6. 39

Alfvén, H. (1950), *Cosmical Electrodynamics*, first edition ed., Oxford, Clarendon Press, London. 1, 4, 15, 18, 129

Alfvén, H., and C.-G. Faelthammar (1963), *Cosmical Electrodynamics*, second edition ed., Oxford, Clarendon Press, London. 1, 13, 52

Arnoldy, R. L. (1971), Signature in the Interplanetary Medium for Substorms, *Journal of Geophysical Research*, *76*(22), 5189–5201, doi:10.1029/JA076i022p05189. 29

Axford, W. I. (1964), Viscous interaction between the solar wind and the Earth's magnetosphere, *Planetary and Space Science*, *12*, 45–53, doi:10.1016/0032-0633(64)90067-4. 133

Axford, W. I., and C. O. Hines (1961), A Unifying Theory of High-Latitude Geophysical Phenomena and Geomagnetic Storms, *Canadian Journal of Physics*, *39*(10), 1433–1464, doi:10.1139/p61-172. 24, 26, 133

Baker, D. N., T. I. Pulkkinen, V. Angelopoulos, W. Baumjohann, and R. L.

McPherron (1996), Neutral line model of substorms: Past results and present view, *Journal of Geophysical Research*, *101*, 12,975–13,010, doi:10.1029/95JA03753. 42, 44, 124

Bargatze, L. F., R. L. McPherron, and D. N. Baker (1986), Solar Wind-Magnetosphere Energy Input Functions, in *Solar Wind-Magnetosphere Coupling*, edited by Y. Kamide and J. A. Slavin, pp. 101–109, Terra Scientific, Tokyo. 34

Baumjohann, W., and R. A. Treumann (1997), *Basic Space Plasma Physics*, Imperial College Press, London. 3, 5, 6, 9, 10, 11, 15, 16

Baumjohann, W., M. Hesse, S. Kokubun, T. Mukai, and T. Nagai (1999), Substorm dipolarization and recovery, *Journal of Geophysical Research*, *104*(A11), 24,995–25,000, doi:10.1029/1999JA900282. 41

Belian, R. D., T. E. Cayton, and G. D. Reeves (1995), Quasi-Periodic Global Substorm Generated Flux Variations Observed at Geosynchronous Orbit, *Space Plasmas: Coupling Between Small and Medium Scale Processes, Geophysical Monograph Series*, *86*, doi:10.1029/GM086p0143. 48

Bhattarai, S. K., and R. E. Lopez (2013), Reduction of viscous potential for northward interplanetary magnetic field as seen in the LFM simulation, *Journal of Geophysical Research: Space Physics*, *118*(6), 3314–3322, doi:10.1002/jgra.50368. 133

Birkeland, K. R. (1908), *The Norwegian Aurora Polaris Expedition 1902-1903, vol. 1*, H. Aschehoug & Co., Christiania. 21, 27, 37, 40, 110

Blanchard, G. C., and R. L. McPherron (1995), Analysis of the linear response function relating AL to VBs for individual substorms, *Journal of Geophysical Research*, *100*(A10), 19,155–19,165, doi:10.1029/95JA01341. 31

Blanchard, G. T., L. R. Lyons, O. De la Beaujardiere, R. A. Doe, and M. Mendillo (1996), Measurement of the magnetotail reconnection rate, *Journal of Geophysical Research*, *101*(A7), 15,265–15,276, doi:10.1029/96JA00414. 28

Blanchard, G. T., C. L. Ellington, L. R. Lyons, and F. J. Rich (2001), Incoherent scatter radar identification of the dayside separatrix and measurement of magnetic reconnection, *Journal of*

Geophysical Research, *106*(A5), 8185–8195, doi:10.1029/2000JA000262. 28, 29

Blockx, C., J. C. Gérard, M. Meurant, B. Hubert, and V. Coumans (2005), Far ultraviolet remote sensing of the isotropy boundary and magnetotail stretching, *Journal of Geophysical Research: Space Physics*, *110*(A11), doi:10.1029/2005JA011103. 31, 32, 121

Boakes, P. D., S. E. Milan, G. A. Abel, M. P. Freeman, G. Chisham, B. Hubert, and T. Sotirelis (2008), On the use of IMAGE FUV for estimating the latitude of the open/closed magnetic field line boundary in the ionosphere, *Annales Geophysicae*, *26*(9), doi:10.5194/angeo-26-2759-2008. 33, 73

Boakes, P. D., S. E. Milan, G. A. Abel, M. P. Freeman, G. Chisham, and B. Hubert (2009), A statistical study of the open magnetic flux content of the magnetosphere at the time of substorm onset, *Geophysical Research Letters*, *36*(4), 1–5, doi:10.1029/2008GL037059. 67

Borovsky, J. E., and J. Birn (2014), The Solar Wind Electric Field Does Not Control the Dayside Reconnection Rate, *Journal of Geophysical Research: Space ...*, pp. 1–10, doi:10.1002/2013JA019193.Received. 33

Borovsky, J. E., R. J. Nemzek, and R. D. Belian (1993), The Occurrence Rate of Magnetospheric-Substorm Onsets: Random and Periodic Substorms, *Journal of Geophysical Research*, *98*(A3), 3807–3813, doi:10.1029/92JA02556. 48, 125

Borovsky, J. E., M. Hesse, J. Birn, and M. M. Kuznetsova (2008), What determines the reconnection rate at the dayside magnetosphere?, *Journal of Geophysical Research*, *113*(A7), A07,210, doi:10.1029/2007JA012645. 33

Boynton, R. J., M. a. Balikhin, S. a. Billings, H. L. Wei, and N. Ganushkina (2011), Using the NARMAX OLS-ERR algorithm to obtain the most influential coupling functions that affect the evolution of the magnetosphere, *Journal of Geophysical Research*, *116*(A5), A05,218, doi:10.1029/2010JA015505. 35

Bruntz, R., R. E. Lopez, M. Wiltberger, and J. G. Lyon (2012a), Investigation of the viscous potential using an MHD simulation, *Journal of Geophysical Research: Space Physics*, *117*(3), 1–9, doi:10.1029/2011JA017022. 133

Bruntz, R., R. E. Lopez, S. K. Bhattarai, K. H. Pham, Y. Deng, Y. Huang, M. Wiltberger, and J. G. Lyon (2012b), Investigating the viscous interaction and its role in generating the ionospheric potential during the Whole Heliosphere Interval, *Journal of Atmospheric and Solar-Terrestrial Physics*, *83*, 70–78, doi:10.1016/j.jastp.2012.03.016. 133

Burch, J. L. (2000), IMAGE mission overview, *Space Science Reviews*, *91*, 1–14, doi:10.1023/A:1005245323115. 55, 93

Caan, M. N., R. L. McPherron, and C. T. Russell (1977), Characteristics of the Association Between the Interplanetary Magnetic Field and Substorms, *Journal of Geophysical Research*, *82*(29), 4837–4842, doi:10.1029/JA082i029p04837. 27, 105

Cai, X., and C. R. Clauer (2009), Investigation of the period of sawtooth events, *Journal of Geophysical Research*, *114*, A06,201, doi:10.1029/2008JA013764. 48

Cai, X., and C. R. Clauer (2013), Magnetospheric sawtooth events during the solar cycle 23, *118*(10), 6378–6388, doi:10.1002/2013JA018819. 36

Cai, X., C. R. Clauer, and A. J. Ridley (2006a), Statistical analysis of ionospheric potential patterns for isolated substorms and sawtooth events, *Annales Geophysicae*, *24*, 1977–1991, doi:10.5194/angeo-24-1977-200. 48, 49

Cai, X., M. G. Henderson, and C. R. Clauer (2006b), A statistical study of magnetic dipolarization for sawtooth events and isolated substorms at geosynchronous orbit with GOES data, *Annales Geophysicae*, *24*, 3481–3490, doi:10.5194/angeo-24-3481-2006. 48, 93, 122

Carter, J., S. Milan, J. Coxon, M.-T. Walach, and B. Anderson (2016), Average field-aligned current configuration parameterized by solar wind conditions, *Journal of Geophysical Research A: Space Physics*, *121*(2), 1294–1307, doi:10.1002/2015JA021567. 132

Chapman, S., and V. C. A. Ferraro (1931), A New Theory of Magnetic Storms, *Terrestrial Magnetism and Atmospheric Electricity*, *36*(2), doi:10.1029/TE036i002p00077. 18, 20

Chapman, S., and V. C. A. Ferraro (1941), The Geomagnetic Ring Current: I - Its Radial Stability, *Terrestrial Magnetism and Atmospheric Electricity*, *46*(1931), doi:10.1029/TE046i001p00001. 20

Chisham, G., M. Lester, S. E. Milan, M. P. Freeman, W. a. Bristow, a. Grocott, K. a. McWilliams, J. M. Ruohoniemi, T. K. Yeoman, P. L. Dyson, R. a. Greenwald, T. Kikuchi, M. Pinnock, J. P. S. Rash, N. Sato, G. J. Sofko, J. P. Villain, and a. D. M. Walker (2007), A decade of the Super Dual Auroral Radar Network (SuperDARN): Scientific achievements, new techniques and future directions, *Surveys in Geophysics*, *28*(1), 33–109, doi:10.1007/s10712-007-9017-8. 51, 60, 63

Chisham, G., M. P. Freeman, G. A. Abel, M. M. Lam, M. Pinnock, I. J. Coleman, S. E. Milan, M. Lester, W. A. Bristow, R. A. Greenwald, G. J. Sofko, and J.-P. Villain (2008), Remote Sensing of the Spatial and Temporal Structure of Magnetopause and Magnetotail Reconnection from the Ionosphere, *Reviews of Geophysics*, *46*(RG1004), doi:10.1029/2007RG000223. 28, 29

Clausen, L. B. N., J. B. H. Baker, J. M. Ruohoniemi, S. E. Milan, J. C. Coxon, S. Wing, S. Ohtani, and B. J. Anderson (2013), Temporal and spatial dynamics of the regions 1 and 2 Birkeland currents during substorms, *Journal of Geophysical Research: Space Physics*, *118*(6), 3007–3016, doi:10.1002/jgra.50288. 67

Coroniti, F. V., and C. F. Kennel (1973), Can the ionosphere regulate magnetospheric convection?, *Journal of Geophysical Research*, *78*(16), 2837–2851, doi:10.1029/JA078i016p02837. 26, 40, 133

Coumans, V., C. Blockx, J. C. Gérard, B. Hubert, and M. Connors (2007), Global morphology of substorm growth phases observed by the IMAGE-SI12 imager, *Journal of Geophysical Research: Space Physics*, *112*(11), 1–13, doi:10.1029/2007JA012329. 67

Cowley, S. W. H. (1982), The Causes of Convection in the Earth's Magnetosphere: A Review of Developments During the IMS, *Reviews of Geophysics and Space Physics*, *20*(3), 531–565, doi:10.1029/RG020i003p00531. 133

Cowley, S. W. H., and M. Lockwood (1992), Excitation and decay of solar wind-driven flows in the magnetosphere-ionophere system, *Annales geophysicae*, *10*, 103–115. vi, 25, 26, 27, 66, 68

Cowley, S. W. H., and M. Lockwood (1996), Time-dependent flows in the coupled solar wind-magnetosphere-ionosphere system, *Advances in Space Research*, *18*(8), 141–150, doi:10.1016/0273-1177(95)00972-8. 25

Cowley, S. W. H., J. P. Morelli, and M. Lockwood (1991), Dependence of Convective Flows and Particle Precipitation in the High-Latitude Dayside Ionosphere on the X and Y Components of the Interplanetary Magnetic Field, *Journal of Geophysical Research*, *96*(A4), 5557–5564, doi:10.1029/90JA02063. 88

Coxon, J. C., S. E. Milan, L. B. N. Clausen, B. J. Anderson, and H. Korth (2014), A superposed epoch analysis of the regions 1 and 2 Birkeland currents observed by AMPERE during substorms, *Journal of Geophysical Research: Space Physics*, *119*, 1–13, doi:10.1002/2014JA020500. 67, 132

Craven, J. D., and L. A. Frank (1985), The Temporal Evolution of a Small Auroral Substorm as Viewed from High Altitudes with Dynamics Explorer 1, *Geophysical Research Letters*, *12*(7), 465–468, doi:10.1029/GL012i007p00465. 32, 39

Craven, J. D., and L. A. Frank (1987), Latitudinal Motions of the Aurora During Substorms, *Journal of Geophysical Research: Space Physics*, *92*(A5), 4565–4573, doi:10.1029/JA092iA05p04565. 39

Davies, J. A., M. Lester, S. E. Milan, and T. K. Yeoman (1999), A comparison of velocity measurements from the CUTLASS Finland radar and the EISCAT UHF system, *Annales Geophysicae*, *17*(7), 892–902, doi:10.5194/angeo-17-892-1999. 89

Davis, T. N., and M. Sugiura (1966), Auroral electrojet activity index AE and its universal time variations, *Journal of Geophysical Research*, *71*(3), doi:10.1029/JZ071i003p00785. 27, 59

De La Beaujardière, O., D. Alcayde, J. Fontanari, and C. Leger (1991), Seasonal Dependence of High-Latitude Electric Fields, *Journal of Geophysical Research*, *96*(A4), 5723–5735, doi:10.1029/90JA01987. 73

DeJong, A. D., and C. R. Clauer (2005), Polar UVI images to study steady magnetospheric convection events: Initial results, *Geophysical Research Letters*, *32*(24), L24,101, doi:10.1029/2005GL024498. 47

DeJong, A. D., X. Cai, C. R. Clauer, and J. F. Spann (2007), Aurora and open magnetic flux during isolated substorms, sawteeth, and SMC events, *Annales Geophysicae*, *25*, 1865–1876, doi:10.5194/angeo-25-1865-2007. 98, 108

DeJong, A. D., A. J. Ridley, and C. R. Clauer (2008), Balanced reconnection intervals : four case studies, *Annales Geophysicae*, *26*, 3897–3912, doi:10.5194/angeo-26-3897-2008. 94, 106

DeJong, A. D., A. J. Ridley, X. Cai, and C. R. Clauer (2009), A statistical study of BRIs (SMCs), isolated substorms, and individual sawtooth injections, *Journal of Geophysical Research*, *114*, A08,215, doi:10.1029/2008JA013870. 45, 94, 106

Doyle, M. A., and W. J. Burke (1983), S3-2 measurements of the polar cap potential, *Journal of Geophysical Research*, *88*(A11), 9125, doi:10.1029/JA088iA11p09125. 133

Drake, K. A., R. A. Heelis, M. R. Hairston, and P. C. Anderson (2009), Electrostatic potential drop across the ionospheric signature of the low-latitude boundary layer, *Journal of Geophysical Research: Space Physics*, *114*, A04,215, doi:10.1029/2008JA013608. 133

Drayton, R. A., A. V. Koustov, M. R. Hairston, and J.-P. Villain (2005), Comparison of DMSP cross-track ion drifts and SuperDARN line-of-sight velocities, *Annales Geophysicae*, doi:10.5194/angeo-23-2479-2005. 89

Dungey, J. W. (1961), Interplanetary Magnetic Field and the Auroral Zones, *Physical Review Letters*, *6*(2), 47–48, doi:10.1103/PhysRevLett.6.47. 17, 24, 26

Dungey, J. W. (1963), Interactions of solar plasma with the geomagnetic field, *Planetary and Space Science*, *10*, 223–237, doi:10.1016/0032-0633(63)90020-5. 24, 25, 26

Eather, R. H., and S. B. Mende (1972), Systematics in auroral energy spectra, *Journal of Geophysical Research*, *77*(4), 660–673, doi:10.1029/JA077i004p00660. 32

Evans, J. V., A. F. Nagy, H. Friedman, and D. S. Intriligator (1981), Solar-terrestrial research for the 1980's, *Committee on Solar-Terrestrial Research, National Research Council, National Academy Press, Washington, DC.* 17

Fairfield, D. H., and L. J. Cahill (1966), Transition region magnetic field and polar magnetic disturbances, *Journal of Geophysical Research*, *71*(1), doi:10.1029/JZ071i001p00155. 24, 26, 29

Farris, M. H., and C. T. Russell (1994), Determining the standoff distance of the bow shock: Mach number dependence and use of models, *Journal of Geophysical Research*, *99*(A9), 17,681–17,689, doi:10.1029/94JA01020. 54

Finlay, C. C., S. Maus, C. D. Beggan, T. N. Bondar, a. Chambodut, T. a. Chernova, a. Chulliat, V. P. Golovkov, B. Hamilton, M. Hamoudi, R. Holme, G. Hulot, W. Kuang, B. Langlais, V. Lesur, F. J. Lowes, H. Lühr, S. Macmillan, M. Mandea, S. McLean, C. Manoj, M. Menvielle, I. Michaelis, N. Olsen, J. Rauberg, M. Rother, T. J. Sabaka, a. Tangborn, L. Tøffner-Clausen, E. Thébault, a. W. P. Thomson, I. Wardinski, Z. Wei, and T. I. Zvereva (2010), International Geomagnetic Reference Field: the eleventh generation, *Geophysical Journal International*, *183*(3), 1216–1230, doi:10.1111/j.1365-246X.2010.04804.x. 61, 62

Forsyth, C., a. N. Fazakerley, I. J. Rae, C. E. J. Watt, K. Murphy, J. a. Wild, T. Karlsson, R. Mutel, C. J. Owen, R. Ergun, a. Masson, M. Berthomier, E. Donovan, H. U. Frey, J. Matzka, C. Stolle, and Y. Zhang (2014), In situ spatiotemporal measurements of the detailed azimuthal substructure of the substorm current wedge, *119*(2), 927–946, doi:10.1002/2013JA019302. 120

Foster, J. C., and H. B. Vo (2002), Average characteristics and activity dependence of the subauroral polarization stream, *Journal of Geophysical Research: Space Physics*, *107*, doi:10.1029/2002JA009409. 87

Frank, L. A., and J. D. Craven (1988), Imaging results from Dynamics Explorer 1, *Reviews of Geophysics*, *26*(2), 249–283, doi:10.1029/RG026i002p00249. 39

Freeman, M. P. (2003), A unified model of the response of ionospheric convection to changes in the interplanetary magnetic field, *Journal of Geophysical Research: Space Physics*, *108*(A1), 1–13, doi:10.1029/2002JA009385. 86, 88

Freeman, M. P., and S. K. Morley (2004), A minimal substorm model that explains the observed statistical distribution of times between substorms, *Geophysical Research Letters*, *31*(12), L12,807, doi:10.1029/2004GL019989. 105

Freeman, M. P., and S. K. Morley (2009), No evidence for externally triggered substorms based on superposed epoch analysis of IMF B z, *Geophysical Research Letters*, *36*(21), L21,101, doi: 10.1029/2009GL040621. 105

Freeman, M. P., and D. J. Southwood (1988), The effect of magnetospheric erosion on mid- and high-latitude ionospheric flows, *Planetary and Space Science*, *36*(5), 509–522, doi:10.1016/0032-0633(88)90110-9. 66

Frey, H. U., S. B. Mende, V. Angelopoulos, and E. F. Donovan (2004), Substorm onset observations by IMAGE-FUV, *Journal of Geophysical Research*, *109*(A10), A10,304, doi:10.1029/2004JA010607. 44, 79, 93, 94, 95, 96, 98, 120

Gillies, R. G., G. C. Hussey, G. J. Sofko, K. A. McWilliams, R. A. D. Fiori, P. Ponomarenko, and J. P. St.-Maurice (2009), Improvement of SuperDARN velocity measurements by estimating the index of refraction in the scattering region using interferometry, *Journal of Geophysical Research: Space Physics*, *114*(A07305), doi:10.1029/2008JA013967. 89

Gillies, R. G., G. C. Hussey, G. J. Sofko, D. M. Wright, and J. A. Davies (2010), A comparison of EISCAT and SuperDARN F-region measurements with consideration of the refractive index in the scattering volume, *Journal of Geophysical Research: Space Physics*, *115*(A06319), doi:10.1029/2009JA014694. 89

Gillies, R. G., G. C. Hussey, G. J. Sofko, P. V. Ponomarenko, and K. A. McWilliams (2011), Improvement of HF coherent radar line-of-sight velocities by estimating the refractive index in the scattering volume using radar frequency shifting, *Journal of Geophysical Research: Space Physics*, *116*(1), 1–12, doi:10.1029/2010JA016043. 89

Gillies, R. G., G. C. Hussey, G. J. Sofko, and K. A. McWilliams (2012), A statistical analysis of SuperDARN scattering volume electron densities and velocity corrections using a radar frequency shifting technique, *Journal of Geophysical Research: Space*

Physics, *117*(A08320), doi:10.1029/2012JA017866. 89

Gold, T. (1959), Motions in the Magnetosphere of the Earth, *Journal of Geophysical Research*, *64*(9), 1219 – 1224, doi:10.1029/JZ064i009p01219. 15

Gosling, J. T., R. M. Skoug, D. J. McComas, and C. W. Smith (2005), Direct evidence for magnetic reconnection in the solar wind near 1 AU, *Journal of Geophysical Research: Space Physics*, *110*, doi:10.1029/2004JA010809. 14

Grant, I. S., and W. R. Phillips (1990), *Electromagnetism*, second edi ed., John Wiley & Sons, Manchester. 2, 10, 11

Greenspan, M. E., P. B. Anderson, and J. M. Pelagatti (1986), Characteristics of the Thermal Plasma Monitor (SSIES) for the Defense Meteorological Satellite Program (DMSP), Spacecraft S8 through S10, *Tech. rep.*, Air Force Geophysics Laboratory, Hanscom Air Force Base, Massachusetts, doi:AFGL-TR-86-0227. 57

Greenwald, R. A., K. B. Baker, J. R. Dudeney, M. Pinnock, T. B. Jones, E. C. Thomas, J.-P. Villain, J.-C. Cerisier, C. Senior, C. Hanuise, R. D. Hunsucker, G. Sofko, J. Koehler, E. Nielsen, R. Pellinen, A. D. M. Walker, N. Sato, and H. Yamagishi (1995), Darn/Superdarn; A Global View of the Dynamics of High-Latitude Convection, *Space Science Reviews*, *71*, 761–796, doi:10.1007/BF00751350. 60

Grocott, A., S. Cowley, J. Sigwarth, J. Watermann, and T. K. Yeoman (2002), Excitation of twin-vortex flow in the nightside high-latitude ionosphere during an isolated substorm, *20*, 1577–1601, doi:10.5194/angeo-20-1577-2002. 67

Grocott, A., S. W. H. Cowley, and J. B. Sigwarth (2003), Ionospheric flow during extended intervals of northward but By-dominated IMF, *Annales Geophysicae*, *21*(2), 509–538, doi:10.5194/angeo-21-509-2003. 67

Grocott, A., S. E. Milan, T. K. Yeoman, N. Sato, A. S. Yukimatu, and J. A. Wild (2010), Superposed epoch analysis of the ionospheric convection evolution during substorms: IMF By dependence, *Journal of Geophysical Research*, *115*(A00I06), doi:10.1029/2010JA015728. 69

Gussenhoven, M. S., D. A. Hardy, and N. Heinemann (1987), The Equatorward Boundary of Auroral Ion Precipitation, *Journal of Geophysical Research*, *92*(A4), 3273, doi:10.1029/JA092iA04p03273. 123

Hairston, M. R., and R. A. Heelis (1996), Analysis of ionospheric parameters based on DMSP SSIES data using the DBASE4 and NADIA programs, *Tech. rep.*, Phillips Laboratory, Directorate of Geophysics, Hanscom Air Force Base, Massachusetts. 57

Harang, L. (1946), The Mean Field of Disturbance of Polar Geomagnetic Storms, *Terrestrial Magnetism and Atmospheric Electricity*, *51*(3), 353–380, doi:10.1029/TE051i003p00353. 88

Heaviside, O. (2011), *Electromagnetic Waves, Cambridge Library Collection Monograph*, reprint ed., Cambridge University Press, Cambridge, UK. 92

Heelis, R. A., and W. B. Hanson (1998), Measurements of Thermal Ion Drift Velocity and Temperature Using Planar Sensors, *Measurement Techniques in Space Plasmas: Particles, Geophys. Monogr. Ser.*, *102*(61), doi:10.1029/GM102p0061. 57

Heelis, R. A., and P. H. Reiff (1985), Observations of magnetospheric convection from low altitudes, *Advances in Space Research*, *5*(4), 349–362, doi:10.1016/0273-1177(85)90161-9. 133

Henderson, M. G. (2004), The May 23, 1986 CDAW-9C interval: A sawtooth event, *Geophysical Research Letters*, *31*(11), L11,804, doi:10.1029/2004GL019941. 36, 48, 94

Henderson, M. G., G. D. Reeves, R. Skoug, M. F. Thomsen, M. H. Denton, S. B. Mende, T. J. Immel, P. C. Brandt, and H. J. Singer (2006), Magnetospheric and auroral activity during the 18 April 2002 sawtooth event, *111*(April 2002), 1–15, doi:10.1029/2005JA011111. 48, 49, 122, 123

Heppner, J. P. (1954), Time Sequences and Spatial Relations in Auroral Activity During Magnetic Bays at College, Alaska, *Journal of Geophysical Research*, *59*(3), doi:10.1029/JZ059i003p00329. 40

Heppner, J. P. (1972), The Harang Discontinuity in Auroral Belt Ionospheric Currents, in *A collection of articles on cosmic geophysics dedicated to the memory of Professor L. Harang on the seventieth anniversary of his birth 19 April 1972*, edited by J. Holtet and A. Egeland, 29 ed., pp. 105–120, Geofysiske Publikasjoner; Universitetsforlage. 88

Heppner, J. P., and N. C. Maynard (1987), Empirical high-latitude electric field models, *Journal of Geophysical Research*, *92*(A5), 4467–4489, doi: 10.1029/JA092iA05p04467. 24, 63

Heppner, J. P., N. F. Ness, C. S. Scearce, and T. L. Skillman (1963), Explorer 10 Magnetic Field Measurements, *Journal of Geophysical Research*, *68*(1), 1–46, doi:10.1029/JZ068i001p00001. 17

Hesse, M., J. Birn, and R. A. Hoffman (1997), On the mapping of ionospheric convection into the magnetosphere, *Journal of Geophysical Research*, *102*(A5), 9543–9551, doi:10.1029/96JA03999. 132

Hines, C. O. (1986), Origins of the 1961 Axford-Hines Paper on Magnetospheric Convection, *Eos*, *67*(33), doi: 10.1029/EO067i033p00634-02. 24, 26

Hones, J., E. W. (1985a), Plasma flow in the near and distant geomagnetic tail, *Advances in Space Research*, *5*(4), 375–389, doi:10.1016/0273-1177(85)90164-4. 39

Hones, J., E. W. (1985b), The Poleward Leap of the Auroral Electrojet as Seen in Auroral Images, *Journal of Geophysical Research*, *90*(A6), 5333–5337, doi:10.1029/JA090iA06p05333. 39, 41

Hones, J., E. W., D. N. Baker, S. J. Bame, W. C. Feldman, J. T. Gosling, D. J. McComas, R. D. Zwickl, J. A. Slavin, E. J. Smith, and B. T. Tsurutani (1984a), Structure of the Magnetotail at 220 RE and its Response to gGeomagnetic Activity, *Geophysical Research Letters*, *11*(1), 5–7, doi: 10.1029/GL011i001p00005. 39

Hones, J., E. W., T. Pytte, and J. West, H. I. (1984b), Associations of Geomagnetic Activity With Plasma Sheet Thinning and Expansion: A Statistical Study, *Journal of Geophysical Research*, *89*(A7), 5471–5478, doi:10.1029/JA089iA07p05471. 39

Hones, J., E. W., C. D. Anger, J. Birn, J. S. Murphree, and L. L. Cogger (1987), A Study of a Magnetospheric Substorm Recorded by the Viking Auroral Imager, *Geophysical Research Letters*, *14*(4), 411–414, doi:10.1029/GL014i004p0041. 39

Huang, C.-S., and X. Cai (2009), Magnetotail total pressure and lobe magnetic field at onsets of sawtooth events and their relation to the solar wind, *Journal of Geophysical Research*, *114*, A04,204, doi:10.1029/2008JA013807. v, 49, 50

Huang, C.-S., A. D. DeJong, and X. Cai (2009), Magnetic flux in the magnetotail and polar cap during sawteeth, isolated substorms, and steady magnetospheric convection events, *Journal of Geophysical Research*, *114*, A07,202, doi:10.1029/2009JA014232. 36, 98, 108

Hubert, B. (2016), Private communication via email. vi, 71, 72

Hubert, B., S. E. Milan, A. Grocott, C. Blockx, S. W. H. Cowley, and J.-C. Gérard (2006), Dayside and nightside reconnection rates inferred from IMAGE FUV and Super Dual Auroral Radar Network data, *Journal of Geophysical Research*, *111*(A3), A03,217, doi:10.1029/2005ja011140. 29, 33, 38, 39, 67, 71, 73

Hubert, B., S. E. Milan, A. Grocott, S. W. H. Cowley, and J. C. Gerard (2008), Open magnetic flux and magnetic flux closure during sawtooth events, *Geophysical Research Letters*, *35*(23), 1–6, doi:10.1029/2008GL036374. 67

Iijima, T., and T. Nagata (1972), Signatures for substorm development of the growth phase and expansion phase, *Planetary and Space Science*, *20*(7), 1095–1112, doi:10.1016/0032-0633(72)90219-X. v, 40, 41

Iijima, T., and T. A. Potemra (1976), Field-aligned currents in the dayside cusp observed by Triad, *Journal of Geophysical Research*, *81*(34), 5971–5979, doi:10.1029/JA081i034p05971. 21

Imber, S. M. (2008), Auroral and Ionospheric Flow Measurements of Magnetopause Reconnection During Intervals of Northward Interplanetary Magnetic Field, Ph.D. thesis, University of Leicester. 90

Imber, S. M. (2016), Private communication via email. 90

Imber, S. M., S. E. Milan, and B. Hubert (2007), Observations of significant flux closure by dual lobe reconnection, *Annales Geophysicae*, *25*(7), 1617–1627, doi:10.5194/angeo-25-1617-2007. 23, 134

James, M. K. (2014), ULF Waves Driven By Recently-Injected Energetic Particle Populations Abstract, Phd thesis, University of Leicester. v, 43

Kamide, Y., and N. Balan (2016), The importance of ground magnetic data in specifying the state of magnetosphere ionosphere coupling: a personal view, *Geoscience Letters*, *3*(1), doi:10.1186/s40562-016-0042-7. 44, 51

Kamide, Y., W. Baumjohann, I. A. Daglis, W. D. Gonzalez, M. Grande, J. A. Joselyn, R. L. McPherron, J. L. Phillips, E. G. D. Reeves, G. Rostoker, A. S. Sharma, H. J. Singer, B. T. Tsurutani, and V. M. Vasyliunas (1998), Current understanding of magnetic storms: Storm-substorm relationships, *Journal of Geophysical Research*, *103*(A8), 17,705–17,728, doi:10.1029/98JA01426. 41

Kavanagh, A. J., G. Lu, E. F. Donovan, G. D. Reeves, F. Honary, J. Manninen, and T. J. Immel (2007), Energetic electron precipitation during sawtooth injections, pp. 1199–1214, doi:10.5194/angeo-25-1199-2007. 49

Kepko, L., R. L. McPherron, O. Amm, S. Apatenkov, W. Baumjohann, J. Birn, M. Lester, R. Nakamura, T. I. Pulkkinen, and V. Sergeev (2015), Substorm Current Wedge Revisited, *Space Science Reviews*, *190*, 1–46, doi:10.1007/s11214-014-0124-9. 119, 120

King, J. H., and N. E. Papitashvili (2005), Solar wind spatial scales in and comparisons of hourly Wind and ACE plasma and magnetic field data, *Journal of Geophysical Research: Space Physics*, *110*, 1–9, doi:10.1029/2004JA010649. 54, 70

Kissinger, J. E., R. L. McPherron, T.-S. Hsu, and V. Angelopoulos (2011), Steady magnetospheric convection and stream interfaces: Relationship over a solar cycle, *Journal of Geophysical Research*, *116*(January), A00I19, doi:10.1029/2010JA015763. v, vi, 45, 46, 47, 93, 94, 95, 96, 97, 98, 106, 109

Kissinger, J. E., R. L. McPherron, T.-S. Hsu, V. Angelopoulos, and X. Chu (2012), Necessity of substorm expansions in the initiation of steady magnetospheric convection, *Geophysical Research Letters*, *39*, L15,105, doi:10.1029/2012GL052599. 93, 106, 107, 131, 135

Kivelson, M. G., C. T. Russell, D. Burgess, J. Carlson, H. C., A. Egeland, C. K. Goertz, W. J. Hughes, A. J. Hundhausen, M. G. Kivelson, J. G. Luhmann, R. L. McPherron, E. R. Priest, C. T. Russell, R. J. Strangeway, R. J. Walker, and R. A. Wolf (1995), *Introduction to Space Physics*, Cambridge University Press, Cambridge, doi:10.1063/1.2807586. 12, 53

Langmuir, I. (1929), The Interaction of Electron and Positive Ion Space Charge in Cathode Sheats, *Physical Review Letters*, *33*, 954–989, doi:10.1103/PhysRev.33.954. 1

Lin, R. P., and K. A. Anderson (1966), Evidence for Connection of Geomagnetic Tail Lines to the Interplanetary Field, *Journal of Geophysical Research*, *71*(17), 4213–4217, doi:10.1029/JZ071i017p04213. 25

Lockwood, M. (1991), On flow reversal boundaries and transpolar voltage in average models of high-latitude convection, *Planetary and Space Science*, *39*(3), 397–409, doi:10.1016/0032-0633(91)90002-r. 86

Lockwood, M. (1997), Relationship of dayside auroral precipitations to the open-closed separatrix and the pattern of convective flow, *Journal of Geophysical Research*, *102*(A8), 17,457 – 17,487, doi:10.1029/97JA01100. 31

Lockwood, M., and S. W. H. Cowley (1992), Ionospheric convection and the substorm cycle, in *International Conference on Substorms*. vi, 26, 27, 66, 68

Lockwood, M., and M. P. Freeman (1989), Recent ionospheric observations relating to solar-wind-magnetosphere coupling, *Philosophical Transactions of the Royal Society*, *328*, 93–105, doi:10.1098/rsta.1989.0026. 87

Lockwood, M., and S. K. Morley (2004), A numerical model of the ionospheric signatures of time-varying magnetic reconnection : I . ionospheric convection, *Annales Geophysicae*, *22*, 73–91, doi:10.5194/angeo-22-73-2004. 86

Lockwood, M., S. Fuselier, A. D. M. Walker, and F. Søraas (1998), A Summary of the Nato ASI on Polar Cap Boundary Phenomena, in *Polar Cap Boundary Phenomena, Proceedings of the NATO Advanced Study Institue*, edited by J. Moen, A. Egeland, and M. Lockwood, pp. 415–432, Kluwer Academic Publishers, Longyearbyen, Svalbard, Norway. 32

Lockwood, M., M. Hairston, I. Finch, and A. Rouillard (2009), Transpolar voltage and polar cap flux during the substorm cycle and steady convection events, *Journal of Geophysical Research*, *114*(A1), A01,210, doi:10.1029/2008JA013697. 67, 71

Lockwood, M., M. J. Owens, L. A. Barnard, S. Bentley, C. J. Scott, and C. E. Watt (2016), On the origins and timescales of geoeffective IMF, *Space Weather*, *14*(6), 406–432, doi:10.1002/2016SW001375. 54

Lyons, L. R. (1995), A new theory for magnetospheric substorms, *Journal of Geophysical Research*, *100*(A10), 69–81, doi:10.1029/95JA01344. 105

Makita, K., C.-I. Meng, and S.-I. Akasofu (1988), Latitudinal Electron Precipitation Patterns During Large and Small IMF Magnitudes for Northward IMF Conditions, *Journal of Geophysical Research*, *93*(A1), 97–104, doi:10.1029/JA093iA01p00097. 31

McIlwain, C. E. (1974), Substorm Injection Boundaries, in *Magnetospheric Physics, Proceedings of the Advanced Summer Institute Held at Sheffield, U.K., August 1973*, edited by B. M. McCormac, pp. 143–154, Springer Netherlands, doi:10.1007/978-94-010-2214-9_13. 40

McPherron, R. L. (1970), Growth phase of magnetospheric substorms, *Journal of Geophysical Research*, *75*(28), 5592–5599, doi:10.1029/JA075i028p05592. 38

McPherron, R. L., C. T. Russell, and M. P. Aubry (1973), Satellite Studies of Magnetospheric Substorms on August 15,1968; 9. Phenomenological Model for Substorms, *Journal of Geophysical Research*, *78*(16), doi:10.1029/JA078i016p03131. v, 40, 42

McPherron, R. L., T. P. O'Brien, and S. Thompson (2005), Solar wind drivers for steady magnetospheric convection, in *Multiscale Coupling of Sun-Earth Processes*, edited by A. T. Y. Lui, Y. Kamide, and G. Consolini, chap. 2: Space S, pp. 113–124, Elsevier Science B.V., Amsterdam. 45, 93, 106, 134

McPherron, R. L., J. M. Weygand, and T.-S. Hsu (2008), Response of the Earth's magnetosphere to changes in the solar wind, *Journal of Atmospheric and Solar-Terrestrial Physics*, *70*(2-4), 303–315, doi:10.1016/j.jastp.2007.08.040. 36

McWilliams, K. A., J. B. Pfeifer, R. L. McPherron, and H. U. Frey (2006), SuperDARN and IMAGE WIC observations during intervals of steady magnetospheric convection, in *International Conference on Substorms-8*, pp. 175–180. 126

McWilliams, K. A., J. B. Pfeifer, and R. L. McPherron (2008), Steady magnetospheric convection selection criteria: Implications of global SuperDARN convection measurements, *Geophysical Research Letters*, *35*(9), L09,102, doi:10.1029/2008GL033671. 45, 94

Meier, R. R. (1991), Ultraviolet spectroscopy and remote sensing of the upper atmosphere, *Space Science Reviews*, *58*(1), 1–185, doi:10.1007/BF01206000. 56

Mende, S. B., H. Heetderks, H. U. Frey, M. Lampton, S. P. Geller, S. Habraken, E. Renotte, C. Jamar, P. Rochus, J. Spann, S. A. Fuselier, J.-C. Gerard, R. Gladstone, S. Murphree, and L. Cogger (2000a), Far ultraviolet imaging from the IMAGE spacecraft. 1. System design, *Space Science Reviews*, *91*, 243–270, doi:10.1007/978-94-011-4233-5_8. 55, 56, 93, 111

Mende, S. B., H. Heetderks, H. U. Frey, J. M. Stock, M. Lampton, S. P. Geller, R. Abiad, O. H. W. Siegmund, S. Habraken, E. Renotte, C. Jamar, P. Rochus, J.-C. Gerard, R. Sigler, and H. Lauche (2000b), Far Ultraviolet Imaging from the IMAGE Spacecraft. 3. Spectral Imaging of Lyman-α and OI 135.6 nm, in *The IMAGE Mission*, edited by J. L. Burch, chap. 3, pp. 287–318, Springer Netherlands, doi:10.1007/978-94-011-4233-5_10. 55

Mende, S. B., H. Heetderks, H. U. Frey, M. Lampton, S. P. Geller, R. Abiad, O. H. W. Siegmund, A. S. Tremsin, J. Spann, H. Dougani, S. A. Fuselier, A. L. Magoncelli, M. B. Bumala, S. Murphree, and T. Trondsen (2000c), Far ultraviolet imaging from the IMAGE spacecraft. 2. Wideband FUV imaging, *Space Science Reviews*, *91*, 271–285, doi:10.1023/A:1005227915363. 55, 93

Mende, S. B., H. U. Frey, B. J. Morsony, and T. J. Immel (2003), Statistical behavior of proton and electron auroras during substorms, *Journal of Geophysical Research: Space Physics*, *108*(A9), doi:10.1029/2002JA009751. 30, 31, 32, 44, 120, 121, 122

Meng, C.-I., and K. Liou (2004), Substorm timings and timescales: A new aspect, *Space Science Reviews*, *113*(1-2), 41–75, doi:10.1023/B:SPAC.0000042939.88548.68. 41, 44, 120

Meng, C.-I., and K. Makita (1986), Dynamic Variations of the Polar Cap, in *Solar Wind-Magnetosphere Coupling*, edited by Y. Kamide and J. A. Slavin, pp. 605–631, Terra Scientific, Tokyo. 26, 27, 38

Milan, S. E. (2004), Dayside and nightside contributions to the cross polar cap potential: placing an upper limit on a viscous-like interaction, *Annales Geophysicae*, *22*, 3771–3777, doi:10.5194/angeo-22-3771-2004. 67, 71, 89, 133

Milan, S. E. (2013), Modeling Birkeland currents in the expanding/contracting polar cap paradigm, *Journal of Geophysical Research: Space Physics*, *118*(9), 5532–5542, doi:10.1002/jgra.50393. 62, 63, 67, 70, 86, 129, 132, 135

Milan, S. E. (2015), *Magnetospheric Plasma Physics: The Impact of Jim Dungey's Research*, chap. 2. Sun et Lumière, pp. 1–271, doi:10.1007/978-3-319-18359-6_2. 21, 26

Milan, S. E. (2016), Private communications. 132

Milan, S. E., M. Lester, S. W. H. Cowley, K. Oksavik, M. Brittnacher, R. A. Greenwald, G. Sofko, and J.-P. Villain (2003), Variations in the polar cap area during two substorm cycles, *Annales Geophysicae*, *21*, 1121–1140, doi:10.5194/angeo-21-1121-2003. 26, 27, 67

Milan, S. E., J. A. Wild, B. Hubert, C. M. Carr, E. A. Lucek, J. M. Bosqued, J. F. Watermann, and J. A. Slavin (2006), Flux closure during a substorm observed by Cluster, Double Star, IMAGE FUV, SuperDARN, and Greenland magnetometers, *Annales Geophysicae*, *24*, 751–767, doi:10.5194/angeo-24-751-2006. 47, 119, 120

Milan, S. E., G. Provan, and B. Hubert (2007), Magnetic flux transport in the Dungey cycle: A survey of dayside and nightside reconnection rates, *Journal of Geophysical Research*, *112*(A1), A01,209, doi:10.1029/2006JA011642. 26, 27, 50, 67, 79

Milan, S. E., J. Hutchinson, P. D. Boakes, and B. Hubert (2009a), Influences on the radius of the auroral oval, *Annales Geophysicae*, *27*, 2913–2924, doi:10.5194/angeo-27-2913-2009. 26, 123

Milan, S. E., a. Grocott, C. Forsyth, S. M. Imber, P. D. Boakes, and B. Hubert (2009b), A superposed epoch analysis of auroral evolution during substorm growth, onset and recovery: open magnetic flux control of substorm intensity, *Annales Geophysicae*, *27*(2), 659–668, doi:10.5194/angeo-27-659-2009. 67, 120

Milan, S. E., T. A. Evans, and B. Hubert (2010), Average auroral configuration parameterized by geomagnetic activity and solar wind conditions, *Annales Geophysicae*, *28*(4), 1003–1012, doi:10.5194/angeo-28-1003-2010. 123

Milan, S. E., J. S. Gosling, and B. Hubert (2012), Relationship between interplanetary parameters and the magnetopause reconnection rate quantified from observations of the expanding polar cap, *Journal of Geophysical Research*, *117*(A3), A03,226, doi:10.1029/2011JA017082. 27, 35, 36, 67, 70, 71, 94

Milan, S. E., S. Imber, and M. Lester (2013), ECLAT SuperDARN User Guide, *Tech. rep.*, University of Leicester. 73, 74, 87

Milan, S. E., S. M. Imber, J. A. Carter, M.-T. Walach, and B. Hubert (2016), What controls the local time extent of flux transfer events?, *Journal of Geophysical Research: Space Physics*, doi:10.1002/2015JA022012. 87

Milan, S. E., L. Clausen, J. Coxon, J. Carter, M.-T. Walach, K. Laundal, N. Østgaard, P. Tenfjord, J. Reistad, K. Snekvik, H. Korth, and B. J. Anderson (2017), Overview of solar wind-magnetosphere-ionosphere-atmosphere coupling and the generation of magnetospheric currents, *Space Science Reviews.* v, 19, 20, 21, 22

Morley, S. K., and M. P. Freeman (2007), On the association between northward turnings of the interplanetary magnetic field and substorm onsets, *Geophysical Research Letters*, *34*(8), L08,104, doi:10.1029/2006GL028891. 105

Morley, S. K., and M. Lockwood (2006), A numerical model of the ionospheric signatures of time-varying magnetic reconnection: III. Quasi-instantaneous convection responses in the Cowley-Lockwood paradigm, *Annales Geophysicae*, *24*, 961–972, doi:10.5194/angeo-24-961-2006. 88

Mottelay, P. F. (1893), *William Gilbert of Colchester, Physician of London, On the Loadstone and Magnetic Bodies and on the Great Magnet the Earth*, Bernard Quaritch, London. 1, 23

Mozer, F. S., and P. Bruston (1966), Properties of the auroral-zone electron source deduced from electron spectrums and angular distributions, *Journal of Geophysical Research*, *71*(19), 4451–4460, doi: 10.1029/JZ071i019p04451. 32

Murphy, K. R., I. R. Mann, I. J. Rae, C. L. Waters, H. U. Frey, A. Kale, H. J. Singer, B. J. Anderson, and H. Korth (2013), The detailed spatial structure of field-aligned currents comprising the substorm current wedge, *Journal of Geophysical Research: Space Physics*, *118*(12), 7714–7727, doi:10.1002/2013JA018979. 120

Ness, N. F. (1965), The Earth's Magnetic Tai, *Journal of Geophysical Research*, *70*(13), doi:10.1029/JZ070i013p02989. 17, 24

Newell, P. T., and J. W. Gjerloev (2011), Evaluation of SuperMAG auroral electrojet indices as indicators of substorms and auroral power, *Journal of Geophysical Research*, *116*(A12), A12,211, doi:10.1029/2011JA016779. 79, 125

Newell, P. T., and C.-I. Meng (1990), Intense kev energy polar rain, *Journal of Geophysical Research: Space Physics*, *95*(A6), 7869–7879, doi:10.1029/JA095iA06p07869. 32

Newell, P. T., S. Wing, C.-I. Meng, and V. Sigillito (1991), The auroral oval position, structure, and intensity of precipitation from 1984 onward: An automated on-line data base, *Journal of Geophysical Research: Space Physics*, *96*(A4), 5877–5882, doi:10.1029/90JA02450. 32

Newell, P. T., K. Liou, T. Sotirelis, and C.-I. Meng (2001), Auroral precipitation power during substorms: A Polar UV Imager-based superposed epoch analysis, *Journal of Geophysical Research*, *106*(A12), 28,885, doi:10.1029/2000JA000428. 120

Newell, P. T., T. Sotirelis, K. Liou, C. I. Meng, and F. J. Rich (2007), A nearly universal solar wind-magnetosphere coupling function inferred from 10 magnetospheric state variables, *Journal of Geophysical Research: Space Physics*, *112*(1), 1–16, doi:10.1029/2006JA012015. 33, 34, 35, 36

Newell, P. T., T. Sotirelis, K. Liou, and F. J. Rich (2008), Pairs of solar wind-magnetosphere coupling functions: Combining a merging term with a viscous term works best, *Journal of Geophysical Research: Space*

Physics, *113*(4), 1–10, doi:10.1029/2007JA012825. 34, 35, 36

O'Brien, T. P., S. M. Thompson, and R. L. McPherron (2002), Steady magnetospheric convection : Statistical signatures in the solar wind and AE, *Geophysical Research Letters*, *29*(7), doi:10.1029/2001GL014641. 44, 45, 107

Øieroset, M., T. D. Phan, M. Fujimoto, R. P. Lin, and R. P. Lepping (2001), In situ detection of reconnection in the Earth's magnetotail, *Letters to Nature*, *412*, 414–416, doi:10.1038/35086520. 14, 15

Panofsky, W. K. H., and M. Phillips (1956), *Calssical Electricity and Magnetism*, first edition ed., Addison-Wesley Publishing Company, Reading, Massachusetts. 2, 10

Partamies, N., and T. I. Pulkkinen (2009), Different magnetospheric modes: solar wind driving and coupling efficiency, *Annales Geophysicae*, *27*(11), 4281–4291, doi:10.5194/angeo-27-4281-2009. 36

Paschmann, G., B. U. O. Sonnerup, I. Papamastorakis, N. Sckopke, G. Haerendel, S. J. Bame, J. R. Asbridge, J. T. Gosling, C. T. Russell, and R. C. Elphic (1979), Plasma acceleration at the Earth's magnetopause: evidence for reconnection, *Nature*, *282*(5736), 243–246, doi:10.1038/282243a0. 23

Perreault, P., and S.-I. Akasofu (1978), A Study of Geomagnetic Storms, *Geophysical Journal of the Royal Astronomical Society*, *54*, 547–573, doi:10.1111/j.1365-246X.1978.tb05494.x. 27, 33, 34, 35

Petschek, H. E. (1964), Magnetic Field Annihilation, in *The Physics of Solar Flares, Proceedings of the AAS-NASA Symposium*, edited by W. N. Hess, SP-50, pp. 425–439, National Aeronautics and Space Administration, Science and Technical Information Division, Washington, DC, doi:10.1007/s13398-014-0173-7.2. 23

Phan, T., H. U. Frey, S. Frey, L. Peticolas, S. Fuselier, C. Carlson, H. Rème, J.-M. Bosqued, A. Balogh, M. Dunlop, L. Kistler, C. Mouikis, I. Dandouras, J.-A. Sauvaud, S. Mende, J. McFadden, G. Parks, E. Moebius, B. Klecker, G. Paschmann, M. Fujimoto, S. Petrinec, M. F. Marcucci, A. Korth, and R. Lundin (2003), Simultaneous Cluster and IMAGE observations of cusp reconnection and auroral proton spot for northward IMF, *Geophysical Research Letters*, *30*(10), 1509, doi:10.1029/2003GL016885. 14

Pulkkinen, T. I., N. Partamies, R. L. McPherron, M. Henderson, G. D. Reeves, M. F. Thomsen, and H. J. Singer (2007), Comparative statistical analysis of storm time activations and sawtooth events, *Journal of Geophysical Research*, *112*(A1), A01,205, doi:10.1029/2006JA012024. 49, 93

Pulkkinen, T. I., M. Palmroth, H. E. J. Koskinen, T. V. Laitinen, C. C. Goodrich, V. G. Merkin, and J. G. Lyon (2010), Magnetospheric modes and solar wind energy coupling efficiency, *Journal of Geophysical Research*, *115*, A03,207, doi:10.1029/2009JA014737. 36

Pytte, T., R. L. McPherron, and S. Kokubun (1976), The Ground Signatures of the Expansion Phase During Multiple Onset Substorms, *Planetary and Space Science*, *24*(12), 1115–1132, doi:10.1016/0032-0633(76)90149-5. 39

Pytte, T., R. L. McPherron, E. W. Hones, and H. I. West (1978), Multiple-satellite studies of magnetospheric substorms: Distinction between polar magnetic substorms and convection-driven negative bays, *Journal of Geophysical Research*, *83*(A2), 663–679, doi:10.1029/JA083iA02p00663. 44

Reiff, P. H., R. W. Spiro, and T. W. Hill (1981), Dependence of polar cap potential drop on interplanetary parameters, *Journal of Geophysical Research*, *86*(A9), 7639–7648, doi:10.1029/JA086iA09p07639. 133

Reistad, J. P., N. Østgaard, K. M. Laundal, and K. Oksavik (2013), On the non-conjugacy of nightside aurora and their generator mechanisms, *Journal of Geophysical Research: Space Physics*, *118*, 3394–3406, doi:10.1002/jgra.50300. 69

Rich, F. J., and M. Hairston (1994), Large-scale convection patterns observed by DMSP, *Journal of Geophysical Research*, *99*(A3), 3827–3844, doi:10.1029/93JA03296. 57

Richmond, A. D., and Y. Kamide (1988), Mapping electrodynamic features of the high-latitude ionosphere from localized observatories: technique, *Journal of Geophysical Research*, *93*(A6), 5741–5759, doi:10.1029/JA093iA06p05741. 48

Rishbeth, H. (1988), Basic physics of the ionosphere: a tutorial review, *Journal of the Institution of Electronic and Radio Engineers*, *58*(6S), S207, doi: 10.1049/jiere.1988.0060. 66

Rostoker, G. (1986), Comment on 'The poleward leap of the auroral electrojet as seen in auroral images' by Edward W. Hones, Jr., *Journal of Geophysical Research*, *91*(A5), 5879–5880, doi: 10.1029/JA091iA05p05879. 39

Ruohoniemi, J. M., and K. B. Baker (1998), Large-scale imaging of high-latitude convection with Super Dual Auroral Radar Network HF radar observations, *Journal of Geophysical Research*, *103*(A9), 20,797, doi:10.1029/98JA01288. 89

Ruohoniemi, J. M., and R. A. Greenwald (1996), Statistical patterns of high-latitude convection obtained from Goose Bay HF radar observations, *Journal of Geophysical Research*, *101*(A10), 21,743, doi:10.1029/96JA01584. 88, 89

Ruohoniemi, J. M., and R. A. Greenwald (2005), Dependencies of high-latitude plasma convection: Consideration of interplanetary magnetic field, seasonal, and universal time factors in statistical patterns, *Journal of Geophysical Research: Space Physics*, *110*(A09204), doi:10.1029/2004JA010815. 80

Ruohoniemi, J. M., R. A. Greenwald, K. B. Baker, J.-P. Villain, C. Hanuise, and J. Kelly (1989), Mapping High-Latitude Plasma Convection With Coherent HF Radars, *Journal of Geophysical Research*, *94*(A10), 13,463–13,477, doi:10.1029/JA094iA10p13463. 60, 63

Russell, C. T., and R. L. McPherron (1973), Semiannual variation of geomagnetic activity, *Journal of Geophysical Research*, *78*(1), 92–108, doi:10.1029/JA078i001p00092. 42, 53

Sandholt, P. E., C. J. Farrugia, J. Moen, and B. Lybekk (1998), The Dayside Aurora and its Regulation by the Interplanetary Magnetic Field, in *Polar Cap Boundary Phenomena, Proceedings of the NATO Advanced Study Institue*, edited by J. Moen, A. Egeland, and M. Lockwood, pp. 189–208, Kluwer Academic Publishers, Longyearbyen, Svalbard, Norway. 32

Schunk, R. W., and A. F. Nagy (2000), *Ionospheres - Physics, Plasma Physics and Chemistry*, Cambridge University Press, Cambridge, UK. 9, 10, 11

Sergeev, V. A., E. M. Sazhina, N. A. Tsyganenko, J. Å. Lundblad, and F. S∅raas (1983), Pitch-angle scattering of energetic protons in the magnetotail current sheet as the dominant source of their isotropic precipitation into the nightside ionosphere, *Planetary and Space Science*, *31*(10), 1147–1155, doi:10.1016/0032-0633(83) 90103-4. 31, 121

Sergeev, V. A., R. J. Pellinen, and T. I. Pulkkinen (1996), Steady Magnetospheric Convection: A Review of recent results, *Space Science Reviews*, *75*, 551–604, doi:10.1007/BF00833344. 44, 47, 93, 107, 111

Sergeev, V. A., M. V. Kubyshkina, K. Liou, P. T. Newell, G. Parks, R. Nakamura, and T. Mukai (2001), Substorm and convection bay compared: Auroral and magnetotail dynamics during convection bay, *Journal of Geophysical Research*, *106*(A9), 18,843, doi:10.1029/2000JA900087. 47, 125, 126

Shirai, H., K. Maezawa, M. Fujimoro, T. Mukai, T. Yamamoto, Y. Saito, S. Kokubun, and N. Kaya (1997), Drop-off of the polar rain flux near the plasma sheet boundary, *Journal of Geophysical Researc*, *102*(A2), 2271–2278, doi:10.1029/96JA02600. 32, 33

Shue, J.-H., J. K. Chao, H. C. Fu, C. T. Russell, P. Song, K. K. Khurana, and H. J. Singer (1997), A new functional form to study the solar wind control of the magnetopause size and shape, *Journal of Geophysical Research*, *102*(A05), 9497–9511, doi: 10.1029/97JA00196. 54

Shukhtina, M. A., and S. E. Milan (2014), ECLAT System Level Data Product report (D430.1), *Tech. Rep. 2001*, doi:10.1007/978-90-481-3499-1. 56, 57, 70, 73, 74, 76, 77, 94, 105

Singer, S. F. (1957), A new model of magnetic storms and aurorae, *EOS Transactions, AGU*, *38*(2), 175–190, doi:10.1029/TR038i002p00175. 18

Siscoe, G. L., and T. S. Huang (1985), Polar cap inflation and deflation, *Journal of Geophysical Research*, *90*(A1), 543–547, doi:10.1029/ JA090iA01p00543. 26, 27, 63, 66

Sonett, C. P., E. J. Smith, D. L. Judge, and J. Coleman, P. J. (1960), Current Systems in the Vestigial Geomagnetic Field: Explorer VI, *Physical Review Letters*, *4*(4), 161–163, doi:10.1103/ PhysRevLett.4.161. 17

Sonnerup, B. U. Ö. (1974), Magnetopause Reconnection Rate, *Journal of Geophysical Research*, *79*(10), 1546–1549, doi:10.1029/JA079i010p01546. 33

Sundberg, K. Å. T., J. A. Cumnock, and L. G. Blomberg (2009), Reverse convection potential: A statistical study of the general properties of lobe reconnection and saturation effects during northward IMF, *Journal of Geophysical Research*, *114*(A6), A06,205, doi:10.1029/2008JA013838. 133

Vasyliunas, V. M. (1975), Theoretical Models of Magnetic Field Line Merging , 1, *Reviews of Geophysics and Space Physics*, *13*(1), doi:10.1029/RG013i001p00303. 23

Vaughan, S. (2013), *Scientific Inference: Learning from Data*, Cambridge University Press. 76, 137

Walach, M.-T., and S. E. Milan (2015), Are Steady Magnetospheric Convection Events Prolonged Substorms?, *Journal of Geophysical Research: Space Physics*, *120*, doi:10.1002/2014JA020631. 36, 45, 48, 77, 117, 122, 123, 125

Walach, M.-T., and S. E. Milan (2016), The irregular pulse of the magnetosphere, *Astronomy and Geophysics*, *57*(1), 1.34–1.36, doi:10.1093/astrogeo/atw041. 25

Walker, A. D. M. (1998), HF Radars as a Tool for Conjugate Studies of Magnetospheric Phenomena, in *Polar Cap Boundary Phenomena*, edited by J. Moen, A. Egeland, and M. Lockwood, pp. 141–156. 60

Wanliss, J. A., and K. M. Showalter (2006), High-resolution global storm index: Dst versus SYM-H, *Journal of Geophysical Research*, *111*(A2), A02,202, doi:10.1029/2005JA011034. 60

Wild, J. A., E. E. Woodfield, and S. K. Morley (2009), On the triggering of auroral substorms by northward turnings of the interplanetary magnetic field, *Annales Geophysicae*, *27*, 3559–3570, doi:10.5194/angeo-27-3559-2009. 105

Winningham, J. D., and W. J. Heikkila (1974), Polar cap auroral electron fluxes observed with isis 1, *Journal of Geophysical Research*, *79*(7), 949–957, doi:10.1029/JA079i007p00949. 32

Xu, L., A. V. Koustov, J. Thayer, and M. A. Mccready (2001), SuperDARN convection and Sondrestrom plasma drift, *Annales Geo-*

physicae, *19*(7), 749–759, doi:10.5194/angeo-19-749-2001. 89

Xu, L., a.V. Koustov, J. Xu, R. Drayton, and L. Huo (2008), A 2-D comparison of ionospheric convection derived from SuperDARN and DMSP measurements, *Advances in Space Research*, *42*(7), 1259–1266, doi:10.1016/j.asr.2007.06.044. 89

Yang, J., F. R. Toffoletto, and Y. Song (2010), Role of depleted flux tubes in steady magnetospheric convection: Results of RCM-E simulations, *Journal of Geophysical Research: Space Physics*, *115*(A00111), doi:10.1029/2010JA015731. 47, 125

Yokoyama, T., K. Akita, T. Morimoto, K. Inoue, and J. Newmark (2001), Clear Evidence of Reconnection Inflow of a Solar Flare, *The Astrophysical Journal Letters*, *546*, L69–L72, doi:10.1086/318053. 14